THE BOLIVIAN SUBANDES AND BEYOND:

LINKING WEDGE DEFORMATION PROCESSES ACROSS MULTIPLE TIMESCALES

A DISSERTATION SUBMITTED TO THE GRADUATE DIVISION OF THE UNIVERSITY OF HAWAIIʻI AT MĀNOA IN PARTIAL FULFILLMENT OF THE REQUIREMENTS FOR THE DEGREE OF

DOCTOR OF PHILOSOPHY

IN

GEOLOGY AND GEOPHYSICS

MAY 2016

By

Jonathan R. Weiss

Dissertation Committee:

James H. Foster, Chairperson
Benjamin A. Brooks
Garrett Ito
Gregory F. Moore
Clinton P. Conrad
Steven Businger

Keywords: mountain belt, orogenic wedge, Andes, Subandes, Bolivia, GPS, numerical modeling, reflection seismology, thrust fault, seismic hazard

ACKNOWLEDGEMENTS

I thank Ben Brooks for knocking on my office door in the summer of 2010 and offering me the opportunity to return to the field of active tectonics for my dissertation studies. The last five and half years have been tremendous. I've conducted rewarding field and laboratory work and made good friends in Bolivia and Argentina. I've been challenged to step outside of my comfort zone and have benefited both professionally and personally from Ben's guidance. I owe a debt of gratitude to my committee members and coauthors. In particular I thank James Foster for taking over as my primary advisor midway through my dissertation studies and for serving as my GPS guru. I also thank Garrett Ito for his mentorship and for the time and enthusiasm he has dedicated to our wedge modeling project. Greg Moore served on both my MS and PhD committees and has provided guidance and gentle nudges to maintain forward momentum. I thank the faculty, staff, and students of the Department of Geology and Geophysics at UH Manoa. I have had the pleasure to work and study on the 8th floor of POST for almost 16 years and have taken advantage of the open door policy. In particular I'd like to thank Brian Taylor and Steve Martel for providing me the opportunity to choose between MS projects in Marine Geophysics and Structural Geology when I arrived in 2000. I took the former and spent many years exploring the high seas but the latter has maintained a strong pull and this dissertation reflects the diverse set of skills I have acquired along the way due in no small part to the excellent education I have received from G&G professors including but not limited to Steve Martel, Paul Wessel, Janet Becker, Clint Conrad, Garrett Ito, and Neil Frazer. I thank Arjun Aryal, Samuel Howell, and Brian Boston for their help during my PhD studies and Kolja Rotzoll, Todd Bianco, and

Aisha Morris for their longstanding friendships and advice. I thank former colleagues at the NOAA Coral Reef Ecosystem Division and John Rooney in particular. John was a mentor, collaborator, coauthor, supervisor and most of all a friend. He will not be forgotten. Finally, I thank my family for their continued love, support, and patience. My wife, Julia, has been my rock during this process. I would not have made it here without her confidence and patience. The road has been challenging. We have navigated it successfully and now embark on the next chapter of our lives with our wonderful son Onno, who I also thank for his patience and cuteness.

ABSTRACT

Contractional wedges including subaerial fold-and-thrust belts and submarine accretionary prisms are fundamental features associated with mountain building and subduction and the largest earthquakes on Earth occur on the gently dipping fault planes (décollements) that underlie them. Despite a sound understanding of the basic mechanics that govern whole-wedge structure over geologic timescales and a growing body of studies that have characterized the deformation associated with historic to recent earthquakes, first order questions remain about wedge deformation processes active over intermediate seismotectonic timescales. In this dissertation I take a multidisciplinary approach to answering some of these questions while focusing on the active Subandean fold-and-thrust belt of southern Bolivia. In Chapter 1 I use elastic dislocation modeling of fault-related folds imaged in seismic reflection data to obtain probabilistic estimates of Bolivian wedge-front fault ages and slip rates. My results show that at least half and as much as all of the whole-wedge shortening rate is accommodated by wedge front fault system. The structures comprising this system pose a major source of seismic hazard. In Chapter 2 I use GPS data to examine the affect of subduction zone earthquakes on the backarc surface velocity field and to assess locking and strain accumulation rates on the Subandean décollement. The new velocity field reveals north to south changes in the deformation character of the backarc orogenic wedge including close to a factor of two decrease in the wedge loading rate and décollement locked width from north to south. A comparison of shortening rates over multiple timescales points towards a situation where the northern and southern wedge may be at different stages of the widening-thickening cycle. In Chapter 3 I use a

continuum mechanics-based, finite difference method to investigate the spatiotemporal distribution of deformation during orogenic wedge growth. Model wedges match first-order critical taper predictions, exhibit widening-thickening cycles similar to active wedges, and show that as much as 75% of surface faulting occurs in the wedge interior. I explain thrust fault formation near the surface and subsequent down-dip propagation using a simple elastic solution and relate model results to the protothrust zones of active submarine accretionary prisms.

TABLE OF CONTENTS

Acknowledgements ii

Abstract iv

List of Tables x

List of Figures xi

Chapter 1: Spatial and temporal distribution of deformation at the front of the Andean orogenic wedge in southern Bolivia 1

Abstract 1

1.1 Introduction 2

1.2 Tectonic Setting and Previous Work 6

1.3 Data and Approach 8

1.4 Quaternary Wedge-front Structures 9

1.5 Timing of Wedge-front Fault Initiation 11

1.5.1 Vertical Separation Diagrams 11

1.5.2 Conversion From Time to Depth 13

1.5.3 Growth Onset Age Estimates 13

1.5.4 Growth Onset Age Results 15

1.6 MTFS Fault Parameter Estimation 17

1.6.1 Elastic Dislocation Modeling 17

1.6.2 Dip-slip Estimates 24

1.6.3 Dip-slip Rate Estimates 28

1.6.4 Mandeyapecua Fault (MF) Dip-slip Rate Estimates 29

1.6.5 Composite Wedge-front Fault Slip Rate Estimates 33

1.7 Discussion 37

1.8 Conclusions 41

Acknowledgements 42

Figures 44

Appendix A 52

Appendix B 58

Chapter 2: Isolating active orogenic wedge deformation in the southern Subandes of Bolivia 67

Abstract 67

2.1 Introduction 68

2.2 Deriving the GPS Velocity Field 74

2.2.1 GPS Data Acquisition and Processing 74

2.2.2 Seasonal Signal Estimation 77

2.2.3 Plate Boundary Earthquake Perturbation and Characterization 78

2.2.4 Velocity Error Estimation 86

2.3 New Crustal Velocity Field for the Central Andean Backarc 88

2.3.1 Map-view Pattern 88

2.3.2 Velocity Profiles 89

2.3.3 Backarc Velocity Field Modeling 92

2.4 Discussion of Modeling Results 96

2.5 Conclusions 101

Acknowledgements 103

Figures 104

Appendix C 117

Chapter 3: Numerical models of accretionary wedge growth:

Insights on the evolution of surface faulting and the wedge front 127

Abstract 127

3.1 Introduction 128

3.2 Previous Work 131

3.3 Numerical Modeling Approach 133

3.4 Numerical Model Results 136

3.4.1 General Wedge Evolution 136

3.4.2 Wedge Taper Angles 137

3.4.3 Active Surface Faulting 138

3.4.4 Propagation of the Wedge Front 140

3.4.5 Top-down Thrust Formation 143

3.4.6 Stress Analysis and Cause of Top-down Propagation 145

3.5 Discussion 149

3.6 Conclusions 154

Figures 156

References 167

LIST OF TABLES

Table **Page**

Table A1 Growth Onset Age Estimates 53

Table 2.1 Corrected GPS Site Velocities 116

Table C1 Horizontal Reference Frame Site Statistics 123

Table C2 Tocopilla Earthquake Empirical Characterization Parameters 124

Table C3 White and Power Law Noise Statistics 125

Table C4 Uncorrected GPS Site Velocities 126

LIST OF FIGURES

Figure **Page**

Figure 1.1 Regional Location Map and Cross Section 45

Figure 1.2 Seismic Line and Well-log Locations and Neotectonic Fault Map 45

Figure 1.3 Vertical Separation Diagram Method 46

Figure 1.4 Growth Onset Age Results 47

Figure 1.5 Elastic Dislocation Modeling Method 48

Figure 1.6 Dip-slip Magnitude and Dip-slip Rate Probability Distributions 49

Figure 1.7 Mandeyapecua Fault Dip-slip Rates 50

Figure 1.8 Profile-based Analysis of Wedge-front Fault Slip Rates 51

Figure A1 Seismic Lines and VSD Examples 54

Figure A2 Fault Parameter Distributions 55

Figure A3 Modeling Results Using Offset Horizons 56

Figure A4 Profile-based Analysis Using Composite Dip-slip Rates 57

Figure B1 Elastic Dislocation Folds vs. Kinematic Folds 63

Figure B2 Area-of-Relief Method Applied to Guanacos Structure 64

Figure B3 Area-of-Relief Method Applied to Synthetic Folds 65

Figure B4 Plane-strain Assumption Test 66

Figure 2.1 Interseismic GPS Velocity Field 104

Figure 2.2 North and East Seasonal Signals 105

Figure 2.3 North, East, and Up Annual Seasonal Cycles 106

Figure 2.4 North, East, and Up Semiannual Seasonal Cycles 107

Figure 2.5 Eastward Displacements for Earthquake-affected Sites 108

Figure 2.6 Simplified Tocopilla Earthquake Affect 109

Figure 2.7 Typical Subduction Zone Earthquake-affected Timeseries 110

Figure 2.8 Eastward Components of Timeseries for Select Sites 111

Figure 2.9 New Central Andean Backarc Velocity Field 112

Figure 2.10 Profile Views of Velocity Field 113

Figure 2.11 Elastic Dislocation Modeling Results 114

Figure 2.12 Shortening Rate Estimate Comparison 115

Figure C1 Horizontal Reference Frame Site Velocities 118

Figure C2 Up Seasonal Signals 119

Figure C3 Pre-Tocopilla Site Velocities 120

Figure C4 Postseismic Amplitudes and Comparison with Seismological Results 121

Figure C5 Uncorrected vs. Corrected Velocity Profiles 122

Figure 3.1 Numerical Model Setup and Example Model Run 156

Figure 3.2 SiStER Wedges with Variable Basal Strengths 157

Figure 3.3 SiStER Surface Slope Evolution 158

Figure 3.4 Surface Faulting Distribution 159

Figure 3.5 Wedge-front Propagation 160

Figure 3.6 New Thrust-front Fault Formation 161

Figure 3.7 Stress State in Front of the Wedge 162

Figure 3.8 SiStER Wedge Basal Shear Stress 163

Figure 3.9 Theoretical vs. Model Length Scale "L" 164

Figure 3.10 Real-world Examples of Near Surface Thrust Fault Formation 165

Figure 3.11 SiStER Viscous Upper Layer Model Time Steps..... 166

Chapter 1

Spatial and temporal distribution of deformation at the front of the Andean orogenic wedge in southern Bolivia

Published as:

Weiss, J. R., B. A. Brooks, J. R. Arrowsmith, and G. Vergani (2015), Spatial and temporal distribution of deformation at the front of the Andean orogenic wedge in southern Bolivia, *Journal of Geophysical Research: Solid Earth*, *120*(3), 1909-1931, doi:10.1002/2014JB011763

Key points:

- We provide probabilistic estimates of fault ages and slip rates for the ~400-km-long Subandean orogenic wedge-front fault system in southern Bolivia
- At least half and as much as all of the previously determined wedge-loading rate is accommodated at the wedge-front
- The wedge-front faults pose a major source of seismic hazard to the region

Abstract

New observations from an active orogenic wedge help link the seismotectonic behavior of individual faults to wedge deformation rates and patterns over multiple timescales. We provide the first detailed constraints on the distribution and timing of deformation at the front of the Andean orogenic wedge in southern Bolivia, where a recent study suggests that great ($M_w > 8$) earthquakes could rupture the master fault underlying the wedge. We use stratigraphic relationships across fault-related folds and elastic dislocation modeling of seismic reflection horizons to obtain probabilistic estimates of

wedge-front fault ages and slip rates. Our analyses reveal that at least half of the previously determined GPS-based wedge-loading and Quaternary whole-wedge shortening rates are absorbed across a 20-40-km-wide wedge-front zone consisting of 1-4 en-echelon and partially to fully overlapping faults and folds associated with blind thrust faults. The difference between our slip rates and the geodetic/geologic observations combined with evidence for activity across internal wedge structures supports the notion that non-steady state mass balance conditions coupled with elevated erosional efficiency result in distributed wedge deformation. The orogenic wedge in southern Bolivia behaves in a similar fashion to the Taiwanese and Himalayan ranges; slip accumulates at down-dip locations along the master fault and is released incrementally by earthquakes that rupture the wedge-front fault zone. The faults and folds comprising this zone pose a major source of seismic hazard. Accumulating slip is also released in the wedge interior and older, internal wedge faults must be considered in any future assessment of regional earthquake risk.

Keywords: orogenic wedge deformation, Subandes, Bolivia, seismic hazard, continental neotectonics

1.1 Introduction

The largest earthquakes on Earth occur on the gently dipping fault planes that underlie contractional orogenic wedges [*Kanamori*, 1977; *Kumar et al.*, 2010]. Of the 10 largest events ever recorded, 9 occurred in submarine accretionary prisms and 1 occurred

in a subaerial fold and thrust belt [*Chen and Molnar*, 1977; *Hsu et al.*, 2006; *Kanamori*, 1977; *Lay et al.*, 2005; *Stein and Toda*, 2013]. Because low-angle thrust faults cut through a thicker portion of the brittle crust compared to higher-angle faults, more fault area is available for rupture, resulting in greater coseismic moment release [*Scholz*, 1998]. Theoretical understanding of contractional wedges has focused mostly on their evolution over timescales much greater than typical earthquake cycles [*Dahlen*, 1990; *Davis et al.*, 1983]. Recently, however, a conceptual framework for incremental wedge deformation has arisen that considers depth-dependent frictional properties of the master fault, or décollement, underlying the wedge [e.g. *Avouac*, 2008; *Hu and Wang*, 2008; *Scholz*, 1998; *Wang and Hu*, 2006]. In this view, velocity strengthening behavior and continuous slip characterize deeper portions of the décollement whereas velocity weakening and stick-slip behavior characterize the shallow, locked portions of the fault. The transition between these two zones is where earthquakes will tend to nucleate. Geodetic observations of surface displacement gradients crossing subaerial orogenic wedges are consistent with the inference of slipping-to-locked transitions along décollements causing elastic strain to accumulate within a wedge [e.g. *Bilham et al.*, 1997; *Brooks et al.*, 2011b; *Hsu et al.*, 2003].

How incremental slip is accommodated in a wedge can vary: rupture may reach the wedge front [*Fujiwara et al.*, 2011; *Ito et al.*, 2011; *Kido et al.*, 2011]; shallow folding may absorb the slip [*Lavé and Avouac*, 2000; *Simoes et al.*, 2007b]; or variously oriented splay faults might break [*Hubbard and Shaw*, 2009; *Melnick et al.*, 2012; *Moore et al.*, 2007; *Pflaker*, 1972]. In the Himalayas, for example, there is the suggestion that the majority of

the accumulating strain is released along a single thrust-front structure [*Lavé and Avouac*, 2000] whereas up to three frontal structures appear to be active in Taiwan [*Hsu et al.*, 2009; *Simoes et al.*, 2007a]. Further, recent observations of great earthquakes reveal that postseismic afterslip can occur either up-dip [*Hsu et al.*, 2006] or down-dip [*Lin et al.*, 2013; *Paul et al.*, 2007] from the main event and account for significant amounts of energy release.

Determining where fault slip is likely to occur in a wedge is challenging but particularly important for estimating the seismic potential, ground motions, and earthquake hazards for population concentrations near active fold-and-thrust belts such as the Himalayas [*Bilham et al.*, 2001], Taiwan [*Simoes et al.*, 2007a], and the eastern margin of the Andes [*Brooks et al.*, 2011b]. Both analogue and numerical models of wedge deformation are capable of resolving discrete strain localization and deformation on individual faults or fault-bend folds with complex movement histories influenced by stratigraphic and other heterogeneities [e.g. *Adam et al.*, 2005; *Cubas et al.*, 2008; *Mary et al.*, 2013a; *Stockmal et al.*, 2007]. Coupled climate-tectonic models [e.g. *Cruz et al.*, 2010; *Hilley and Strecker*, 2004; *Mary et al.*, 2013b; *Whipple and Meade*, 2004] also provide some guidance and indicate that the balance between accretionary (F_A) and erosional (F_E) flux determines where deformation is to be expected in an active subaerial wedge. In general, high erosion rates result in narrow mountain belts (e.g. Taiwan and New Zealand) whereas more slowly eroding orogens will be wider (e.g. the southern Subandes of Bolivia). Non-steady wedges ($F_A \neq F_E$) having larger F_A or smaller F_E will attain greater widths by means of

cratonward propagation [*Brooks et al.*, 2011b; *Whipple and Meade*, 2004]. Alternatively, when $F_A<F_E$, wedge width will decrease, as has been postulated for the northern Subandes of Bolivia [*McQuarrie et al.*, 2008b]. Numerical models based on the minimum work approach [e.g. *Del Castello and Cooke*, 2007; *Masek and Duncan*, 1998] suggest that unsteady mass balance conditions ($F_A>F_E$) promote widely distributed deformation along several faults whereas steady-state wedges ($F_A=F_E$) exhibit focused deformation on a limited number of wedge-front structures [*Yagupsky et al.*, 2014].

The models described above are useful for predicting deformation patterns over geologic timescales but are limited in their ability to address earthquake cycle deformation. Recently, DeDontney and Hubbard [2012] combined critical wedge theory with dynamic rupture models to provide theoretical constraints on the likely path of rupture propagation during a wedge earthquake. They showed that fault frictional strength, stress state, and intersection angle dictate whether or not rupture will be confined to the basal surface or will propagate onto a fault branch. Dynamic wedge rupture models are still in their infancy and require detailed knowledge of the wedge stress state and fault geometry. However, they have the potential to enhance our ability to relate the seismic cycle to long-term wedge deformation and to assess where and how wedge earthquake rupture will occur.

Despite the advances mentioned above, more observations of active wedge deformation are needed to test model predictions and place results from heavily studied locales (e.g. Taiwan and the Himalayas) in a global context. The principal objective of this

paper is to constrain the timing, magnitude, and rates of fault slip towards the up-dip limit of an active orogenic wedge and to compare these results with the geodetically-derived slip accumulation rate. We focus on the tip of the active fold-and-thrust belt comprising the Southern Subandes of Bolivia (SSA) where *Brooks et al.* [2011b] suggest that great *(M_w* > 8) events could rupture large portions of the master décollement. We derive probabilistic estimates of the initiation ages and slip rates of the active wedge-front faults and relate our results to observations from other active wedges, emerging views on incremental wedge deformation, and regional seismic hazard.

1.2 Tectonic Setting and Previous Work

Ongoing subduction of the Nazca plate beneath South America drives the rise of the Andes Mountains. The megathrust earthquakes that occur along the western margin of the mountain belt are one manifestation of this convergence [*Kanamori*, 1977; *Moreno et al.*, 2010; *Norabuena et al.*, 1998]. Crustal shortening across the Andean backarc orogenic wedge, which includes the Eastern Cordillera, Interandean Zone, and Subandes (Figure 1.1) has led to ~250 km of contraction since ~45 Ma including a Neogene phase focused primarily in the Subandes [*Baby et al.*, 1997; *Dunn et al.*, 1995; *McQuarrie*, 2002b]. The ~500-km-long thin-skinned fold-and-thrust belt of the SSA is the surface manifestation of this episode of backarc deformation.

Recent studies focused on the structure and timing of faults comprising the Subandean fold-and-thrust belt have established that since ~8.5-12.5 Ma deformation has

progressed primarily from west to east via a series of east-verging thrust faults that root in a shallow-dipping décollement (Figure 1.1) [e.g. *Echavarria et al.*, 2003; *Gubbels et al.*, 1993; *McQuarrie*, 2002b; *McQuarrie et al.*, 2005; *Uba et al.*, 2009]. The ~60-100 km of crustal shortening estimated for the SSA [*Dunn et al.*, 1995; *Giraudo and Limachi*, 2001; *McQuarrie*, 2002b; *Uba et al.*, 2009] is facilitated by a thick sequence of laterally continuous Paleozoic-Mesozoic marine sediments with detachment horizons that promote thin-skinned tectonics and the formation of continuous folds, cored by thrust faults that cut the entire sedimentary section and extend along nearly the full length of the orogenic wedge [*Dunn et al.*, 1995; *Giraudo and Limachi*, 2001; *McQuarrie*, 2002a]. The marine sequence is overlain by ~7.5 km of late Cenozoic siliclastic sediments deposited when deformation was focused in the Eastern Cordillera [*Uba et al.*, 2009].

There is general agreement that the wedge-front structure(s) formed at ~1.5-2.7 Ma and that the SSA Plio-Quaternary deformation rate is ~7-13 mm/yr [*Echavarria et al.*, 2003; *Mugnier et al.*, 2006; *Oncken et al.*, 2007; *Uba et al.*, 2009]. However, there is no consensus regarding how this deformation is currently distributed. Further, the rapid eastward decrease in GPS horizontal velocities across the SSA from ~10 mm/yr on the central Andean Plateau to ~0 mm/yr on the foreland Chaco plain (Figure 1.1) and limited evidence for recent deformation on older Subandean structures suggests strain accumulation beneath the Subandean belt and strain release in earthquakes as large as M_w > 8 along the frontal thrust fault system [*Brooks et al.*, 2011b] similar to what has been proposed for Taiwan and the Himalayas [*Avouac*, 2008]. The large seismic potential

estimated for the SSA is partially attributed to its great width (>100 km), which has formed in response to low rates of erosion and precipitation over the Neogene Period, and non-steady mass balance that promoted rapid wedge widening [*Horton*, 1999; *Masek et al.*, 1994; *McQuarrie et al.*, 2008a; *Montgomery et al.*, 2001].

Despite these results and evidence, including newly identified faulted late Holocene surfaces, of recent activity across multiple wedge-front faults [*Brooks et al.*, 2011b; *Lavenu et al.*, 2000; *Orme et al.*, 2015], there is no historical earthquake record of earthquakes >M_w 5 associated with the frontal fault system. Other than an analysis of the morphology of the range-crossing Rio Pilcomayo to infer recent thrust fault activity [*Mugnier et al.*, 2006] and the identification of eroding hanging wall terraces in a few satellite images [*Lamb*, 2000] no detailed neotectonic studies exist. Additionally, despite numerous published structural cross-sections there is no unifying map-view depiction of or nomenclature for SSA wedge-front structures.

1.3 Data and Approach

Our study utilizes industry-acquired seismic reflection lines covering much of the SSA wedge front (Figure 1.2). These data are a combination of publicly available lines, some of which have been previously published [e.g. *Dunn et al.*, 1995; *Moretti et al.*, 1996; *Uba et al.*, 2009], and proprietary data stored in-house at PlusPetrol S.A. We focus on the lines located between the easternmost range-front faults and the adjacent lowland sedimentary basin. Structures occupying this zone are characterized by low surface relief compared to

the thrust faults and associated anticlines to the west. A subset of the seismic data, oriented perpendicular to the strike of the wedge-front faults, image the foreland sediments folded into broad fault-related anticlines and horizons that exhibit thinning and other geometries characteristic of syn-depositional folding.

Our general approach, discussed in detail below, is to first map the distribution of wedge-front faults by identifying stratigraphic layers deposited during fault slip and associated fold growth. These so-called growth strata [*Suppe et al.*, 1992] are used in combination with regional sedimentation rates to determine the timing of initiation of fault-related folding. We then use elastic half space modeling [*Meade*, 2007; *Okada*, 1985; 1992] of subsurface folds imaged in the seismic data and the timing results to compute fault slip rates. Although there are many fault-related fold models, we choose to use dislocations in an elastic half space because the method is well-suited for modeling geologic structures that result from repeated earthquakes [*Ellis and Densmore*, 2006; *Healy et al.*, 2004b; *King et al.*, 1988; *Stein et al.*, 1988] and so that we may frame the entire problem in a probabilistic manner and derive probability distributions of the fault model parameters [e.g. *Bird*, 2007; *Brooks and Frazer*, 2005; *Zechar and Frankel*, 2009].

1.4 Quaternary Wedge-front Structures

We present a new map of the SSA wedge-front fault system based on the structures identified in seismic reflection data, surface fault traces apparent in satellite-derived (SRTM) topography, and a low-altitude over-flight of the thrust front (Figure 1.2).

Previously published fault maps for the region typically show a simplified fault geometry including the Mandeyapecua fault (MF) as a single structure extending from north to south for nearly 500 km or few, incorrectly located fault segments [e.g. *Barnes and Heins*, 2009; *Dunn et al.*, 1995; *Giraudo and Limachi*, 2001; *Lamb*, 2000; *McQuarrie*, 2002b; *Uba et al.*, 2009]. Our new fault map illustrates that the SSA thrust-front is composed of multiple en-echelon and partially to fully overlapping faults and folds associated with blind thrust faults. We refer to these faults as the Mandeyapecua thrust fault system (MTFS).

Fault-related topography varies along-strike; the same fault is expressed as a continuous scarp in some locations and buried with no surface expression in others. The most prominent example of this variability is related to the MF, which is the longest wedge-front fault extending from north to south for ~300 km. The southern portion of the fault crosses a broad topographic high bounded by the Ibibobo fault and associated scarp to the east and the Tiguipa fault and associated buried fold to the west. MF-related topography dies off dramatically near the Rio Parapeti. The fault creates a sinuous scarp for ~50 km near 20°S and discontinuous outcrops of back-dipping strata visible in the SRTM data combined with fault/fold scarps crossing actively farmed fields help map the trace of the MF across this central portion of the wedge-front. The MF disappears in the subsurface at ~19.5°S before reemerging at ~19°S. Additional structures associated with topography that varies along strike include the Rio Seco, Guanacos, and Ibibobo faults. The Tacobo/Curiche, Ubicuy, San Lorenzo, Tiguipa, and La Vertiente faults do not create surface topography and are identified by the presence of subsurface folds in the seismic data.

1.5 Timing of Wedge-front Fault Initiation

1.5.1 Vertical Separation Diagrams

Stratigraphic relationships across the fault-related folds allow us to constrain the timing of growth onset of the SSA wedge-front structures. Sediments deposited prior to deformation are sub-horizontal and laterally continuous. When a thrust fault initiates at depth and propagates up-section, previously deposited (pre-growth) horizons are folded but their thickness remains constant across the fold. Sediments deposited during fault growth, however, do not maintain a constant thickness but rather thin or pinch-out towards and across the fold axis. This thinning is due to a reduction in the accommodation space available for sediment deposition and/or elevated rates of erosion above the growing fold [*Burbank et al.*, 1996; *Burbank and Anderson*, 2012; *Davis et al.*, 1983; *Suppe et al.*, 1992]. Previous authors have demonstrated the possibility of reconstructing fold growth kinematics using the geometry of growth strata [*Cardozo and Brandenburg*, 2014; *Suppe et al.*, 1992; *Vergés et al.*, 1996]. We are interested in determining the onset of fault-related folding to constrain MTFS timing. We accomplish this by identifying growth strata in the seismic lines and creating a series of vertical separation diagrams (VSD) (Figures 1.3 and A1).

The VSD is based on the idea that information about the sedimentary and tectonic history of a region can be gained by analyzing the depth to stratigraphic horizons above growing structures [*Bischke*, 1994; *Suppe et al.*, 1992]. The approach was successfully used to constrain the growth onset ages of the southern continuation and termination of the

southern Subandes in northwestern Argentina [*Echavarria et al.*, 2003]. In general, the VSD is created by measuring the vertical distance between the surface and layers of the same age at two different locations and plotting this distance versus the total vertical depth to the structurally higher location [*Bischke*, 1994]. When sedimentation rates are equal in the two locations, the vertical separation between layers of different ages will remain constant throughout the sedimentary (seismic) section. However, if sedimentation rates differ the VSD will show an inflection. The change in structural conditions that occurs above a growing fold is one way to alter the sedimentation rate.

To construct the VSD's, we identify seismic lines where growth strata are evident, digitize horizons deposited prior to and during deformation, measure the vertical distance from the surface to the digitized horizon on or adjacent to the fold crest and on the fold limb, subtract the two values and plot this difference in two-way travel time (TWTT) versus the TWTT of the horizon on or adjacent to the fold crest (Figures 1.3 and A1). The resulting VSD's exhibit common characteristics. Deeper in the seismic section, the vertical separation between points on and away from the folds are typically constant within a few tens of milliseconds (TWTT). Near the shallow portion of the folds the separation between adjacent points decreases sharply. This abrupt decrease in vertical separation indicates the initiation of fault-related folding and we interpret inflections or kinks in the VSD to represent new subsurface fault formation.

1.5.2 Conversion from Time to Depth

The VSD method was originally proposed for locations with depth and/or age control [*Bischke*, 1994]. However, due to the lack of depth-converted seismic data for the SSA, we use well-log information to convert the horizon picks from TWTT to depth. We incorporate ~70 well-logs located east of fold-and-thrust belt between the range front and the adjacent lowlands in our analysis (Figure 1.2). Some of the well-log depths have been correlated with the seismic data multiple times and we include all of these to create a dataset consisting of 372 separate depth-TWTT curves. To account for along-strike variations in sediment velocity we gather well-logs that fall within one latitudinal degree bins and create depth-TWTT curve envelopes by fitting polynomial functions to the two curves that encompass the entire range of data within each bin. For the southern MTFS, since no well-logs are located from 21-22° S, we create a well-log envelope that includes picks from 20-23° S. Minimum and maximum depths for each VSD kink are then computed using the corresponding well-log envelope (Figure 1.3).

1.5.3 Growth Onset Age Estimates

Ideally, ages are assigned to growth onset based on stratigraphic correlation. However, since the shallowest dated horizon in our study area is the 2.1±0.2 Ma base of the Emborozú Formation [*Uba et al.*, 2006; *Uba et al.*, 2009], we estimate a range of growth onset ages for each structure using regional sedimentation rates for the SSA combined with the minimum and maximum depths described above. The locations where we apply the VSD analysis are situated between the mountain front, where the Emborozú Formation

reaches a maximum thickness of ~2000 m, and the 1000 m Emborozú Formation isopach contour [*Barnes and Heins*, 2009; *Uba et al.*, 2006]. We divide the formation thickness (1000-2000 m) by the formation age (1.9-2.3 Ma) to compute a sedimentation rate range of 0.435-1.053 mm/yr. For comparison, this range straddles the average Neogene sediment accumulation rate of ~0.714 mm/yr [*Uba et al.*, 2007]. We use the isopach-based rates instead of the average rate for two reasons. First, incorporating the variation in sediment thickness and uncertainty in the age information falls more in line with the probabilistic approach we adopt in our analyses. Second, the isopach-based range in sedimentation rates is more representative of the along-strike variability expected in a depositional system where a climate-induced north to south decrease in erosion and rainfall has been in place for at least the past few Myr [*Barnes et al.*, 2012; *Strecker et al.*, 2007b].

We convert the TWTT's associated with the VSD kinks to minimum and maximum depths using one-way travel times (½ × TWTT) and the corresponding well-log envelopes. We convert these depth estimates to minimum (maximum) growth onset ages ($A_{min(max)}$) by dividing the minimum (maximum) depths ($D_{min(max)}$) by the maximum (minimum) sedimentation rates ($S_{max(min)}$) using the 0.435-1.053 mm/yr range in sedimentation rates described above (Figure 1.3):

$$A_{min(max)} = \frac{D_{min(max)}}{S_{max(min)}}. \tag{1.1}$$

1.5.4 Growth Onset Age Results

The map view of MTFS growth onset ages provides regional constraints on the timing and pattern of SSA wedge-front deformation (Figure 1.4 and Table A1). Our analysis indicates that the wedge-front fault system initiated between 150-2350 ka, which generally agrees with previous estimates of wedge-front structure formation at ~1.5-2.7 Ma [*Echavarria et al.*, 2003; *Mugnier et al.*, 2006]. No definitive spatial patterns emerge from the growth onset age map but there are indications that structures in the south are generally slightly older than those in the north. The age range of the southern faults, including, from west to east, La Vertiente, Tiguipa, Mandeyapecua, and Ibibobo is 350-2340 ka whereas the age range of the northern structures is 215-1900 ka. Although there is significant overlap in these age ranges, the La Vertiente structure and portions of the Mandeyapecua fault are clearly older than any of the northern structures. The difference in growth onset ages between the northern and southern wedge front is apparent when focusing on the MF and the 1.5 Ma initiation age estimated by *Uba et al.* [2009] in the south and our growth onset age range of 288-1387 ka for the northern tip of the fault.

An exception to the difference described above is apparent in the San Lorenzo structure, the easternmost fault in our study area. The relatively young age range of 156-786 ka indicates a recent phase of deformation and central wedge-front widening as subsurface faulting and associated low-amplitude folding propagates eastward into the foreland basin sediments. The San Lorenzo structure appears similar to the wedge-front

Jollín structure in northern Argentina [*Ramos et al.*, 2004], which is a subsurface fault with little to no surface expression located ~10 km to the east of the emergent wedge-front faults. Both are presumably the youngest Subandean structures in the region. In addition to San Lorenzo, some of the youngest minimum growth onset ages are also associated with the Guanacos and Ibibobo faults indicating that in general the easternmost MTFS structures may be the youngest.

The regional view of growth onset indicates that north of ~19.25° S all of the structures initiated between 216-1900 ka. However, in detail the northern portion of the study area (Figure 1.4) reveals more complexity than what is suggested by the regional view. For example, where Line 3138-26 crosses overlapping structures, the Rio Seco and Tacobo/Curiche faults appear to have formed nearly synchronously at 352-1770 ka whereas the age range for the adjacent portion of the Guanacos fault is slightly younger (309-1499 ka). To the south, where Line 5072-21 crosses the study area, the Tacobo/Curiche fault is older than the flanking portions of both the Ubicuy and Guanacos faults.

Where more than one growth onset age estimate is available for individual structures, subtle along-strike variations in fault timing also exist. For example, we estimate growth onset ages in 6 locations along the Guanacos fault (Figure 1.4). The oldest ages (358-1718 ka) are located near the center of the fault (Line 5066-21) and the ages decrease to the north and south. However, with the exception of the one older age range

estimate, the portion of the fault north of the Rio Grande is of comparable age to the portion of the fault immediately south of the river alternatively indicating synchronous onset along almost the entire length of the fault with a more recent phase of southward propagation of the buried portion of the fault where the age is youngest (216-1073 ka on Line 5072-21).

In summary, the growth onset ages do not indicate any particular style of fault growth. No distinct patterns emerge that definitively indicate SSA wedge-front faulting has progressed from west to east or vice versa Rather, the growth onset ages reveal a random pattern of fault initiation for both the northern and southern portions of the study area. There are, however, subtle indications that 1) wedge-front faults in the south are slightly older than those in the north and 2) the easternmost structures including San Lorenzo and portions of Ibibobo and Guanacos are the youngest faults across the MTFS.

1.6 MTFS Fault Parameter Estimation

1.6.1 Elastic Dislocation Modeling

Stratigraphic relationships across fault-related folds combined with velocity models from well-logs and regional sedimentation rates constrain the timing of growth onset for wedge-front structures. However, the seismic data typically do not directly image the faults. We further explore fault geometries and slip parameters associated with the displacement fields of seismic reflection horizons using elastic dislocation theory (Figure 1.5).

Dislocations in a homogenous linear elastic half space have long been used to investigate the effects of the earthquake cycle including derivation of fault parameters and associated coseismic, postseismic, and interseismic displacement fields that closely match surface measurements [e.g. *Bevis et al.*, 2001; *Bilham et al.*, 1997; *Brooks et al.*, 2003; *Okada*, 1985; *Savage*, 1983; *Vergne et al.*, 2001]. Despite the inherent infinitesimal strain assumption, elastic dislocation theory has also proven useful for investigating intermediate- to large strain phenomena formed by repeated earthquakes including surface and subsurface folding above blind thrust faults, precisely the features found at the leading edge of fold-and-thrust belts [*Benedetti et al.*, 2000; *Ellis and Densmore*, 2006; *Healy et al.*, 2004a; b; *Hilley et al.*, 2010; *King et al.*, 1988; *Myers et al.*, 2003; *Mynatt et al.*, 2007; *Shamir and Eyal*, 1995; *Stein et al.*, 1988; *Ward and Valensise*, 1994].

Here we adopt an approach similar to *Healy et al.* [2004b] who use the *Okada* [1992] method combined with a non-linear inversion technique to extract fault slip and fault geometry information from deformed stratigraphy on depth-converted seismic reflection data. *Healy et al.* [2004b] state that although fault-related folds are not initially obvious candidates, an elastic dislocation model yields results that are reproducible, geologically realistic, and consistent with direct seismic interpretations. Further, they show that when modeling large-scale, fault-related structures, the difference between a relaxed viscoelastic solution (perhaps more representative of the long-term mechanical behavior of fault-

related folds) and a purely elastic one is negligible and permits choice of the more computationally efficient (elastic) approach.

In addition to the studies mentioned above, which set the precedent for modeling fault-related folds using elastic dislocation theory, we prefer the elastic dislocation approach over other kinematic [e.g. fault-propagation and fault-bend folding; *Brandes and Tanner*, 2014] and geometric techniques [e.g. area-of-relief; *Epard and Groshong*, 1993; *Gonzalez-Mieres and Suppe*, 2006; 2011] because we find the former generally do a poor job of reproducing structures with smooth profiles like the SSA subsurface folds and the latter, when applied to our data, give unintuitive results suggesting the method may not be generally applicable. Geologic structures, including fault-related folds, form primarily as a result of the crustal deformation that accumulates during repeated earthquakes [*Ellis and Densmore*, 2006; *King et al.*, 1988; *Stein et al.*, 1988] with postseismic affects representing, typically, a small portion (~10%) of the total deformation field [*Stein and Ekstrom*, 1992]. Coseismic displacements are well predicted by purely elastic models [*King et al.*, 1988; *Stein and Barrientos*, 1985; *Stein and King*, 1984; *Stein et al.*, 1988] and repeated earthquakes that result in relatively small across-strike wavelength folds in regions of large continental crust thickness such as the SSA are probably not associated with much postseismic viscous relaxation. The folds imaged at the front of the SSA most likely represent the smoothed deformation field resulting from repeated slip events (earthquakes) on buried thrust faults. Therefore, an elastic model is a reasonable first approximation that yields predictions of surface displacement fields with accuracy

equivalent to the more computationally expensive viscoelastic or layered models [e.g. *Ellis and Densmore*, 2006; *King et al.*, 1988].

Finally, the computational efficiency associated with dislocations in an elastic half space permits us to investigate a large number of models and create probability distributions of the model parameters. These distributions provide estimates of the aleatoric errors associated with our particular model choice, data uncertainty, and also capture some of the variability introduced by our simplifying assumptions (e.g. plane strain). The distributions do not provide information on the epistemic uncertainties, which would require comparisons with other models (e.g. kinematic, viscoelastic, plastic, etc.) and is beyond our goal of providing first-order constraints on SSA wedge-front deformation.

To model the displacement field associated with each horizon we first identify and digitize horizons that can be confidently traced across folds imaged in the seismic reflection data. Next we depth convert the horizons using the well-log envelope-based velocity models resulting in minimum and maximum depths for each horizon. We compute the mean horizon depth and use the variation about the mean to construct the data covariance matrix C_d for subsequent analysis (Figure 1.5):

$$C_d = \begin{bmatrix} \begin{bmatrix} \sigma_x^2 & 0 \\ 0 & \sigma_y^2 \end{bmatrix}_1 & \cdots & 0 \\ \vdots & \ddots & \vdots \\ 0 & \cdots & \begin{bmatrix} \sigma_x^2 & 0 \\ 0 & \sigma_y^2 \end{bmatrix}_N \end{bmatrix} \tag{1.2}$$

where σ_X and σ_Z are the standard deviations in the horizontal (X) and vertical (Z), directions and N is the number of observation points along the horizon. Whereas the variations about the mean in the vertical (Z) direction come from the minimum/maximum horizon depths, we add a constant horizontal error equivalent to half the shot point interval to each observation point (+/- 25 m) for the horizontal (X) variations about the mean (Figure 1.5). We assume the horizontal and vertical variations about the mean are not correlated and therefore all non-diagonal entries in C_d are zero.

Our analysis requires a reference layer (or datum) that represents the position of both the model and data horizon prior to deformation. Following the method of *Healy et al.* [2004b], we define the reference layer by joining the extreme endpoints of the digitized horizons and extending this line out in both directions a specified distance in the plane of the seismic section. This definition of the reference horizon, which we use as input to the elastic dislocation modeling, typically preserves the gentle westward dip of the foreland stratigraphy (Figure 1.5).

We calculate displacements for positions along the reference layer by imposing uniform slip on dislocations embedded in a homogenous elastic half space. The relationship between the deformed horizon and the dislocation geometry is described by:

$$d = G(m) \tag{1.3}$$

where d is the deformation data vector, m is a vector of parameters describing the dislocation geometry and slip, and G is a matrix of Green's functions relating slip across the dislocation to deformation of the elastic half space.

In order to make the problem computationally tractable, we reduce the typical nine parameter problem to five by making the following simplifying assumptions: the dislocation is very long in the along-strike (Y) direction, the seismic section is oriented perpendicular to the strike of the dislocation, and there is no strike-slip component of displacement across the dislocation surface. These assumptions result in modeled deformation that is essentially plane strain. The remaining five dislocation parameters include 1) the position of the upper right hand tip (dx), 2) the depth, 3) the down-dip width, 4) the dip (θ), and 5) the magnitude of the dip-slip component of displacement (Figure 1.5). We further limit the parameter space by only permitting dip-slip motion in a reverse sense and allowing the position of the fault tip to vary only slightly with respect to the fold crest location. Finally, we define reasonable *a priori* ranges for each of the 5 free parameters (e.g. fault dip 10°-80°) and divide this range in to an equal number of increments resulting in n^p unique dislocations where n is the number of increments and p is the number of parameters.

For each dislocation we compute the deformed horizon position by adding the horizontal and vertical components of displacement to the regional horizon at predefined observation points. We quantify the misfit M using the weighted residual sum of squares:

$$M = \left[d - G(m)^T \right] C_d^{-1} \left[d - G(m) \right] \tag{1.4}$$

where *d* and *G(m)* in this case contain the X and Z coordinates of a digitized seismic horizon and a deformed model horizon corresponding to one particular dislocation geometry, respectively, and *d-G(m)* is the difference between these two horizons. For our residual sum of squares calculation, the model and data X coordinates are identical and *M* represents the vertical difference in Z between the two horizons. We compute *M* for the n^p dislocations, which results in a multi-dimensional matrix with each entry corresponding to the misfit associated with one unique dislocation (Figure 1.5). This grid search approach where we assess the goodness of fit between the data and the model for all the specified dislocations is possible because the number of model parameters is relatively small.

We obtain probabilistic estimates of the model parameter distributions by converting the misfit to probabilities using the following joint probability density function [e.g. *Menke*, 1989]:

$$p(d) \sim \exp\left\{ -\tfrac{1}{2} M \right\} \tag{1.5}$$

We use the joint probabilities *p(d)* to create marginal probability distributions (mpd) for each of the five dislocation parameters by summing the probabilities over each dimension of the parameter space except the parameter of interest for the marginal and scaling the resulting probability distributions so that the integrated probabilities are equal to one (Figure 1.5).

1.6.2 Dip-slip Estimates

We model subsurface folds in 25 separate locations and produce fault parameter mpds for each wedge-front structure (Figures 1.6 and A2). We focus on the dip-slip parameter because, combined with the growth onset ages, they provide dip-slip rates that can be directly compared to the long- and short-term slip rates determined from geology and geodesy respectively. We include probability distributions for the additional fault parameters in the auxiliary information (Figure A2). As with the growth onset ages described above, variations in the amount of dip-slip characterize the front of the SSA.

Peak model dip-slip magnitudes are all ≤2.5 km and most are <2 km. Along-strike variations in dip-slip mpd maxima occur where we compute more than one mpd for an individual structure (Figure 1.6 and A2). These variations often mimic the fault-related topography. For example, we estimate dip-slip in 7 locations along the mapped trace of the Guanacos fault. The mpd maxima gradually decrease from north to south with the highest values (≥2 km) located in the north where fault-related surface relief reaches a maximum of ~30 m. In contrast, for the mpds south of the Rio Grande, dip-slip mpd maxima are all ≤1.1 km and gradually decrease southward, where little if any surface relief is associated with the fault.

In addition to the Guanacos fault, other wedge-front structures exhibit along-strike variations in dip-slip magnitude. Two estimates are available for the Rio Seco structure. The northern mpd has a maxima at ~2 km and the southern <1 km. This along-strike

decrease in dip-slip mimics the southward decrease in fault-related topography. The Ibibobo fault exhibits the same pattern except that fault-related topography and dip-slip maxima decrease to the north. The Tacobo/Curiche, San Lorenzo, and Tiguipa faults are buried and associated with little if any surface relief. However, dip-slip maxima are larger for the estimates near the centers of the faults and decrease towards the fault ends. The along-strike patterns reflect the variation in the amplitudes of the corresponding subsurface folds imaged in the seismic reflection data.

Some dip-slip mpds have peaks close to 0 km including the two estimates associated with the Ubicuy fault and the southernmost estimates for the Tacobo/Curiche, Guanacos, and San Lorenzo faults. These correspond to folds with low-amplitudes and short wavelengths and indicate that very little slip has occurred across (portions of) the faults. Therefore the Ubicuy fault has not contributed much to regional deformation whereas the other faults with dip-slip peaks near 0 km have accumulated less slip near their ends than centers.

The dip-slip mpds in nearly all locations are positively skewed with the maximum probability and a short tail located near lower values of dip-slip and a longer tail extending towards the higher values. This occurs because we search only positive values of dip-slip associated with reverse slip across the dislocation surface. Imposing no slip results in a poor fit to the folded horizon, elevated misfit, and a correspondingly low probability. As we increase the amount of dip-slip, the fit improves and the probability increases until a peak

is reached. As we continue to increase the amount of dip-slip beyond the peak value and to unreasonable values the probability slowly decreases resulting in a positively skewed mpd. Additionally, we also attribute some of the positive skew to the trade-off between dip-slip and the width of the dislocation where high values of dip-slip and small dislocation widths result in misfit values comparable to the more geologically plausible combination of low values of dip-slip and larger dislocation widths

We use offset rather than continuous, folded horizons as input to the dislocation modeling in locations where the Mandeyapecua (see section 6.4) and La Vertiente faults have cut through and offset adjacent strata (Figure A3). In contrast to the positively skewed probability distributions that characterize the majority of our dip-slip estimates, Gaussian or nearly normally distributed mpds are associated with these two locations. The narrower and less-skewed probability distributions indicate that the offset strata limit the range of possible fault parameter results compared to locations where we model folded horizons.

In addition to the dip-slip estimates described above, we normalize the sum of the individual mpds for faults with more than one dip-slip estimate [*Zechar and Frankel*, 2009] to create composite dip-slip probability distributions (Figure 1.6). The composite mpds represent dip-slip distributions for the entire fault/structure and are typically multimodal due to the summing, which preserves the peaks of the individual mpds. Clear examples of

this multimodality can be seen in the individual and composite mpds for the Mandeyapecua, Guanacos, Rio Seco, and Tacobo/Curiche faults (Figure 1.6).

Wedge-front faults exhibit along-strike variations in fault width that mimic the dip-slip estimates described above (Figure A2). For example, both peak dip-slip and width decrease systematically from north to south along the Guanacos fault (Figure A2) as does fault-related surface topography. The Rio Seco structure exhibits similar correspondence between dip-slip, width, and surface topography. The width and dip-slip estimates for the Tacobo/Curiche structure also covary. We adopt the common simplifying assumption that modeled deformation is plane strain by making the dislocation length infinite in an along-strike (N-S) direction [e.g. *Ellis and Densmore*, 2006; *Healy et al.*, 2004b; *Stein and Ekstrom*, 1992] while recognizing that the real-world lengths of shallow crustal faults are finite. The covariance between dip-slip magnitude, dislocation width (and surface topography) that we observe along some of the wedge-front structures points towards their true, finite nature. Tests of the plane-strain assumption using finite-length dislocations show that we underestimate the slip magnitude only if observations come from the very edge of the fault. Although this appears to be the case in some locations (e.g. northern and southern ends of Ibibobo and Guanacos, respectively; Figure 1.6), when we consider the seismic line spacing, which is usually on the order of 2-5 km, all of our model sites are located far enough away from the fault ends that the plane strain assumption is valid.

1.6.3 Dip-slip Rate Estimates

We combine dip-slip magnitudes and ages by convolving the respective probability distributions to yield a dip-slip rate mpd for each location where we estimate fault parameters [e.g. *Bird*, 2007; *Zechar and Frankel*, 2009]. Our dip-slip mpds result from the elastic dislocation modeling whereas we represent the fault ages as boxcar distributions with the boxcar edges corresponding to the minimum and maximum growth onset ages from the VSD analysis (Figure 1.5). For structures where we have multiple growth onset ages, we create a composite, whole-fault age boxcar using the absolute minimum and maximum age estimates for the structure. We then convolve the composite dip-slip estimates with whole-fault growth onset age boxcars to create the composite dip-slip rate estimates (Figure 1.6).

In no location do the composite dip-slip rate mpd maxima exceed ~4 mm/yr (Figure 1.6). For faults with dip-slip peaks at ≤1 km, such as the Ubicuy fault, the resulting dip-slip rate peaks are ≤1 mm/yr. For faults with larger dip-slip maxima, such as the Guanacos and Percheles faults, the composite dip-slip rate mpd peaks are at 1-2 mm/yr. Other wedge-front fault dip-slip rate mpd peaks lie within the 0-4 mm/yr range.

As with the dip-slip distributions, the dip-slip rate mpds are positively skewed with the peak probability and a short tail located near lower dip-slip rate values and a longer tail extending towards the higher values. Since we start with asymmetric dip-slip mpds, we do not expect to see symmetric dip-slip rate distributions. Rather, convolution with the age

boxcars preserves or accentuates the skewed appearance of the resulting dip-slip rate mpds. Further, Bird [2007] shows that long-term geologic slip rates are typically not symmetric even when the probability distributions for slip and age are symmetrical because of the convolution of two independent random variables and in particular the partial derivatives that result from dividing the slip distribution by the age distribution. Slip values for active faults, often reported as a mean value with standard deviations, are represented by Gaussian mpds. When convolved with similarly symmetric or boxcar age distributions, the resulting slip-rate distributions are always skewed [*Bird*, 2007; *Toké et al.*, 2012; *Zechar and Frankel*, 2009]. For example, *Toké et al.* [2012] compute a positively skewed slip-rate distribution along a portion of the San Andreas fault with a Gaussian displacement and boxcar age distribution.

1.6.4 Mandeyapecua Fault (MF) Parameter Estimates

Despite the presence of newly identified SSA wedge-front structures, the MF is the longest and presumably principal active fault in the region (Figure 1.2). A large amount of inferred offset across the MF is manifest in the seismic data as steeply dipping horizons adjacent to the fault that typically terminate in a zone lacking seismic coherency where the fault breaches the surface making picking horizons for subsequent modeling difficult. This is the primary reason why we are unable to estimate growth onset ages for the central (and southern) portions of the MF using the VSD technique resulting in the conspicuous gap in growth onset ages from 19.25-20.75° S (Figure 1.4). Therefore, we derive dip-slip and dip-

slip rate estimates for the MF using a mix of VSD analysis, modeling results and published interpretations (Figure 1.7).

The seismic data image the northern tip of the MF between the adjacent Ubicuy and Tacobo/Curiche structures (see line 5049-21 location in Figure 1.4). There, stratigraphic thinning towards the MF permit a growth onset age range of 288-1387 ka (A1) to be calculated using the VSD method. Further, MF-related offset is small enough that we can confidently correlate horizons on both sides of the fault and model the deformation field to create a dip-slip mpd (D1; Figure A2). A combination of the VSD boxcar and dip-slip mpd yields a northern MF dip-slip rate distribution with a peak at ~0.8 mm/yr (A1∗D1, Figure 1.7).

The MF-related offset imaged in the seismic data and discontinuous surface scarps associated with the central MF further south suggest the northern estimate (D1) is not representative of the fault as a whole. Therefore, we use age information and an interpreted seismic reflection profile across the southern portion of the wedge front near 21° S from *Uba et al.* [2009] and balanced depth interpretations across the south-central and southern wedge front near 20.5° S and 21.25° S respectively from Dunn et al. [1995] (Figure 1.6) to help further constrain MF timing and slip.

Uba et al. [2009] provide estimates of the formation ages of major Subandean structures including the MF. They suggest that between ca. 4 and <2 Ma deformation

migrated eastward from the San Antonio range (San in Figure 1.1) across reactivated structures arriving at the MF at 1.5 Ma. We use this information to create a Gaussian age distribution for the MF with a mean of 1.5 Ma and a standard deviation of 0.5 Ma (A2; 1.5±0.5 Ma). We model the interpreted horizons from *Uba et al.* [2009], which have been correlated across the MF, and derive parameter distributions including a dip-slip mpd with a well-defined peak at ~2.5 km (Figure 1.6 and D2; Figure A2). We combine these two estimates to create a dip-slip rate mpd for the southern MF with a peak at ~1.5 mm/yr (A2∗D2, Figure 1.7).

A visual comparison of the digitized seismic horizons from *Uba et al.* [2009] and the dislocation model output reveals a poor fit with respect to footwall deformation (Figure A1.3). Additionally, a direct measurement of the slip across the MF using a depth-converted version of the horizons from *Uba et al.* [2009] indicates ~1 km of dip-slip on the MF, which is much less than the mpd peak rate of ~2.5 km for the same location. These difference likely result from the horizon we use for the dislocation modeling, which is folded across buried structures on both the fore- and back-limbs of the Mandeyapecua fault and presumably records the additional deformation associated with these structures (Figure A1.3). *Dunn et al.* [1995] present an interpretation for the MF near 21.25° S (Figure 1.6) with ~4 km of offset across the fault. To deal with these discrepancies we create an additional estimate of southern MF dip-slip by combining the direct measurements from the Uba et al. [2009] and *Dunn et al.* [1995] interpretations in a boxcar dip-slip distribution with the edges at 1 and 4 km (D3). We convolve the boxcar with the Gaussian age

distribution (A2; 1.5±0.5 Ma) resulting in a dip-slip rate mpd with a peak at ~1.3 mm/yr (A2∗D3, Figure 1.8).

For the central MF near 20.5°S we measure 6.75 and 7.5 km of slip from two balanced depth interpretations presented in *Dunn et al.* [1995] (Figure 1.6) and use these estimates to create a Gaussian slip distribution (D4; 7.125 ± 0.375 km). Since we have no corresponding age control for the central MF, we combine the northern VSD-based growth onset age range and the southern age information from *Uba et al.* [2009] to create a whole-MF boxcar age distribution with edges at 288 ka and 2 Ma (A3). We convolve these two distributions to create a dip-slip rate mpd with a peak located at ~3.9 mm/yr (A3∗D4, Figure 1.7), which is 3-4 times greater than the rate estimated for the northern and southern portions of the fault.

Using the information described above, we create additional MF dip-slip rate distributions by filling in the remaining entries of a 4x3 matrix composed of the 4 dip-slip and 3 age distributions resulting in 12 separate dip-slip rate estimates (Figure 1.7). After excluding the two smallest distributions with peaks near 0.5 mm/yr (A2∗D1 and A3∗D1), the largest distribution with a peak near 5.6 mm/yr (A1∗D4), and the widest distribution with no distinct peak (A1∗D3), the remaining distributions cluster in two groups including a minimum and maximum group with peaks less than and greater than 3 mm/yr respectively. We compute the mean distribution for each group and use them as MF dip-

slip rate end members (Figure 1.7), which we include in the composite, profile-based estimates described below.

1.6.5 Composite Wedge-front Fault Slip Rate Estimates

To facilitate a comparison of our fault dip-slip rates with independently estimated shortening and wedge-loading rates and to expand our analysis beyond individual structures we create wedge-front fault slip rate estimates for a series of thrust-front crossing profiles (Figure 1.8). The profile-based estimates can be thought of as summations of the individual fault-based estimates. Probability theory states that the probability distribution of the sum of two or more independent random variables is the convolution of their respective probability distributions [*Aster et al.*, 2005; *Bird*, 2007]. Therefore, we estimate composite slip rates for the wedge-front fault system by convolving the probability distributions of overlapping faults that intersect the profiles (Figure 1.8). In a statistical sense the slip-rate mpds are independent and a convolution is the proper way to combine the estimates from adjacent structures. We keep in mind, however, that the faults are likely connected at depth; either as branch faults and/or because they directly intersect the basal décollement. We convolve the individual mpds because we are interested in estimating the total wedge-front fault slip rate or how much slip has reached the MTFS over its lifetime. Instead of using the multimodal, composite dip-slip rate mpds (Figure 1.6) for the convolution, we create dip-slip rate distributions for each location where dislocation modeling was performed by convolving the individual dip-slip mpds (Figure A2) with the composite growth onset age boxcars resulting in probability distributions

with a single peak or distinct maxima (Figure 1.8). We use this approach to preserve the along-strike variations in dip-slip distributions that characterize faults with more than one estimate. However, where profiles cross faults with no co-located dip-slip mpd (e.g. Rio Seco in profile 2), we use the composite dip-slip mpds. We include profiles created using only the composite dip-slip rate mpds in the supplementary information (Figure A4).

We chose the profile locations so that each portion of the wedge front where we have information about fault behavior is represented in the analysis, to capture the observed along-strike variations in dip-slip for individual structures, and to provide a sense for how much total slip is absorbed by the wedge front fault system and if this amount varies along strike. The composite mpds (red distributions in Figure 1.8) generally have broad distributions with the peaks located to the right of the sum of the individual mpd peaks due to the weight that resides in their tails. In contrast, the convolution of purely Gaussian distributions would result in a composite mpd with a peak that is equal to the sum of the individual maxima.

Figure 1.8 shows the results of the profile-based analysis of dip-slip rates including a comparison with the long-term (several Myr) shortening rate of 7-13 mm/yr calculated from balanced cross sections [*Mugnier et al.*, 2006 and references therein] and the geodetically determined slip rate on the locked portion of the décollement beneath the SSA of ~10 mm/yr [*Brooks et al.*, 2011b]. These rates are comparable because we view the geologic and geodetic estimates as long- and short-term wedge-loading rates, respectively,

that can be accommodated by slip along any orientation of fault at any wedge location. Our composite, profile-based dip-slip rate estimates represent the portion accommodated at the wedge-front. For example, profile 1 intersects overlapping portions of the Percheles and Rio Seco structures. These two faults alone do not accommodate the long-term shortening rate because their dip-slip rate mpd peaks are much less than 7-13 mm/yr. The composite slip rate estimate for this profile is the convolution of the northern Rio Seco and Percheles fault mpds and the resulting distribution has a peak at ~4.6 mm/yr. Therefore only its tail overlaps the 7-13 mm/yr corridor indicating that, in this location, ~1/2 of both the mean geologic and geodetic shortening rates are absorbed by dip-slip motion at the wedge-front.

Profile 2 intersects the central Rio Seco and northern Guanacos faults. For the composite estimate we convolve the Rio Seco whole-fault dip-slip rate mpd and a Guanacos dip-slip rate mpd created by convolving the second from the north Guanacos dip-slip mpd (Line 3138-26, Figure 1.4 and Figure A2) with the whole-fault age boxcar (219-763 ka). Again, as with profile 1, neither the two faults alone or the composite estimate with a peak at ~4.5 mm/yr accommodate the long-term shortening or the modern wedge-loading rates.

We create the remaining profiles (3-8) in a similar fashion; dip-slip rate mpds on or near the profile locations are convolved to create the composite slip rate estimate. We use the composite dip-slip mpds for profile-fault intersections with no co-located dip-slip

estimate. A few additional points are worth mentioning. From west to east profile 4 intersects the Ubicuy, Mandeyapecua, Tacobo/Curiche, and Guanacos faults. However, we exclude MF from the profile 4 composite estimate because the profile crosses the very northern tip of the fault where the seismic data reveal MF-related offset restricted to deep in the seismic section and not extending to the shallow subsurface (MF? in Line 5072-12; Figure A1). The broad composite dip-slip rate mpd for profile 4 has no distinct maxima. Profiles 5-8 cross portions of the wedge-front with a larger inferred MF contribution and we include both the minimum and maximum mean dip-slip rate mpds in the composite estimates as dashed and solid distributions in Figure 1.8 respectively. For example, profile 6 intersects the Mandeyapecua and San Lorenzo faults. When we convolve the San Lorenzo dip-slip rate mpd with the minimum MF estimate, the composite mpd is broad with a peak at ~4.4 mm/yr. In contrast, the maximum MF-based composite estimate has a peak at ~7.9 mm/yr. Where the MF is the only wedge-front fault along portions of the central MTFS (e.g. 20-20.5° S), its maximum end-member rate accounts for ~1/2 of the independently estimated shortening rates.

In the south, the composite MTFS dip-slip rates are generally higher than in north. For example, the peak composite rates for profile 7 and 8 are ~7.3 (~10.55) mm/yr and ~10.7 (~13.9) mm/yr respectively using the minimum (maximum) MF mpds. For both of these the estimated MTFS dip-slip rate distribution peaks meet or surpass the GPS-derived wedge-loading and mean geologic shortening rates of ~10 mm/yr.

1.7 Discussion

Our analysis of the spatiotemporal distribution of SSA wedge-front deformation, combined with recent geodetic results [*Brooks et al.*, 2011b], yields a more complete view of how a major continental orogenic wedge accommodates deformation from time-scales ranging from a few years to hundreds of thousands of years. In particular, our observations help place constraints on emerging theories of incremental orogenic wedge deformation [e.g. *Cubas et al.*, 2008; *DeDontney and Hubbard*, 2012; *Del Castello and Cooke*, 2007; *Mary et al.*, 2013b; *Scharer et al.*, 2004; *Yagupsky et al.*, 2014]. Our principal finding is that, of the ~10 mm/yr of geodetically-determined slip accumulating towards the back of the wedge [*Brooks et al.*, 2011b], ~50% (in the north) and as much as 100% (in the south) is accommodated by the ~20-40-km-wide wedge-front zone comprising 1-4 faults and associated folds (Figure 1.8). The composite dip-slip rate estimates for all 8 of the profiles overlap the range in Quaternary shortening rates. These results suggest that although the wedge-front faults accommodate much of the geologic shortening, structures other than those at the wedge front are currently active [e.g. *Echavarria et al.*, 2003; *Lamb*, 2000; *Mugnier et al.*, 2006]. The presence and continuity of prominent fault scarps associated with the MTFS for a distance of at least 400 km along strike [*Brooks et al.*, 2011b] combined with our new results strongly suggests that earthquake ruptures reach the frontal fault zone.

Given the correspondence between cumulative slip rates at the wedge front, the Plio-Quaternary deformation rate, and the GPS-based wedge loading rate (Figure 1.8),

combined with the lack of large recorded or historical earthquakes, we can place some constraints on SSA earthquake behavior. If the accumulated slip at the back of the wedge is released in ~1 m slip events along the décollement, then the recurrence interval of these events would be ~100 years assuming a geodetically-determined slip accumulation rate of ~10 mm/yr. Based on standard earthquake scaling relationships [*Kanamori*, 1983; *Scholz*, 1998], this results in ~M_w 7.5 events. Alternatively, accumulated slip released in ~10 m slip events, results in a ~1000 year recurrence interval and >M_w 8 earthquakes. Given the lack of both historical earthquake records and paleoseismic investigations in the region it is difficult to place quantitative constraints on these estimates. We favor the large slip, long recurrence interval scenario since there is no record of major earthquakes. Regardless, based on the 150-2350 ka initiation age of the MTFS deduced from our VSD analysis (Figure 1.4), the wedge-front fault system is probably the result of thousands of earthquakes that have either ruptured the surface or resulted in growth folding. The active wedges in both the Himalayas and Taiwan exhibit a similar type of behavior with slip accumulation at down-dip locations along the basal décollement and coseismic rupture that breaks the locked segment and propagates to the wedge-front faults and folds [*Lavé et al.*, 2005; *Simoes et al.*, 2007a]. The major difference between these wedges and the SSA is that in both Taiwan and the Himalayas, where the loading rates are significantly faster, large wedge-front earthquakes have occured in the recent past [*Chen and Molnar*, 1977; *Kao and Chen*, 2000; *Kumar et al.*, 2010] and there is evidence suggesting they occur frequently with recurrence intervals of ~150-250 years (M_w 7-7.5) in Taiwan [*Dominguez*

et al., 2003] and ~500-3000 years in the Himalayas (M_w 8-9) [*Feldl and Bilham*, 2006; *Kumar et al.*, 2006].

We can now begin to interpret our observations as the time-integrated manifestation of earthquakes nucleating at down-dip positions along the décollement and propagating towards the surface with multiple potential branching points in the form of structures at the back, middle, and front of the wedge. *DeDontney and Hubbard* [2012] propose that the wedge stress state, and in particular contrasts in the static strength of the basal and branch faults, govern which path a dynamic rupture will take during a wedge earthquake. Although our results place no constraints on this process specifically, they do indicate that at least half of the slip reaches the wedge-front deformation zone, pointing towards the existence of a long-term (~Myrs) control on the rupture path of wedge earthquakes. This control might take the form of décollement and branch fault static frictional strength variations that drive dynamic rupture propagation either towards the wedge tip or the towards the older, internal wedge structures. One way that branch rupture could be inhibited is if the basal décollement is weak compared to the branch faults [*DeDontney and Hubbard*, 2012].

Similarly, although they do not explicitly model the dynamic earthquake rupture process, *Yagupsky et al. [2014]* use the minimum work approach [e.g. *Del Castello and Cooke*, 2007; *Masek and Duncan*, 1998] to investigate the affects of different mass balance conditions on the distribution of wedge deformation. They show that for a non-steady state

wedge ($F_A \neq F_E$) a relative increase in erosional flux (F_E), when compared to accretionary flux (F_A), will result in a phase of wedge deformation during which there is synchronous activity at the thrust front and on internal wedge structures. A comparison of Subandean denudation and accretion rates suggests an overall non-steady-state situation ($F_A >> F_E$) since at least ~6 Ma that favors wedge widening via eastward wedge-front propagation [*Brooks et al.*, 2011b]. Superimposed on this non-steady-state situation, however, is a relative increase in F_E in the form of elevated, monsoon-induced precipitation and erosional efficiency since the late Miocene [*Barnes et al.*, 2006; *Brooks et al.*, 2011b; *Strecker et al.*, 2007a; *Uba et al.*, 2009]. Therefore, our results, which indicate at least half of the deformation is absorbed by the frontal structures, combined with geomorphic evidence of activity across internal wedge structures (Figure 1.1) [*Echavarria et al.*, 2003; *Lamb*, 2000; *Mugnier et al.*, 2006] indicate that although wedge widening may characterize the overall SSA development, a relative increase in F_E could have resulted in a wedge with distributed fault activity.

In light of the modeling results discussed above, it appears that erosion, which acts to redistribute wedge material, and long-lived static stress conditions may be coupled across the SSA. This coupling between erosion and static stress could explain the deformation pattern revealed by our analysis. However, fault frictional properties can be quite variable over relatively small spatial and temporal scales [*Scholz*, 1998; *Wang and Hu*, 2006]. The growth onset age estimates, which indicate no definitive across-strike (west to east) pattern of fault activation across the MTFS, could be a manifestation of this variability

on a more local scale than the entire wedge. Earthquakes that nucleate at depth on the basal fault and propagate up-dip may chose a path determined by fault frictional conditions that vary either randomly, over the hundred thousand year time scale of our observations, or with each slip event. There are few theoretical studies that address the expected activity of individual faults and folds in an orogenic wedge over this intermediate time scale, but considering the large changes in fault frictional properties associated with coseismic slip [*Lapusta*, 2009], the random pattern of fault initiation across the ~20-40 km wide frontal zone and the geomorphic evidence for active internal faults should, perhaps, not be surprising. The continuous surface scarps and presence of growth strata suggest that faults within the frontal zone should all be considered active at least over the past ~100,000 years and that determining which of the frontal faults is likely to rupture in a future event is a difficult task.

1.8 Conclusions

Our analysis of SSA wedge-front deformation results in a new detailed map of the active structures comprising the MTFS and probabilistic estimates of deformation onset ages and fault parameters including dip-slip magnitude. We combine these estimates to produce the first fault slip rate estimates in the form of probability distributions for all wedge-front faults that, when compared to the long-term shortening rate of 7-13 mm/yr and the geodetically-derived slip accumulation rate of ~10 mm/yr, provide an estimate of the portion of whole-wedge deformation accommodated at the wedge front. Our results show that at least half and as much as all of the accumulating slip is transferred to a 20-40-

km-wide zone consisting of 1-4 partially overlapping to en-echelon thrust faults, some of which create surface topography whereas others are subsurface and identified only in the seismic data. With respect to the timing of the wedge-front fault initiation, we find subtle evidence for wedge-front faults in the south that are slightly older than those in the north and easternmost structures that may be the youngest faults across the MTFS. However, the growth onset age ranges overlap significantly and overall random nucleation characterizes the across-strike behavior of the wedge-front faults. The Subandean orogenic wedge in southern Bolivia appears to behave in a similar fashion to the Taiwanese and Himalayan ranges where much of the Plio-Quaternary shortening is absorbed by wedge-front faults distributed across an active zone that is a few tens of kilometers wide. We suspect that static stress conditions combined with and/or stemming from elevated erosional efficiency over the past few Myr result in the observed deformation localization at the wedge tip and the inferred activity across internal wedge structures. Our results support the emerging view of incremental wedge deformation where slip accumulates at down-dip locations along a décollement and is released incrementally by earthquakes that rupture wedge-front and internal faults. The focused deformation that absorbs at least half of the shortening across the MTFS indicates that the wedge-front structures, including the previously unidentified blind faults, pose a major risk to the region.

Acknowledgements

This study was supported by the National Science Foundation (grant EAR-1443317). We thank A. Echalar and R. Tinta of the Instituto Geográfico Militar de Bolivia for assistance with field logistics. We thank P.N. Legarreta and D. Apreda of Pluspetrol S.A. for facilitating

access to the seismic data archive. We thank L.N. Frazer and A. Aryal of the University of Hawaii for helpful discussions regarding the statistical analysis of modeling results and Brian Boston (University of Hawaii) for his advice on kinematic and geometric approaches. We thank K.M. Johnson (Indiana University) and K.M. Scharer (USGS) for their careful reading and suggestions that significantly improved this manuscript. The paper also benefits greatly from the reviews of associate editor Paul Tregoning, Nadine McQuarrie, and an anonymous reviewer. The Generic Mapping Tools software [*Wessel et al.*, 2013] was used to prepare Figure 1.1. This is SOEST contribution 9276.

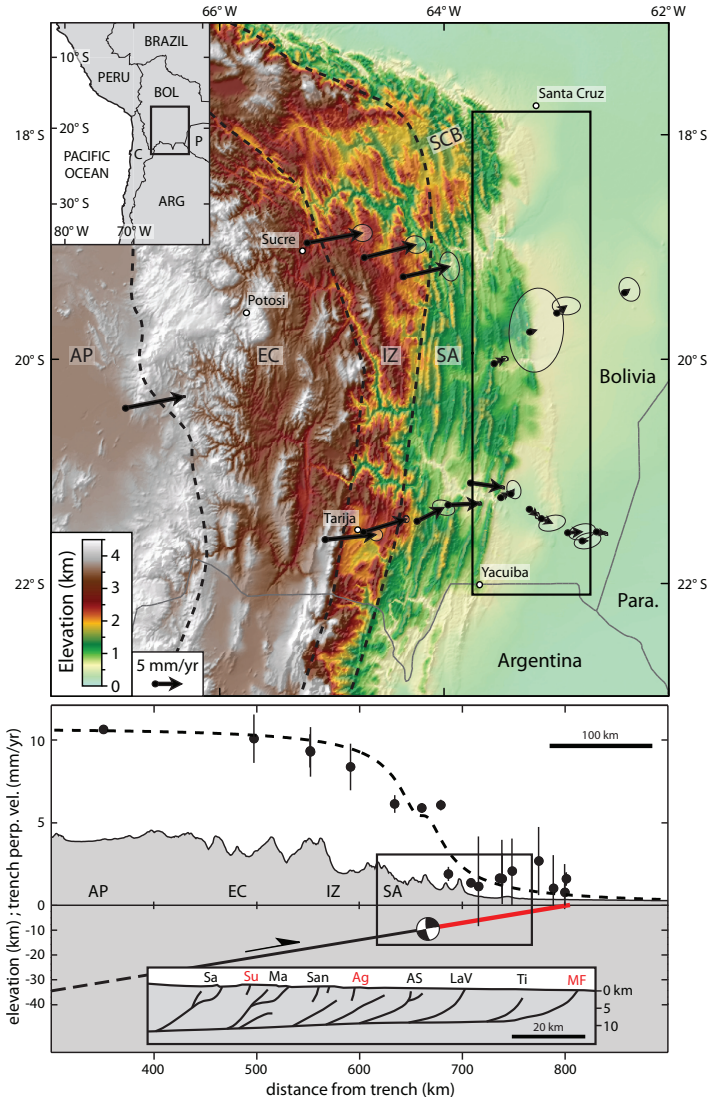

Figure 1.1 (Top) Shuttle Radar Topographic Mission (SRTM) topography and GPS-derived velocity field (black vectors) with 2σ error ellipses [Brooks et al., 2011b] from the central Andes in Bolivia with approximate positions of major physiographic provinces from *McQuarrie et al.* [2005] separated by dashed black lines. The black rectangle indicates the wedge-front region shown in Figures 2.2, 2.4, and 2.6-2.8. (Bottom) Cross sectional view of central Andean topography and crustal velocities. Black circles are the trench-perpendicular component of the GPS velocities with 2σ error bars. The black dashed line is the best model from the *Brooks et al.* [2011b] inversion. The solid black line beneath the GPS data is a topographic profile across the central Andes at ~20° S. The dipping line in the subsurface is a schematic representation of the sub-horizontal fault (décollement) underlying the range. The down-dip (black) portion of the fault represents the zone of continuous slip whereas the up-dip (red) portion represents the locked zone. In the conceptual incremental wedge deformation framework, earthquakes (focal mechanism) nucleate at the slipping to locked interface and propagate up-dip towards the surface. The inset is a regional structural cross section from *Uba et al.* [2009] including the décollement underlying the range and steeper thrust faults that intersect the décollement and breach or come close to the surface. Faults labeled in red are those for which there is evidence of recent activity. AP=Andean Plateau; EC=Eastern Cordillera; IZ=Interandean Zone; SA=Subandes; MF=Mandeyapecua fault; Ti=Tiguipa fault; LaV=La Vertiente fault; AS=Agua Salada; Ag=Aguarague; San=San Antonio; Ma=Mandiyuti; Su=Suaruru; Sa=Salinas.

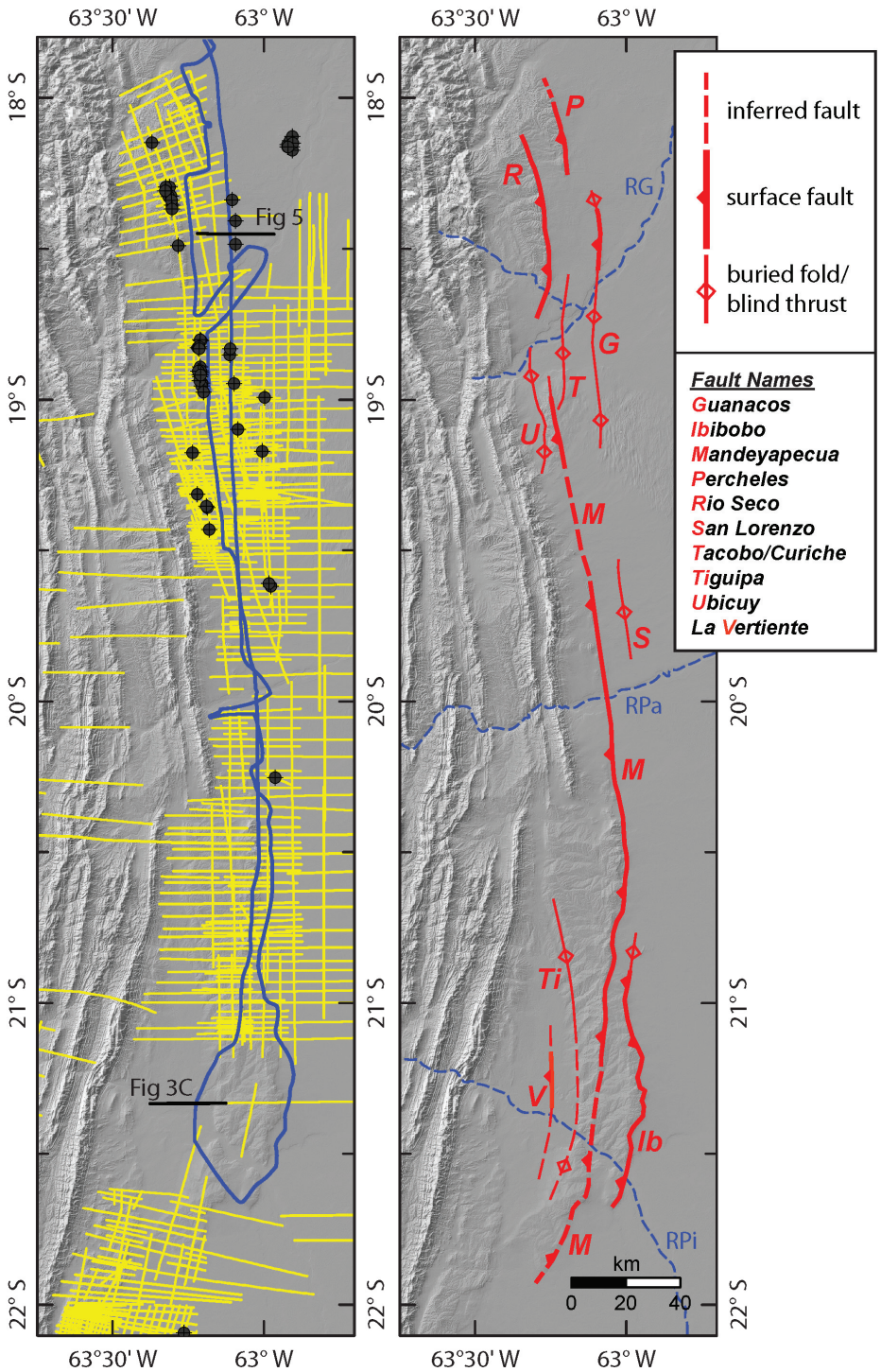

Figure 1.2 (Left) Hill-shaded SRTM topography with the seismic reflection dataset used in this study (yellow), the wedge-front reconnaissance flight path (blue), and the wells used for the TWTT-depth conversions described in the text (gray). Additional wells used in the analysis are located just south and east of the map region for the 22-23° S and 20-21° S corridors respectively. (Right) Neotectonic fault map of the Bolivian Subandes including the major wedge-front-crossing rivers. RG=Rio Grande; RPa=Rio Parapeti; RPi=Rio Pilcomayo.

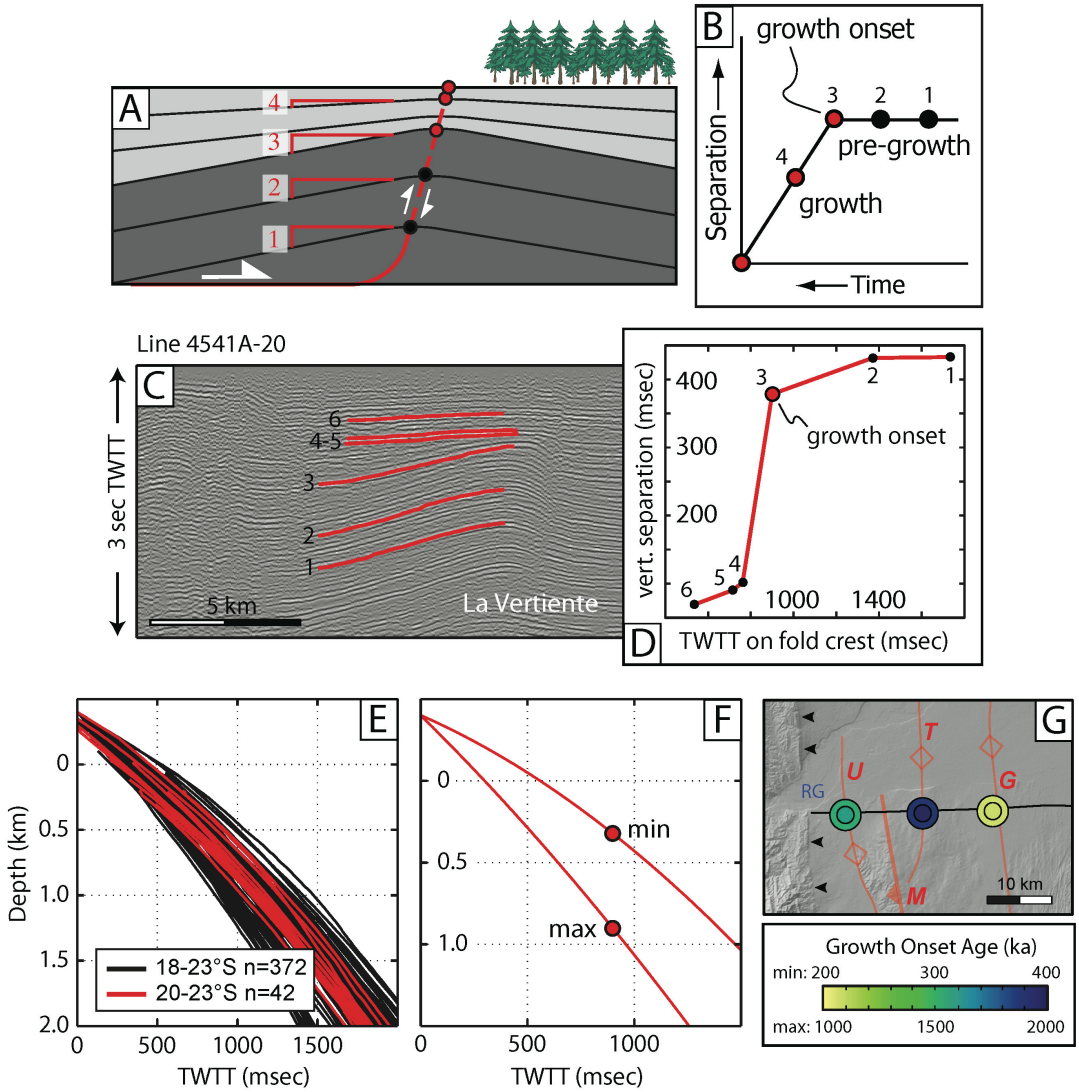

Figure 1.3 (A) Schematic representation of a fault-related growth fold [*Burbank et al.*, 1996]. Pre-growth strata are dark gray and growth strata are light gray. Numbered horizons illustrate the vertical separation between a location on and off of the fold crest. (B) VSD based on the horizons shown in (A). (C) Representative seismic reflection line crossing the La Vertiente structure. See Figure 2 for the line location. Interpreted horizons used for the VSD analysis are shown in red. (D) VSD for the portion of the La Vertiente structure shown in (C). The kink in the curve is assigned to growth onset. A detailed description of the VSD method is provided in the methods section of the text. A few additional VSD's are shown in supplementary information. (E) Two-way travel time to depth curves for all well-logs (black) and those in the 20-23° S latitudinal bin (red). (F) The well-log envelope used to compute minimum and maximum depths associated with the VSD kink. (G) The minimum/maximum depths combined with the range of sedimentation rates determined for the wedge-front drainage basins result in minimum/maximum growth onset ages. The ages are displayed as nested circles with the inner (outer) circle corresponding to the minimum (maximum) growth onset ages. Here we show ages for the three adjacent structures imaged in Line 5072-21 (see Figure 4 for the line location and Figure fs01 for the corresponding VSD's). Fault nomenclature and symbols are the same as in Figure 1.2. Black arrowheads point to easternmost range-front structure located west of the wedge-front. RG=Rio Grande.

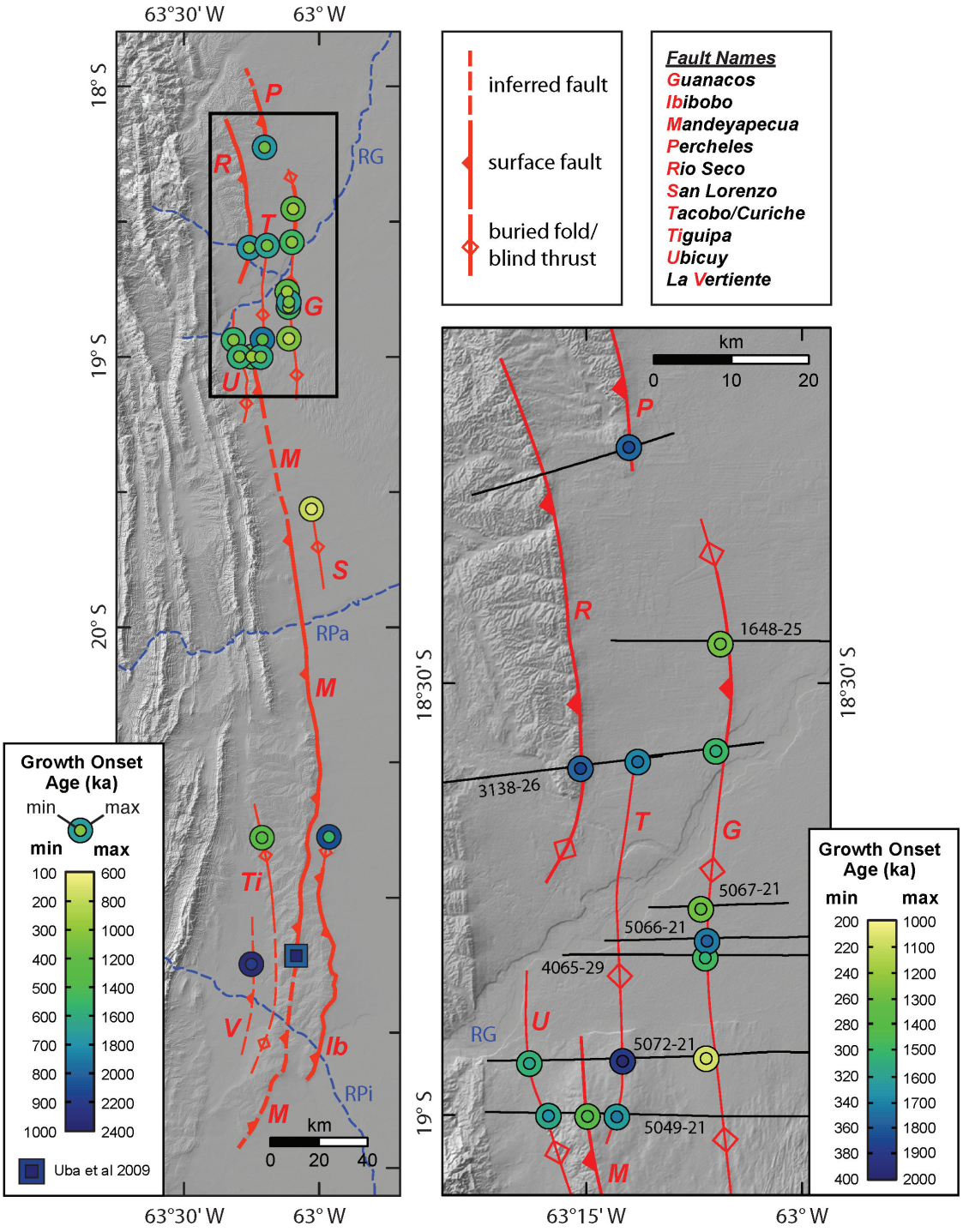

Figure 1.4 (Left) Growth onset age results for all wedge-front structures. We use an initiation age of 1.5±0.5 Ma for the southern portion of the Mandeyapecua fault based on results from *Uba et al.* [2009]. Fault nomenclature and symbology are the same as in Figure 1.2. V=La Vertiente. (Right) Close-up view of the northern structures with a rescaled color ramp to highlight growth onset age variations that are not obvious from the regional view. Seismic lines referred to in the text are labeled. RG=Rio Grande.

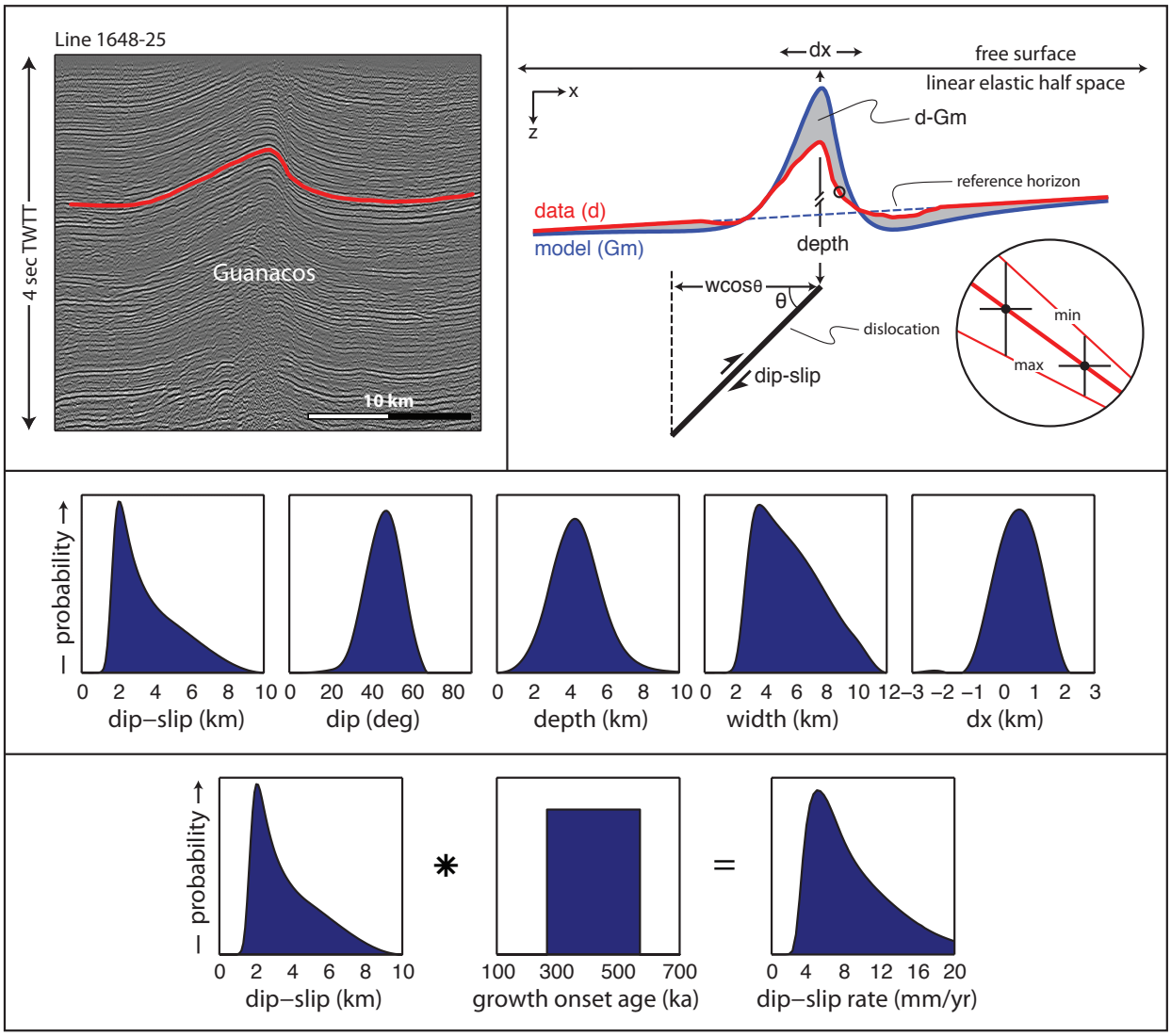

Figure 1.5 Elastic dislocation modeling and grid search inversion for fault parameters. (Top left) A continuous horizon imaged across the Guanacos structure in Line 1648-25 (see Figures 2.2 and 2.4 for line location) is digitized and depth converted using the well-log envelopes. (Top right) We connect the endpoints of the depth-converted horizon (red) and extended them in the plane of the seismic line to create the reference horizon (dashed blue line), which we use as input to the elastic dislocation modeling. We reduce the typical nine parameter to five including depth, width, dip (θ), dip-slip, and the horizontal position of the dislocation tip (dx). For each combination of parameters we compute a model horizon (blue) and assess the goodness of fit between the model and the data (gray area between the curves) by computing the residual sum of squares. Also shown in the circle is a close-up of how we use the variation about the mean horizon depth to construct the data covariance matrix. The main text contains a more detailed description of the method. (Middle) The misfit between the model and data is used to compute marginal probability distributions (mpd) for each of the 5 model parameters. (Bottom) Dip-slip rates for the wedge front structures are computed by convolving the dip-slip mpd with the growth onset age mpd, which in this case, is a boxcar with the edges corresponding to the minimum and maximum growth onset age estimates.

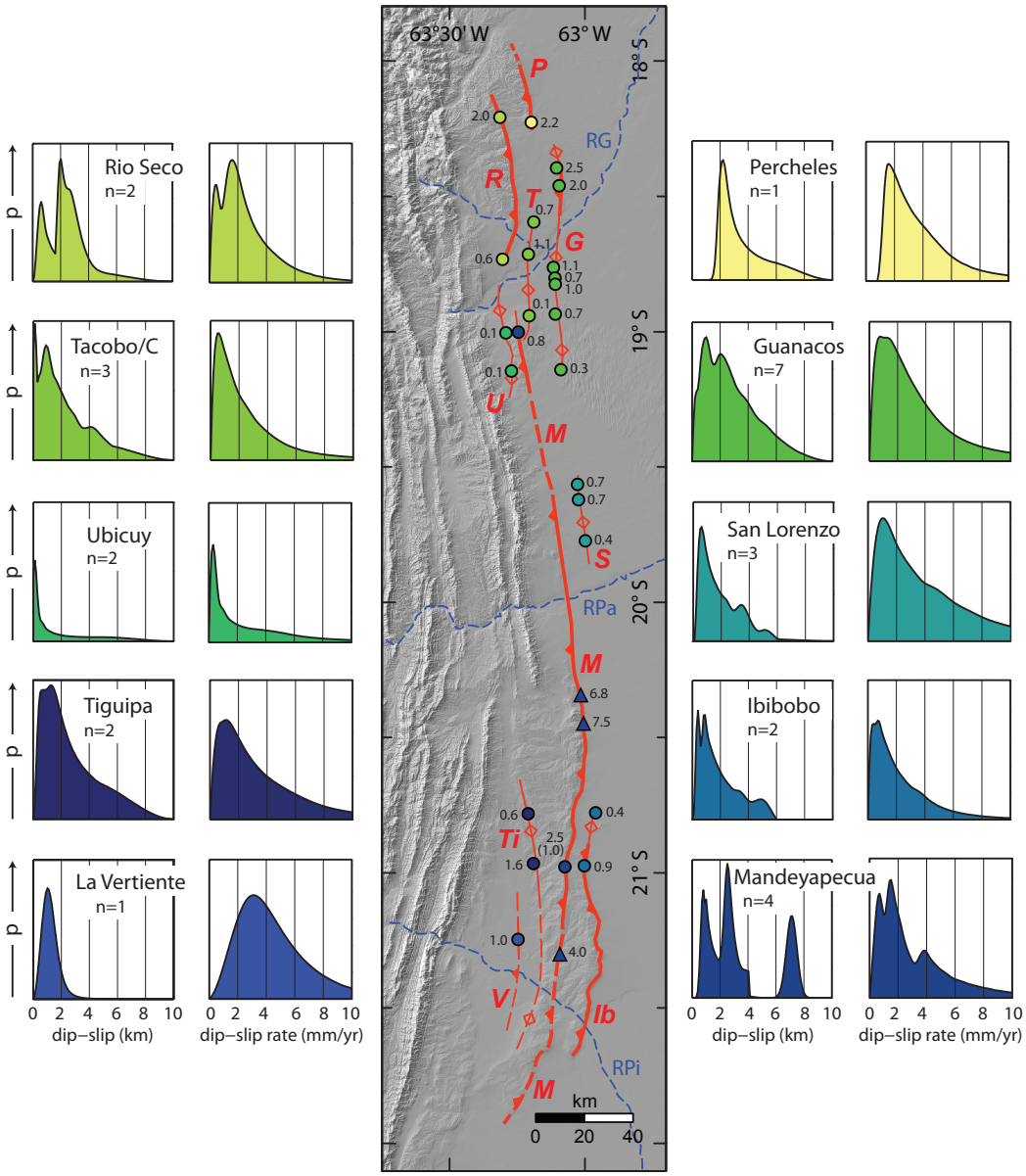

Figure 1.6 Composite dip-slip and dip-slip rate mpds for all structures with the number of estimates for each structure indicated. The composite dip-slip magnitude mpds result from normalizing the sum of the individual mpds for faults with more than one dip-slip estimate (e.g. n=7 for Guanacos). The composite dip-slip rate mpds result from convolving the composite dip-slip magnitude mpds with the whole-fault age boxcar using the absolute minimum and maximum age estimates for the structure. The colored circles on the map correspond to the locations where we model dip slip. The small numbers adjacent to the circles indicate the peak dip-slip magnitude for that location. For the southern MF, the number in parentheses corresponds to the amount of slip measured from the *Uba et al.* [2009] interpreted seismic section. The small blue triangles represent the estimates measured from the structural cross sections presented in *Dunn et al.* [1995]. The composite dip-slip rate estimate for the Mandeyapecua fault is based on the 4 dip-slip estimates and the whole-fault growth onset age described in the text. See the auxiliary information (Figure fs02) for the individual dip-slip and other geometric fault parameter probability distributions. Fault nomenclature and symbols are the same as in Figures 2.2 and 2.4.

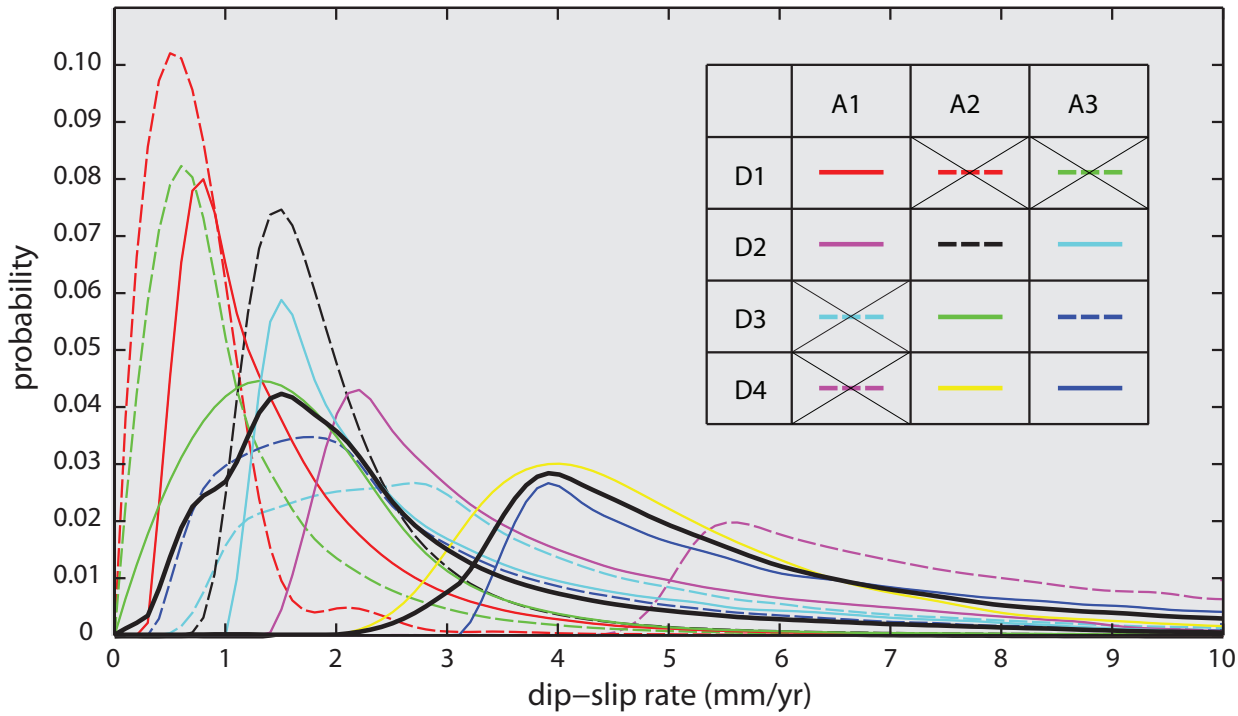

Figure 1.7 Mandeyapecua fault dip-slip rate distributions computed using various combinations of the dip-slip (D1-D4) and growth-onset age (A1-A3) estimates for the structure. A detailed description of how we created the mpds is provided in the text. The minimum and maximum dip-slip rate distributions are heavy black lines. The mpds excluded from the mean calculations are crossed off in the legend.

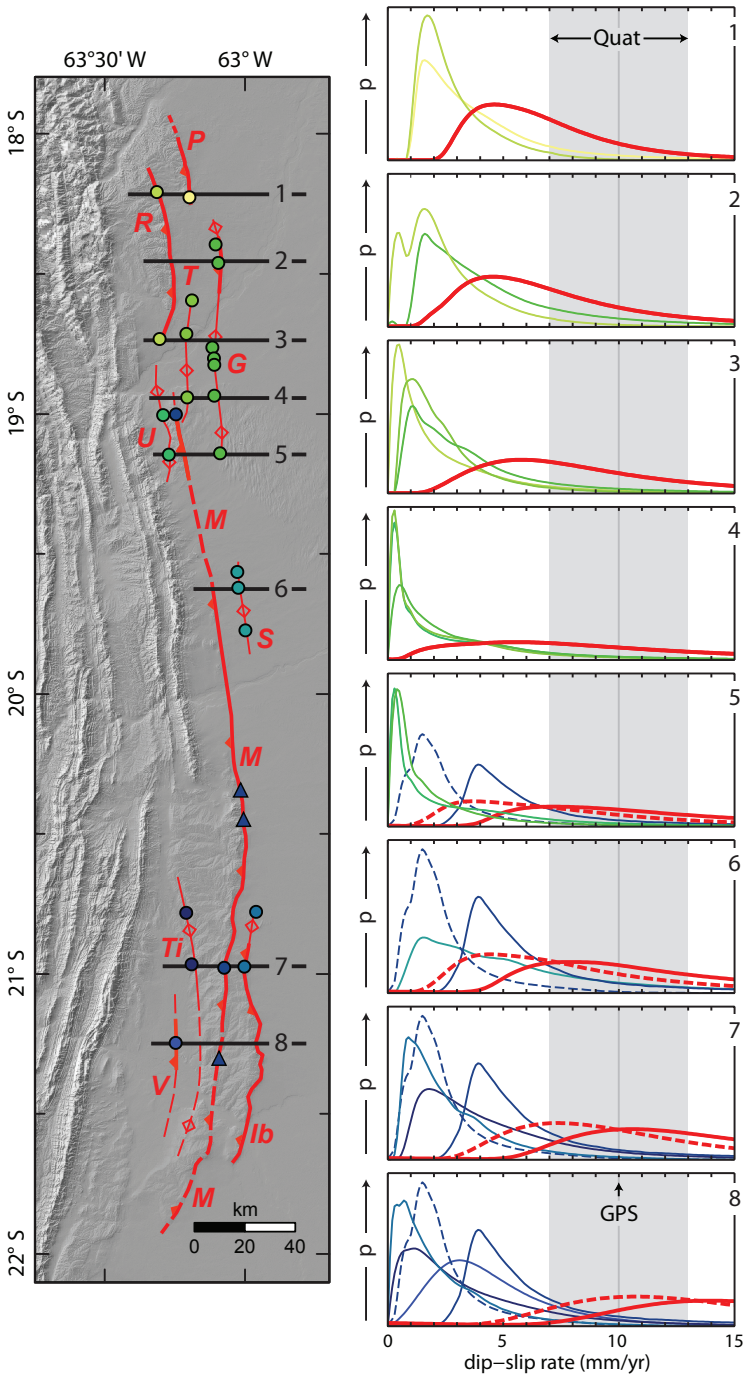

Figure 1.8 Profile-based analysis of wedge-front fault dip-slip rates. (Left) Map showing the numbered profile locations. (Right) Fault and composite dip-slip rate mpds for the profiles. Dip-slip rate probability distribution colors correspond to estimates from different faults. The composite, profile-based estimates are shown as red distributions. Profiles 5-8 include the minimum and maximum MF dip-slip rates shown in Figure 7. The minimum mpds and corresponding composite estimates are dashed whereas the maximum mpds and corresponding composite estimates are solid. The gray bar spans the 7-13 mm/yr range of shortening rates determined from geologic studies. The GPS-based wedge-loading rate is ~10 mm/yr.

Appendix A

Spatial and temporal distribution of deformation at the front of the Andean orogenic wedge in southern Bolivia

Jonathan R. Weiss[1*], Benjamin A. Brooks[2], J. Ramón Arrowsmith[3], Gustavo Vergani[4]

1. Department of Geology and Geophysics, University of Hawai'i at Manoa, Honolulu, Hawaii, USA.

2. U.S. Geological Survey Earthquake Science Center, Menlo Park, California, USA.

3. School of Earth and Space Exploration, Arizona State University, Tempe, Arizona, USA.

4. Pluspetrol S.A., Buenos Aires, Argentina

Journal of Geophysical Research - Solid Earth - 2014

This supplemental data set includes minimum and maximum growth onset ages computed from the vertical separation diagram (VSD) analysis in Table A1, a representative wedge-front-crossing seismic reflection line that images three adjacent wedge-front structures and the corresponding vertical separation diagrams in Figure A1, fault parameters distributions from the elastic dislocation modeling in Figure A2, examples of the data and modeling results using offset horizons are in Figure A3, and the profile-based analysis of wedge-front fault dip-slip rates using the composite dip-slip rate estimates for each of the profiles in Figure A4.

Table A1 Growth onset age estimates

Structure	Line	Lon	Lat	min (ka)	max (ka)
Guanacos	1648-25	-63.0947	-18.4546	261.84	1284.27
Guanacos	REP-1636-25	-63.0996	-18.5783	308.92	1499.44
Guanacos	5067-21	-63.1172	-18.7611	264.16	1294.94
Guanacos	SCPS-4065-29	-63.1122	-18.8181	305.73	1484.98
Guanacos	5072-21A	-63.1111	-18.9346	216.41	1072.89
Guanacos	5066-21	-63.1101	-18.7986	357.63	1718.39
Ibibobo	4551-20	-62.9618	-20.7780	409.69	1476.46
La Vertiente	4541A-20	-63.2500	-21.2480	698.25	2337.89
La Vertiente*	4541A-20	-63.2500	-21.2480	557.05	1926.61
Mandeyapecua	5049-21	-63.2486	-19.0013	288.46	1386.54
Percheles	1695-25	-63.2010	-18.2270	367.57	1762.64
Rio_Seco	3138-26	-63.2570	-18.5987	369.23	1770.03
San Lorenzo	5056-21	-63.0264	-19.5650	156.15	786.37
Tacobo/Curriche	3138-26	-63.1906	-18.5907	351.86	1692.65
Tacobo/Curriche	5072-21A	-63.2079	-18.9376	399.48	1903.75
Tacobo/Curriche	5049-21	-63.2144	-19.0020	343.67	1624.46
Tiguipa	4551-20	-63.2097	-20.7812	349.19	1283.65
Ubicuy	5072-21A	-63.3162	-18.9401	316.92	1535.67
Ubicuy	5049-21	-63.2941	-19.0009	332.59	1577.22

* end of La Vertiente growth strata formation

Table A1 Minimum and maximum growth onset ages computed from the VSD analysis. See the main text for a more detailed description of the method. For the La Vertiente structure we estimate a growth onset age from the kink in the VSD curve corresponding to horizon 3 in main text Figures 1.4 C and D. The additional La Vertiente estimate (*) is associated with the cessation of growth strata formation and corresponds to horizons 4/5 in Figures 1.4 C and D of the main text.

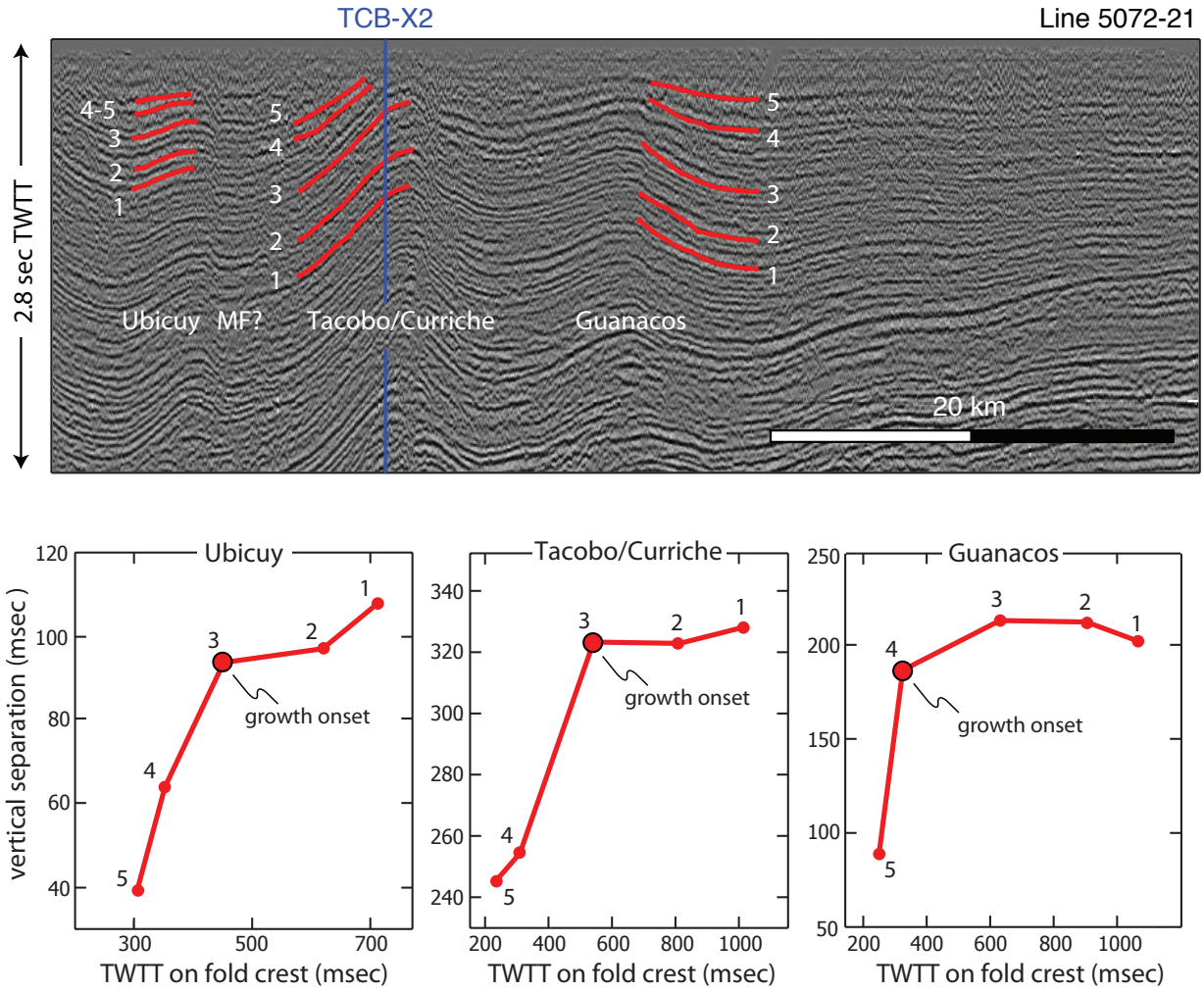

Figure A1 (Top) Representative wedge-front-crossing seismic reflection line. See Figures 2 and 3G in the main text for the line location. Interpreted horizons across portions of the adjacent Ubicuy, Tacobo/Curiche, and Guanacos structures used for the vertical separation diagram (VSD) analysis are shown in red. Well TCB-X2, which pierces the Tacobo/Curiche structure, is also shown. (Bottom) VSD's for the structures imaged in Line 5072-21. The kink in the curve is assigned to growth onset. A detailed description of the VSD method is provided in the methods section of the main text. MF=Mandeyapecua fault.

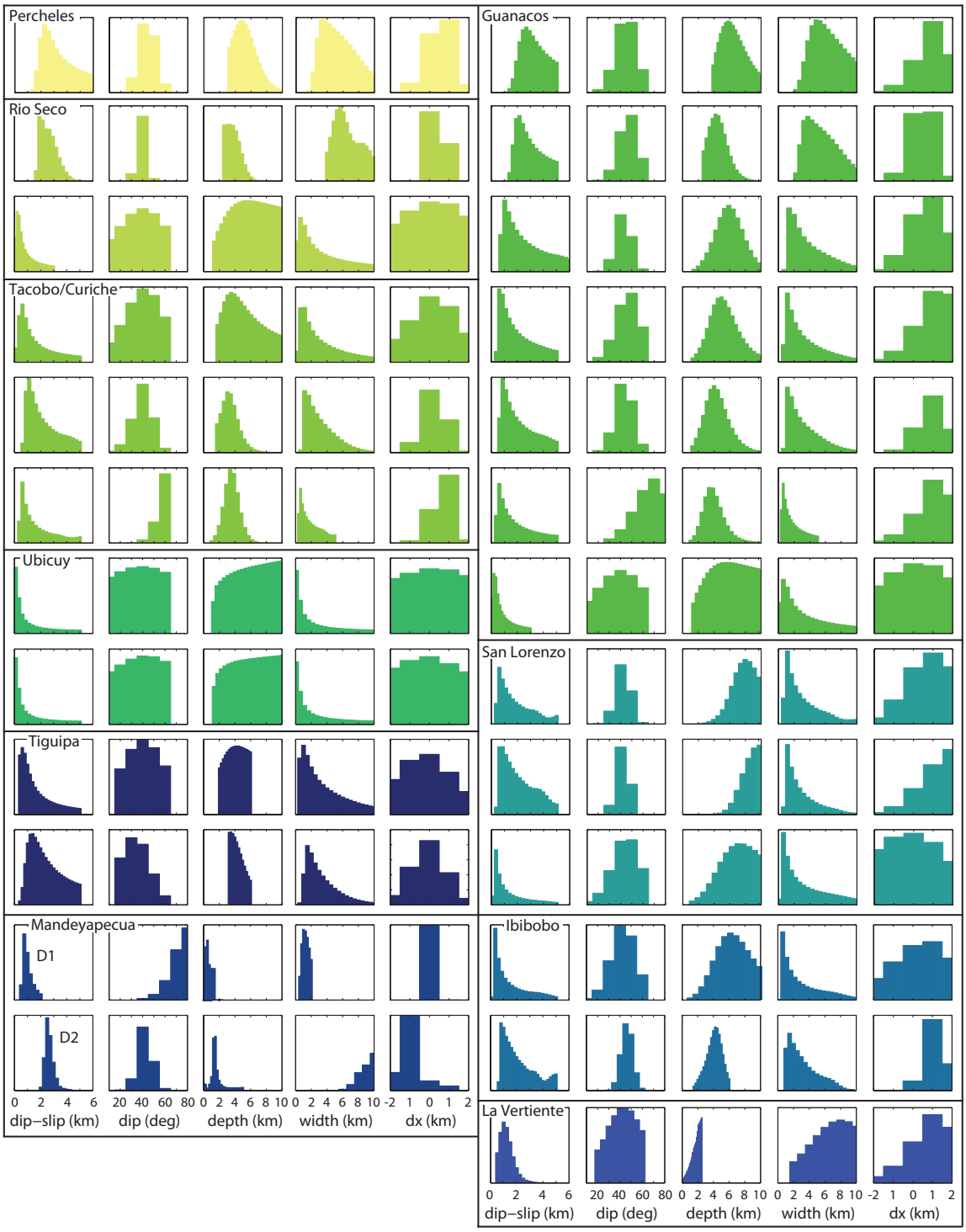

Figure A2 Fault parameters distributions from the elastic dislocation modeling. The modeling locations are indicated by colored circles in Figures 1.6 and 1.8 in the main text and Figure A4. For example, we model fault parameters at 7 locations along the length of the Guanacos structure. The resulting mpds from top to bottom correspond to the colored circles on the map overlain on the Guanacos fault trace from north to south. Expanded views of the parameter distributions for the Mandeyapecua (D2) and La Vertiente faults are shown in Figure A3.

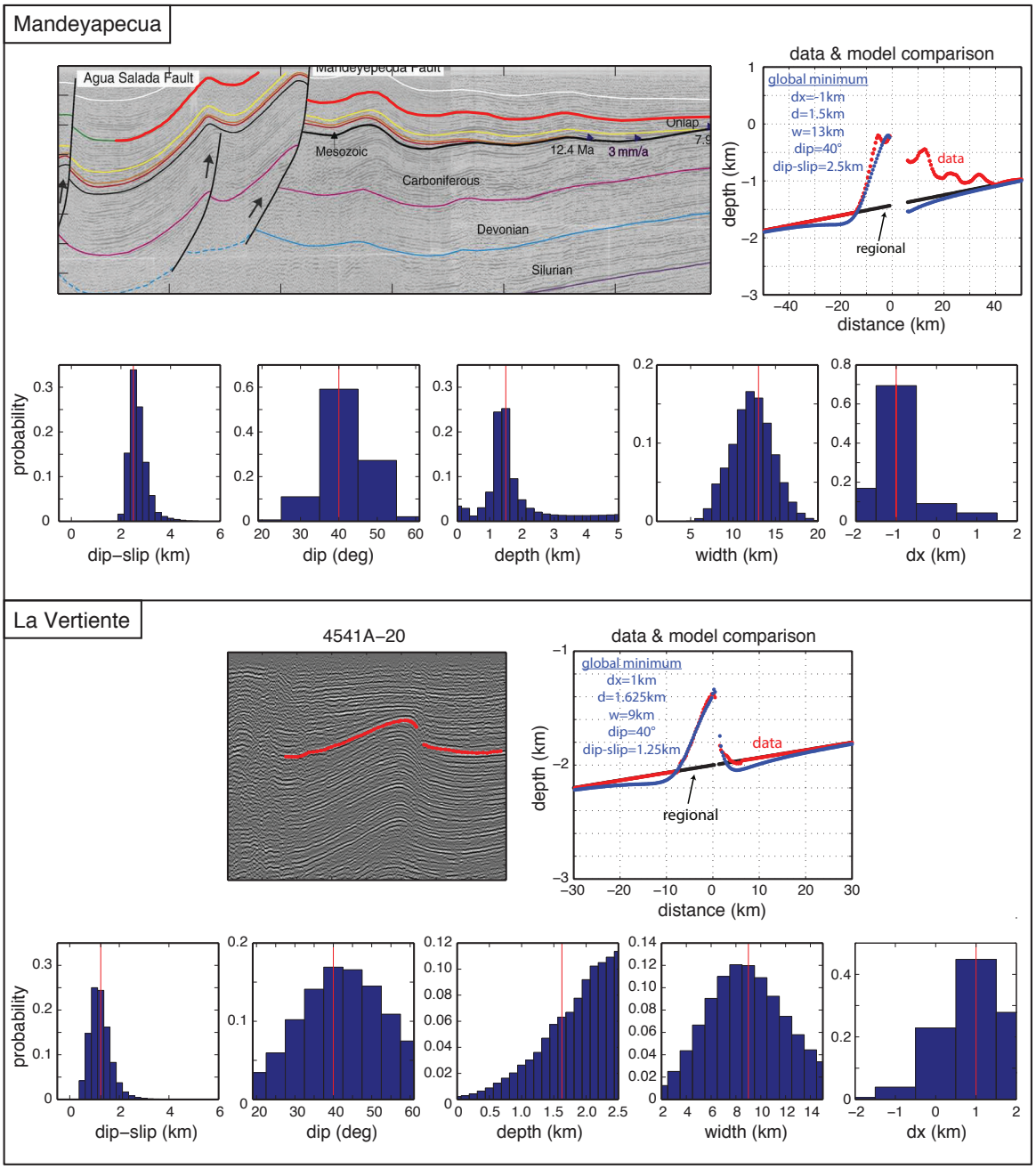

Figure A3 Modeling results using offset horizons. (Top) Mandeyapecua fault. The top left panel shows the interpreted seismic line from Uba et al. [2009] with the digitized horizon used in the modeling in red. The top right panel shows the depth-converted horizon in red and the best-fit model output and fault parameters in blue. The regional horizon constructed by fitting a straight line through the interpreted horizon endpoints is shown in black. Also shown are the probability distributions for the 5 model parameters with the global minimum indicated with a vertical red line. (Bottom) La Vertiente fault. The top left panel shows the seismic section and offset horizon used to model La Vertiente deformation. The top right panel is the same as for the Mandeyapecua fault with the data horizon in red, the best-fit model horizon in blue, and the regional horizon used to create the model in black. The fault parameter probability distributions are shown in the bottom panel with the red vertical line indicating the model space global minimum.

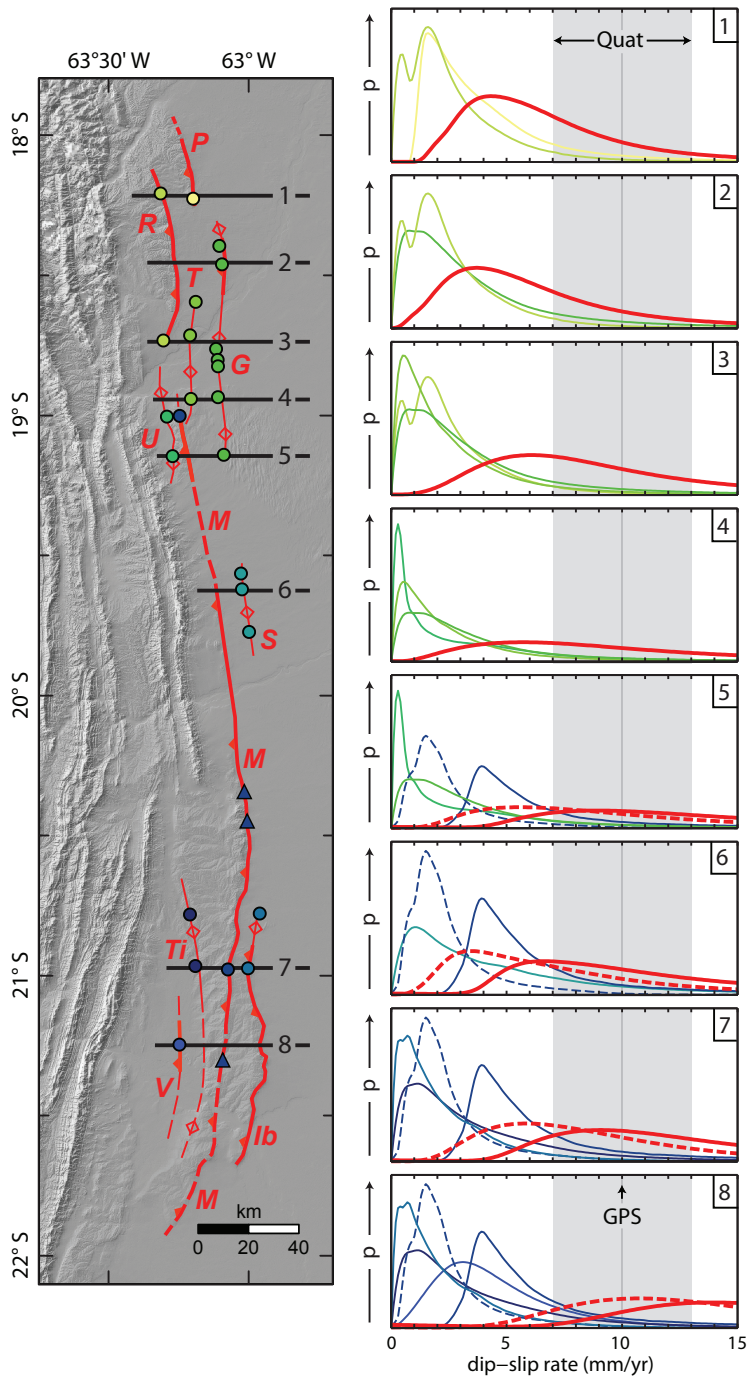

Figure A4 Profile-based analysis of wedge-front fault dip-slip rates using the composite dip-slip rate estimates for each of the profiles in contrast to the individual dip-slip mpds that are used in Figure 1.8 of the main text. (Left) Map showing the numbered profile locations. (Right) Fault and composite dip-slip rate mpds for the profiles. Distribution colors correspond to the different faults and the composite estimates are in red. Profiles 5-8 include the minimum (solid blue line) and maximum (dashed blue line) MF dip-slip rates from Figure 1.7 of the main text. The minimum mpd and corresponding composite estimate are dashed. For comparison, we indicate the 7-13 mm/yr range of shortening rates determined from geologic studies and the GPS-based wedge-loading rate of ~10 mm/yr.

Appendix B

Response to editor/reviewers regarding manuscript:

Spatial and temporal distribution of deformation at the front of the Andean orogenic wedge in southern Bolivia

In response to the reviewer and associate editor suggestions, we compare ED results with those stemming from kinematic and geometric techniques. Figure B1 shows a qualitative comparison of ED-generated folds to structures created using the kinematic fault-propagation fold, fault-bend fold, and trishear models. For each model suite we prescribe similar fault geometries and slip magnitudes. Neither fault-propagation nor fault-bend fold models compare well with ED and both produce boxy structures that are unrealistic when compared to the SSA subsurface folds. At a minimum, the fault-bend fold model structures have wavelengths and amplitudes that are mildly similar to ED.

Of the three kinematic approaches we tested, the trishear fold amplitudes and wavelengths look most similar to ED. This similarity is not surprising considering trishear was developed as an alternative to the kink band models in order to reproduce folds with smooth profiles and broad-crested anticlines like those seen in the field [*Allmendinger*, 1998; *Erslev*, 1991; *Hardy and Ford*, 1997]. For the trishear model shown in Figure B1 we use a propagation to slip (P/S) ratio of 2.5 and a trishear angle of 80°. We are encouraged by the similarity and note that trishear has been used to successfully model structures comparable in size and tectonic setting to those at the Subandean wedge front [e.g. *Cardozo and Brandenburg*, 2014; *Cardozo et al.*, 2011; *Yue et al.*, 2011].

We follow the suggestion of reviewer 1 and also test the area-of-relief method [*Gonzalez-Mieres and Suppe*, 2006; 2011], which is a geometric technique used to determine shortening as a function of height for folded stratigraphic horizons in well-imaged structures. The method is based on the relationship between structural relief and

shortening and the notion that the slope of structural relief for a number of stratigraphic horizons versus the height or the horizons above the detachment or any reference level is equal to the shortening [*Epard and Groshong*, 1993]. The area-of relief method is performed in the thickness domain, which is the seismic line flattened to a specific mapped stratigraphic horizon. Measurements in this domain are independent of any assumptions or knowledge of the locations or existence of detachment horizons and are especially useful in low-relief or stratigraphically complex areas

When applying the area-of-relief method it is important to note that in compression, thickness relief (ΔA) and height (ΔH) are positive for horizons above the flattening level and negative for horizons below the flattening level. Also, the method was initially developed for detachment folds, which are characterized by a linear, progressive upward increase of area of structural relief within the pre-growth section. Although not explicitly stated by the publications, the approach also specifies the sign of ΔA based on the location of the excess area with respect to the dashed lines connecting the horizon endpoints. If the excess area is above the dashed line ΔA is positive and vice versa.

Figure B2 shows an example of the area-of-relief method from the northern Subandean wedge front. We digitize and depth convert 4 well-imaged pre-growth horizons across a fold related to the buried portion of the Guanacos fault (Figure B2a). The conversion to depth (Figure B2b) is done using the well-log envelopes described in the main text. We choose horizon 1 as the flattening horizon and compute the area of the region between the flattened horizon and the line connecting the two endpoints of the horizon (Figure B2c). The excess area (gray region in Figure B2c) for horizons 2, 3 and 4 is located beneath the line connecting the two horizon endpoints. This is opposite the schematic and natural examples presented in *Gonzalez-Mieres and Suppe* [2006]; where the excess area is above the line connecting the horizon endpoints. Therefore, although the absolute value of the measurements for the Guanacos example are positive, direct application of the method yields negative ΔA values that decrease up-section. The slope of the best best-fit line through the data is also negative. Measurements from pre-growth

strata in 19 wedge-front locations all exhibit the same behavior (i.e. negative ΔA values that decrease up-section).

Of relevance to the observed discrepancy is the application of the area-of-relief method to growth horizons deposited during deformation [*Gonzalez-Mieres and Suppe*, 2011]. *Gonzalez-Mieres and Suppe* [2011] state that an upward decrease in the area of relief is associated with growth strata and that this is manifest in the area-of-relief graphs by a negative slope on the best-fit to the growth measurements ($\Delta A/\Delta H<0$). Although this is the pattern we observe, our measurements come from layers that are clearly pre-growth as they record no signs of syn-depositional folding. Horizons are sub-horizontal adjacent to and across the folds and exhibit no growth strata patterns such as on-lap or thinning across the fold axis. In contrast, growth patterns clearly characterize the shallow, near-surface stratigraphy above horizon 4.

We can think of a few reasons why the area-of-relief method gives unexpected results. Visual examination of the interpreted horizons reveals that their amplitudes and wavelengths do not increase up-section. This stated requirement for the method is met by detachment folds, for which the approach was initially developed. The faults we are dealing with are dipping and this difference may invalidate the approach. *Yue et al.* [2011] is the only study we can find that successfully applies the area-of-relief method to a (dipping) fault-bend fold. The method is meant to be generally applicable but our tests suggest that without modifications this may not be the case.

Another possible reason for the discrepancy is that our seismic data may not image the full extent of the structures required to correctly apply the area-of-relief method. Figure B3 shows the method applied to synthetic folds generated using ED. When we extend the observation grid to 10 km on either side of the fault we observe a rollover or change in sign of the ΔA values that results from not capturing the full extent of the fold (Figure B2c). However, when we extend the observation grid to 20 km on either side of the fault we capture the entire fold and observe the expected up-section linear increase in the

excess area (Figure B2d). If this difference is the culprit, we can not apply the area-of-relief method to our data because the seismic lines are truncated or the fold geometry is complicated by the proximity of adjacent structures. These issues do not impact our application of ED.

Finally, many of the fold models and the area-of-relief method assume that bed length and thickness do not change during folding (conservation of area). Violation of this assumption due to tectonic compaction, for example, may be another reason why the technique does not work for the Subandean structures. If the beds thinned substantially during folding the status quo area-of-relief method will not work.

In response to the concern expressed by reviewer 2 regarding the appropriateness of the plan strain assumption we perform a test in which we deform synthetic model horizons above a finite length rectangular elastic dislocation (Figure B4). The test uses a dislocation that is 100-km-long, which contrasts the very long fault used in the manuscript. The actual value we use for the length of the dislocation is arbitrary. To test if the estimates of fault slip magnitude from locations very close to the mapped termination of a fault we impose a known amount of dip-slip (1 km) on the finite length fault and extract profiles from the deformation field that cross progressively closer to the edge of the dislocation at 10%, 5%, and 1% of the fault length from the fault end. These profiles simulate the seismic reflection lines used in our analysis that cross close to the mapped termination of the buried faults. We use the profiles as observations for our parameter grid search but assume they cross the center of a very long dislocation (e.g. plane strain). A comparison of the probability distributions from the grid search with the known slip will reveal if the method can recover the true dip-slip value at distances very close to the fault edge.

At a distance of 10% and 5% of the fault length from the fault end the global minimum of the error space is exactly the true dip-slip value of 1 km. The peak of the probability distributions for 10% and 5% are at 1 km and 0.8 km, respectively. Only at the

very edge of the fault do we significantly underestimate this value; the global minimum and peak dip slip for the 1% example are both 0.6 km.

The reviewer 2 concern regarding plane strain and finite fault length may in part be due to the model locations shown in Figure 1.6 from the main text, which appear very close to the fault edges. In reality, however, the ED modeling is performed in locations that coincide with the last seismic line where the folds are apparent in the subsurface data. When we consider the spacing of the seismic lines, which is typically no less than 1 km and usually on the order of 2-5 km, and the size of the symbols used to mark the ED locations, our estimates come from locations that are 100's-1000's of m's away from the very edges of the faults. This information, combined with the test illustrated in Figure B4, indicates the model locations are located far enough away from the fault edges that the plane strain assumption is valid. If anything our estimates are conservative in that we may slightly underestimate the "true" dip-slip approaching the fault ends.

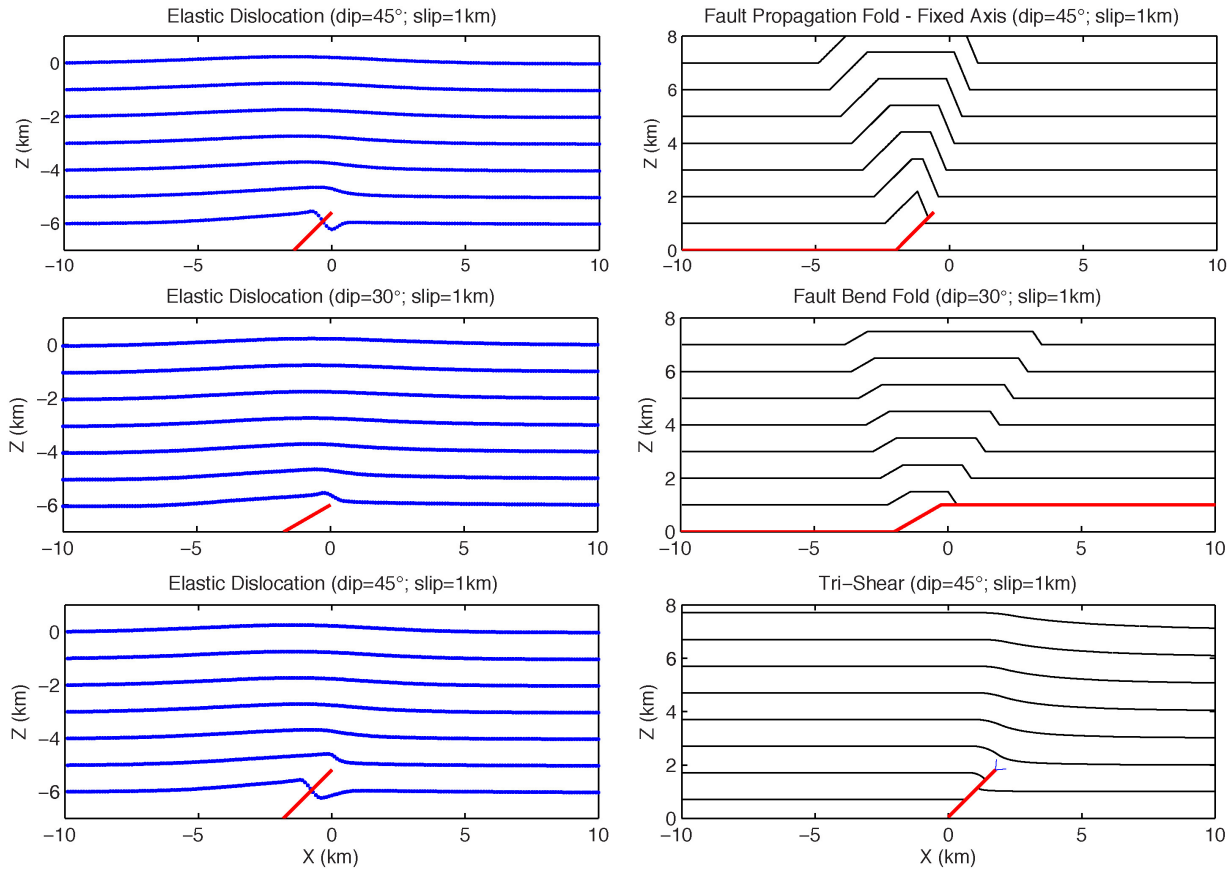

Figure B1 Visual comparison of elastic dislocation model (ED) folds (left) and those stemming from commonly used kinematic techniques including, from top to bottom, fault-propagation fold, fault-bend fold, and trishear. Fault parameters (dip and angle) for each suite of models are comparable. Only the trishear technique compares favorably with the ED results.

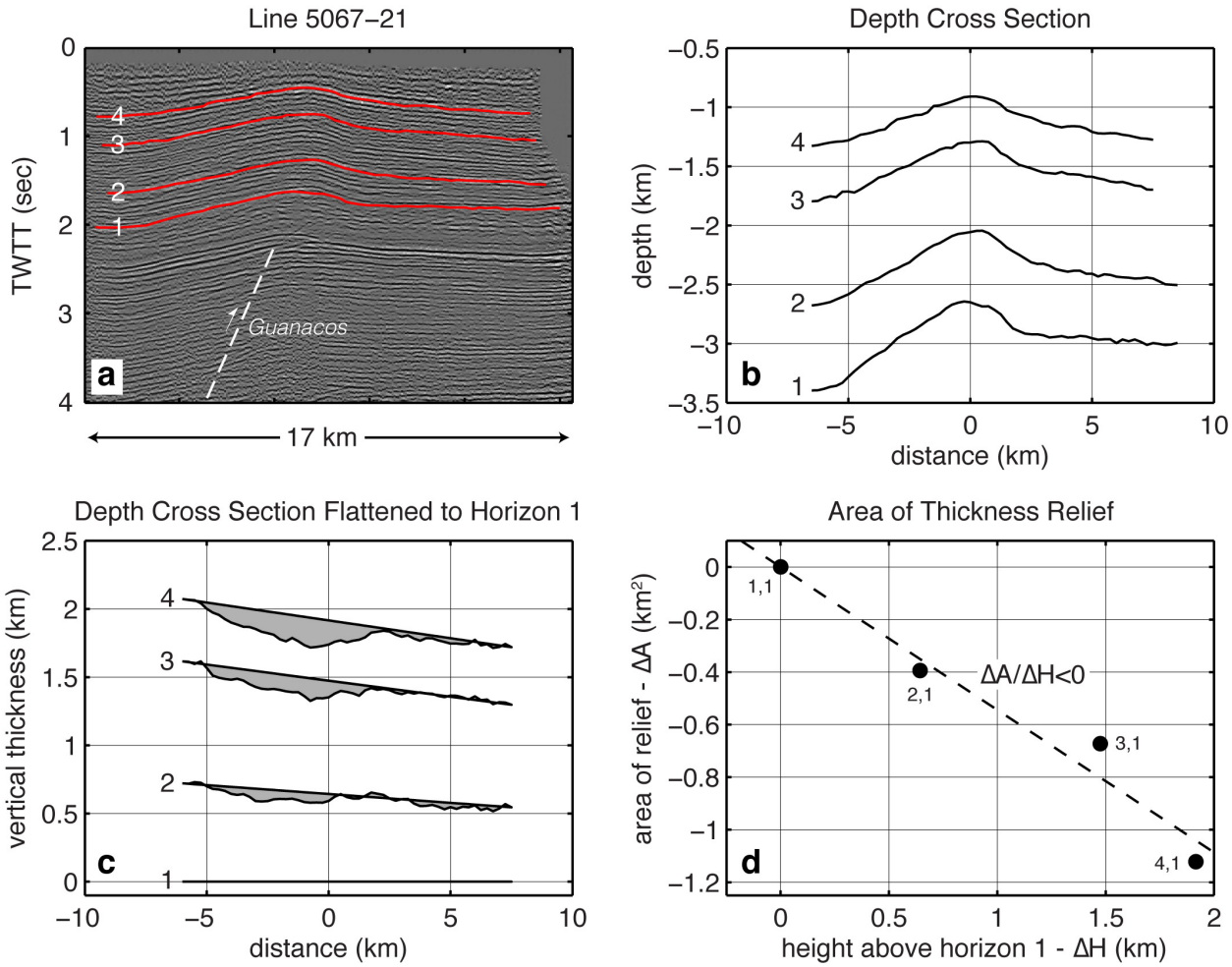

Figure B2 Area-of-relief method applied to the Guanacos structure. Note that stratigraphy above horizon 4 exhibits growth characteristics whereas strata below horizon 4 are pre-growth. (a) Seismic line 5067-21 with interpreted pre-growth horizons in red. (b) Depth-converted horizons. (c) Depth-converted horizons flattened with respect to horizon 1. Note that the excess area (gray) falls beneath the line connecting the horizon endpoints resulting in negative ΔA values with increasing ΔH. (d) Area of relief versus height above horizon 1 for the for pre-growth stratigraphy. Excess area becomes more negative moving up-section resulting in a situation where $\Delta A/\Delta H>0$.

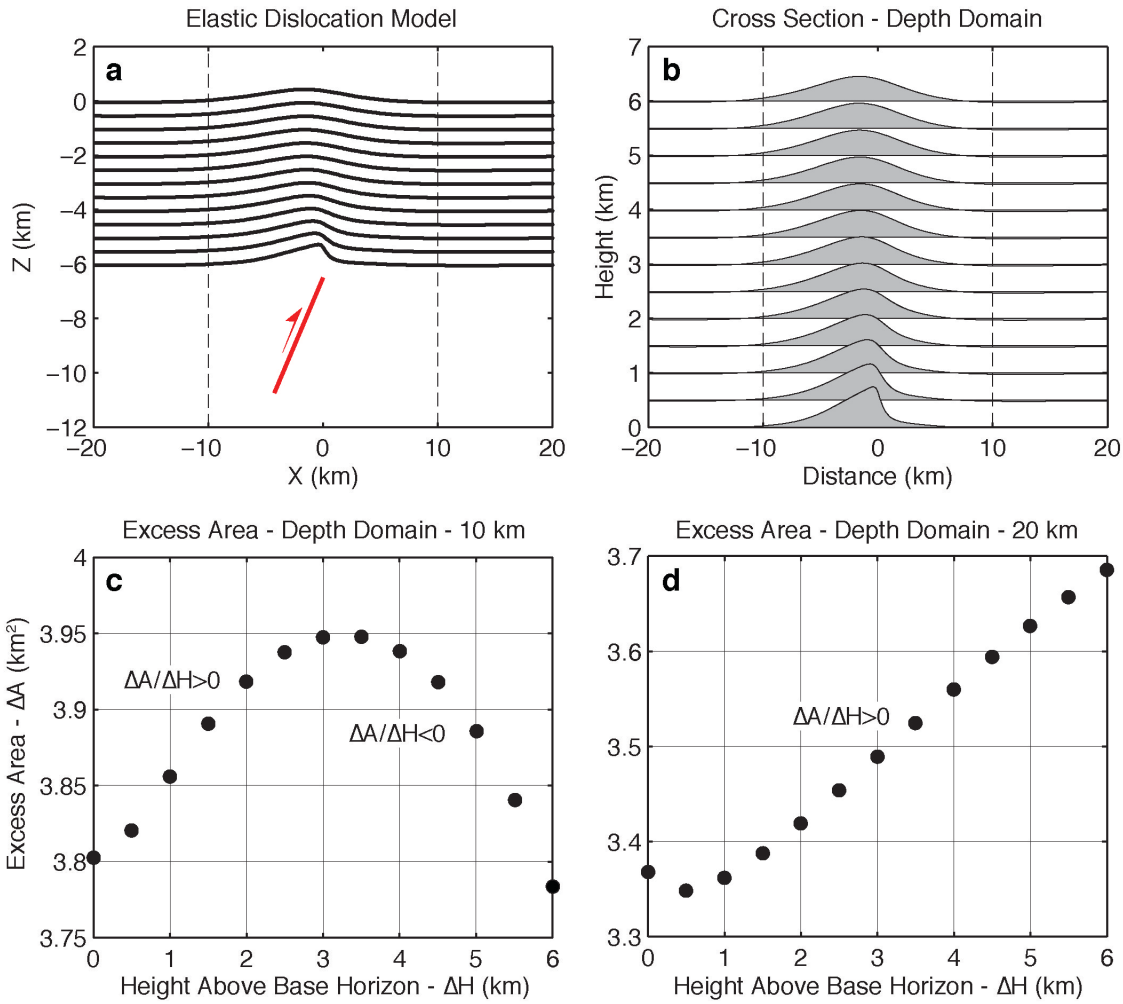

Figure B3 Area-of-relief (excess area) method applied to synthetic ED folds. (a) Synthetic folds generated above a 45° dipping dislocation. (b) The excess area is shaded gray. Conversion to the thickness domain (flattening) is not necessary because there is no regional slope. (c) Excess area plotted versus height for horizons measured to ±10 km from the fault tip (see dashed vertical lines in a and b). Note the rollover and decreasing ΔA with decreasing depth that begins at ΔH=3 km. (d) Excess area plotted versus height for horizons measured to ±20 km from the fault tip. ΔA increases with increasing ΔH.

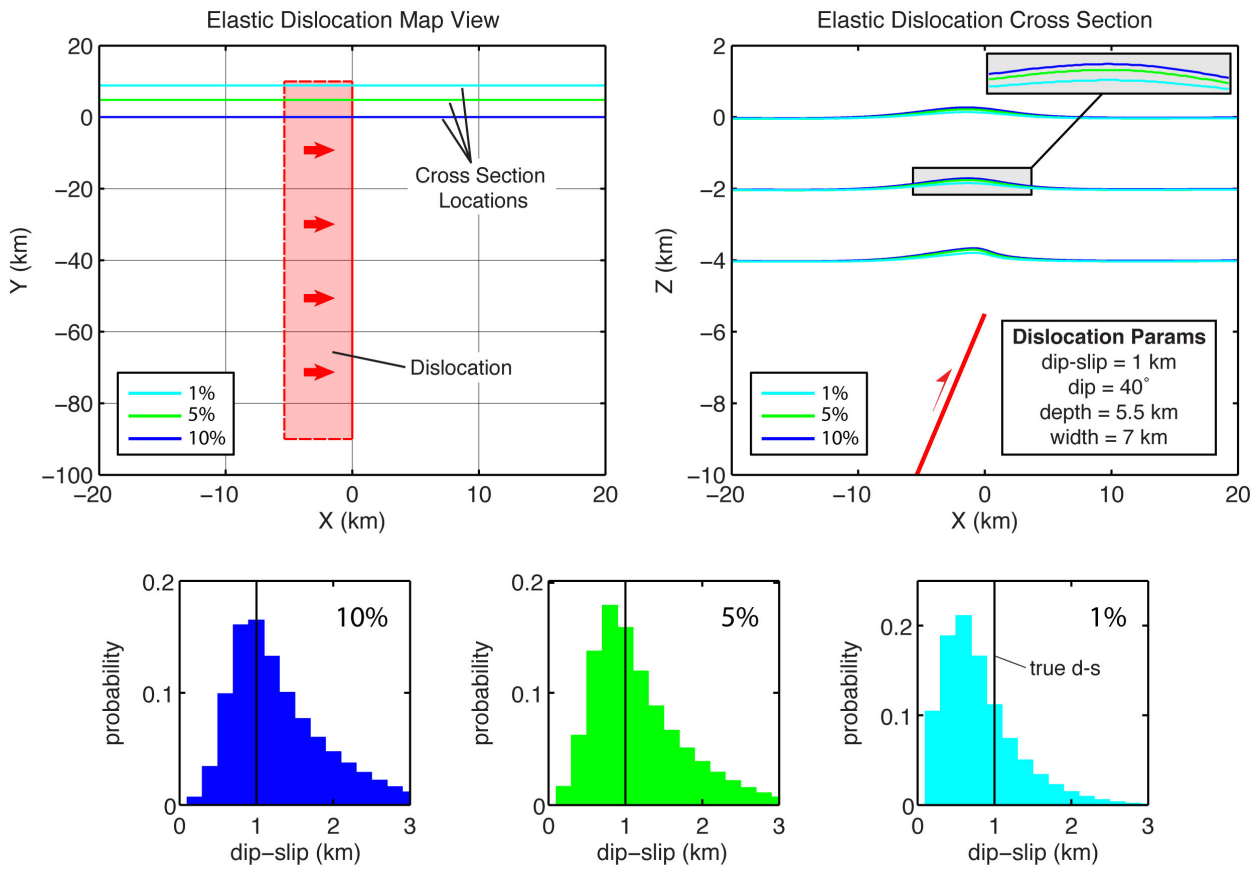

Figure B4 Plane-strain assumption test. Upper left panel shows the map view of a model dislocation with the location of observation lines near the fault edge. Upper right panel shows a cross-section view of the same model dislocation with synthetic beds located at 0, -2, and -4 km below the surface. The bottom three panels show the probability distribution for the dip-slip parameter from the grid search assuming plane-strain. The true dip-slip value is indicated by a vertical black line. The colors in all panels correspond to distance from the fault edge (e.g. the 10%, 5%, and 1% models are respectively located 10 km, 5 km, and 1 km from the edge of a 100 km-long-fault). The grid search inversion recovers the true dip-slip value (global minimum dip-slip = 1 km) at distances of 5% and 10%. The inversion underestimates the true dip-slip value almost directly above the fault edge at 1%.

Chapter 2

Isolating active orogenic wedge deformation in the southern Subandes of Bolivia

In preparation for publication as:

Weiss, J. R., B. A. Brooks, J.H. Foster, M. Bevis, A. Echalar, D. Caccamise, J. Heck, E. Kendrick, K. Ahlgren, D. Raleigh, R. Smalley Jr., and G. Vergani. Isolation active orogenic wedge deformation in the southern Subandes of Bolivia

Key points:

- A new GPS velocity field for the central Andean backarc recognizes and removes the signal of large subduction zone earthquakes
- The velocity field reveals along–strike changes in the deformation character of the backarc orogenic wedge
- There is close to a factor of two difference/decrease in the wedge loading rate and décollement locked width from north to south
- Departure from a simple, single décollement model suggestive of structural complexity including multiple active décollements and/or internal wedge deformation characterizes the south
- A comparison of wedge shortening rates over multiple timescales may indicate the northern and southern wedge are at different stages of the underthrusting-accretion cycle

Abstract

A new GPS-derived surface velocity field for the central Andean backarc permits an assessment of orogenic wedge deformation across the southern Subandes of Bolivia, where recent studies [*Brooks et al.*, 2011a; *Brooks et al.*, 2011b] suggest that great earthquakes (>M_w 8) are possible. We find that the backarc is not isolated from the main plate boundary

seismic cycle. Rather, signals from megathrust earthquakes contaminate the velocity field at distances greater than 800 km from the Chile trench. Two new wedge-crossing velocity profiles, corrected for seasonal and earthquake affects and oriented perpendicular to the strike of backarc fold-and-thrust belt structures, reveal distinct regions that reflect 1) locking of the main plate boundary across the high Andes, 2) the location of and loading rate at the back of orogenic wedge and 3) an east flank velocity gradient indicative of décollement locking beneath the Subandes. Modeling of the active, Subandean portions of the profiles indicates along-strike variations in both the décollement locked width (W_L) and wedge loading rate; the northern wedge décollement has a W_L of ~100 km while accumulating slip at a rate of ~14 mm/yr whereas the southern wedge has a W_L of ~61 km and a slip rate of ~7 mm/yr. When compared to Quaternary whole-wedge and thrust front estimates of geologic shortening and evidence for Holocene internal wedge deformation, the new GPS-derived wedge-loading rates may indicate the southern wedge has recently transitioned to a phase of thickening via reactivation of preexisting internal structures. In contrast, we suspect that the northern wedge is undergoing an accretion or widening phase primarily via slip on relatively young thrust front faults.

2.1 Introduction

The gently dipping fault planes ('décollements') beneath active orogenic wedges are home to some of the largest earthquakes on Earth [*Kanamori*, 1977; *Lay and Bilek*, 2007]. The 2004 Sumatra-Andaman (M_w 9.2), 2010 Maule (M_w 8.8), and 2011 (M_w 9.0) Tohoku earthquakes are three recent examples where rupture of the shallow megathrust beneath

the submarine accretionary wedge resulted in a destructive tsunami [*Fujiwara et al.*, 2011; *Lay et al.*, 2005; *Vigny et al.*, 2011]. In addition to oceanic subduction zones, décollements underlying subaerial orogenic wedges at plate boundaries and within continental interiors are also capable of generating large thrust earthquakes [*England and Jackson*, 2011; *Hubbard et al.*, 2015]. Examples include the 1999 Chi-Chi, Taiwan (M_w 7.6), 2008 Wenchuan, China (M_w 7.9), historical great earthquakes along the Himalayan thrust front [*Bollinger et al.*, 2014; *Hubbard and Shaw*, 2009; *Kao and Chen*, 2000; *Sapkota et al.*, 2013], and the recent 2015 Ghorka, Nepal (M_w 7.8) event, which ruptured a previously locked portion of the main basal décollement but did not propagate to the Himalayan thrust front [*Avouac et al.*, 2015; *Elliott et al.*, 2016; *Lindsey et al.*, 2015].

Although indispensable for investigating the basic mechanics and forcing mechanisms of orogenic wedge deformation, the critical wedge theory [e.g. *Dahlen et al.*, 1984; *Davis et al.*, 1983; *Whipple*, 2009; *Whipple and Meade*, 2004] is limited in its ability to address incremental fault slip processes acting over short to intermediate seismotectonic timescales, including the wedge earthquakes described above. Investigating the seismotectonics of wedges and in particular how slip on the décollement reaches the wedge front is a relatively young field of study. Work from a limited number of locations suggests that focused wedge-front deformation characterizes many active subaerial fold-and-thrust belts [*Lavé and Avouac*, 2000; *Simoes et al.*, 2007a; *Weiss et al.*, 2015]. In contrast, the Ghorka earthquake demonstrates that slip during large thrust events may be confined to deeper portions of the décollement [*Avouac et al.*, 2015]. A recent combination

of critical wedge theory with dynamic rupture models has shown that fault frictional strength, stress state, and intersection angle will control whether or not a wedge earthquake will be confined to the décollement or will propagate towards the surface on a branch fault [*DeDontney et al.*, 2012]. Additional studies focused on the non-steady state conditions of wedges have revealed episodic wedge growth in the form of alternating cycles of wedge thickening via internal deformation on preexisting (internal) structures and wedge widening via the initiation of new frontal thrusts [*Del Castello and Cooke*, 2007; *Yagupsky et al.*, 2014].

Despite these advances, first order questions remain regarding the forces that drive active wedge deformation. For example, what provides the push at the back of an active wedge and what are the slip rates on the basal décollements? Do these attributes vary in space and time and can they be quantified to better understand wedge boundary conditions? One approach researchers have adopted to gain insights in to the large-scale forces that drive continental deformation uses surface velocity gradients and a thin sheet model of viscous fluid flow to describe the bulk behavior of the lithosphere [*England and McKenzie*, 1982; *England and Molnar*, 1997; *Houseman and England*, 1986; *Lamb*, 2000]. An important outcome of the thin viscous sheet approximation is the hypothesis that variations in crustal thickness or related surface topography generate buoyancy forces that can drive the kinematics of large-scale deformation [*England and Jackson*, 1989]. Maximum gradients in surface velocity-derived buoyancy forces that parallel the regional topographic

gradients provide strong evidence for the fluid-like behavior of deforming regions [*England and Molnar*, 1997; *Lamb*, 2000].

Over the past few decades, as high precision Global Positioning System (GPS) timeseries lengthen [e.g. *Lin et al.*, 2013; *Reilinger et al.*, 2006; *Segall and Davis*, 1997; *Tregoning et al.*, 2013; *Vigny et al.*, 2005; *Wang et al.*, 2012] and satellite radar interferometry emerges as a well-established technique for measuring surface displacements [e.g. *Bürgmann et al.*, 2000; *Simons*, 2007; *Wright*, 2002], it has become possible to investigate the kinematics of crustal deformation at unprecedented temporal and spatial resolutions. A natural outcome of these advances in space-based techniques is to ask if we can use the resultant surface displacement fields to investigate crustal deformation at levels similar to detailed geologic interpretations (i.e. structural cross-sections), which reveal complicated subsurface geometries including duplexes, multiple detachment levels, fault propagation folds, etc. [e.g. *McQuarrie*, 2002b; *Poblet and Lisle*, 2011; *Suppe and Medwedeff*, 1990; *Yue et al.*, 2005]. For example, how do the large-scale forces driving continental deformation interact with the individual structures?

The Andes have served as a particularly attractive target for crustal deformation studies primarily because the highly seismogenic plate boundary along the western margin of the mountains provides the opportunity to investigate all aspects of the earthquake deformation cycle [*Wang et al.*, 2012]. The steadily accumulating deformation that produces mountain ranges can also be investigated in the Andes. The southern Subandes

(SSA) of Bolivia, comprising the east flank of the central Andean plateau, are a classic fold-and-thrust belt [*Davis et al.*, 1983] with well-known structures and deformational timing, making them an excellent target for active orogenic wedge investigations [*Brooks et al.*, 2003; *Brooks et al.*, 2011b; *Kendrick et al.*, 2006; *McQuarrie*, 2002b; *Mugnier et al.*, 2006; *Uba et al.*, 2009; *Weiss et al.*, 2015].

Bevis et al. [2001] presented one of the first GPS-derived velocity fields for the central Andean backarc and described a localized velocity gradient across the Subandean zone, suggesting a shallow décollement underlying the Subandean range is freely slipping towards the mountain interior and locked near the thrust front. However, due to the limited GPS data available at the time, they did not attempt to model details of the locking. Subsequently, *Brooks et al.* [2011b] presented and modeled a denser backarc GPS network, which reveals a strong east flank velocity gradient (EFVG), and suggested that the décollement underlying the wedge is locked down-dip for ~85-100 km while accumulating slip at a rate of ~10 mm/yr. Despite the low levels of modern and historical seismicity, the authors propose that a single strain-releasing event, rupturing the entire décollement locked width, could generate an earthquake of >M_w 8.5 on average every thousand years.

To further advance our understanding of the seismotectonics of orogenic wedge deformation in general and the SSA in particular we need to derive accurate surface displacement fields. Across the central Andean backarc a significant challenge relates to isolating the strain associated with orogenic processes from the much larger elastic signals

associated with the forearc and subduction zone plate boundary [*Bevis et al.*, 2001]. The SSA lie over 500 km to the east of the Nazca-South America plate boundary (Figure 2.1); previously this was thought to be far enough away that locking of the main plate interface does not dominate the crustal deformation signal [e.g. *Bevis et al.*, 2001; *Brooks et al.*, 2011b; *Lamb*, 2000].

Almost two decades have passed since publication of the first geodetic results from the central Andes [e.g. *Bevis et al.*, 2001; *Brooks et al.*, 2003; *Kendrick et al.*, 2006; *Norabuena et al.*, 1998]. Now that more GPS data are available for the region and in the aftermath of numerous large submarine subduction zone earthquakes including the 2007 M_w 7.7 Tocopilla, 2010 M_w 8.8 Maule, 2014 M_w 8.2 Pisagua, and 2015 M_w 8.3 Illapel, Chile earthquakes [*Delouis et al.*, 2009; *Hayes et al.*, 2014; *Moreno et al.*, 2010; *Schurr et al.*, 2014; *Schurr et al.*, 2012; *Ye et al.*, 2015] we are better equipped to reexamine the effect of forearc earthquakes on the backarc velocity field, and to assess locking and strain accumulation rates on the décollement beneath the active backarc orogenic wedge. Here we present new GPS-derived surface velocities for the central Andean backarc. We find that plate boundary large earthquakes at the Chile trench affect the entire backarc velocity field including sites on the adjacent foreland basin. After characterizing and removing the velocity perturbation associated with the Tocopilla earthquake, we isolate the long-term interseismic velocities and find north to south variations in the rate of contraction across the wedge and the width of the region over which the décollement becomes locked near the wedge front.

Specifically, both the wedge contraction rate and the décollement locked width in the north are significantly larger than in the south.

2.2 Deriving the GPS Velocity Field

2.2.1 GPS Data Acquisition and Processing

The GPS data used in this study come from sites that are part of large regional geodetic networks, some of which have been in place since the 1990's, including CAP (the Central Andes Project) [*Bevis et al.*, 1999; *Brooks et al.*, 2003; *Kendrick et al.*, 2001] and SNAPP (the South America-Nazca Plate Motion Project) [*Norabuena et al.*, 1998]. These networks include a mix of continuously operating GPS (cGPS) sites and survey-mode GPS (sGPS) sites that are ideally occupied for a minimum of 36-48 hours over consecutive days at one to two year intervals (Figure 2.1).

Brooks et al. [2011b] provide GPS-based velocity estimates for central Andean backarc GPS sites installed from 2000 to 2003 with a total time-span of 3 or more years. Here we improve on the *Brooks et al.* [2011b] velocity field by including ~4 years of additional cGPS data and sGPS data collected during site reoccupations in 2011, 2012, and 2013. We also reoccupied a subset of backarc sGPS sites in mid-2014 in response to the 2014 M_w 8.2 Pisagua, Chile earthquake (Figure 2.1).

The vast majority of the velocity estimates presented in *Brooks et al.* [2011b] are derived from sGPS sites, which have larger positional uncertainties than cGPS sites due to

their short occupation times and susceptibility to errors such as those associated with equipment setup [*Bevis et al.*, 1997]. In contrast, cGPS data-derived velocities are more accurate due to the massive averaging of their daily network solutions and because the data are time continuous permitting the recognition of real and artificial jumps and removal of the latter. Our analysis includes data from ~10 new cGPS sites established across the backarc since 2009. We also include data from Altiplano and foreland basin sGPS sites established in 2007 and 2009 and occupied an average of 3 times. These newer sGPS sites are not included in the *Brooks et al.* [2011b] analysis. We typically consider data from cGPS sites established for 3 years or more and sGPS sites with 3 or more occupations and a total time-span greater than 3 years (Table 2.1). We also include some shorter time-span (2-3 years) cGPS sites recognizing that their position and velocity uncertainties are larger than the longer-lived sites. The greater length of the GPS time series combined with the addition of new sites results in improved backarc coverage compared to previous studies [*Bevis et al.*, 2001; *Brooks et al.*, 2011b; *Norabuena et al.*, 1998]. Due to difficulties associated with traversing the Subandes by vehicle, our GPS network lies essentially within reach of the northern Route 6, which connects Sucre to Camiri, and the southern Route 11, which connects Tarija to Villamontes (Figure 2.1). Both roads cross the Subandes in an approximately east-west direction resulting in GPS sites that lie along two wedge-crossing profiles, which we refer to as the Sucre and Tarija profiles. At their narrowest point (~63.5° W) the two sets of sites are separated by ~100 km but they are typically >200 km apart (Figure 2.1).

Our field, processing, and velocity analysis methods in South America have been described previously [*Bevis et al.*, 1997; *Bevis et al.*, 2001; *Bevis et al.*, 1999; *Brooks et al.*, 2003; *Brooks et al.*, 2011b; *Kendrick et al.*, 2001; *Kendrick et al.*, 2003; *Kendrick et al.*, 2006; *Kendrick et al.*, 1999]. To summarize, for each daily solution we process all the available data using GAMIT [*King and Bock*, 2000], which estimates the 3-D relative position of ground stations and satellite orbits and GLOBK [*Herring*, 2000], which merges the daily regional with global solutions for International GNSS Service (IGS) sites. Since we are interested primarily in regional deformation we refrain from the global stacking common to large-scale scale plate motion studies and instead stack only stations on the South American and Nazca plates and a few sites on adjacent plates and minimize motions of stations located on the stable core of the South American craton. We express our velocities in a craton-fixed reference frame with horizontal and vertical velocities of less than 1 mm/yr (Table C1 and Figure C1). Specifically, we use 44 cGPS stations primarily located in Brazil to create the horizontal reference frame. These sites have a total RMS horizontal velocity of 0.66 mm/yr. The total RMS velocity of the 35 cGPS sites used to constrain the vertical reference frame is 0.94 mm/yr. We estimate central Andean site velocities in this stable reference frame by performing linear fits through the daily positions for each station in the network while minimizing the misfit across the entire network. Below we describe a few additional modifications to our velocity estimation approach.

2.2.2 Seasonal Signal Estimation

Seasonal perturbations due to climate driven deformation of the solid earth affect the GPS time series and must be taken in to account when calculating site velocities [*Bevis and Brown*, 2014; *Blewitt and Lavallée*, 2002] (Figures 2.2 and C1), particularly when sGPS site occupations were performed at different times of the year. These changes in lithospheric loading due primarily to surface water, snow and ice are of particular concern in our study area, which lies between the Amazon rainforest to the northeast and glaciated portions of the Andes to the west. Pronounced rainfall gradients across and along the Andean backarc [*Strecker et al.*, 2007a] also contribute to the seasonal signals present in our time series. *Bevis et al.* [2005] show annual displacement cycles driven by seasonal variations in the mass of water residing in the Central Amazon Basin with peak vertical amplitudes of close to 40 mm with horizontal cycles an order of magnitude less.

We account for seasonal cycles in our GPS time series data for each of the NEU (north, east, and up) coordinates using a sinusoidal function consisting of one annual and one semi-annual term [e.g. *Bevis and Brown*, 2014; *Langbein*, 2004]:

$$seasonal_{NEU} = \sum_{k=1}^{n_F} \left[s_{k_{NEU}} \sin(\omega_k t) + c_{k_{NEU}} \sin(\omega_k t) \right] \tag{2.1}$$

where s_k and c_k are the sine and cosine amplitudes at frequency ω_k and n_F is the number of frequencies or harmonics used to model the displacement cycles. For our purposes $n_F = 2$ and:

$$\omega_k = \frac{2\pi}{\tau_k}, \quad \tau_1 = 1\,\text{year} \quad \text{and} \quad \tau_2 = 1/2\,\text{year}.$$

We estimate the best-fit seasonal cycle amplitudes for cGPS site time series with little to no data gaps. A number of cGPS sites do not fit this criteria and we cannot directly estimate seasonals for sGPS sites. We therefore interpolate the best-fitting annual and semiannual amplitudes and phases for sites that do fit this criteria onto a regular grid and find that whereas a consistent regional pattern characterizes the annual component of the seasonals, the semiannual component varies between stations in an irregular, non-predictable way (Figures 2.3 and 2.4). Based on these results, we extract only the annual component from the interpolated grid for cGPS sites without seasonal estimates, and for all sGPS sites and we include a semiannual component only for cGPS sites where it can be estimated directly from the data.

2.2.3 Plate Boundary Earthquake Perturbation and Characterization

Initial analysis of the Subandean cGPS site time series revealed unexpected perturbations most noticeable in the eastward displacements at times corresponding to recent Chilean earthquakes and in particular the 14 November 2007 M_w 7.7 Tocopilla event [*Delouis et al.*, 2009; *Schurr et al.*, 2012] (Figure 2.5). We initially noticed the perturbation as a change in velocity for the IGS cGPS site UNSA in northwestern Argentina. A velocity change at UNSA is also apparent in association with the 2010 M_w 8.8 Maule, Chile earthquakes [*Moreno et al.*, 2010]. Subsequent analysis of the Bolivian cGPS site time series revealed a Tocopilla-related velocity field perturbation at all of the Altiplano and Subandean cGPS sites where data exist prior to the earthquake including SUCE and SCRZ

(Figure 2.5). These two Bolivian sites were not affected by the Maule earthquake but do show clear coseismic offsets and postseismic responses associated with the 2014 M_w 8.2 Pisagua, Chile earthquake [*Hayes et al.*, 2014; *Schurr et al.*, 2014].

We find a regional pattern of post-quake eastward velocity decrease when we subtract the post-Tocopilla from the pre-Tocopilla best-fit velocities (Figure 2.6). Because the central Andean backarc region and the southern Subandean profile sites in particular were affected by the Tocopilla event, failure to recognize and account for earthquake-related transients in the GPS time series could result in inaccurate site velocity estimates (Figure 2.8). Therefore, one of our initial goals is to characterize the Tocopilla-related perturbation recorded in the GPS data in order to create a velocity field uncontaminated by plate boundary earthquakes. We reserve a similar examination of the Pisagua earthquake-related perturbation for a future effort and exclude post-Pisagua portions of the GPS time series from the analysis presented here.

In order to correct the backarc velocity field we assume the earthquake-affected sites will not experience a permanent change in velocity but rather eventually return to their interseismic or pre-quake velocity prior to the next major earthquake [*Wang et al.*, 2012]. To characterize the velocity perturbation we adopt an empirical approach similar to recent studies of major strike-slip earthquakes [e.g. *Ergintav et al.*, 2009; *Hearn*, 2003]. GPS sites close to the earthquake epicenter in northern Chile behave in a fashion comparable to observations from other large earthquakes. This behavior includes a large coseismic offset

followed by postseismic deformation in the form of superimposed rapidly and more slowly decaying transients (Figure 2.7). Poroelastic rebound, after-slip on or near the rupture zone, and near- and far-field viscoelastic relaxation of the upper mantle and/or lower crust are generally thought to control this behavior [*Barbot and Fialko*, 2010; *Bevis and Brown*, 2014; *Ergintav et al.*, 2009; *Hearn*, 2003; *Meade et al.*, 2013; *Wang et al.*, 2012].

We model the NEU components of the GPS time series using a linear combination of an interseismic velocity, a coseismic step, a postseismic term with up to three characteristic time constants and the previously described seasonal term [e.g. *Bevis and Brown*, 2014]:

$$model_{NEU} = interseismic_{NEU} + coseismic_{NEU} + postseismic_{NEU} + seasonal_{NEU} \tag{2.2}$$

where

$$interseismic_{NEU} = a0_{NEU} + (t - t0)b_{NEU} \tag{2.3}$$

where t is time, $a0_{NEU}$ are the y intercepts of best-fit lines to the pre-quake portions of the NEU components of the GPS time series residuals, b_{NEU} are the slopes of the best-fit lines or the interseismic/pre-quake velocities, $t0$ is the time of the earthquake,

$$coseismic_{NEU} = coseismic_step_{NEU} \cdot ystep \tag{2.4}$$

where $coseismic_step_{NEU}$ are the coseismic displacements measured from the GPS data and $ystep$ is the unit step (Heaviside) function consisting of zeroes before the earthquake and ones after the earthquake. Finally,

$$postseismic_{NEU} = ystep \sum_{i=1}^{3} (A_{i_{NEU}} (1 - \exp(-tstep / \tau_i))) \tag{2.5}$$

where A_{iNEU} are the amplitudes of the *i*th exponential terms, τ_i is the time constant of the *i*th exponential term and *tstep* is the time since the earthquake. Our choice of exponentials for postseismic characterization is not meant to point towards any particular underlying geophysical control on the process (e.g. viscoelastic relaxation) but rather is a computational convenience; logarithmic or spline functions, for example, can fit the data equally well [*Bevis and Brown*, 2014; *Ergintav et al.*, 2009; *Hearn*, 2003].

We find that for near-field (with respect to the trench) sites in northern Chile 2-3 exponential terms with τ_1 on the order of one to a few days, τ_2 on the order of 10's to 100's of days, and τ_3 on the order of 5-20 years are necessary to fully describe the postseismic portion of the GPS time series (Figure 2.7). For mid- and far-field sites like UNSA and those across the backarc, the postseismic response is manifest as a change in velocity (Figure 2.8), which suggests that the timescale of the underlying deformation process is slow compared to the time that has elapsed since the Tocopilla earthquake and that our post-quake observation time-span of ~7 years is not sufficient to fully characterize the long-term regional transient behavior [*Ergintav et al.*, 2009].

We find that three exponential terms are not required to adequately describe the backarc transients. Rather, a single term with a time constant (τ_3) of ~5-10 years results in a good fit to the Subandean sites (compare Figure 2.5 and τ_3 in Figure 2.7) with the exception of SUCE (Figure 2.5) where a single intermediate decay term (τ_2=~1 year) provides the best fit to the data. For the vast majority of our Subandean sites we simplify

the postseismic parameter estimation by fixing a single decay time of 10 years and estimating the best-fit long-term exponential term amplitudes (A_3; Table C2).

Our empirical characterization of the GPS time series requires two additional components: coseismic offsets and pre-quake/interseismic site velocities. Coseismic offsets associated with the Tocopilla earthquake are not typically observed or are minimal at the backarc cGPS sites that existed prior to the earthquake (Figure 2.5). The mid-field Altiplano site UYNI is the only Bolivian cGPS site where we can compute a statistically significant coseismic displacement (Figure 2.8; Table C2). Offsets may be present at other Bolivian sites but data gaps around the time of the earthquake or little to no pre-quake data prevent us from estimating a coseismic step. Further, we have no way of directly estimating nor do we need an estimate of the Tocopilla-related coseismic offset at GPS sites established after the earthquake. Only for sites with pre-quake data do we attempt to estimate coseismic offsets and only where the estimates are statistically significant (i.e. offset>σ_{offset}) do we incorporate them in our analysis.

The postseismic portion of the timeseries can be represented as a linear combination of the interseismic velocity and the postseismic transient. Our general approach involves subtracting the seasonal signal from the GPS site time series and performing a nonlinear, least squares regression (Levenberg-Marquardt method) to find the parameters that best describe the coseismic and postseismic portions of the time series with no *a priori* constraints on the model parameters. For sites with pre-quake data (e.g.

SUCE and SCRZ, Figure 2.5; UYNI, Figure 2.8), we estimate the interseismic portion of the model directly from the NEU time series and search for the best-fit coseismic steps and long-term exponential decay amplitudes.

For sites that did not exist prior to the earthquake (e.g. COLO and COCI; Figure 2.8), and with only a limited postseismic time-window, we are unable to robustly isolate these two components. Instead, to characterize the postseismic transients for sites without pre-quake data, we use an *a priori* estimate of the pre-quake surface velocity. We estimate an *a priori* interseismic velocity field using sites with sufficient pre-quake data to interpolate on to a regular grid and create a map of interseismic surface velocities (Figure C2). This is a good approximation of the backarc interseismic velocity field considering the regional distribution of sites with pre-quake estimates and because a large megathrust earthquake had not occurred on the central Andean portion of the Chile trench for ~130 years prior to the Tocopilla and subsequent Pisagua events [*Schurr et al.*, 2014; *Schurr et al.*, 2012]. For sites established after the Tocopilla event we extract the interseismic surface velocities from the interpolated grid and solve for the long-term exponential decay amplitudes only.

Once we have estimates for all the parameters, we subtract the coseismic and postseismic portions of the model from the GPS site time series and compute new best-fit velocities for each site (Table 2.1). For sites with pre-quake data the new velocities are similar to the pre-quake values. For sites without pre-quake data, the new velocity estimates mimic the interseismic values from the interpolated grid. Crucially, by adopting a

conservative approach to estimating the errors, which we describe in the following section, the incorporation of *a priori* interseismic velocities for some sites should not unduly constrain our model towards these specific values.

Figure 2.8 shows examples of the eastward displacements for select backarc sites where the best-fit postseismic amplitudes are negative and the corrected eastward velocities are greater than the uncorrected values. We expect this behavior due to the geometry of the megathrust with respect to the backarc (Figures 2.1 and 2.6). Slip during a subduction zone earthquake like the Tocopilla and Pisagua events results in predominantly seaward coseismic displacement of the upper plate and affected GPS sites typically record westward coseismic and postseismic motions (Figures 2.1, 2.7 and 2.8) [e.g. *Lin et al.*, 2013]. However, the Tocopilla earthquake-related results for the central Andean backarc exhibit substantial and often unexpected variability with respect to both the sign and magnitude of the best-fit exponential decay amplitudes (Figure C3). We cannot rule out that this variability is the result of over-fitting the relatively sparse sGPS data and cGPS time series that begin after the earthquake since the few cGPS sites established prior to the earthquake generally behave as expected (Figure 2.6). However, the confidence intervals on the postseismic parameters suggest this is not the case (Table C2) and our conservative velocity errors (see Section 2.4 and Table 2.1) account for the possibility that our approach is inadequate. Further, the distinct characteristics of the Sucre and Tarija profiles, described in detail in Section 2.2, are present in the uncorrected data and merely

accentuated in the corrected data (Figure C4) lending further support to our approach and results.

We can think of a few physical factors that possibly contribute to the variability in postseismic amplitudes. First, numerical studies of postseismic relaxation using quasi-realistic rheologies (e.g. layered viscoelastic, power-law) often show variable behavior similar to our observations particularly in the far-field regions with respect to the rupture zone [e.g. *Barbot and Fialko*, 2010; *Hearn*, 2003]. The Subandean GPS network is located hundreds of kilometers northeast of the Tocopilla earthquake epicenter and coseismic slip maxima (Figure 2.6). Second, the crust and lithospheric mantle structure beneath the central Andes is complex with along- and across-strike variations in crustal thickness, the presence of the strong edge of the Brazilian craton underthrusting the backarc as far west as ~65.5° W, and evidence for lower crust delamination with pockets of high and low P wave velocity material in the upper mantle [*Beck and Zandt*, 2002] (Figure C3). This complexity lies beneath the GPS network and so likely affects details of the far-field postseismic response. Third, small-scale variations in the poroelastic properties of the Subandean lithosphere could also be a factor. Different crustal rock types exhibit a large range in poroelastic moduli [*Barbot and Fialko*, 2010] and we suspect that variable rheologies are often juxtaposed across large-offset thrusts in the heavily deformed backarc [e.g. *McQuarrie*, 2002b].

2.2.4 Velocity Error Estimation

The presence of time-correlated, colored noise (e.g. flicker, random-walk, power-law) in the GPS time series [*Hackl et al.*, 2011; *Langbein and Johnson*, 1997; *Mao et al.*, 1999; *Williams et al.*, 2004; *Zhang et al.*, 1997] must be accounted for to create an accurate representation of the regional deformation field. Here we use the *Langbein* [2004] method to compute Gaussian and power-law noise statistics (Table C3) and associated velocity uncertainties (Table 2.1) for the cGPS site time series corrected for Tocopilla earthquake-related deformation and seasonal periodicities. The power-law noise model describes many geophysical phenomena [*Agnew*, 1992] and represents an average of the flicker and random-walk noise present in GPS data [*Langbein*, 2012; *Mao et al.*, 1999; *Zhang et al.*, 1997]. Further, in their comprehensive study of cGPS time series error, *Williams et al.* [2004] report that a power law noise model best describes the data.

For the central Andean backarc cGPS sites we find that when assuming "standard", uncorrelated Gaussian error model, the N, E, and U velocity errors are on average underestimated by factors of 9.0, 8.5, and 5.8, respectively, compared to the white and power law noise model. These factors are on the high end but comparable to previous studies, which show that velocity errors are underestimated by factors ranging from 2 to 11 if a purely white noise model is assumed [*Hackl et al.*, 2011; *Mao et al.*, 1999; *Williams et al.*, 2004; *Zhang et al.*, 1997]. For direct comparison, in their analysis of cGPS data from the Central Andes, *Kendrick et al.* [1999] find that velocity errors increase by a factor of ~2.5 when they account for temporally correlated noise in their position time series. We suspect

that their low scaling factor compared to our analysis is due to the generally poorer quality solutions available at the time resulting in higher daily position scatter (i.e. white noise), which dominated their error budget.

We use a modified version of the method outlined in *Williams* [2003] to compute velocities and associated uncertainties (white and power-law noise) for the sGPS sites. We assume that the colored noise present in the GPS data does not vary regionally and form the data covariance matrix using the mean NEU white and power-law noise amplitudes. We adopt the maximum NEU power-law exponents/indices estimated from the cGPS time series (Table C3) as a conservative measure to account for any residual long-period "noise" introduced during our previous correction steps. We perform a standard least squares inversion using this covariance matrix. Finally, we assume the *a priori* noise model is imperfect and scale the formal model covariance by the mean square error of the sGPS time series residuals to obtain a conservative measure of the total velocity uncertainties that reflects the combined white and power-law noise. The Gaussian model underestimates the sGPS errors by factors of 6.2, 4.7, and 8.7 for the NEU coordinates, respectively, compared to the white and power law noise model. This reduction in scale factor when compared to those for the cGPS is in agreement with our expectation that standard errors for sGPS sites with long time-spans will not be as underestimated as the standard errors as for the shorter time-span cGPS sites [e.g. *Zhang et al.*, 1997]. We report the total (white and power-law noise) and standard errors (Table 2.1), and use the total estimates as weighting factors

in our velocity field modeling. We also report the uncorrected velocities and associated standard errors in the supplementary information (Table C4).

2.3. New Crustal Velocity Field for the Central Andean Backarc

2.3.1 Map-view Pattern

The corrected backarc velocity field reveals first-order characteristics similar to previous results for the Central Andes [e.g. *Bevis et al.*, 1999; *Brooks et al.*, 2011b; *Kendrick et al.*, 2001; *Norabuena et al.*, 1998]. Vectors are generally oriented sub-parallel to the ~N78˚E Nazca-South America convergence direction [*Angermann et al.*, 1999; *Kendrick et al.*, 2003] (Figures 2.1 and 2.9). In detail, however, the new data reveal a clockwise rotation in the orientation of the vectors from west to east. The mean azimuth of vectors located west of a line of longitude that passes through Tarija (TRJA in Figure 2.9) is ~N74˚E. In contrast, the mean azimuth of Subandean site vectors located between TRJA and the thrust front is ~N89˚E. The rotation is most pronounced across the southern, Tarija profile where the mean Subandean azimuth is ~N96˚E compared to ~N82˚E for the northern profile. The rather abrupt change in Tarija profile vector azimuths roughly coincides with the boundary between the Interandean Zone and the SSA (Figure 2.9).

The velocity vector rotation we observe is consistent with elastic models of oblique plate convergence, which show a decrease in surface velocity obliquity (with respect to the orientation of the trench axis) moving away from the subduction zone towards the plate interior [*Bevis and Martel*, 2001]. However, despite the notion that the interseismic velocity

field reflects elastic, non-permanent deformation, the observed rotations are also consistent with longer-term, geologic results. *Allmendinger et al.* [2005] show that GPS data from south of the Andean axis of topographic symmetry [*Gephart*, 1994; *Isacks*, 1988] generally exhibit counterclockwise rotations, which are consistent with those recorded by paleomagnetic and geologic indicators, and suggest the interseismic velocity field partially reflects long-term, inelastic crustal deformation patterns. Based on late Miocene-Quaternary fold and fault information, early GPS results, and paleomagnetic data, *Lamb* [2000] compute a central Andean horizontal velocity field representative of regional deformation over the last few hundred thousand years. Like we do, they show that vectors in the high Andes are sub-parallel to the relative plate convergence direction but change to be nearly perpendicular to the range front across the Subandes. Our new velocity field suggests that Subandean structures, which have generally formed from west to east in a foreland-breaking sequence over the past ~10 Myr [e.g. *Uba et al.*, 2009], may exert a strong control on the modern surface deformation pattern across the SSA. The strike of the Subandean anticlines and synclines changes from north to south and the vectors are by and large oriented orthogonal to these features (Figure 2.9). This observation is broadly consistent with a model of ductile deformation of the Bolivian lithosphere driven by crustal thickness and topography-induced gravitational stresses [*Lamb*, 2000].

2.3.2 Velocity Profiles

Horizontal surface velocities gradually decrease away from the Chile trench and GPS sites located east of the thrust front are essentially not moving with respect to the stable

core of the South American craton. Again, this is not dissimilar to previous GPS results for the region and authors have invoked elastic models of plate boundary locking and the seismic cycle combined with a component of backarc convergence to explain this pattern [e.g. *Bevis et al.*, 2001; *Bevis et al.*, 1999; *Norabuena et al.*, 1998]. Our choice of profile azimuths, perpendicular to the strike of the Subandean ranges, has a modest effect on the projected velocity magnitudes in only the southern profile. The Tarija profile orientation (N100˚E) is oblique to the vectors west of TRJA but sub-parallel to the mean azimuth of the southern profile Subandean site vectors (96˚E) resulting in an apparent reduction of the projected velocities for high Andes sites but only a slight change in the profile-parallel SSA velocities. An example of the projection-related reduction in velocities can be seen at the cGPS site UYNI, which has projected northern and southern profile velocities of 15.67 and 13.84 mm/yr respectively.

The GPS velocity profiles (Figure 2.10) exhibit features that reflect orogenic wedge processes. These features are not simply a product of our profile azimuth choice and persist if we project the velocities perpendicular to the Chile trench or on to a latitudinal profile. Despite the general eastward decrease in velocities associated with locking of the main plate boundary, both profiles exhibit a 100-150 km-wide zone of roughly constant velocity (that we term a velocity 'plateau') with western edges at distances of ~300 km and ~200 km from the thrust front for the northern and southern profiles, respectively. The northern velocity plateau is at ~12 mm/yr, whereas the southern velocity plateau is at ~6 mm/yr and is less well-defined due to a group of sites near Entre Rios, Bolivia (ENRI;

Figure 2.10) with projected velocities ≤5 mm/yr. For each plateau, the western edge of the constant velocity region roughly coincide with the Eastern Cordillera (EC)/Interandean Zone (IAZ) boundary (Figure 2.10). This coincidence is significant because the EC is generally viewed as the backstop or bulldozer [e.g. *Davis et al.*, 1983] driving SSA deformation since ~10 Ma [*Allmendinger et al.*, 1983; *Gubbels et al.*, 1993; *Kley*, 1996]. Thus the ~100-150 km-wide, constant velocity plateaus apparent in the new GPS-derived velocity field delineate both the back of the wedge, including the inactive (IAZ) and active (SSA) portions, and the approximate slip rate or wedge loading rate on the basal décollement.

East of the velocity plateaus, both profiles both exhibit sharp velocity decreases before reaching ~0 mm/yr adjacent to the thrust front. The distance over which the reductions in velocity occur are ~100 km and ~50 km for the northern and southern profiles, respectively. We refer to these decreases as the northern and southern east flank velocity gradients (nEFVG and sEFVG) and note that the velocities decrease to ~0 mm/yr ~30-40 km west of the thrust front (Figure 2.10). Again, as with the velocity plateaus, the nEFVG is prominent and clearly defined by ~9 sites west of CAMR whereas the sEFVG is far less distinct due to its narrow width and the lack of GPS sites immediately adjacent to VMON and YCBA (Figure 2.10).

The location of the EFVGs with respect to the Subandean structures also varies along-strike. The western limit of the wide, nEFVG corresponds to the IAZ/SSA boundary

and its eastern edge is located near the range front (as opposed to thrust front) Charagua anticline (Figures 2.9 and 2.10). In contrast, the narrow sEFVG lies exclusively within the front of the active wedge encompassing only the first couple of range-front thrusts.

2.3.3 Backarc Velocity Field Modeling

To investigate strain accumulation across the Subandean orogenic wedge we model the eastern portion of the corrected GPS velocity field, including the constant velocity plateaus described above, using rectangular dislocations in an elastic half space [*Okada*, 1985]. This approach is commonly used to investigate interseismic stress and strain accumulation at subduction zones and is also valid for modeling surface displacements associated with large intracontinental thrust faults including the décollements of active orogenic wedges [*Bilham et al.*, 1997; *Brooks et al.*, 2011b; *Hsu et al.*, 2003; *Vergne et al.*, 2001]. We exclude velocities for sites located west of the velocity plateaus as locking of the main plate boundary at the Chile trench has been examined in detail by others [e.g. *Bevis et al.*, 2001; *Chlieh et al.*, 2011; *Kendrick et al.*, 2006; *Norabuena et al.*, 1998].

Brooks et al. [2011b] stacked central Andean backarc surface velocities onto a single Chile trench-perpendicular profile. Here we model the northern and southern sites separately as our denser, more precise dataset provides an opportunity to investigate along-strike variations in the décollement properties. The strike of the Subandean structures changes from north to south so we project the northern and southern data on to ENE- and ESE-oriented profiles, respectively, to view and model the sites in a structure-

perpendicular reference frames (Figure 2.9). For example, although separated in map-view by ~85 km, the cGPS sites VMON and YCBA are located on the eastern flank of the Aguarague anticline (Figure 2.11). Only if we project the Tarija profile sites on to an azimuth oriented approximately perpendicular to the strike of this structure do they plot adjacent to one another.

We simulate continuous, uniform slip on the gently dipping décollement at the base of the wedge using the seismic cycle or back-slip model of strain accumulation and release at a subduction zone [*Savage*, 1983]. In this model strain accumulation is attributed to steady aseismic slip at depth on the basal fault towards the mountain interior while the shallow, up-dip portion of the fault remains locked. By superposing elastic dislocation solutions for a steady-state, reverse fault with stable sliding along its entire length and a shallow back-slip fault with equal yet opposite motion (normal slip) we impose a no-slip condition on the up-dip portion of the dislocation that represents the locked portion. As a result, the maximum gradient in the horizontal velocity field overlies the slipping-to-locked transition [*Bilham et al.*, 1998; *Okada*, 1985; *Savage*, 1983].

We compare the dislocation model and GPS surface velocities and explore the multidimensional parameter space using a grid search inversion approach [e.g. *Weiss et al.*, 2015]. We compare all three components of the velocity field (NEU) to the model noting that inclusion of the vertical velocities helps constrain the depth to the slipping-to-locked transition in particular. We reduce the typical nine parameter problem to five by making

the following simplifying assumptions: the dislocation is very long (across-strike) and wide (along-strike), each profile is oriented perpendicular to the strike of the underlying dislocation, the up-dip limit of the dislocation is located directly beneath the easternmost emergent thrust front structures, and there is no opening mode component of displacement across the dislocation. We also assign a standard Poisson's ratio of 0.25. These assumptions leave us with five dislocation parameters for our grid search including 1) dip, 2) strike-slip, 3) dip-slip, 4) down-dip width of the locked zone (W_L), and 5) depth to slipping-to-locked transition. We define unique dislocation geometries by varying each of these parameters and computing the weighted sum of squares misfit between the model and data where the data are the corrected NEU velocities and the weighting factors are the corresponding standard deviations (Table 2.1). We present our results in the form of probability distributions of the dislocation parameters (Figure 2.11). Although we refrain from placing any *a priori* constraints on the model parameters for our grid search we note that balanced cross sections from the region indicate that the Subandean décollement is sub-horizontal with a dip of ~2° at a depth of 10±5 km beneath the surface [*Baby et al.*, 1997; *Dunn et al.*, 1995; *Giraudo and Limachi*, 2001; *McQuarrie*, 2002b].

The dislocation parameter distributions for the profiles reveal different behavior for portions of the wedge located ~200 km apart. In the north, the model indicates that the décollement is sub-horizontal, dipping gently to the west (<5°) and slipping at rates of ~14 mm/yr (*U2*; dip-slip) and ~1 mm/yr (*U1* sinistral; left-lateral strike slip). The width of the locked zone (W_L) is ~100 km and the depth to the slipping-to-locked transition is ~13 km.

The reported peak parameter distribution values all fall within the 95% confidence regions of the *Brooks et al.* [2011b] results and are consistent with some structural and geophysical observations (Figure 2.11). For example, the model dislocation dip and depth are within the values suggested by regional cross sections. The slipping-to-locked transition from the best model, which we define as the peaks (modes) of the corresponding probability distributions, intersects both the basal décollement from published cross sections [*Dunn et al.*, 1995; *Giraudo and Limachi*, 2001] and the 300 °C isotherm calculated from the backarc geothermal gradient [*Currie and Hyndman*, 2006]. The latter intersection is particularly significant as 300 °C indicates the approximate transition from velocity-strengthening (continuous creep) to velocity weakening (stick-slip) behavior in quartzo-feldspathic rocks, which is where earthquakes will tend to nucleate [*Scholz*, 1988; *Scholz*, 1998]. The probability distribution peak for the dip-slip parameter of 14 mm/yr, which we equate to the loading rate at the back of the orogenic wedge, also compares favorably with the SSA Plio-Quaternary shortening rate estimates of 7-13 mm/yr [*Mugnier et al.*, 2006 and references therein] and is slightly faster than the *Brooks et al.* [2011b] best model value of 11.1 mm/yr .

The southern profile model results indicate that the décollement is also sub-horizontal, dipping gently to the west (<5°), while slipping at rates of ~7 mm/yr (U2; dip-slip), which is within the range of Plio-Quaternary shortening estimates but one half of the northern rate, and ~4 mm/yr (U1 sinistral; left-lateral strike slip). The southern W_L of ~61 km is significantly less than the northern W_L and the slipping-to-locked transition depth of

~7 km falls within the 10±5 km range constrained by balanced cross-sections from the region (e.g. *Allmendinger and Zapata* [2000]).

2.4 Discussion of Modeling Results

Although we have already drawn comparisons between geologic observations and our new GPS velocity field and modeling results, a few additional points are worth mentioning. Apart from some minor differences in W_L and the dip-slip rate, our northern profile results are nearly identical to *Brooks et al.* [2011b] and suggest that rupture nucleates somewhere between the slipping-to-locked transition and the thrust front and may propagate up-dip towards the thrust front resulting in shallow fault-related folding and/or surface rupture [*Brooks et al.*, 2011b; *Weiss et al.*, 2015]. The well-defined, smooth nEFVG pattern is indicative of locking on the basal décollement and not motion of individual surface faults or fault blocks [e.g. *Lamb and Smith*, 2013].

The Tarija profile results are less straightforward suggesting a more detailed modeling approach may be required to match some of the geologic information. We suspect that the southern subsurface complexity, which is readily apparent when comparing the two geologic cross sections (Figure 2.11), may be influencing the GPS results. In the vicinity of the Tarija profile, in addition to the primary detachment surface located at the base of the Silurian Kirusillas Formation, a shallower, secondary décollement exists within the Devonian Los Monos shale (Figure 2.11). The faults that generated both the Villamontes and La Vertiente structures cut up from the shallow detachment, which also links the large

Aguarague surface fold and additional wedge-interior faults, including the Suaruro structure, to the deeper, primary detachment [*Dunn et al.*, 1995; *Giraudo and Limachi*, 2001; *Uba et al.*, 2009]. The location of the southern slipping-to-locked transition, to the east of the presumed active Aguarague and Suaruro thrusts [*Lamb*, 2000; *Mugnier et al.*, 2006], and closer to the shallower décollement, combined with the fact that simultaneous activity of both detachments is actually required to restore the geologic cross-section in the vicinity of the southern profile [*Dunn et al.*, 1995], probably indicates that both are active.

We suggest that the complex southern velocity plateau may be a manifestation of a number of factors including the presence of active thrust ramps, the relative motions of individual fault blocks above the creeping portion of the system, and evidence for multiple active décollements. We find it interesting that the mean shortening rate estimate for the Aguarague structure from the fluvial incision study of *Mugnier et al.* [2006], which lies above our estimated slipping-to-locked transition, is identical to the southern wedge loading rate of 7 mm/yr. It may be that the stream incision-based rate is a reflection of the continuously slipping portion of the system located to the west of the Aguarague structure.

Figure 2.12 compares our new, GPS-based wedge loading rates with whole-wedge, wedge-front fault system, and fluvial incision-based shortening rate estimates. Published geologic cross-sections for the SSA indicate the long-term (Myr) shortening rate is ~7-13 mm/yr [*Baby et al.*, 1997; *Dunn et al.*, 1995; *Gubbels et al.*, 1993; *Leturmy et al.*, 2000; *McQuarrie*, 2002b; *McQuarrie et al.*, 2005; *Uba et al.*, 2006]. In general, this range of rates

closely matches our GPS-based results of 14 and 7 mm/yr for the northern and southern profiles, respectively; the Sucre and Tarija profile wedge loading rates overlap the upper and lower limits of the range in estimated geologic shortening (Figure 2.12). The suggested north-to-south reduction in the amount of total Subandean shortening moving away from the axis of the prominent bend in the Andean mountain belt (~150 km near Santa Cruz to ~70 km near the Argentinean border over the ~10 Myr duration of Subandean shortening) [*Lamb*, 2000] is also consistent with our new GPS-based results.

However, a marked north-to-south shortening rate discrepancy is apparent when we consider the wedge-front Mandeyapecua thrust fault system (MTFS) [*Weiss et al.*, 2015]. In the south, the various shortening rate estimates, which encompass geologic, neotectonic, and geodetic timescales, show a close agreement (Figure 2.12). More specifically, the MTFS shortening rate for the Tarija profile overlaps both the GPS and whole-wedge rates suggesting that the slip rate at the back of the wedge is accommodated solely by the wedge-front fault system and that this has been the case for the last ~2-3 Myr. On the other hand, evidence for active faulting associated with structures other than those at the wedge front in the vicinity of the Tarija profile, and specifically the Aguarague and Suaruro thrusts (Figure 2.11) [*Lamb*, 2000; *Mugnier et al.*, 2006] seems to be at odds with this result. The apparent discrepancy may reflect the stochastic or chaotic nature of rupture propagation seen in some recent numerical models of wedge deformation [*Mary et al.*, 2013a; *Yagupsky et al.*, 2014], which indicate that faulting can potentially occur spontaneously at any location in the wedge. Our results show that the bulk of the slip reaches the wedge-front

fault system in the south but do not rule out the possibility of some component of internal wedge deformation as well.

Alternatively, the evidence for internal wedge deformation may indicate that the southern SSA has recently transitioned to a different phase of the underthrusting-accretion (i.e. thickening-widening) wedge growth cycle [*Del Castello and Cooke*, 2007]. Analogue and numerical models have shown that wedges evolve via distinct phases of widening, when new thrusts nucleate at the front of the wedge, and thickening via internal (out-of-sequence) deformation on existing structures [*Adam et al.*, 2005; *Del Castello and Cooke*, 2007; *Hoth et al.*, 2007a; *Yagupsky et al.*, 2014].

The geodetic signal associated with this cycle has yet to be documented; but a few lines of evidence point towards a possible correspondence in the SSA. *Mugnier et al.* [2006] calculate shortening rates of 1±1, 7±3.5, and 2.5±1.5 mm/yr for the Mandeyapecua, Aguarague, and Suaruro faults, respectively (Figures 2.11 and 2.12). These rates, which are based on a geomorphic analysis of the southern Subandean-crossing Rio Pilcomayo and presumably represent an average over the Holocene period, suggest most of the recent deformation is absorbed by internal structures and not by the MTFS, which has accommodated most of the Quaternary shortening [*Weiss et al.*, 2015] (Figure 2.12). This cyclicity may be the rule rather than the exception across the southern SSA; *Uba et al.* [2009] present evidence for an older cycle of wedge widening/thickening in the vicinity of the Tarija profile when the deformation front propagated from the western Subandes to

the La Vertiente structure (V in Figure 2.11) between 12 and 6 Ma (widening), subsequently retreated to internal locations (thickening), and advanced to the modern thrust front from 4 to 2 Ma (widening). Taken in the context of these observations, our results point towards the possibility of a rejuvenated phase of underthrusting in the vicinity of the Tarija profile.

The peak of the northern MTFS shortening rate estimate probability distribution lies well beneath the 7-13 mm/yr whole-wedge and the geodetically determined ~14 mm/yr shortening rates, indicating that a slip deficit of at least ~50% may characterize the wedge front in the vicinity of the Sucre profile (Figure 2.12). This also happens to be the youngest part of the MTFS [*Weiss et al.*, 2015]. We are unaware of any neotectonic studies in the vicinity of the northern profile so we cannot directly attribute the deficit to internal wedge deformation or draw such direct comparisons over multiple timescales like we can in the south. Despite few modern and historical earthquakes, there is some distributed crustal seismicity including strike-slip events north of Sucre, a few scattered shallow thrust-related events across the northern SSA and IAZ, and a notable recent cluster of M_w 4.5-5 earthquakes and associated aftershocks across the northern MTFS (Figure 2.9). Based on the aforementioned combination of observation, including modeling results that reveal a simpler picture of strain accumulation and release in slip events that bypass internal structures and rupture faults at the wedge tip, we suggest that the wedge in the vicinity of the Sucre profile is either in or transitioning to a frontal accretion and widening phase. This suggestion is in line with a recent wedge stress state analysis, which posits that in general

megathrust décollement rupture will preferentially propagate to the wedge toe rather than break upward along pre-existing, internal structures [*Hubbard et al.*, 2015].

An alternative explanation for the Sucre profile deficit relates to the correspondence between narrower wedge width, steeper wedge taper angle, and elevated rates of precipitation-induced erosion that characterize the northern SSA [*Barnes et al.*, 2012; *Horton*, 1999; *Masek et al.*, 1994; *McQuarrie et al.*, 2008b; *Whipple*, 2009]. Numerical, analytical, and analogue models all tend to predict a decrease in mountain width and distributed internal wedge deformation in response to a climate-driven increase in erosion rates [e.g. *Cruz et al.*, 2010; *Hilley and Strecker*, 2004; *Mary et al.*, 2013b; *Whipple and Meade*, 2004]. If the observed MTFS shortening rate deficit is a persistent feature, it could point towards long-lived, albeit currently undetected, internal wedge deformation in response to external, climatic forcing. A stream incision analysis of the central range-crossing Rio Parapeti and/or the northern Rio Grande similar to the Rio Pilcomayo investigation in the south [*Mugnier et al.*, 2006] would be one way to address this possibility by quantifying recent internal wedge deformation.

2.5 Conclusions

We present a new surface velocity field for the central Andean backarc based on data from survey and continuous GPS sites across the Altiplano, Eastern Cordillera, Interandean Zone, southern Subandes, and adjacent foreland. Despite the notion that the backarc is isolated from the subduction zone earthquake cycle, we find that large

earthquakes at the Chile trench, and specifically both the 2007 *Mw* 7.7 Tocopilla and 2014 *Mw* 8.2 Pisagua events, perturb the GPS time series. The backarc velocity field, corrected for seasonal and earthquake affects, reveals that surface velocities gradually decrease away from the Chile trench and sites are essentially stable east of the thrust front. Vectors rotate and are perpendicular to the strike of the topography across the fold-and-thrust belt, lending support to the [*Lamb*, 2000] hypothesis that topography-induced stresses are a primary driver of surface deformation. Profile views of the new velocity field reveal distinct regions that reflect 1) locking of the main plate boundary across the high Andes, 2) the location of and loading rate at the back of the orogenic wedge, and 3) an east flank velocity gradient indicative of décollement locking beneath the Subandes. We document a substantial north to south decrease in both the wedge-loading rate (14 vs. 7 mm/yr) and décollement locked width (100 vs. 61 km) but neither the data or correspondence between the model and the geology is as clear in the south and we suggest this may reflect simultaneous activity of multiple detachments and/or motion of internal wedge fault blocks. A comparison of the new GPS modeling results with shortening rates estimated over a range of timescales suggests the northern and southern SSA may be in different phases of the underthrusting-accretion cycle [e.g. *Del Castello and Cooke*, 2007]; the southern wedge appears to have recently transitioned to a thickening phase via internal deformation along preexisting faults (underthrusting) whereas the northern wedge is in a widening phase characterized by faulting at the wedge toe (accretion).

Acknowledgements

This study was supported by the National Science Foundation (grants EAR-1443317 and EAR-1118481). We thank Jeanne Hardebeck of the USGS for providing relocated Bolivian thrust front earthquake information. We thank our collaborators at the Instituto Geográfico Militar de Bolivia including Roger Tinta, Angel Mollericona, Hilario Cruz, Ricardo Carita, and Marcelo Segales. We also thank Andrew Barbour and Eileen Evans of the USGS and Garrett Ito of the University of Hawaii for their careful reading and suggestions that significantly improved the manuscript.

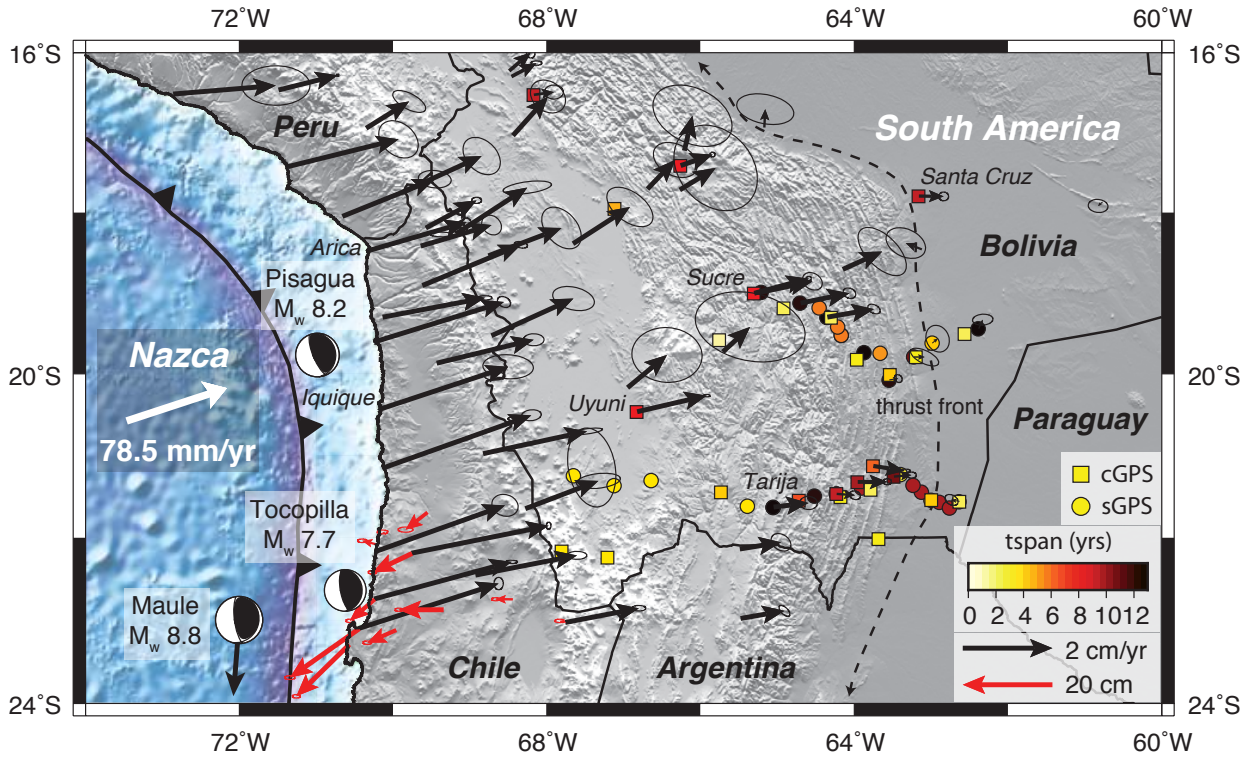

Figure 2.1 Interseismic GPS velocity field in a South America-fixed reference frame based on GPS sites that existed prior to the 2007 M_w 7.7 Tocopilla, Chile earthquake with 95% confidence ellipses overlain on Shuttle Radar Topographic Mission (SRTM) topography (grayscale) and global predicted bathymetry (bluescale). Site velocities are a combination of results from this study and *Kendrick et al.* [2001] Also shown are focal mechanisms for 3 recent subduction zone earthquakes that affected the backarc and near-field Tocopilla earthquake horizontal coseismic displacement vectors in red from [*Bejar-Pizarro et al.*, 2010]. Bolivia GPS networks sites are color-coded by the length of time the site has been in operation. Symbols without an associated velocity vector represent sites that did not exist prior to the Tocopilla earthquake. The offshore location of the Chile trench is shown with a heavy black barbed line. The heavy white vector indicates the direction and magnitude of Nazca-South America plate convergence according to NUVEL-1A. The black dashed line indicates the approximate position of the deformation front at the eastern edge of the Andes. cGPS=continuous GPS site; sGPS=roving/campaign GPS site.

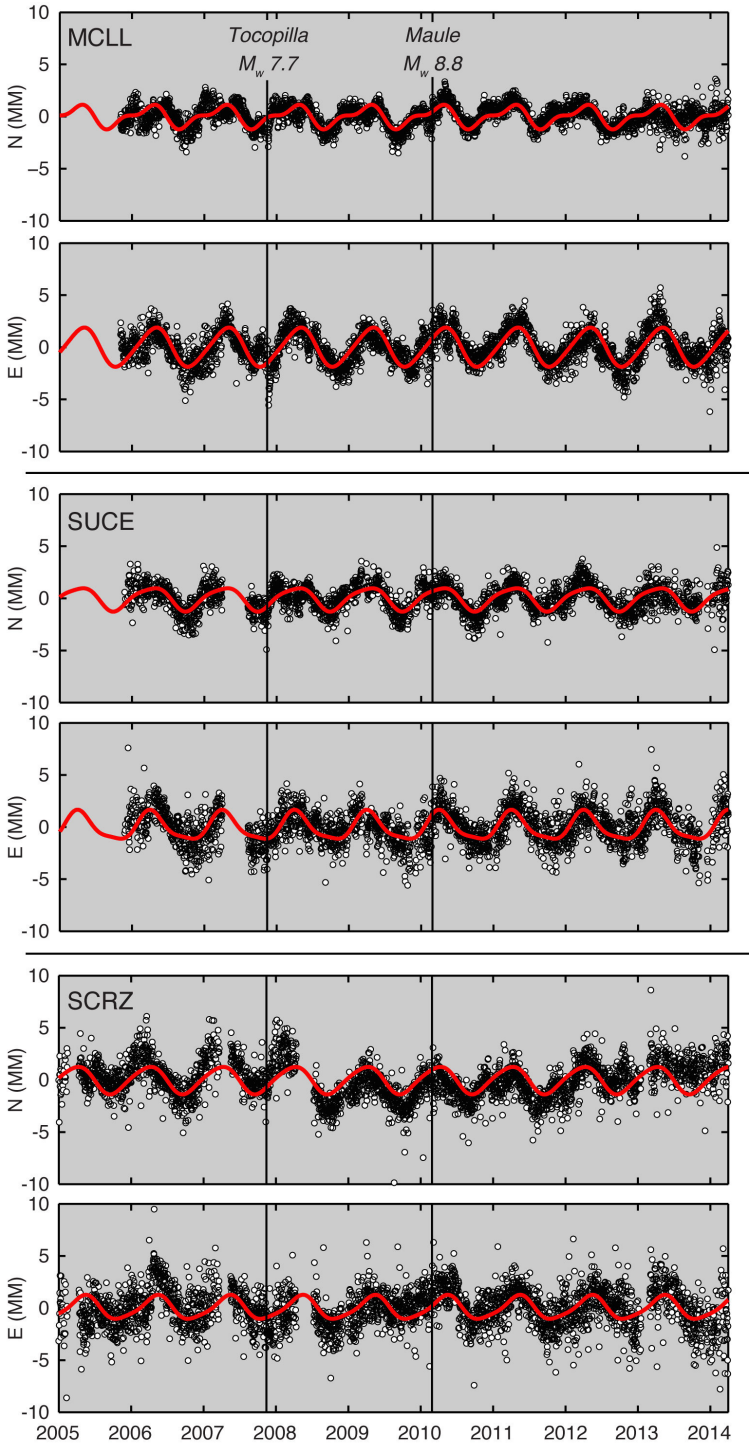

Figure 2.2 Examples of the seasonal perturbations for the North and East components of the GPS time series for central Andean sites located on the forearc (MCLL), backarc (SUCE), and near the front of the Subandean wedge (SCRZ). The interseismic, coseismic, and postseismic signals have been removed leaving just the seasonal component. Daily positions are shown as white circles and the best-fit sinusoidal function to the seasonal is shown in red. The Up components of the time series are shown in Figure C1.

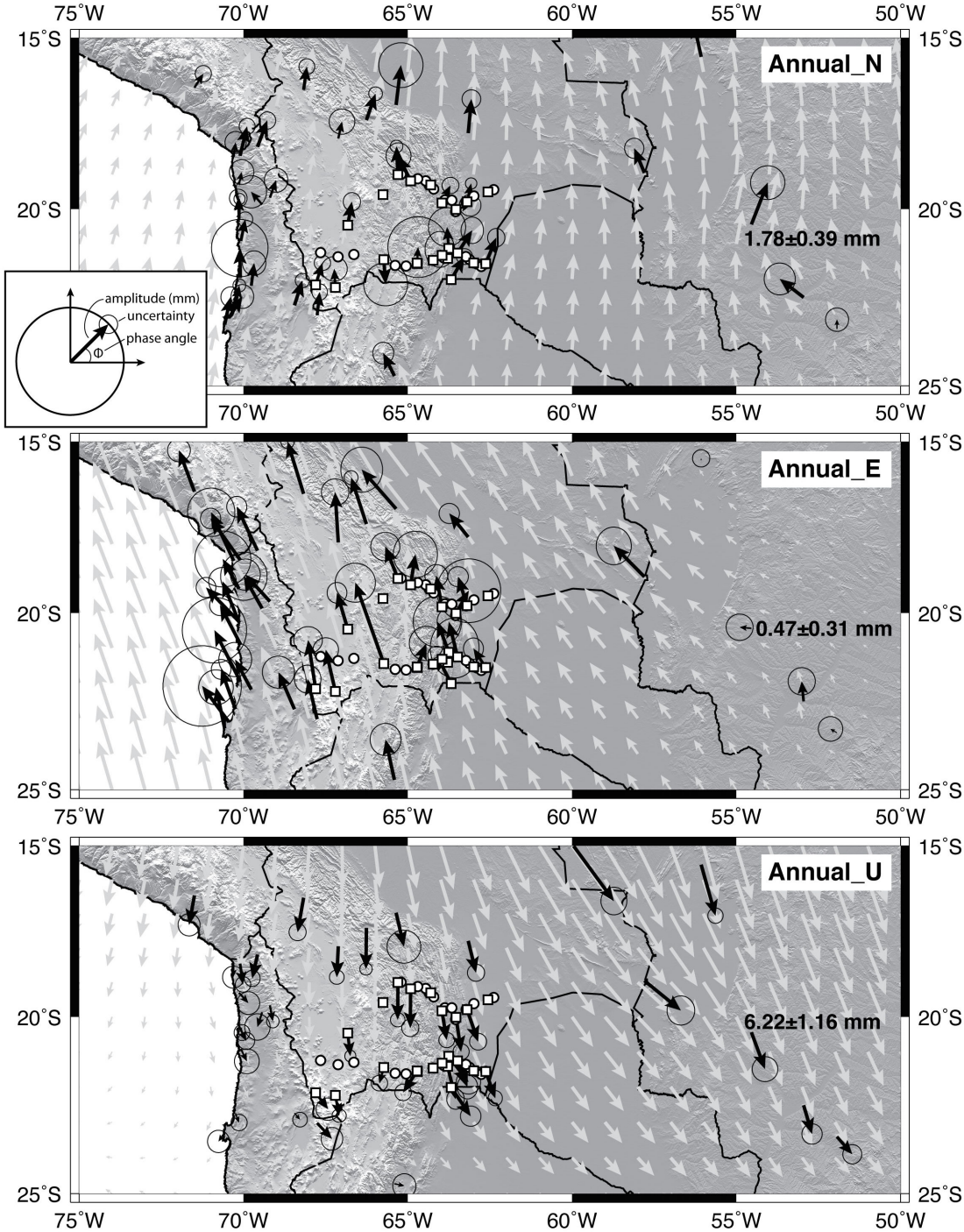

Figure 2.3 North, East, and Up annual seasonal cycles for the central Andes. Black vectors and 2σ error ellipses are estimated directly from the cGPS time series. Gray vectors are the interpolated values. Also shown are the locations of the Bolivian cGPS and sGPS sites as white squares and circles, respectively.

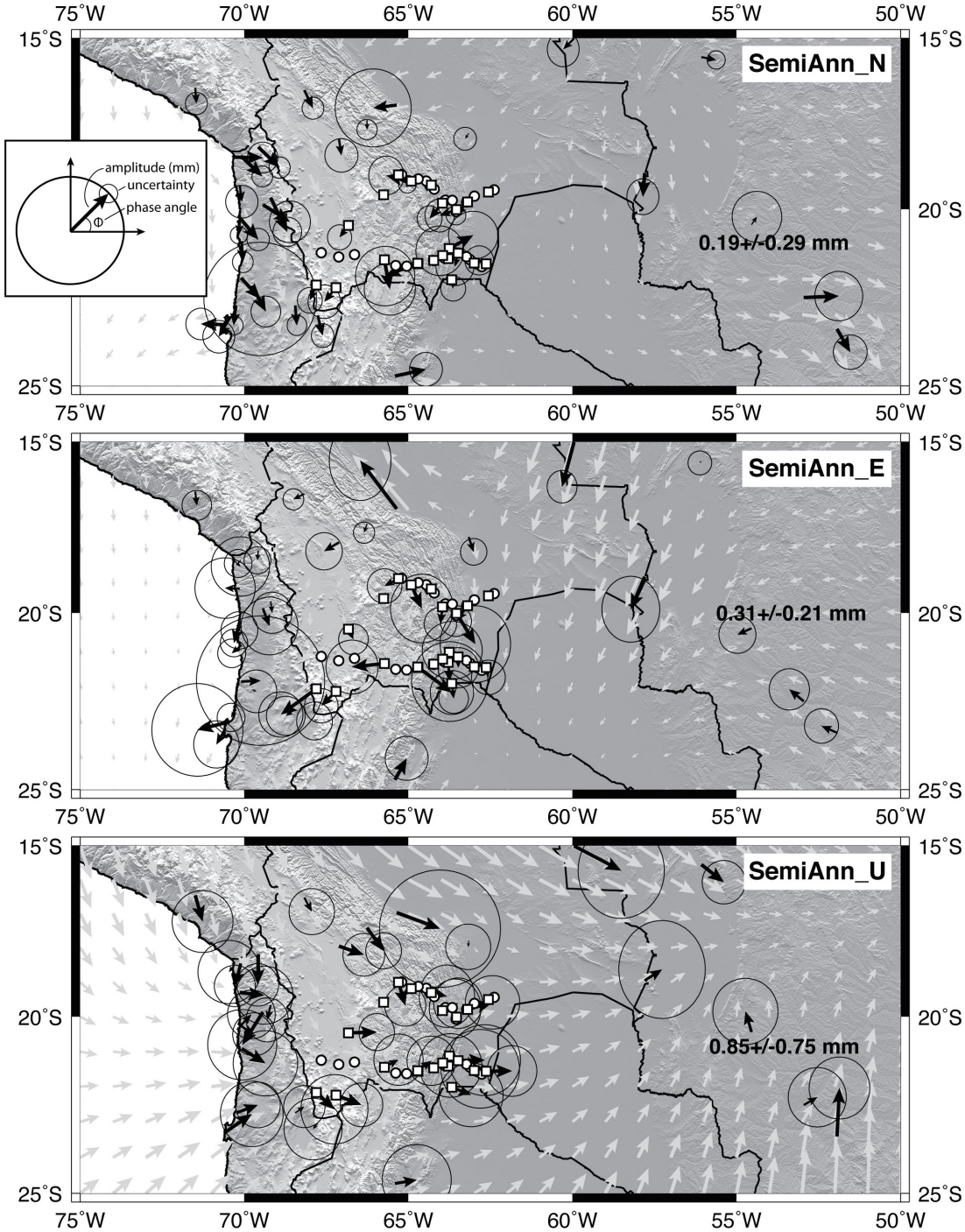

Figure 2.4 North, East, and Up semiannual seasonal cycles for the central Andes. All symbols are the same as in Figure 2.3.

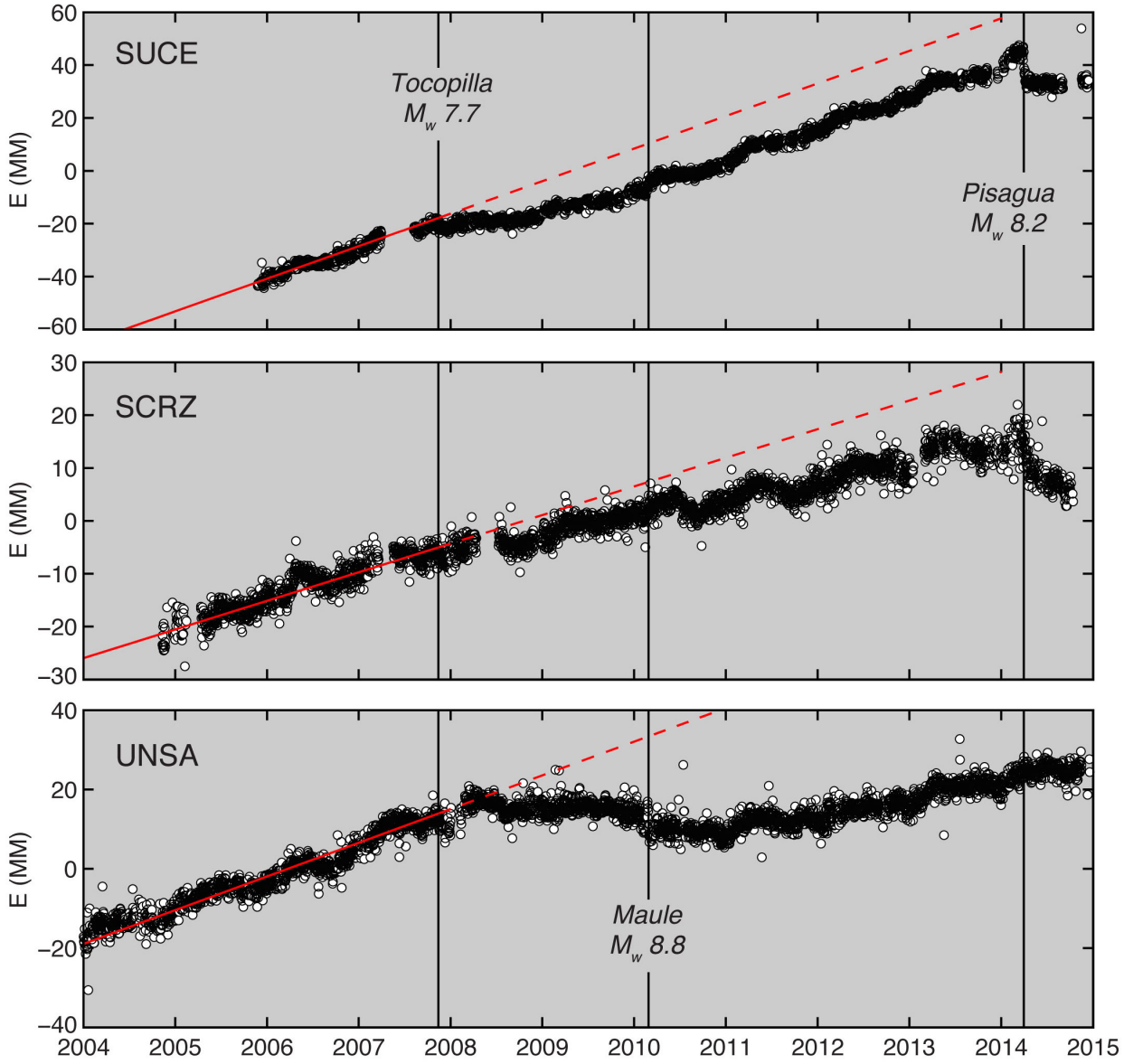

Figure 2.5 Eastward displacements for affected cGPS sites with the earthquake times indicated by vertical black bars. Note that the Tocopilla earthquake perturbed the time series for sites as far away as Santa Cruz, implying that the entire backarc was affected. The Maule earthquake only affected the IGS site UNSA in NW Argentina whereas the Pisagua event affected the Bolivian sites SUCE and SCRZ. The red lines indicate a best-fit velocity for the pre-Tocopilla portions of the time series and an extrapolation of this velocity beyond the time of the earthquake (red dashed) to demonstrate how the time series deviate from the pre-quake velocity.

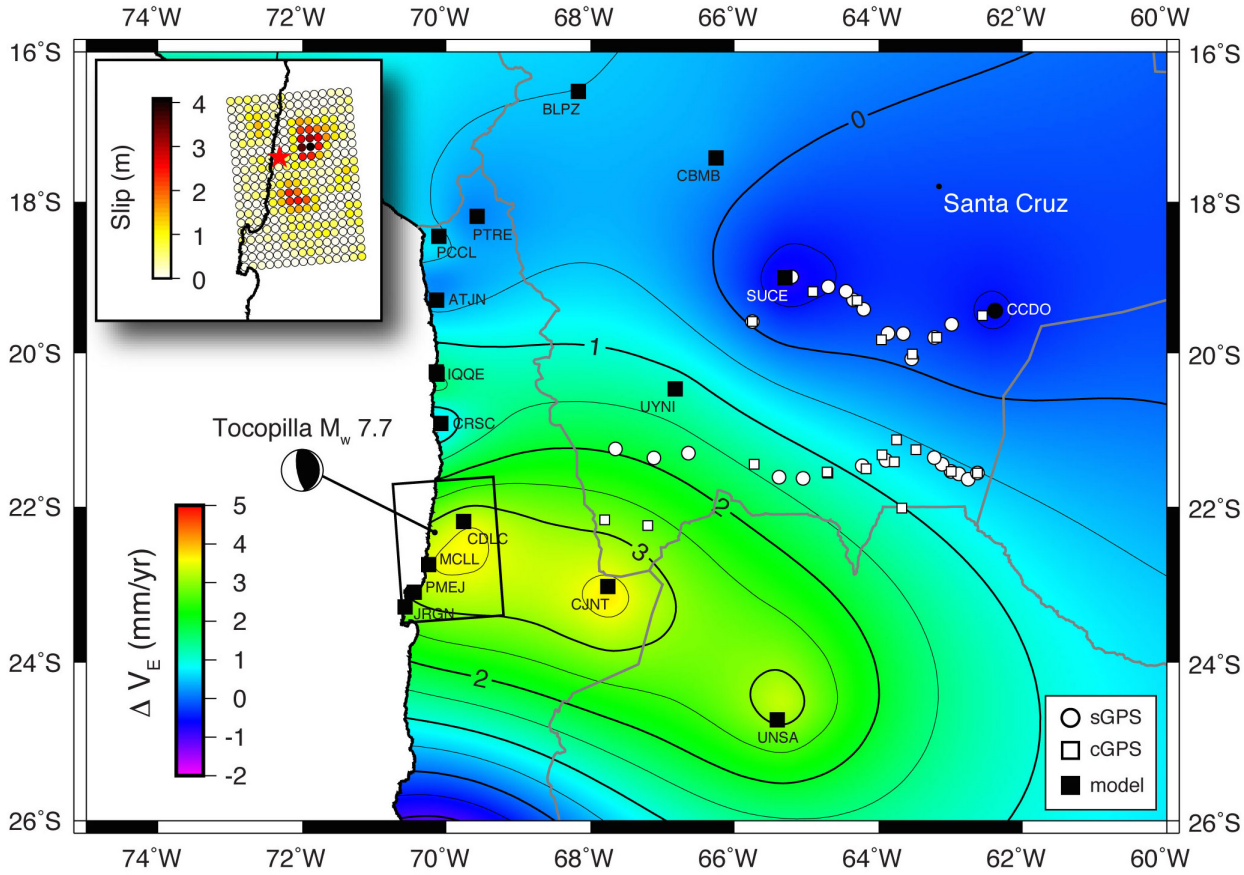

Figure 2.6 Simplified model of the region affect of the Tocopilla earthquake created by subtracting the best-fit post-quake velocity from the best-fit pre-quake velocity for sites that existed prior to the event (black symbols) and interpolating the change in velocity (ΔV_E) across the region. Positive ΔV_E indicate a faster pre-quake velocity. The earthquake-induced perturbation extends across the backarc and affects the GPS network (white symbols). The small black rectangle indicates the position of the USGS slip distribution, which is shown in the inset.

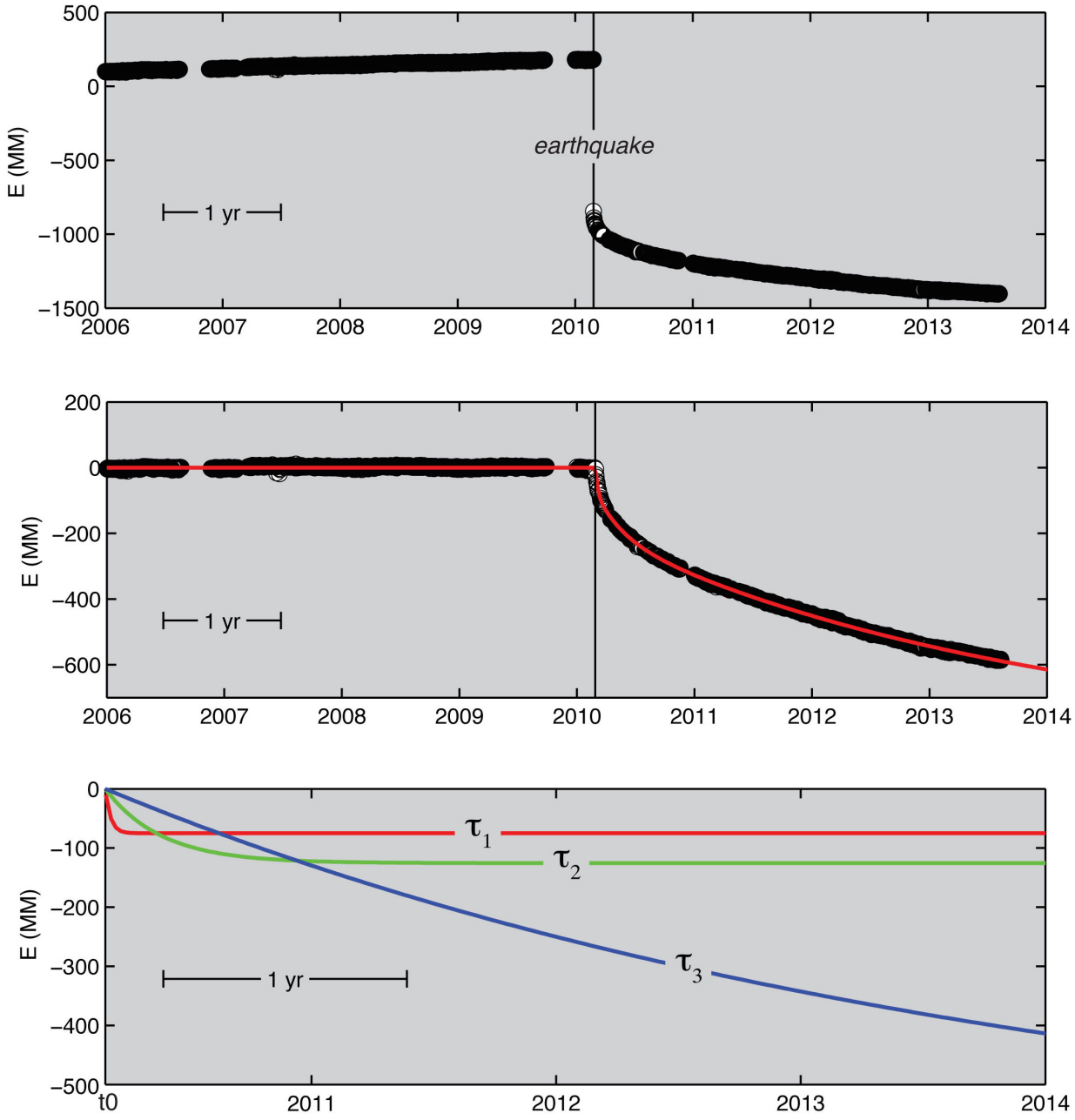

Figure 2.7 (Top) The eastward displacement component of a typical subduction zone earthquake-affected cGPS time series from a site located close to the trench. The site is moving to the east at its interseismic velocity prior to the earthquake, which is marked by a westward coseismic offset and a postseismic decay. (Middle) The same time series with the best fit interseismic velocity and coseismic step removed to illustrate the postseismic signal. (Bottom) The three exponential decay terms that best-fit the postseismic portion of the time series. In this and similar cases the postseismic portion of the time series can be described by the linear superposition of 3 exponential terms with time constants on the order of one to a few days (τ_1), 10's to 100's of days (τ_2), and 5-20 years (τ_3). The central Andean backarc sites are typically well-described by a single exponential term with a time constant on the order of 5-10 years.

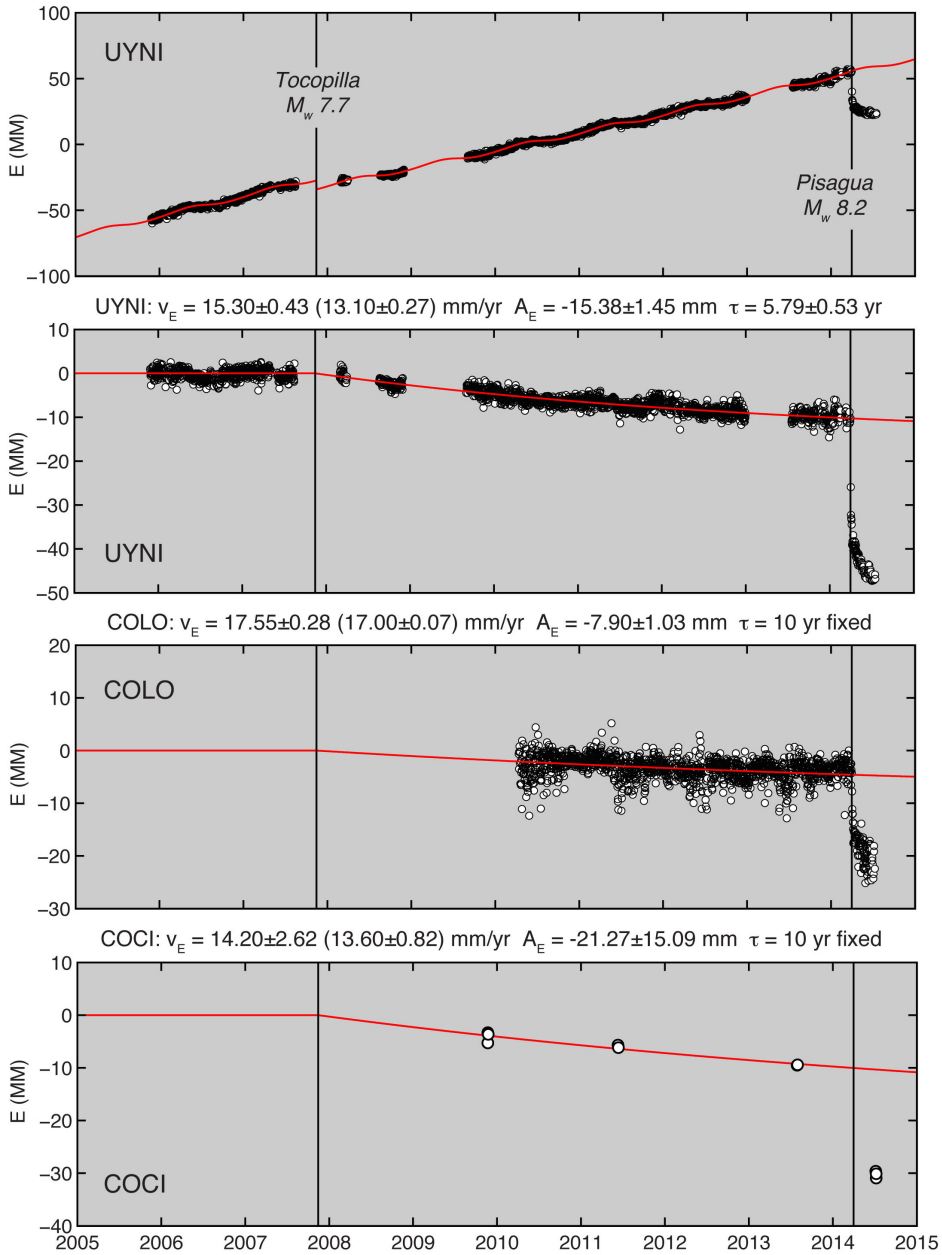

Figure 2.8 Examples of the eastward displacement of time series for select central Andean backarc sites and the best-fit empirical models for the Tocopilla postseismic characterization. The top panel shows daily positions for the Altiplano/Eastern Cordillera site in Uyuni, Bolivia (UYNI) and the model in red, which consists of interseismic, coseismic, postseismic, and seasonal terms. The second panel shows the UYNI time series with the interseismic, coseismic, and seasonal portions removed. Remaining is the postseismic signal, which is best fit by a single exponential term with an amplitude of -15.38 mm and a decay time of 5.80 years. The correction results in an ~2 mm/yr increase in the eastward velocity. The bottom two panels show examples of the postseismic signal for a cGPS site (COLO) established in early 2010 and an sGPS site (COCI) first occupied in late 2009. For both cases the time constant is fixed at 10 years. For all cases we report the best-fit amplitudes and velocities with the corrected errors. The uncorrected values and associated standard errors are in parentheses. The affect of the 2014 Pisagua earthquake can also be seen at each of the stations.

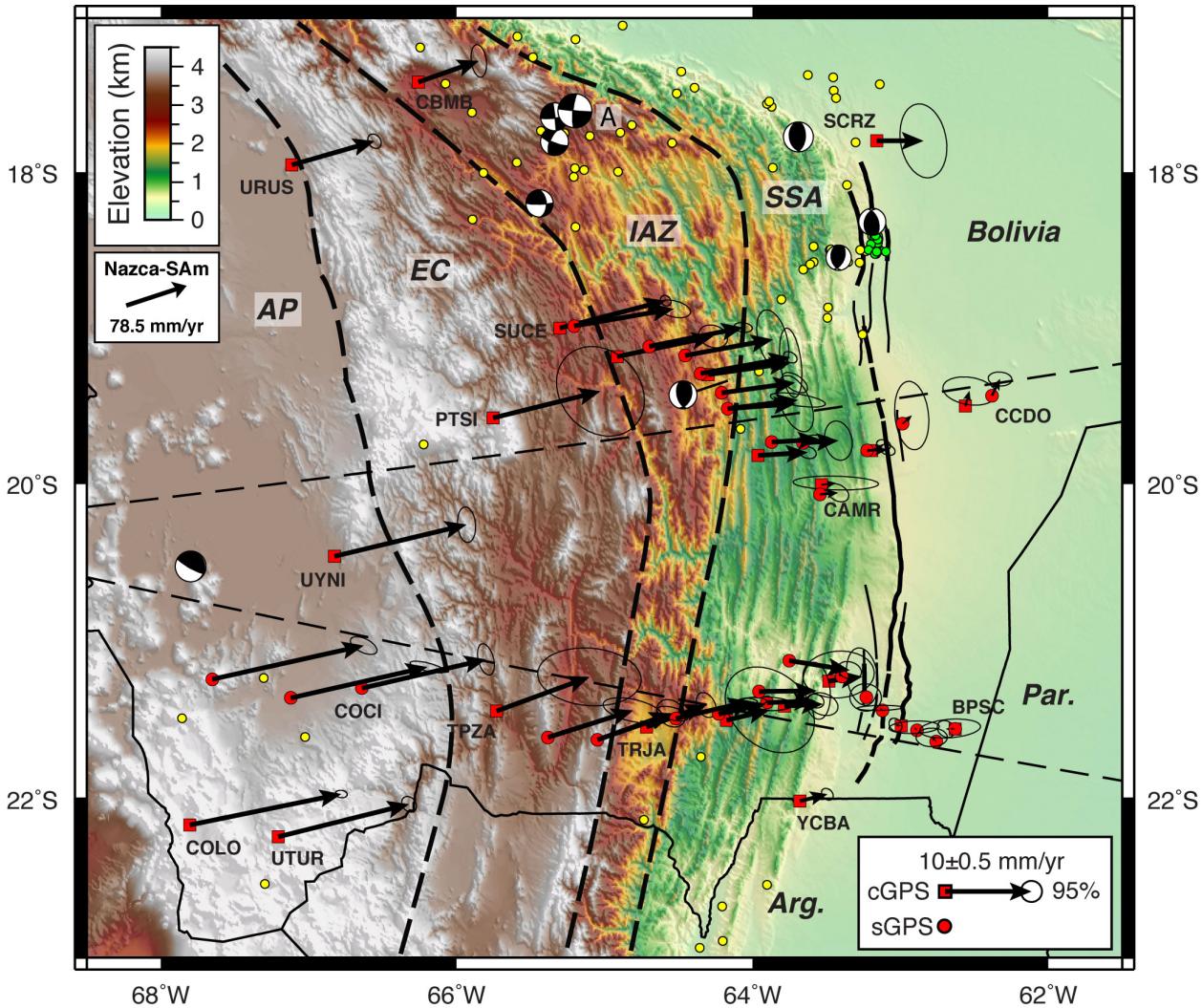

Figure 2.9 The new central Andean backarc velocity field with 95% confidence ellipses based on the corrected errors overlain on SRTM topography. The wedge-front Mandeyapecua thrust fault system (MTFS) from *Weiss et al.* [2015] is shown as thick and thin black lines for surface and buried faults, respectively, all of which dip to the west. Thin dashed black lines indicated the location of the two wedge-crossing profiles from Figures 2.10 and 2.11 and thick black dashed lines indicate the approximate boundaries of the major physiographic provinces. Select GPS sites are labeled with their corresponding 4 letter code. Green hues in the topography color palette emphasize the elongate, linear structures forming the Subandean fold-and-thrust belt. Focal mechanisms are for crustal events (<50 km) from the Global Centroid Moment Tensor database with magnitudes that range from M_w 5.2-6.6. Yellow circles are epicenters for crustal events from the National Earthquake Information Center. Green circles are a swarm of relocated shallow events (<40 km) including two M_w 4.5-5 earthquakes and associated aftershocks that occurred in October 2013 near the northern MTFS. Also shown for reference is the direction and magnitude of Nazca-South America plate convergence according to NUVEL-1A. AP=Altiplano; EC=Eastern Cordillera; IAZ=Interandean Zone; SSA=southern Subandes; A=The 1998 Aiquile, Bolivia (M_w 6.6) earthquake; cGPS=continuous GPS site; sGPS=roving/campaign GPS site; SCRZ=Santa Cruz; SUCE=Sucre; PTSI=Potosi; CAMR=Camiri; CCDO=Cerro Colorado; COCI=Cocani; COLO=Laguna Colorada; UTUR=Uturuncu; TPZA=Tupiza; TRJA=Tarija; YCBA=Yacuiba; BPSC=Puesto Sucre; URUS=Oruro; CBMB=Cochabamba; Arg.=Argentina; Par.=Paraguay.

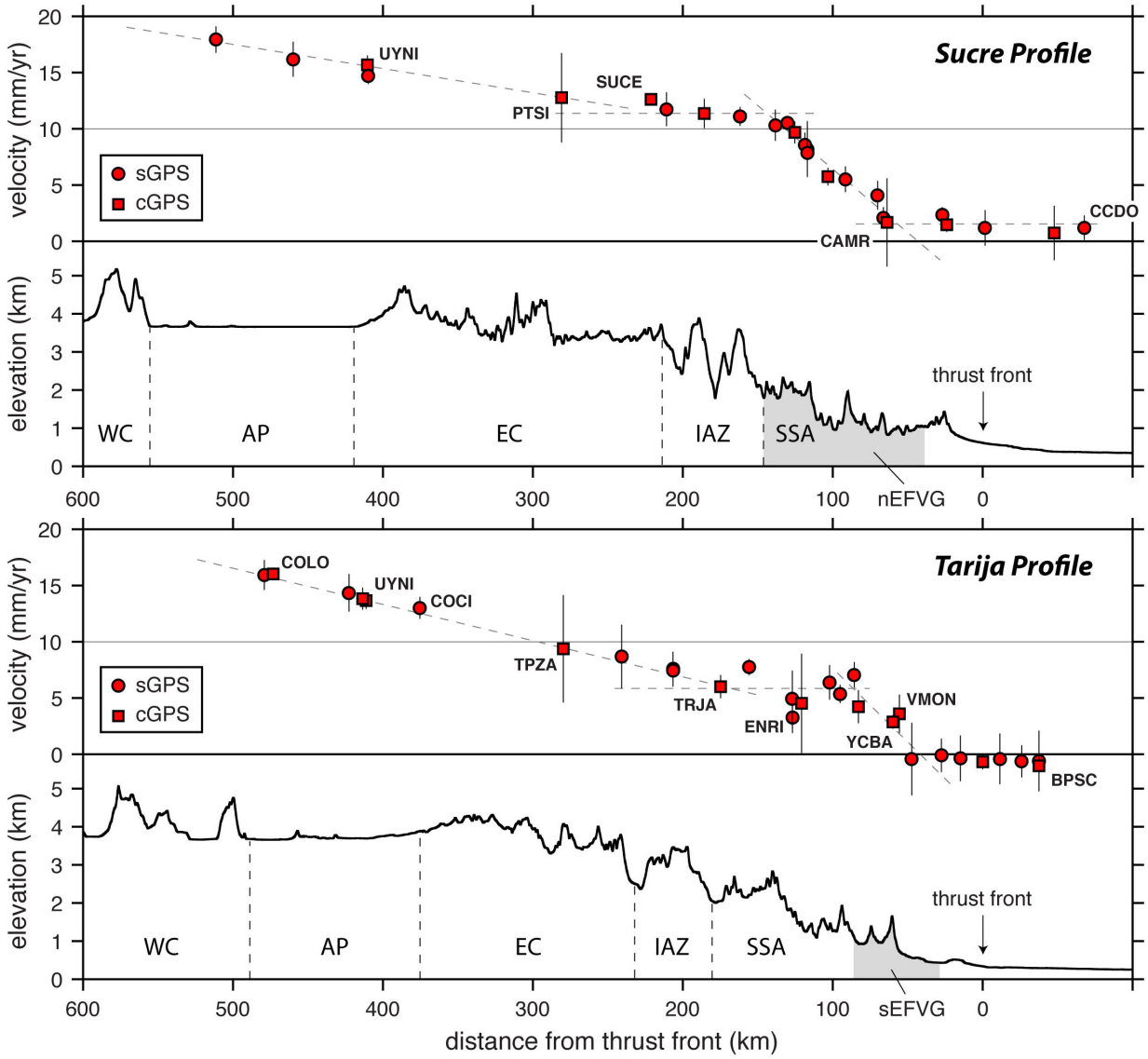

Figure 2.10 Profile views of the new surface velocity field projected perpendicular to the strike of the Subandean structures with corrected two-sigma error bars (top panels) and the corresponding topography (bottom panels). See Figure 2.9 for profile locations. Light dashed lines are hand-drawn fits to the data intended to emphasize the features referred to in the text. The approximate locations of the physiographic boundaries are indicated with vertical dashed lines beneath the topography. The gray shaded region under the topography corresponds to the east flank velocity gradients. Labeled GPS sites are the same as in Figure 2.9. WC=Western Cordillera; AP=Altiplano; EC=Eastern Cordillera; IAZ=Interandean Zone; SSA=southern Subandes; n/sEFVG=northern/southern east flank velocity gradient; VMON=Villamontes; ENRI=Entre Rios.

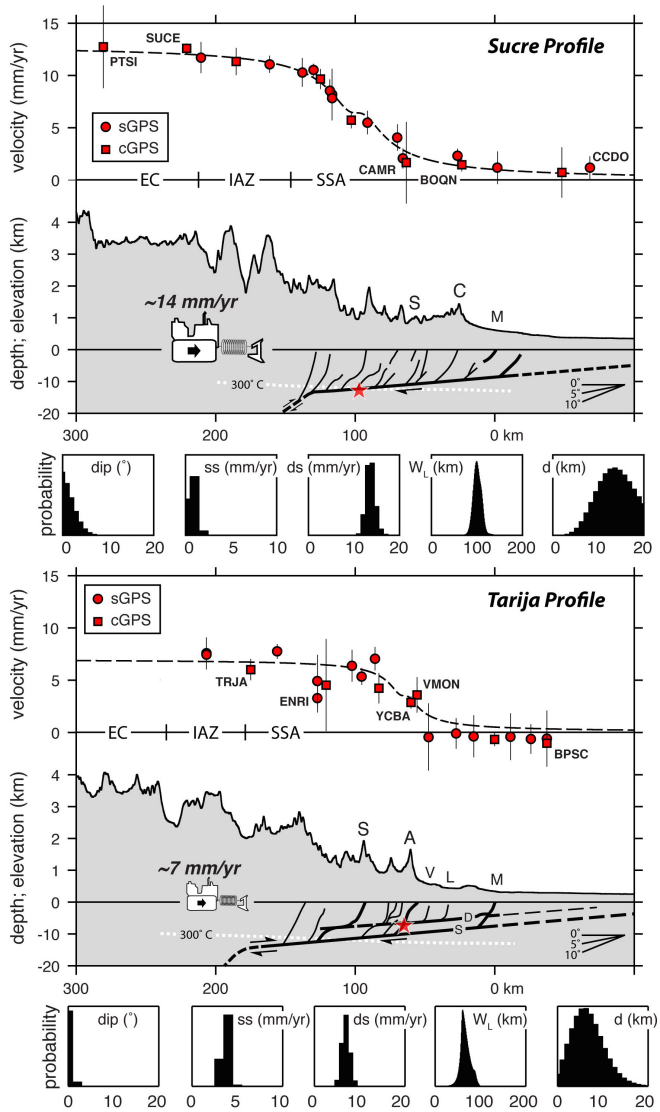

Figure 2.11 Subandean orogenic wedge elastic dislocation modeling results. Top panels show projected velocities and corrected two-sigma error bars for the active wedge portion of the velocity field only. The black dashed line is the best model from the grid search inversion. Select GPS sites are labeled with their 4 letter station codes. The bottom panels show topography extracted from the profiles with faults from published cross sections. Profile locations are shown in Figure 2.9. The northern, Sucre profile and southern, Tarija profile geologic cross sections are profiles D and B from *Giraudo and Limachi* [2001]. The approximate boundaries between the major physiographic provinces are labeled. The star in the subsurface indicates the slipping-to-locked transition from the best model and the white dashed line is the 300°C isotherm calculated from the central Andean backarc geothermal gradient [*Currie and Hyndman*, 2006]. Also shown are the probability distributions for each of the model parameters with the peaks correspond to the aforementioned best model values. Spring-loaded bulldozers are labeled with the wedge-loading rate from the peak of the dip-slip probability distributions. ENRI=Entre Rios; BOQN= Los Boquerones (Charagua); S=Suaruro structure; C=Charagua structure; A=Aguarague structure; V=Villamontes structure; L=La Vertiente structure; M=Mandeyapecua fault; D=detachment surface in Devonian Los Monos shale; S=main detachment in the Silurian Kirusillas Formation; ss=strike-slip; ds=dip-slip; W_L=locked width; d=depth.

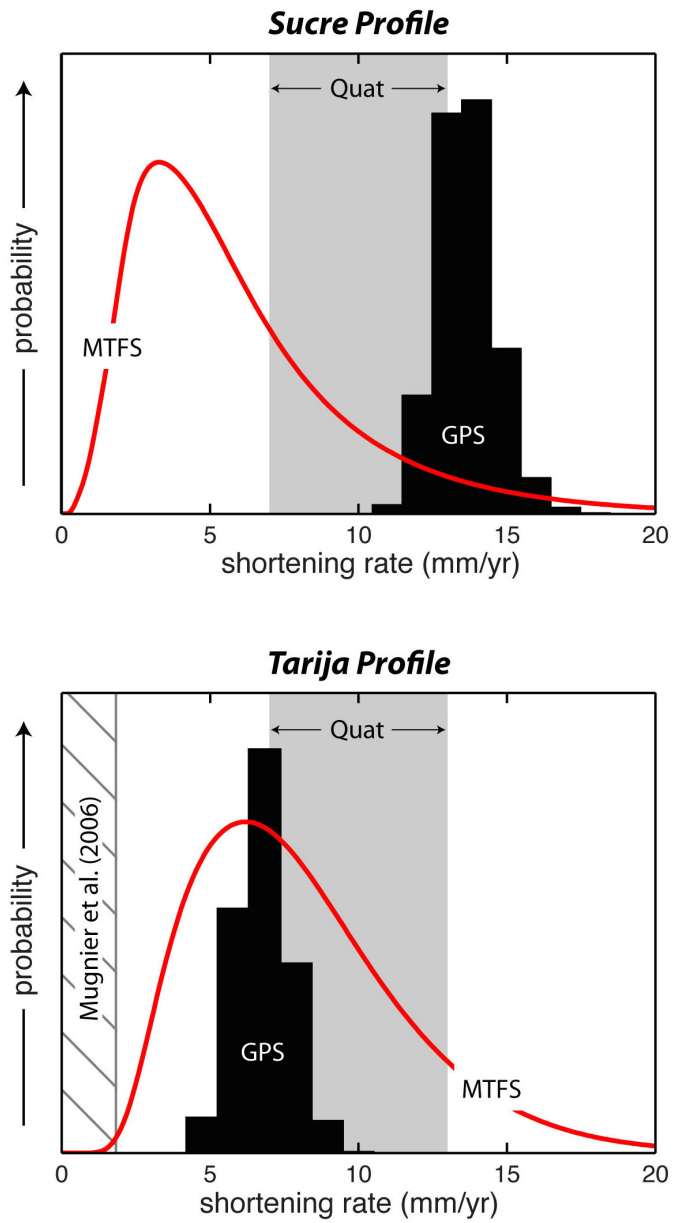

Figure 2.12 A comparison of shortening rate estimates over multiple timescales for the Sucre and Tarija profiles. The gray bars indicate the range in whole-wedge Quaternary shortening rates of 7-13 mm/yr estimated from geologic cross-sections. The black histograms are the dislocation-based modeling results of the new backarc surface velocity field (Figure 2.11). The red curves are composite Quaternary shortening rates for the wedge-front Mandeyapecua thrust fault system based on the dip-slip rate probability distributions from [*Weiss et al.*, 2015]. We compute shortening rates by convolving the dip-slip rate distributions for individual wedge front faults with the corresponding dislocation dip angle distributions. We then sum the shortening rate distributions for individual faults along the profiles shown in Figure 1.8 and then sum the shortening rate estimates along strike for the northern (profiles 1-5) and southern (profiles 7-8) wedge to create the Sucre and Tarija composite shortening rate distributions, respectively. The minimum Mandeyapecua Fault slip rate distributions (see Figures 1.7 and 1.8) are used for both profiles. The hatched region in the Tarija profile comparison indicates the 1±1 mm/yr Holocene shortening rate for the Mandeyapecua (Iguitini) fault from the stream incision analysis of [*Mugnier et al.*, 2006].

Table 2.1 Corrected GPS site velocities[a]

Stnm	sc	Lon	Lat	Vn	Ve	Vu	sigNs	sigEs	sigUs	sigNc	sigEc	sigUc	neCor	tspan
0B54	s	-64.1673	-19.5233	1.02	8.12	0.10	0.17	0.77	1.15	0.34	1.30	1.06	-0.56	5.88
0B85	s	-64.4549	-19.1819	1.86	10.14	-0.27	0.71	0.65	2.23	1.40	0.76	2.41	-0.38	5.88
0B87	s	-64.2072	-19.4211	1.18	8.46	-0.09	0.26	0.41	1.14	0.48	0.60	1.09	-0.55	5.88
0B89	s	-63.6577	-19.7424	0.27	4.08	1.44	0.69	0.33	0.91	0.93	0.66	0.92	-0.16	5.20
ASLO	s	-64.1673	-19.5232	0.59	7.85	-0.11	0.28	0.17	0.43	1.33	0.85	0.50	-0.48	12.82
BLPZ	c	-68.1683	-16.5299	0.52	4.26	2.70	0.01	0.01	0.03	0.15	0.20	0.56	-0.21	9.17
BOQN	c	-63.1947	-19.7907	0.65	1.38	2.13	0.03	0.04	0.15	0.25	0.33	0.77	-0.22	3.36
BPDL	c	-64.2999	-19.3044	1.37	9.57	0.19	0.11	0.08	0.27	1.64	0.53	1.54	-0.35	2.24
BPLB	c	-63.7838	-21.4167	0.22	4.44	3.14	0.06	0.08	0.24	0.54	0.72	1.08	-0.25	2.32
BPSC	c	-62.6297	-21.5620	0.00	-1.06	2.17	0.05	0.07	0.19	0.40	0.42	0.83	-0.21	2.32
BRCH	c	-62.5611	-19.5053	1.73	0.48	1.70	0.07	0.10	0.33	0.67	1.26	0.97	-0.22	2.32
BTRC	c	-64.9149	-19.1886	2.34	11.13	0.97	0.05	0.09	0.22	0.54	0.68	0.94	-0.20	2.31
CAGA	s	-63.2242	-19.7902	0.07	2.34	0.30	0.15	0.17	0.56	0.26	0.36	0.93	-0.30	10.85
CAMR	c	-63.5334	-20.0102	0.21	1.65	2.42	0.03	0.09	0.12	0.33	2.02	0.60	-0.14	4.33
CBMB	c	-66.2588	-17.4166	2.46	7.00	1.10	0.02	0.02	0.03	0.77	0.37	3.43	-0.23	8.39
CCDO	s	-62.3808	-19.4391	1.93	0.93	1.13	0.12	0.17	0.36	0.33	0.56	0.38	-0.09	12.81
CCYA	s	-65.0479	-21.6304	3.03	8.68	4.66	0.19	0.43	0.79	0.35	0.74	0.76	-0.49	9.99
CHYY	s	-63.8694	-19.7364	0.32	5.52	-15.97	0.11	0.22	5.82	0.20	0.59	11.14	-0.34	12.83
CMRI	s	-63.5425	-20.0712	0.19	2.06	-6.71	0.07	0.10	1.17	0.43	0.51	5.59	-0.33	12.14
COCI	s	-66.6405	-21.3035	3.33	14.37	2.09	0.63	0.13	1.91	0.74	0.40	1.76	-0.37	3.69
COLO[p]	c	-67.8040	-22.1674	3.58	17.55	3.05	0.02	0.04	0.10	0.18	0.28	0.72	-0.11	3.96
CULK	s	-67.1211	-21.3657	3.58	15.82	1.82	0.23	0.63	1.26	0.28	0.82	1.18	-0.69	3.71
DRDO	s	-64.3498	-19.2968	1.87	10.37	-0.47	0.09	0.11	6.70	0.27	0.32	14.83	-0.34	12.81
ENRI*	s	-64.2280	-21.4678	1.45	3.78	0.06	0.16	0.30	0.24	0.19	0.73	0.13	0.13	2.84
GLPE	c	-64.1754	-21.5065	1.20	5.01	1.28	0.22	0.35	1.40	2.03	2.11	2.97	-0.29	3.36
IBOB	c	-62.9945	-21.5427	0.11	-0.66	2.76	0.03	0.04	0.12	0.32	0.31	0.54	-0.24	4.38
LPTS[g]	c	-65.7538	-19.5820	3.08	12.44	0.84	0.26	0.33	0.83	2.12	2.08	2.81	-0.20	1.36
M007	s	-63.9008	-21.3953	0.19	5.60	2.20	0.17	0.18	0.75	0.33	0.40	0.84	-0.16	9.88
M009	s	-62.8877	-21.5702	0.35	-0.33	2.68	0.19	0.20	0.30	0.30	1.19	0.21	0.13	9.90
M010	s	-62.7584	-21.6409	0.47	-0.52	2.55	0.24	0.14	0.37	0.44	0.74	0.49	0.01	9.90
M011	s	-63.1210	-21.4456	0.31	-0.29	3.12	0.06	0.39	0.43	0.12	1.07	0.42	0.18	9.89
M012	s	-63.2295	-21.3620	-0.01	-0.10	2.96	0.46	0.20	0.61	0.65	0.75	0.58	-0.03	9.89
MARG	c/s	-63.7520	-21.1291	-1.13	7.00	-1.02	0.10	0.12	0.15	0.42	0.56	0.52	-0.21	6.23
MGDO	c	-63.9623	-19.8223	0.35	5.74	1.08	0.03	0.05	0.14	0.29	0.41	0.70	-0.23	3.36
NTRS	s	-64.2283	-21.4676	1.19	5.43	2.08	0.28	0.81	0.32	0.33	1.30	0.34	-0.13	9.22
PBLA	s	-65.3820	-21.6149	3.12	9.83	4.26	0.56	1.07	1.84	0.60	1.41	1.73	-0.46	3.67
PBOL	s	-62.6294	-21.5619	0.05	-0.60	2.48	0.27	1.10	0.35	0.45	1.44	0.34	0.22	9.90
PLLO	s	-64.5179	-21.4956	2.00	8.56	4.51	0.38	0.29	0.47	0.14	0.36	0.95	-0.30	12.06
SALA	s	-62.9849	-19.6186	0.94	1.05	-2.13	0.50	0.38	2.27	1.62	0.81	2.35	-0.16	4.23
SANA	s	-67.6520	-21.2470	3.90	17.54	1.56	0.15	0.37	1.83	0.42	0.63	1.57	-0.54	3.73
SCRZ	c	-63.1597	-17.7968	-0.01	5.40	-1.68	0.02	0.03	0.04	1.75	1.11	4.81	-0.18	9.38
SUCE	c	-65.3026	-19.0062	3.19	12.27	-0.08	0.02	0.03	0.04	0.25	0.25	0.93	-0.23	8.35
SUCR*	s	-65.2060	-18.9921	1.99	11.56	0.98	0.25	0.56	1.34	0.42	0.79	1.55	-0.36	12.07
TARI	s	-65.0479	-21.6307	3.08	8.52	4.02	0.15	0.29	1.01	0.65	0.68	1.10	-0.24	12.82
TPYO	c/s	-63.9545	-21.3247	0.08	6.63	2.38	0.28	0.15	0.24	1.35	0.66	0.60	-0.17	9.97
TPZA	c	-65.7299	-21.4482	3.95	10.76	2.97	0.06	0.06	0.11	1.37	2.45	5.78	-0.10	4.05
TRJA	c	-64.7165	-21.5495	2.54	6.90	3.46	0.02	0.03	0.08	0.59	0.47	0.69	-0.31	6.87
URUS	c	-67.1144	-17.9528	2.74	9.58	2.13	0.03	0.03	0.07	0.34	0.32	0.74	-0.25	4.57
UTUR[p]	c	-67.2055	-22.2420	3.77	15.15	2.85	0.02	0.03	0.08	0.37	0.35	0.58	-0.24	3.96
UYNI	c	-66.8260	-20.4659	3.66	15.30	-0.60	0.02	0.02	0.02	0.84	0.43	2.11	-0.13	8.34
VMON	c	-63.4836	-21.2589	0.52	3.86	0.65	0.03	0.03	0.04	1.36	0.75	2.81	-0.20	10.65
VMT3*	s	-63.3957	-21.2286	0.21	-0.39	-2.32	0.80	1.17	2.18	1.11	1.69	1.92	0.06	2.91
YCBA	c	-63.6800	-22.0171	0.79	3.19	2.65	0.03	0.04	0.14	0.28	0.28	0.80	-0.28	3.37
ZDNZ	s	-64.6980	-19.1234	2.20	10.88	0.11	0.06	0.14	0.21	0.23	0.43	0.43	-0.18	12.09

[a]GPS site velocities expressed relative to the stable South American plate. Stnm, station code; s, survey (sGPS) site; c, continuous (cGPS) site; c/s, former cGPS site current sGPS site; Lon, longitude; Lat, Latitude; Vn, north component of velocity (mm/yr); Ve, east component of velocity (mm/yr); Vu, up component of velocity (mm/yr); sigNs, standard north error (mm/yr); sigEs, standard east error (mm/yr); sigUs, standard up error (mm/yr); sigNc, corrected north error (mm/yr); sigEc, corrected east error (mm/yr); sigUc, corrected up error (mm/yr); neCor, north-east correlation; tspan, time span of measurement in years. [p]PLUTONS site. [g]GLISN site. *site with no post-Tocopilla observations.

Appendix C

This data set includes a map showing the horizontal reference frame site velocities in Figure C1, examples of the seasonal signal for the Up components of select GPS site time series in Figure C2, the interseismic velocity field used in the Tocopilla earthquake empirical characterization in Figure C3, the best-fit amplitudes for the eastern component of the exponential terms used in the Tocopilla earthquake characterization and comparisons with seismological results in Figure C4, a comparison of the corrected and uncorrected backarc velocities in profile view in Figure C5, statistics for the horizontal reference frame sites in Table C1, the best-fit parameters from the Tocopilla earthquake characterization in Table C2, the white and power law noise statistics for the corrected cGPS and sGPS time series in Table C3, and the uncorrected site velocities and associated standard errors in Table C4.

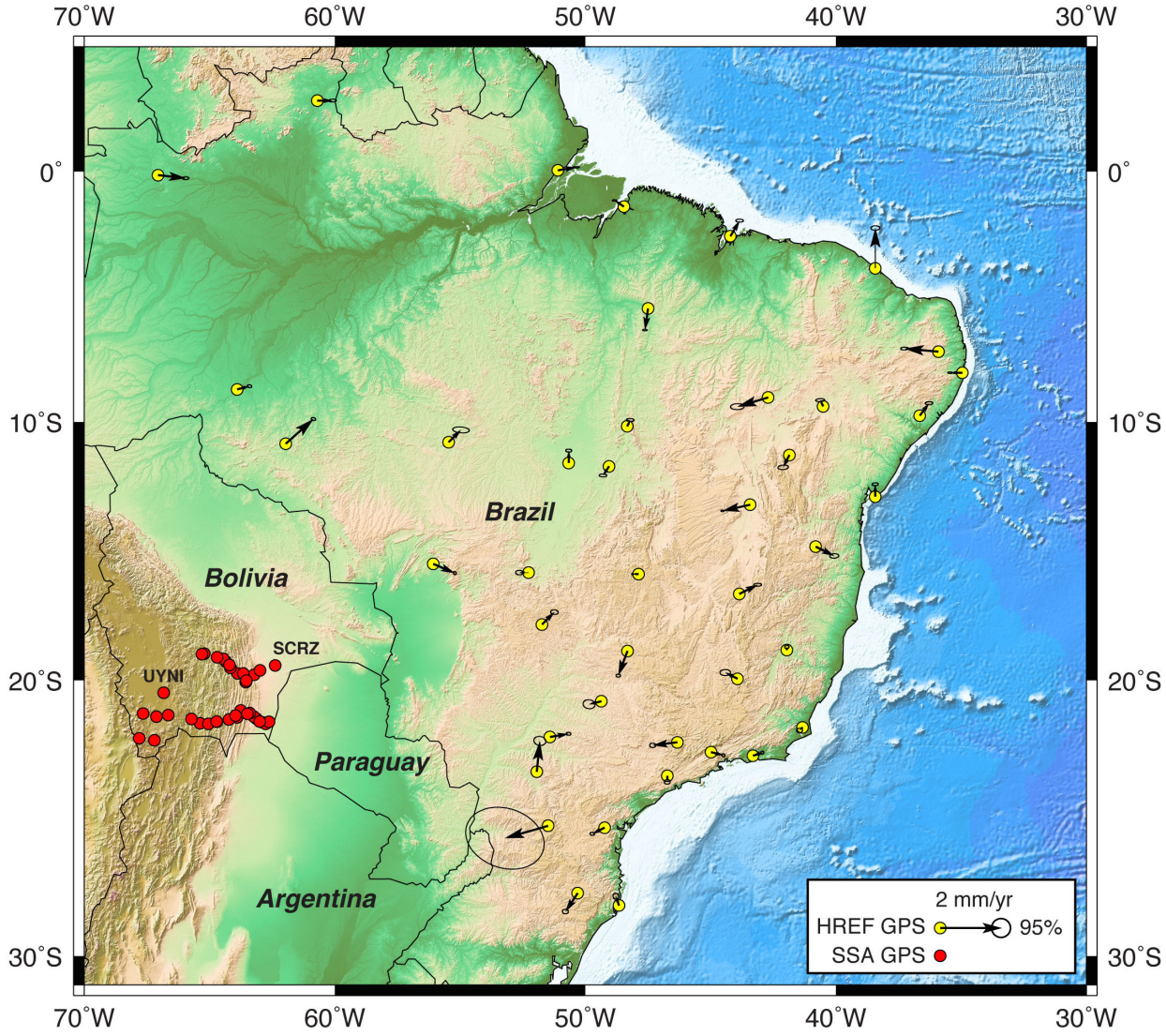

Figure C1 Map showing the locations and velocities of the majority of sites used to define the South American craton-fixed reference frame (yellow circles). The locations of our southern Subandean sites in Bolivia are also shown for reference (red circles).

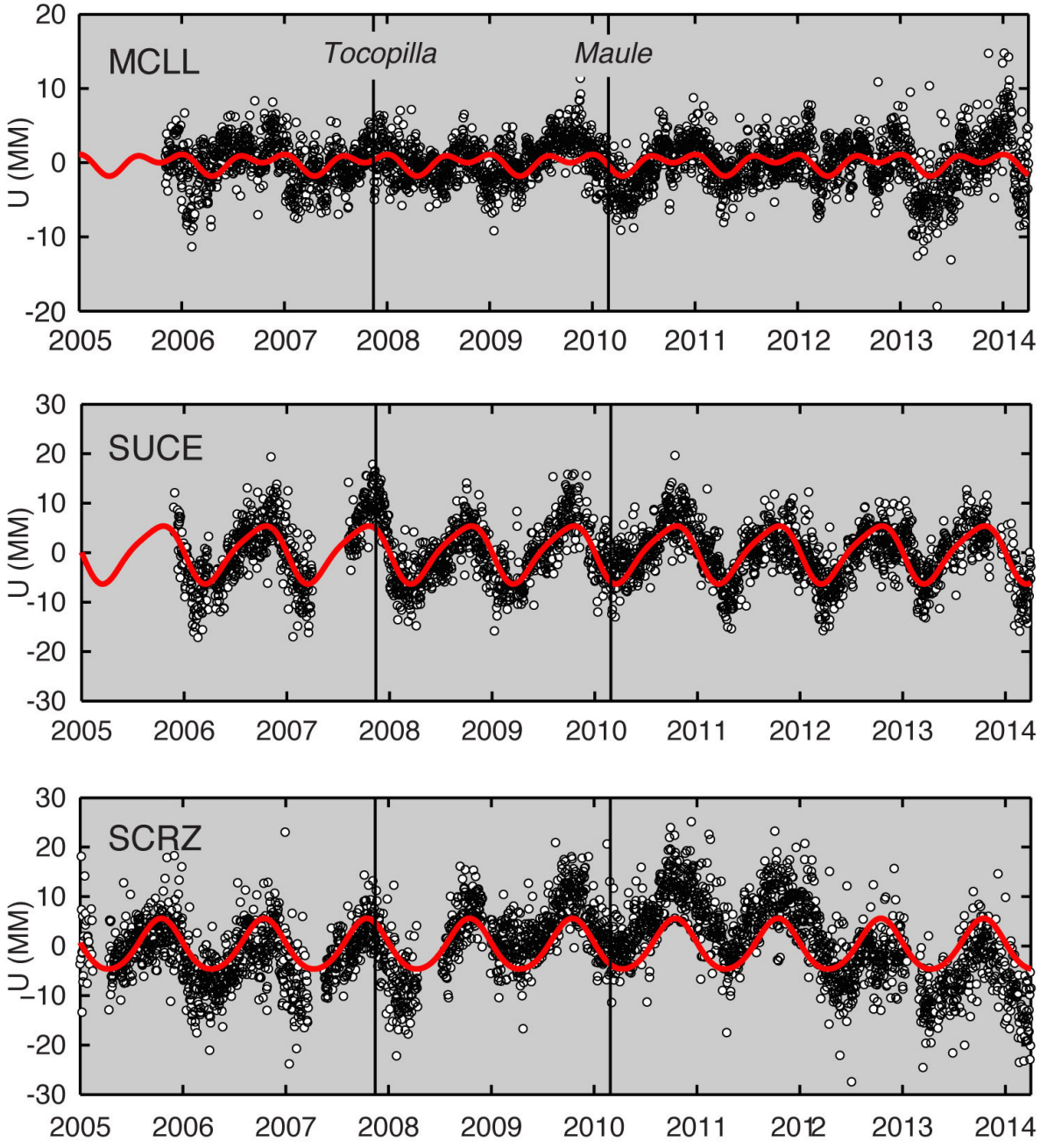

Figure C2 Examples of the seasonal perturbations for the Up components of GPS time series for select central Andean sites located on the forearc (MCLL), backarc (SUCE), and near the front of the Subandean wedge (SCRZ). The interseismic, coseismic, and postseismic signals have been removed leaving just the seasonal component. Daily positions are shown as white circles and the best-fit sinusoidal function to the seasonal is shown in red. The North and East components of the time series are shown in Figure 2.2 of the main text.

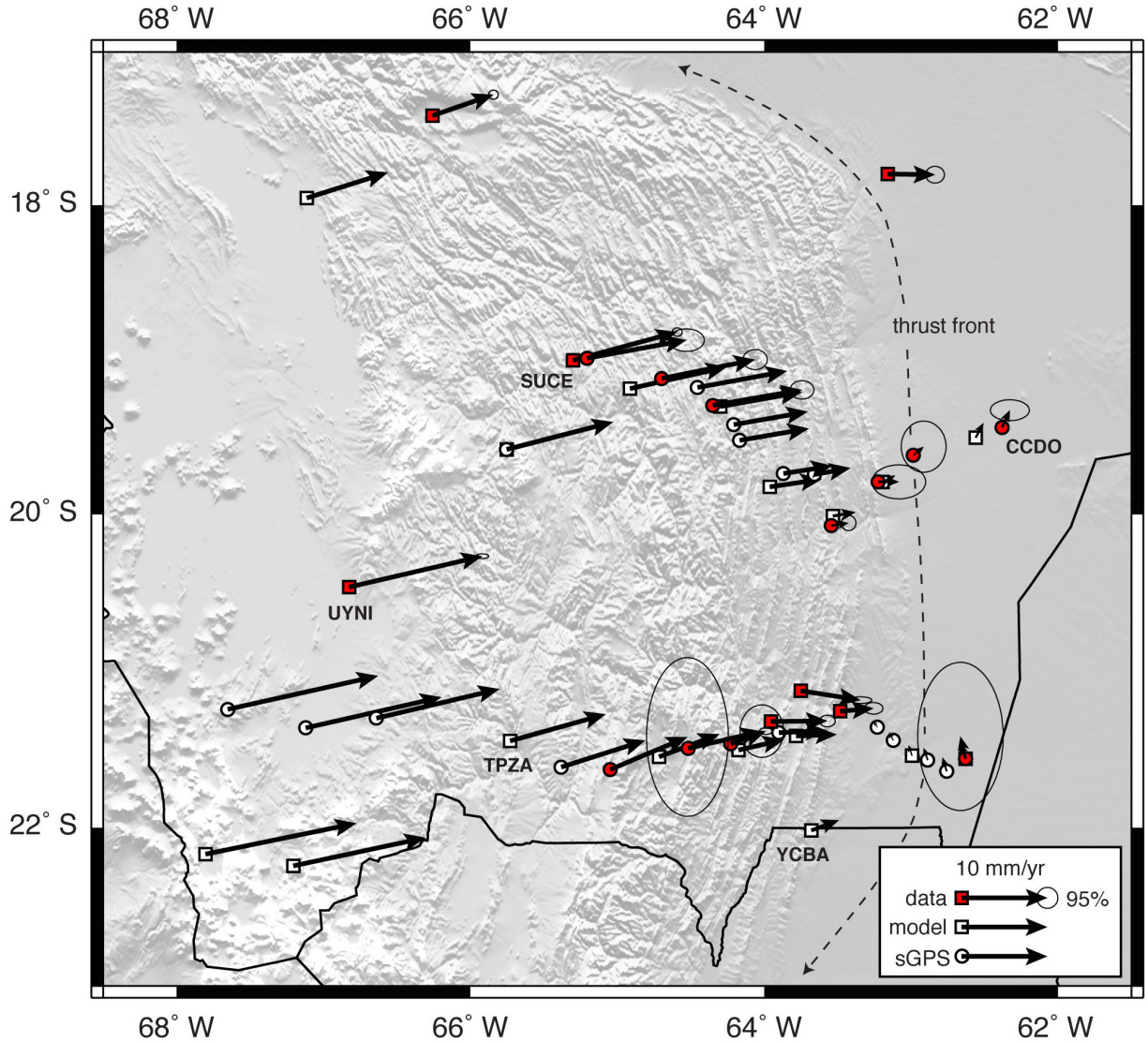

Figure C3 The interseismic or pre-quake velocity field for the Bolivian GPS sites. Red symbols indicate sites that existed prior to the Tocopilla earthquake where a pre-quake velocity and errors (95% confidence ellipses) can be estimated with confidence. White symbols are sites established after the earthquake and associated vectors are constructed by interpolating across the pre-quake sites. Note that sites east of the thrust front (black dashed line) constrain the eastern edge of the interpolation. Numerous sites located west of the mapped region are also used in the interpolation.

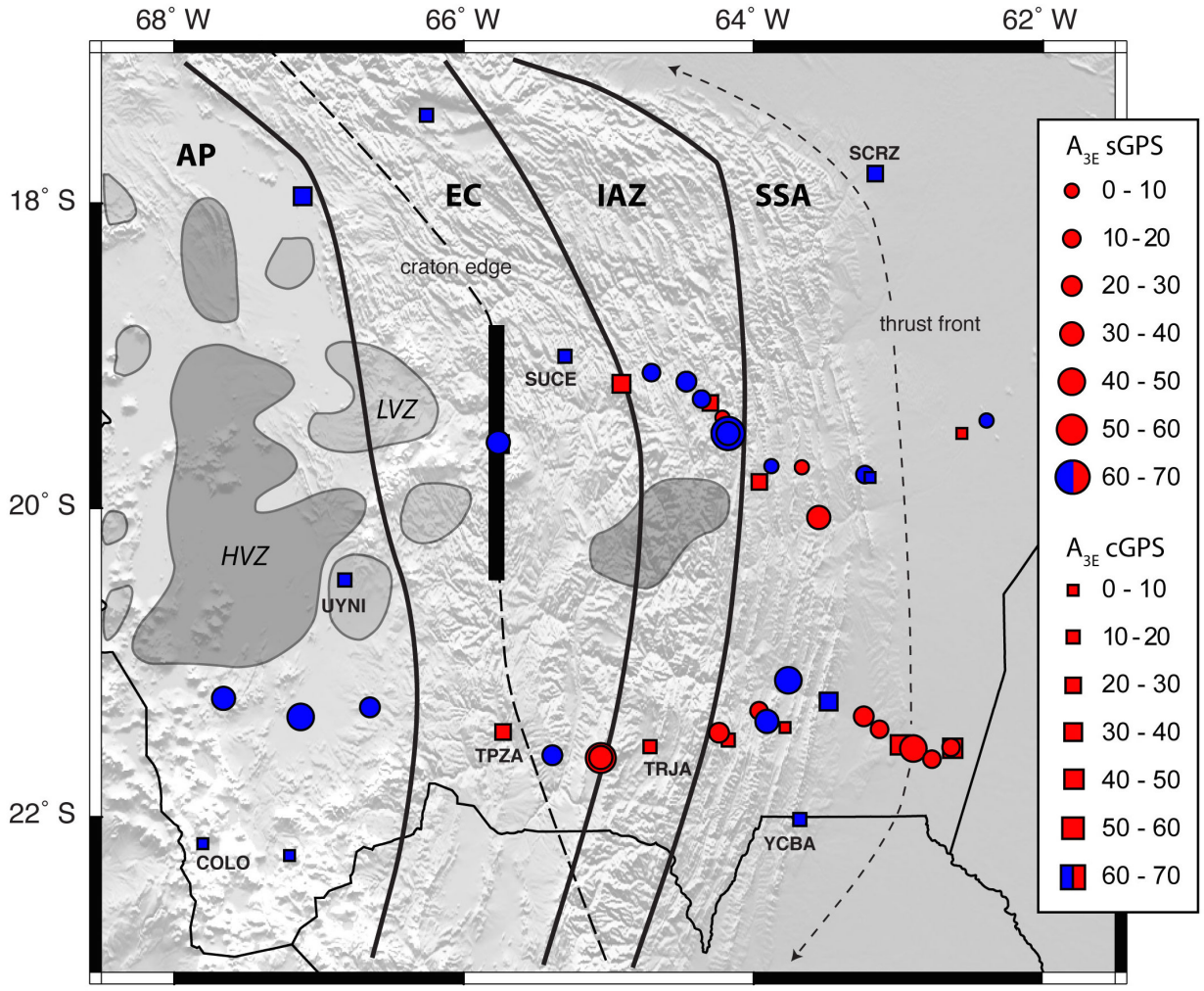

Figure C4 The best-fit amplitudes for the eastern component of the exponential terms used in the Tocopilla earthquake characterization. Squares and circles correspond to cGPS and sGPS sites, respectively. Red and blue symbols indicate sites with positive and negative postseismic amplitudes, respectively. Also shown for comparison are seismological results from [*Beck and Zandt*, 2002] including the western edge of the underthrusting Brazilian craton (black bar) and its along-strike extent (dashed line) and high and low upper mantle P-wave velocity zones. Also shown are the approximate boundaries of the central Andean physiographic provinces (heavy black lines). HVZ=high velocity zone; LVZ=low velocity zone; AP=Altiplano; EC=Eastern Cordillera; IAZ=Interandean Zone; SSA=southern Subandean Zone.

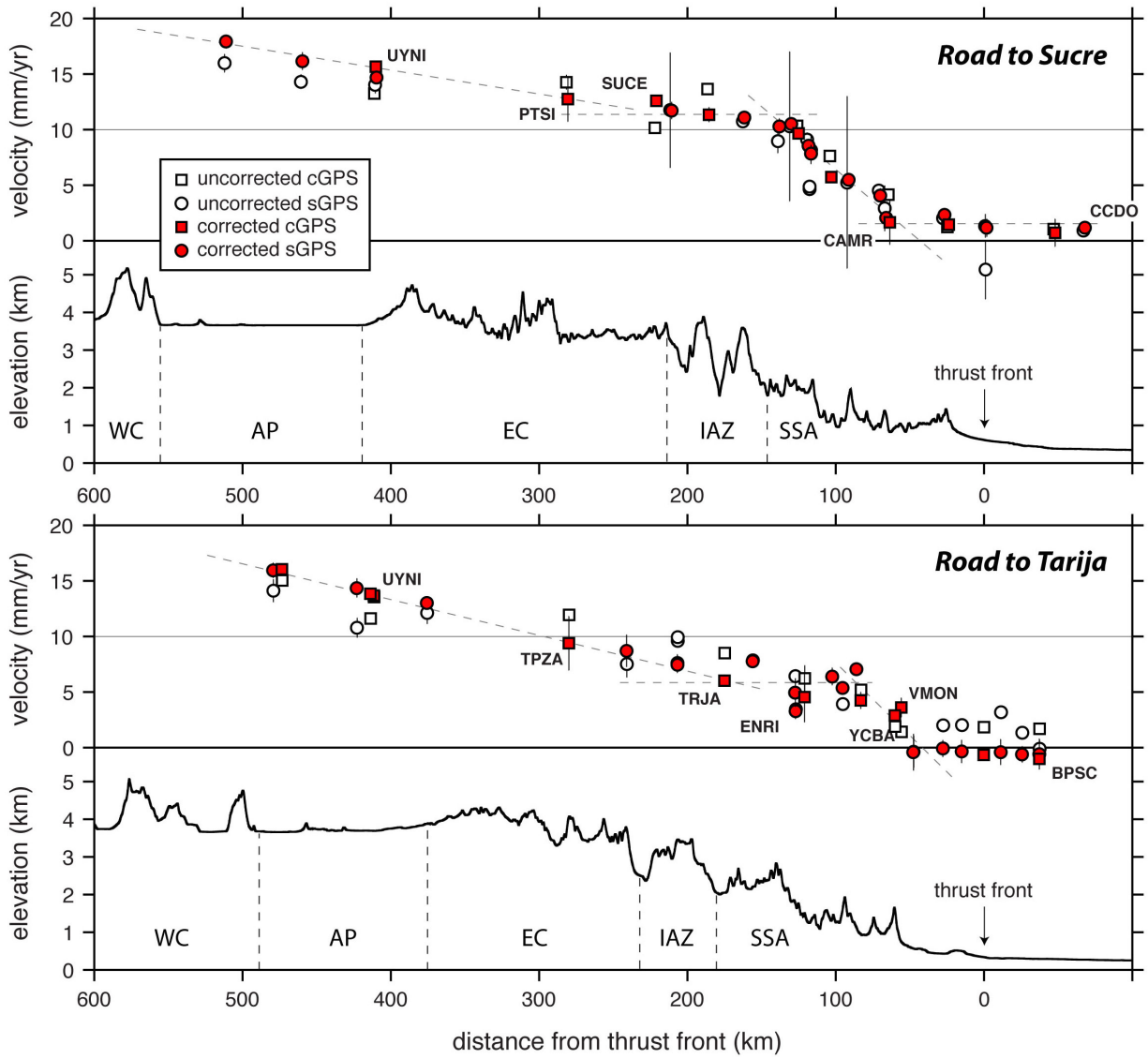

Figure C5 A comparison of the uncorrected (white symbols) and earthquake transient corrected (red symbols) velocities in profile view. Profile projections are the same as Figures 2.10 and 2.11 from the main text (perpendicular to the strike of the Subandean structures. Light dashed lines are hand-drawn fits to the data intended to emphasize the features referred to in the text. Also shown is topography corresponding to the profiles and the approximate locations of the central Andean physiographic boundaries.

Table C1 Horizontal reference frame site statistics[a]

Stnm	Lon	Lat	Tstart	Tend	Tspan	Nobs	Ve	Vn	Vh	sigVe	sigVn	neCor
ALAR	-36.6534	-9.7492	2008.2541	2015.0630	6.81	2265	0.30	0.40	0.50	0.05	0.02	0.08
BAVC	-40.8027	-14.8883	2009.2712	2014.8685	5.60	1833	0.60	-0.30	0.67	0.06	0.03	0.10
BELE	-48.4626	-1.4088	2003.8849	2015.0630	11.18	3772	-0.30	0.20	0.36	0.03	0.01	0.00
BOAV	-60.7011	2.8452	2007.6767	2015.0630	7.39	2556	0.50	0.00	0.50	0.05	0.02	0.07
BRAZ	-47.8779	-15.9475	2000.0000	2015.0219	15.02	5112	-0.20	0.00	0.20	0.01	0.01	-0.03
CEEU	-38.4255	-3.8776	2008.1694	2015.0630	6.89	2144	0.00	1.30	1.30	0.06	0.03	0.05
CHPI	-44.9852	-22.6872	2001.2904	2015.0630	13.77	3961	0.40	-0.10	0.41	0.02	0.02	0.02
CUIB	-56.0699	-15.5553	2000.3470	2015.0630	14.72	4631	0.70	-0.30	0.76	0.02	0.02	-0.15
IMPZ	-47.4972	-5.4918	2000.3552	2015.0630	14.71	4205	-0.10	-0.70	0.71	0.03	0.01	0.01
MAPA	-51.0973	0.0467	2006.0356	2015.0630	9.03	2923	0.60	0.10	0.61	0.04	0.01	0.00
MGMC	-43.8583	-16.7164	2008.2596	2015.0630	6.80	2274	0.60	0.30	0.67	0.05	0.02	0.07
MGUB	-48.2561	-18.9192	2008.0219	2015.0630	7.04	2506	0.00	0.00	0.00	0.04	0.03	-0.03
MTCO	-55.4563	-10.8039	2009.2712	2015.0630	5.79	1859	0.40	0.40	0.57	0.11	0.04	-0.18
MTSF	-50.6635	-11.6193	2008.2541	2015.0630	6.81	2289	0.00	0.40	0.40	0.04	0.02	-0.06
PEPE	-40.5061	-9.3844	2008.0000	2015.0630	7.06	2447	-0.10	0.20	0.22	0.06	0.02	0.11
POVE	-63.8963	-8.7093	2006.0082	2015.0630	9.06	2981	0.40	0.10	0.41	0.03	0.02	-0.18
PPTE	-51.4085	-22.1199	2005.9452	2015.0630	9.12	3189	0.60	0.10	0.61	0.03	0.02	-0.06
RECF	-34.9515	-8.0510	2001.3315	2015.0630	13.73	4240	-0.40	0.00	0.40	0.03	0.01	0.02
ROJI	-61.9597	-10.8639	2008.2541	2015.0630	6.81	2441	0.90	0.80	1.20	0.03	0.02	-0.16
SALU	-44.2125	-2.5935	2007.6767	2015.0630	7.39	2576	0.30	0.50	0.58	0.05	0.02	0.02
SAVO	-38.4323	-12.9393	2007.6795	2015.0630	7.38	2584	0.00	0.40	0.40	0.04	0.02	0.09
TOGU	-49.0491	-11.7467	2008.2541	2015.0630	6.81	2269	-0.20	-0.30	0.36	0.05	0.02	-0.04
TOPL	-48.3307	-10.1711	2008.0000	2014.8548	6.86	2357	0.10	0.20	0.22	0.05	0.02	-0.02
BAIR	-41.8585	-11.3057	2009.0000	2015.0329	6.03	1996	-0.20	-0.40	0.45	0.07	0.03	0.16
BOMJ	-43.4217	-13.2556	2001.7973	2015.0630	13.27	4186	-0.90	-0.20	0.92	0.02	0.01	0.07
GOJA	-51.7261	-17.8833	2008.2623	2015.0630	6.80	2267	0.40	0.40	0.57	0.05	0.03	-0.09
GVAL	-41.9576	-18.8556	2004.4973	2014.2658	9.77	3075	0.00	0.10	0.10	0.03	0.02	0.04
IMBT	-48.6557	-28.2348	2007.6767	2015.0630	7.39	2496	-0.10	0.30	0.32	0.04	0.04	-0.08
MGBH	-43.9249	-19.9419	2009.0795	2015.0630	5.98	2020	-0.40	0.20	0.45	0.07	0.04	0.01
MGIN	-46.3280	-22.3186	2008.0000	2015.0630	7.06	2437	-0.80	-0.10	0.81	0.04	0.03	0.01
MGMC	-43.8583	-16.7164	2008.2596	2015.0630	6.80	2274	0.60	0.30	0.67	0.05	0.02	0.07
MTBA	-52.2647	-15.8900	2008.6585	2015.0630	6.41	2243	-0.30	0.00	0.30	0.05	0.03	-0.06
PBCG	-35.9071	-7.2137	2008.2541	2015.0630	6.81	2358	-1.10	0.10	1.10	0.05	0.02	0.08
PISR	-42.7028	-9.0307	2009.2712	2014.8521	5.58	1857	-1.00	-0.30	1.04	0.09	0.04	0.06
POLI	-46.7303	-23.5557	2007.2849	2015.0630	7.78	2691	0.00	-0.20	0.20	0.04	0.03	0.01
PRGU	-51.4876	-25.3840	2009.2712	2015.0630	5.79	1885	-1.40	-0.40	1.46	0.52	0.41	-0.19
PRMA	-51.9384	-23.4097	2009.2712	2015.0630	5.79	1924	0.10	1.00	1.00	0.08	0.06	-0.09
RIOD	-43.3063	-22.8178	2000.3634	2015.0630	14.70	4542	0.30	0.10	0.32	0.02	0.02	0.07
RJCG	-41.3262	-21.7649	2008.2541	2015.0630	6.81	2390	-0.10	-0.10	0.14	0.04	0.03	0.04
SAGA	-67.0578	-0.1439	2007.7068	2015.0630	7.36	2604	0.90	-0.10	0.91	0.04	0.02	0.00
SCLA	-50.3043	-27.7928	2008.2541	2015.0630	6.81	2424	-0.40	-0.60	0.72	0.04	0.03	-0.05
SJRP	-49.3600	-20.7855	2010.0000	2015.0630	5.06	1735	-0.40	-0.10	0.41	0.08	0.06	-0.09
UBER	-48.3170	-18.8895	2004.5301	2014.2247	9.70	3095	-0.30	-0.80	0.85	0.03	0.02	-0.01
UFPR	-49.2310	-25.4484	2007.6767	2015.0630	7.39	2672	-0.40	-0.20	0.45	0.03	0.02	-0.05

[a]Statistics for continous GPS sites used to create the stable South American plate horizontal reference frame discussed in the main text. Stnm, station code; Lon, longitude; Lat, Latitude; Tstart, first observation epoch; Tend, last observation epoch used in analysis; Tspan, time span of measurement in years; Nobs, number of observation days (epochs) for site used in analysis; Ve, east component of velocity (mm/yr); Vn, north component of velocity (mm/yr); Vh, horizontal component of velocity (mm/yr), $Vh=sqrt(Ve^2+Vn^2)$; sigVne, standard east error (mm/yr); sigVn, standard north error (mm/yr); neCor, north-east correlation.

Table C2 Tocopilla earthquake empirical characterization parameters[a]

Stnm	rc	Lon	Lat	An	sigAn	Ae	sigAe	Au	sigAu	Tau	sigTau	Noff	sigNoff	Eoff	sigEoff	Uoff	sigUoff
0B54	s	-64.1673	-19.5233	-83.32	9.73	-34.28	9.73	-27.58	9.73	10.00	0.00						
0B85	s	-64.4549	-19.1819	12.62	19.15	-24.59	19.15	20.98	19.15	10.00	0.00						
0B87	s	-64.2072	-19.4211	19.76	8.83	4.36	8.83	12.89	8.83	10.00	0.00						
0B89	s	-63.6577	-19.7424	7.29	8.12	5.07	8.12	-17.79	8.12	10.00	0.00						
ASLO	s	-64.1673	-19.5232	-186.48	12.51	-68.23	12.51	-18.51	12.51	10.00	0.00						
BLPZ	c	-68.1683	-16.5299	23.73	0.32	5.06	0.32	-30.71	0.32	10.00	0.00						
BOQN	c	-63.1947	-19.7907	3.73	1.45	-6.01	1.45	-71.28	1.45	10.00	0.00						
BPDL	c	-64.2999	-19.3044	-16.30	2.94	23.31	2.94	-4.06	2.94	10.00	0.00						
BPLB	c	-63.7838	-21.4167	-0.52	2.58	7.64	2.58	-100.72	2.58	10.00	0.00						
BPSC	c	-62.6297	-21.5620	-1.12	2.18	47.50	2.18	-32.24	2.18	10.00	0.00						
BRCH	c	-62.5611	-19.5053	-32.85	3.92	5.37	3.92	-65.93	3.92	10.00	0.00						
BTRC	c	-64.9149	-19.1886	-9.61	2.38	35.10	2.38	-15.57	2.38	10.00	0.00						
CAGA	s	-63.2242	-19.7902	10.69	13.01	-12.38	13.01	-38.72	13.01	10.00	0.00						
CAMR	c	-63.5334	-20.0102	6.98	1.47	-0.28	1.47	-37.92	1.47	10.00	0.00						
CBMB	c	-66.2588	-17.4166	-1.42	4.42	-16.17	1.60	-11.91	19.91	8.69	0.84	-0.59	0.37	-1.59	0.38	-0.49	1.47
CCDO	s	-62.3808	-19.4391	-46.98	5.93	-1.96	5.93	-43.58	5.93	10.00	0.00						
CCYA	s	-65.0479	-21.6304	-48.00	10.98	33.99	10.98	-81.32	10.98	10.00	0.00						
CHYY	s	-63.8694	-19.7364	8.47	143.66	-8.94	143.66	789.53	143.66	10.00	0.00						
CMRI	s	-63.5425	-20.0712	0.42	90.77	34.81	90.77	-60.25	90.77	10.00	0.00						
COCI	s	-66.6405	-21.3035	9.18	15.09	-21.27	15.09	9.18	15.09	10.00	0.00						
COLO[p]	c	-67.8040	-22.1674	26.84	1.03	-7.90	1.03	-35.81	1.03	10.00	0.00						
CULK	s	-67.1211	-21.3657	64.10	10.85	-42.73	10.85	64.10	10.85	10.00	0.00						
DRDO	s	-64.3498	-19.2968	17.64	164.34	-10.19	164.34	-274.22	164.34	10.00	0.00						
GLPE	c	-64.1754	-21.5065	13.14	12.86	13.24	12.86	7.79	12.86	10.00	0.00						
IBOB	c	-62.9945	-21.5427	-3.92	1.48	40.18	1.48	-98.53	1.48	10.00	0.00						
LPTS[g]	c	-65.7538	-19.5820	9.99	11.49	36.57	11.49	-46.40	11.49	10.00	0.00						
M007	s	-63.9008	-21.3953	-10.12	9.76	-37.14	9.76	-70.86	9.76	10.00	0.00						
M009	s	-62.8877	-21.5702	-6.27	3.83	82.68	10.56	-98.58	3.83	10.00	0.00						
M010	s	-62.7584	-21.6409	-34.32	4.23	40.47	9.34	-57.86	4.23	10.00	0.00						
M011	s	-63.1210	-21.4456	-30.35	5.05	47.87	9.67	-92.66	5.05	10.00	0.00						
M012	s	-63.2295	-21.3620	13.73	5.98	49.60	11.12	-102.27	5.98	10.00	0.00						
MARG	c/s	-63.7520	-21.1291	38.84	5.84	-49.42	5.84	-10.02	5.84	10.00	0.00						
MGDO	c	-63.9623	-19.8223	11.52	1.43	23.91	1.43	-35.95	1.43	10.00	0.00						
PBLA	s	-65.3820	-21.6149	-28.01	16.91	-28.85	16.91	-28.01	16.91	10.00	0.00						
PBOL	s	-62.6294	-21.5619	30.94	13.57	15.69	13.57	30.94	13.57	10.00	0.00						
PLLO	s	-64.5179	-21.4956	-36.53	13.15	-7.14	13.15	-80.06	13.15	10.00	0.00						
PTSI	s	-65.7539	-19.5813	61.75	43.75	-32.61	43.75	555.58	43.75	10.00	0.00						
SANA	s	-67.6520	-21.2470	-4.57	13.19	-33.83	13.19	-4.57	13.19	10.00	0.00						
SCRZ	c	-63.1597	-17.7968	12.11	10.45	-27.62	6.63	-69.05	28.81	10.00	0.00	0.12	0.52	-0.99	0.55	-0.42	1.99
SUCE	c	-65.3026	-19.0062	-0.68	1.08	-14.84	0.20	14.51	4.10	1.03	0.03	-0.25	0.38	-2.17	0.53	-4.75	1.60
TARI	s	-65.0479	-21.6307	-41.13	16.76	55.25	16.76	-125.84	16.76	10.00	0.00						
TPYO	c/s	-63.9545	-21.3247	49.65	7.33	16.12	7.33	-83.50	7.33	10.00	0.00						
TPZA	c	-65.7299	-21.4482	-27.66	1.22	24.60	1.22	-41.05	1.22	10.00	0.00						
TRJA	c	-64.7165	-21.5495	-30.68	0.66	15.65	0.66	-80.88	0.66	10.00	0.00						
URUS	c	-67.1144	-17.9528	25.30	0.75	-32.84	0.75	-44.16	0.75	10.00	0.00						
UTUR[p]	c	-67.2055	-22.2420	22.70	0.81	-1.59	0.81	4.06	0.81	10.00	0.00						
UYNI	c	-66.8260	-20.4659	1.54	4.61	-15.38	1.45	-2.37	11.46	5.79	0.53	-4.26	0.68	-6.78	0.72	3.49	1.76
VMON	c	-63.4836	-21.2589	0.99	8.05	-39.77	3.76	-31.64	16.50	9.93	1.62	1.75	1.89	-0.08	2.41	8.67	3.52
YCBA	c	-63.6800	-22.0171	-0.43	1.46	-15.83	1.46	-93.17	1.46	10.00	0.00						
ZDNZ	s	-64.6980	-19.1234	5.64	6.41	-13.32	6.41	-5.61	6.41	10.00	0.00						

[a]Stnm, station code; r, survey (sGPS) site; c, continuous (cGPS) site; c/s, former cGPS site current sGPS site; Lon, longitude; Lat, Latitude; An, north component of postseismic exponential amplitue (mm); Ae, east component of postseismic exponential amplitue (mm); Au, Up component of postseismic exponential amplitue (mm); sigAn, north amplitude standard error (mm); sigAe, east amplitude standard error (mm); sigAu, up amplitude standard error (mm); Tau, exponential decay time (years); sigTau, exponential decay time standard error; Noff, north coseismic offset (mm); Eoff, east coseismic offset (mm); Uoff, up coseismic offset (mm); sigNoff, north coseismic offset standard error; sigEoff, east coseismic offset standard error; sigUoff, up coseismic offset standard error. [p]PLUTONS site. [g]GLISN site.

Table C3 White and power law noise statistics for corrected cGPS time series

	white noise (σ_{wn})			power-law amplitude (σ_{pl})			power-law exponent/index (n)		
STNM	**N**	**E**	**U**	**N**	**E**	**U**	**N**	**E**	**U**
BLPZ*	0.616 +/- 0.019	0.827 +/- 0.028	2.515 +/- 0.097	2.433 +/- 0.136	3.287 +/- 0.109	9.937 +/- 0.605	1.265 +/- 0.051	1.272 +/- 0.121	1.237 +/- 0.058
BOQN	0.638 +/- 0.115	1.226 +/- 0.069	3.265 +/- 9.701	1.742 +/- 0.154	2.440 +/- 0.260	9.711 +/- 9.966	0.549 +/- 0.086	0.993 +/- 0.165	0.825 +/- 3.683
BPDL	0.967 +/- 0.058	1.073 +/- 0.225	3.163 +/- 0.346	3.878 +/- 0.628	2.466 +/- 0.421	9.793 +/- 1.522	1.698 +/- 0.280	0.647 +/- 0.214	1.035 +/- 0.211
BPLB	0.950 +/- 0.062	1.338 +/- 0.078	3.872 +/- 0.249	2.204 +/- 0.411	3.391 +/- 0.631	7.011 +/- 1.415	1.091 +/- 0.204	1.170 +/- 0.185	0.990 +/- 0.228
BPSC	0.586 +/- 0.076	1.089 +/- 0.232	2.712 +/- 0.554	2.021 +/- 0.246	2.120 +/- 0.308	7.161 +/- 0.847	0.761 +/- 0.093	0.769 +/- 0.434	0.734 +/- 0.206
BRCH	1.396 +/- 0.085	2.464 +/- 0.095	3.249 +/- 2.455	1.563 +/- 0.529	2.133 +/- 0.885	9.428 +/- 1.718	1.114 +/- 0.578	1.837 +/- 0.697	0.404 +/- 0.175
BTRC	0.778 +/- 0.048	1.071 +/- 0.116	2.125 +/- 1.054	2.128 +/- 0.300	3.624 +/- 0.428	8.181 +/- 1.018	1.188 +/- 0.203	1.086 +/- 0.186	0.759 +/- 0.273
CAMR	0.836 +/- 0.058	1.343 +/- 0.034	2.457 +/- 1.056	2.638 +/- 0.224	5.548 +/- 0.420	10.186 +/- 1.232	1.052 +/- 0.123	1.830 +/- 0.080	0.730 +/- 0.171
CBMB*	0.699 +/- 0.056	0.769 +/- 0.042	3.349 +/- 0.121	2.373 +/- 0.121	2.291 +/- 0.090	8.205 +/- 0.695	0.850 +/- 0.088	0.614 +/- 0.036	1.042 +/- 0.105
COLO	0.203 +/- 0.035	0.875 +/- 0.139	1.478 +/- 0.400	2.287 +/- 0.117	4.424 +/- 0.251	11.814 +/- 0.546	0.597 +/- 0.035	0.688 +/- 0.039	0.847 +/- 0.052
GLPE	0.857 +/- 1.806	1.388 +/- 0.206	4.411 +/- 0.853	1.133 +/- 1.638	3.606 +/- 1.016	14.743 +/- 4.152	0.260 +/- 0.879	1.248 +/- 0.615	1.102 +/- 0.336
IBOB	1.185 +/- 0.134	2.425 +/- 0.485	3.414 +/- 1.798	3.076 +/- 0.413	4.524 +/- 0.701	9.526 +/- 1.225	0.951 +/- 0.200	0.519 +/- 0.155	0.700 +/- 0.406
LPTS	0.737 +/- 0.555	2.160 +/- 1.131	5.308 +/- 1.955	4.907 +/- 0.709	5.651 +/- 1.317	11.142 +/- 2.667	0.996 +/- 0.264	0.616 +/- 0.325	0.637 +/- 0.397
MGDO	0.802 +/- 0.064	1.193 +/- 0.043	3.623 +/- 0.236	2.013 +/- 0.241	2.511 +/- 0.284	8.139 +/- 0.923	0.971 +/- 0.188	1.217 +/- 0.157	0.867 +/- 0.140
SCRZ*	1.056 +/- 0.020	1.358 +/- 0.022	4.010 +/- 0.071	2.621 +/- 0.152	2.969 +/- 0.170	10.825 +/- 0.561	1.541 +/- 0.111	1.202 +/- 0.086	1.282 +/- 0.065
SUCE*	0.684 +/- 0.033	0.936 +/- 0.035	2.573 +/- 0.143	2.169 +/- 0.144	2.796 +/- 0.144	9.834 +/- 0.569	1.173 +/- 0.118	0.955 +/- 0.056	1.017 +/- 0.066
TPZA	0.699 +/- 0.033	1.334 +/- 0.064	2.768 +/- 0.239	3.993 +/- 0.315	4.453 +/- 0.393	8.991 +/- 0.702	1.608 +/- 0.064	1.427 +/- 0.174	0.807 +/- 0.075
TRJA	0.764 +/- 0.019	1.164 +/- 0.044	3.487 +/- 0.134	2.896 +/- 0.225	4.286 +/- 0.344	8.857 +/- 0.704	1.646 +/- 0.114	1.350 +/- 0.087	1.171 +/- 0.109
URUS	0.633 +/- 0.044	0.848 +/- 0.045	2.479 +/- 0.133	2.957 +/- 0.220	3.334 +/- 0.229	8.415 +/- 0.662	1.257 +/- 0.130	1.163 +/- 0.078	1.137 +/- 0.123
UTUR	0.640 +/- 0.027	0.891 +/- 0.032	1.796 +/- 1.167	2.829 +/- 0.238	2.965 +/- 0.231	8.816 +/- 1.268	1.261 +/- 0.053	1.197 +/- 0.086	0.864 +/- 0.359
UYNI*	0.549 +/- 0.023	0.635 +/- 0.036	1.649 +/- 0.134	2.034 +/- 0.132	2.539 +/- 0.114	7.919 +/- 0.231	1.237 +/- 0.094	0.886 +/- 0.041	0.954 +/- 0.059
VMON*	1.013 +/- 0.079	1.309 +/- 0.137	3.785 +/- 0.978	3.328 +/- 0.249	2.872 +/- 0.259	10.793 +/- 1.036	1.106 +/- 0.133	0.792 +/- 0.153	0.747 +/- 0.220
YCBA	0.719 +/- 0.082	0.955 +/- 0.250	2.408 +/- 0.565	2.108 +/- 0.217	2.648 +/- 0.247	11.314 +/- 0.853	0.818 +/- 0.110	0.632 +/- 0.176	0.774 +/- 0.094
sGPS	0.783	1.247	3.039	2.58	3.343	9.597	1.698	1.837	1.282

*site with pre-Tocopilla observations

Table C4 Uncorrected GPS site velocities[a]

Stnm	Type	Lon	Lat	Vn	Ve	Vu	sigNs	sigEs	sigUs	neCor	tspan
0B54	s	-64.1673	-19.5233	-5.00	5.40	2.30	0.59	0.65	1.14	-0.56	5.88
0B85	s	-64.4549	-19.1819	3.00	8.60	-0.30	1.29	1.12	1.92	-0.38	5.88
0B87	s	-64.2072	-19.4211	2.80	8.80	-0.50	0.57	0.66	1.14	-0.55	5.88
0B89	s	-63.6577	-19.7424	1.00	4.40	-0.40	0.77	0.45	0.69	-0.16	5.20
ASLO	s	-64.1673	-19.5232	-5.40	5.70	1.10	0.19	0.21	0.34	-0.48	12.82
BLPZ	c	-68.1683	-16.5299	2.10	4.80	-0.50	0.02	0.02	0.03	-0.21	9.17
BOQN	c	-63.1947	-19.7907	1.00	1.10	1.90	0.06	0.09	0.11	-0.22	3.36
BPDL	c	-64.2999	-19.3044	0.30	10.40	-1.70	0.17	0.21	0.31	-0.35	2.24
BPLB	c	-63.7838	-21.4167	0.10	5.40	3.50	0.12	0.14	0.18	-0.25	2.32
BPSC	c	-62.6297	-21.5620	0.20	1.80	-0.70	0.10	0.13	0.16	-0.21	2.32
BRCH	c	-62.5611	-19.5053	-0.30	1.10	0.80	0.22	0.26	0.33	-0.22	2.32
BTRC	c	-64.9149	-19.1886	2.00	13.50	-0.10	0.10	0.14	0.17	-0.20	2.31
CAGA	s	-63.2242	-19.7902	0.40	2.00	1.60	0.44	0.62	0.82	-0.30	10.85
CAMR	c	-63.5334	-20.0102	0.60	4.10	0.30	0.08	0.11	0.13	-0.14	4.33
CBMB	c	-66.2588	-17.4166	2.30	5.60	-0.40	0.02	0.02	0.03	-0.23	8.39
CCDO	s	-62.3808	-19.4391	0.30	0.90	1.00	0.22	0.20	0.24	-0.09	12.81
CCYA	s	-65.0479	-21.6304	1.00	10.20	-1.00	0.42	0.35	0.65	-0.49	9.99
CHYY	s	-63.8694	-19.7364	0.70	5.20	-19.50	6.28	8.08	11.45	-0.34	12.83
CMRI	s	-63.5425	-20.0712	0.30	2.90	9.50	1.67	2.13	2.97	-0.33	12.14
COCI	s	-66.6405	-21.3035	4.00	13.60	-3.00	1.33	0.82	1.62	-0.37	3.69
COLO[p]	c	-67.8040	-22.1674	5.40	17.00	0.50	0.05	0.07	0.08	-0.11	3.96
CULK	s	-67.1211	-21.3657	8.00	13.30	0.30	0.86	0.73	1.60	-0.69	3.71
DRDO	s	-64.3498	-19.2968	2.70	10.00	12.50	5.42	7.01	10.10	-0.34	12.81
ENRI	s	-64.2280	-21.4678	1.60	4.00	1.00	0.16	0.30	0.24	0.13	2.84
FD01	s	-62.9848	-19.6185	-3.00	-2.20	3.30	2.49	2.62	2.09	0.10	3.70
GLPE	c	-64.1754	-21.5065	3.20	7.30	0.70	0.89	1.11	1.49	-0.29	3.36
IBOB	c	-62.9945	-21.5427	0.00	1.90	3.20	0.09	0.10	0.13	-0.24	4.38
LPTS[g]	c	-65.7538	-19.5820	3.50	13.90	-0.30	0.52	0.67	0.87	-0.20	1.36
M007	s	-63.9008	-21.3953	-0.20	4.00	1.60	0.38	0.59	0.67	-0.16	9.88
M009	s	-62.8877	-21.5702	0.10	3.30	1.40	0.27	0.56	0.45	0.13	9.90
M010	s	-62.7584	-21.6409	-0.30	1.30	-0.50	0.26	0.47	0.44	0.01	9.90
M011	s	-63.1210	-21.4456	-1.10	1.80	0.50	0.26	0.61	0.48	0.18	9.89
M012	s	-63.2295	-21.3620	0.10	2.10	1.80	0.66	0.44	0.50	-0.03	9.89
MARG	c/r	-63.7520	-21.1291	-0.60	6.50	1.70	0.10	0.12	0.15	-0.21	6.23
MGDO	c	-63.9623	-19.8223	1.40	7.50	1.60	0.07	0.09	0.11	-0.23	3.36
NTRS	s	-64.2283	-21.4676	0.20	6.70	-0.30	0.38	0.63	0.69	-0.13	9.22
PBLA	s	-65.3820	-21.6149	1.20	8.10	-4.50	1.20	1.05	1.86	-0.46	3.67
PBOL	s	-62.6294	-21.5619	1.50	0.30	0.20	0.58	0.84	0.55	0.22	9.90
PLLO	s	-64.5179	-21.4956	0.70	8.30	-1.80	0.38	0.29	0.47	-0.30	12.06
SALA	s	-62.9849	-19.6186	1.00	1.20	2.70	1.22	1.07	1.41	-0.16	4.23
SANA	s	-67.6520	-21.2470	3.70	15.60	0.10	0.97	0.89	1.74	-0.54	3.73
SCRZ	c	-63.1597	-17.7968	0.70	3.60	5.60	0.02	0.03	0.04	-0.18	9.38
SUCE	c	-65.3026	-19.0062	3.20	9.80	-2.00	0.02	0.03	0.04	-0.23	8.35
SUCR	s	-65.2060	-18.9921	2.50	11.50	-41.80	4.18	5.41	8.10	-0.36	12.07
TARI	s	-65.0479	-21.6307	1.60	10.70	0.30	0.46	0.34	0.53	-0.24	12.82
TPYO	c/s	-63.9545	-21.3247	0.80	6.90	-0.40	0.28	0.15	0.24	-0.17	9.97
TPZA	c	-65.7299	-21.4482	1.30	12.70	-0.70	0.07	0.07	0.09	-0.10	4.05
TRJA	c	-64.7165	-21.5495	0.00	8.80	2.60	0.03	0.04	0.05	-0.31	6.87
URUS	c	-67.1144	-17.9528	4.80	7.20	0.80	0.04	0.04	0.06	-0.25	4.57
UTUR[p]	c	-67.2055	-22.2420	4.80	15.30	-3.40	0.04	0.05	0.07	-0.24	3.96
UYNI	c	-66.8260	-20.4659	3.30	12.90	0.10	0.02	0.02	0.02	-0.13	8.34
VMON	c	-63.4836	-21.2589	0.90	1.70	-0.20	0.03	0.03	0.04	-0.20	10.65
VMT3	s	-63.3957	-21.2286	0.30	-0.30	2.80	0.77	1.48	1.31	0.06	2.91
YCBA	c	-63.6800	-22.0171	0.90	2.20	2.50	0.07	0.08	0.11	-0.28	3.37
ZDNZ	s	-64.6980	-19.1234	2.50	10.50	0.50	0.20	0.22	0.29	-0.18	12.09

[a]Uncorrected GPS site velocities expressed relative to the stable South American plate. Stnm, station code; Type, station type; r, survey (sGPS) site; c, continuous (cGPS) site; c/s, former cGPS site current sGPS site; Lon, longitude; Lat, Latitude; Vn, north component of velocity (mm/yr); Ve, east component of velocity (mm/yr); Vu, up component of velocity (mm/yr); sigNs, standard north error (mm/yr); sigEs, standard east error (mm/yr); sigUs, neCor, north-east correlation; tspan, time span of measurement in years. [p]PLUTONS site. [g]GLISN site.

Chapter 3

Numerical models of accretionary wedge growth: insights on the evolution of surface faulting and the wedge front

In preparation for publication as:

Weiss, J.R., G. Ito, B.A. Brooks, J-A Olive, G.F. Moore, and J.H. Foster. Numerical models of accretionary wedge growth: insights on the evolution of surface faulting and the wedge front

Key points:

- A continuum mechanics-based, finite difference method simulates orogenic wedge formation/evolution and matches first-order critical taper predictions
- Results exhibit deformation cycles including internal thrusting similar to active wedges and show that 75% of surface faulting occurs in the wedge interior
- Thrust fault formation near the surface and subsequent down-dip propagation is explained using a simple elastic solution and compared to the protothrust zones of active submarine accretionary prisms

Abstract

We use a two-dimensional, continuum mechanics-based, finite difference method with a visco-elasto-plastic rheology to investigate the distribution of deformation during accretionary wedge growth. The model simulates the contraction of a crustal layer

overlying a weak base (décollement) against a rigid backstop and the spontaneous nucleation and evolution of fault zones due to cohesive, Mohr-Coulomb failure with strain weakening. Consistent with critical taper theory, the average surface slope, width, and wedge-front propagation rate are controlled by the relative frictional strengths of the wedge and décollement. Numerical wedges evolve via episodes of 1) widening as new thrusts nucleate near the surface beyond the wedge toe and propagate down-dip to intersect the décollement and 2) thickening via slip on older, internal fault zones similar to observations from active wedges. We propose a simple analytical elastic solution to explain the top-down propagation behavior and seismic reflection images of the protothrust zones (PTZ) of submarine accretionary prisms. We infer the top of the PTZ to mark the ductile-to-brittle transition in the shallow sediments seaward of the frontal thrust.

3.1 Introduction

Contractional wedges are fundamental features associated with mountain building and subduction. The largest earthquakes on Earth occur on the gently dipping fault planes (décollements) that underlie them [*Brooks et al.*, 2011b; *Fujiwara et al.*, 2011; *Hubbard et al.*, 2015; *Johnson et al.*, 2001; *Kanamori*, 1977; *Kumar et al.*, 2006; *Lavé et al.*, 2005; *Lay et al.*, 2005; *Stein and Toda*, 2013]. Numerous studies of both active and inactive orogenic wedges, including subaerial fold-and-thrust belts and submarine accretionary prisms, have yielded detailed information on their internal structure and evolution. Key characteristics of these folded mountain belts include a gently dipping, weak basal décollement with little deformation of the rocks beneath, a wedge-shaped prism above the décollement that tapers

or thins away from the wedge interior, and large internal deformation and crustal thickening within the wedge facilitated by localized, imbricate faulting and associated folding [*Chapple*, 1978].

In the mid-1980's a series of papers demonstrated that the overall geometry and mechanics of wedges could be described by force balance equations governing the deformation of a pile of non-cohesive brittle material (e.g. sand or snow) being pushed on one side, for example, by a bulldozer [e.g. *Dahlen*, 1990; *Davis et al.*, 1983]. This "critical Coulomb wedge model" explains many aspects of thin-skinned fold-and-thrust belts and accretionary prisms at the whole-wedge scale. For example, by assuming that material within the wedge is everywhere on the verge of Coulomb failure, the theory relates the dips of the wedge surface and base to the internal and basal material properties. Despite its vast contribution to understanding wedge mechanics and its success at matching large-scale observations from real-world wedges, wedge theory is limited in its ability to relate long-term, whole-wedge deformation patterns to the behavior of individual structures over seismotectonic and intermediate geologic timescales. For example, wedge theory does not address how wedges develop from non-critical geometries, ignores elastic processes such including the earthquake cycle (i.e. interseismic locking of the décollement), and temporal variations in the wedge stress state due to factors such as pore pressure and strain hardening/softening [*Del Castello and Cooke*, 2007; *Simpson*, 2011; *Stockmal et al.*, 2007].

A growing body of observations from active wedges in locations such as Taiwan, the Himalayas, and southern Bolivia has shed light on incremental wedge deformation processes acting over seismotectonic time-scales of seconds to thousands of years. Results suggest that strain accumulating on the basal décollement towards the wedge interior is released episodically via earthquakes that build topography by transferring slip from hinterland to foreland positions [e.g. *Hsu et al.*, 2009; *Lavé and Avouac*, 2000; *Simoes et al.*, 2007a; *Weiss et al.*, 2015]. There have been few attempts to place this emerging seismotectonic scheme in the longer-term theoretical wedge framework.

Numerical models have the power to link theoretical predictions to observations of wedges and in particular to illuminate the cyclic behavior between episodes of wedge widening via the initiation of new frontal thrusts and wedge thickening via internal deformation on preexisting structures [e.g. *Del Castello and Cooke*, 2007; *Stockmal et al.*, 2007; *Stolar et al.*, 2007]. These models were shown to resolve deformation on discrete fault zones and fault-bend folds with complex movement histories while behaving generally as predicted by critical wedge theory in a time and space averaged sense [e.g. *Masek and Duncan*, 1998; *Ruh et al.*, 2012; *Simpson*, 2011; *Stockmal et al.*, 2007].

Here we use a two-dimensional, continuum mechanics-based, finite difference method with a visco-elasto-plastic rheology to investigate the spatiotemporal distribution of deformation during wedge growth over intermediate seismotectonic timescales. After demonstrating that model results compare favorably with theoretical predictions we focus

on two aspects of wedge evolution. The first relates to the spatial pattern of surface faulting during model wedge evolution and we find that numerical wedges exhibit alternating cycles of primarily wedge-front and internal deformation similar to natural examples. The second is the formation of new frontal thrust faults, which our models predict to consistently nucleate at or near the surface and propagate down-dip to intersect the décollement. We present a simple mechanical analysis of the stress state in front of the wedge, which explains this observation, and discuss evidence of top-down fault propagation from both mountain belts and submarine accretionary prisms.

3.2 Previous Work

Analogue and numerical methods have long been used to address wedge deformation and evolution. Early numerical approaches focused on large-scale patterns of deformation and uplift across compressional wedges [e.g. *Beaumont et al.*, 1992; *Hardy et al.*, 1998; *Masek and Duncan*, 1998; *Stockmal*, 1983; *Willett et al.*, 1993; *Willett*, 1992; *Willett*, 1999]. These studies typically did not resolve or replicate detailed geologic structures but many included some form of surface processes and demonstrated their first-order control on the structure of wedges. More recently, numerical techniques model wedge evolution by solving the equations of conservation of mass and momentum using finite element [e.g. *Selzer et al.*, 2007; *Simpson*, 2011; *Simpson*, 2009; *Stockmal et al.*, 2007], finite difference [e.g. *Ruh et al.*, 2014; *Ruh et al.*, 2012], or discreet element [e.g. *Hardy et al.*, 2009; *Morgan*, 2015] methods. Boundary conditions simulate the bulldozer push at the back of the wedge and the models employ visco-elasto-plastic rheologies similar to what

we describe in the following section. Entirely different classes of models use geometrical [e.g. *Cubas et al.*, 2008; *Mary et al.*, 2013b] or minimum work [*Cooke and Madden*, 2014; *Del Castello and Cooke*, 2007; *Masek and Duncan*, 1998; *Yagupsky et al.*, 2014] techniques. The numerical approaches have developed to the point where they reproduce many of the details present in both analogue (sandbox) models [e.g. *Adam et al.*, 2005; *Cruz et al.*, 2010; *Hoth et al.*, 2007a; *Malavieille*, 2010; *Storti and McClay*, 1995] and real-world compressional belts while matching critical taper predictions.

Progress has also been made towards linking long-term, whole-wedge theoretical predictions to wedge deformation over short to intermediate seismotectonic (10^3-10^5 years) timescales. For example, *Wang and Hu* [2006] incorporate dynamic behavior in wedge theory and find that the outer wedge switches between stable and critical stress states during the interseismic locking and coseismic slip portions of the subduction zone earthquake cycle, respectively. A recent combination of critical wedge theory with dynamic rupture models shows that fault frictional strength, stress state, and angle of intersection with the weak base will control whether or not a wedge earthquake will be confined to the décollement or will propagate towards the surface on a branch fault [*DeDontney et al.*, 2012]. Finally, efforts have begun to combine Coulomb wedge theory with rate-dependent friction laws to model the spatiotemporal evolution of wedge deformation including the seismic cycle [*van Dinther et al.*, 2014; *Zilio et al.*, 2015]. Despite these results, opportunities still remain to link complex, time-dependent seismotectonic processes to basic wedge mechanics.

3.3 Numerical Modeling Approach

We model the formation and evolution of orogenic wedges using SiStER (Simple Stokes solver with Exotic Rheologies), a 2-D finite difference/particle-in-cell method largely based on the methods presented in *Gerya* [2010]. A detailed description of the technique is presented in *Olive et al.* [in press] so here we provide only a brief overview. SiStER is written in MATLAB® and solves for conservation of mass, momentum, and energy in a 2-D Cartesian continuum assuming material incompressibility. The governing equations are discretized on an Eulerian grid and solved using the direct solver for a systems of linear equations in MATLAB ("backslash") whereas the non-linear terms are handled using Picard iterations. Material properties are passively carried in the velocity field using moving tracer particles and a fourth-order Runga-Kutta method and bilinear interpolation passes properties between nodes and particles.

The method simulates an elasto-plastic rheology; wedge material behaves elastically when deformed over a time scale shorter than its Maxwell characteristic time, and deforms plastically wherever the second invariant of the deviatoric stresses exceeds the yield stress. The yield stress is defined by the Mohr-Coulomb failure criterion,

$$\frac{\sigma_1 - \sigma_3}{2} = -\left(\frac{\sigma_1 + \sigma_3}{2}\right)\sin\phi + C_0 \cos\phi \tag{3.1}$$

where σ_1 is the least compressive stress

$$\sigma_1 = -P(1 - \sin\phi) + C_0 \cos\phi, \tag{3.2}$$

and σ_3 is the most compressive stress

$$\sigma_3 = -P(1+\sin\phi) - C_0 \cos\phi. \tag{3.3}$$

In the equations above P is the mean stress, ϕ is the internal angle of friction of the wedge material, and C_o is the initial material cohesion. To promote strain localization, cohesion decreases linearly with accumulated plastic strain (ε_p) until a critical value (ε_{CRIT}) is reached, at which point cohesion is held at a minimum value (C_{MIN}). We also simulate a healing mechanism, which reduces ε_p over a relatively long time scale and promotes the localization of strain in fault-like zones and inhibits diffuse plastic deformation. By definition, our continuum mechanics approach implies that the model produces shear bands and not fractures with finite offsets. For convenience we refer to these features as thrust faults.

The model simulates the contraction of a sedimentary layer overlying a weak base (décollement) against a rigid backstop. In all of our models the sedimentary wedge layer has an initial, uniform thickness of H=4.5 km, an angle of internal friction of ϕ=30°, a density of ρ_s = 2700 kg·m^{-3}, and a uniform viscosity of $\eta_s = 10^{25}$ Pa·s. One model run, described later in the paper, has a 1-km-thick upper wedge layer with a viscosity of $\eta = 10^{21}$ Pa·s. In our models C_o=20 MPa and C_{MIN}=0 for the wedge. The basal décollement has an initial, uniform thickness of H_d = 0.5 km, the angle of internal friction varies from ϕ=5-30°, and the base is cohesionless. Other décollement material properties are identical to the sedimentary layer.

A (stress) "free" wedge surface is simulated by covering the sediment layer with a layer of fluid with very low viscosity ($\eta_a = 10^{17}$ Pa s) and zero density. We track the evolution of the wedge surface using a chain of closely spaced Lagrangian markers that are initially placed at the air-sediment interface and then advected with the time-varying velocity field. To prevent unrealistically steep or overhanging topography, we incorporated a crude representation of erosion and mass wasting using the linear diffusion equation [e.g. *Hardy and Ford*, 1997; *Ruh et al.*, 2013; *Selzer et al.*, 2007; *Simpson*, 2006]

$$\frac{\partial h}{\partial t} = \kappa \frac{\partial^2 h}{\partial x^2} \tag{3.4}$$

where κ is the coefficient of diffusivity and h is the topography. After the surface is modified by diffusion, all markers above and below the new topographic surface are reassigned material properties of air and rock, respectively. Calculations are run with relatively low values of κ (10^{-8}-10^{-10} m^2/s), which preserves much of the original faulted topography but adequately smoothes out the unrealistic sharp or overhanging features.

The following boundary conditions are used to simulate a contractional wedge (Figure 3.1). The right vertical side of the 2-D model domain is free-slip and imposes the wedge contraction with a leftward (-x) uniform velocity of V_x=-10 mm/yr. The bottom of the model is a no-slip boundary subject to a leftward tangential velocity equivalent to the rate of horizontal contraction. The left hand side of the model domain acts as the wedge backstop and is a rigid, no-slip boundary whereas the top boundary, which corresponds to the top of the sticky air layer, is free-slip and open with zero shear or normal traction so

the material can freely flow in and out of the model domain. We vary the model width and height to ensure the growing wedge topography does not exit the top of the model domain and to minimize right-hand-side boundary affects. For weak bases (e.g. ϕ_b = 5°), the wedge evolves to be thin and wide. In contrast, the strong base models (e.g. ϕ_b = 20°), evolve to be thick and narrow. Recalling that the sediment and décollement layer thicknesses remain constant, the differences in model domain height are taken up by the sticky air layer. Finite difference grid dimensions are 250 m × 250 m and 125 m × 125 m for the coarse and fine models, respectively.

3.4 Numerical Model Results

3.4.1 General Wedge Evolution

The evolution of the numerical wedges begins with the formation of dipping bands of concentrated shear ("thrust faults") near the left-hand-side of the model domain and sequential outward migration of deformation as the models evolve. Figure 3.1 shows an example of this evolution for a simulation with a weak décollement (ϕ_b = 10°). When shear bands initiate, they typically form conjugate, v-shaped pairs that intersect the basal décollement in the same location and form pop-up structures. Shortly after their formation, the forethrusts (verging towards the right-hand-side of the model domain and dipping towards the backstop) become the lower angle of the fault pairs as they typically rotate while accumulating more plastic strain than the backthrusts (verging towards the backstop). This behavior is apparent in all of the model wedges where the initially horizontal décollement material has been advected up in to the sedimentary pile almost

exclusively along the forethrusts (Figures 3.1 and 3.2). Thrusts become back-tilted and rotated as slip preferentially accumulates on a few structures. This behavior is apparent between the backstop and the second forethrust in Figure 3.1 where the intervening fault block has been uplifted and internal faults back-tilted by 6 Myr.

The formation of new v-shaped thrust pairs migrates outwards and away from the backstop, resulting in wedge widening. All the while, fault-bounded topography increases as the portion of the wedge behind the frontal thrust is pushed backwards and up the footwalls of the most active forethrusts. Active deformation occurs as the new frontal thrusts accumulate slip and are temporarily abandoned as deformation migrates to the wedge interior. This pattern repeats itself throughout the evolution of a model wedge and will be discussed in Section 4.4.

3.4.2 Wedge Taper Angles

Figure 3.2 shows a suite of numerical models with different basal coefficients of friction (ϕ_b) after ~10 Myr of contraction. Model wedge surfaces become progressively steeper with increasing ϕ_b. This observation adheres to critical taper theory, which predicts that the wedge taper angle ($\alpha+\beta$) should increase with increasing coefficient of basal friction, μ_b, according to the fundamental critical taper equation [*Dahlen*, 1990]

$$\alpha+\beta=\left(\frac{1-\sin\phi}{1+\sin\phi}\right)\left(\beta+\mu_b\right) \tag{3.5}$$

where α and β are the surface and basal slopes, respectively, and ϕ is the internal friction angle, and μ_b=tanϕ_b. Our model décollements are horizontal (β=0°) so any changes in friction are solely reflected by a change in the wedge surface slope.

Figure 3.3 shows the evolution of the wedge surface slope for the models in Figure 3.2 and a comparison to theoretical α values determined from eq. (4.5) [e.g. *Simpson*, 2011]. Model surface slopes are computed by performing a linear least-squares fit to the model topography between the backstop and the wedge front every 5 time steps (~62.5 kyr). Results show that after an initial equilibration phase of ~1 Myr the wedges achieve surface tapers that are approximately constant for the duration of the model runs with short-period fluctuations due to alternating phases of wedge widening and thickening. The initial equilibration phase in our models was previously recognized by *Simpson* [2011]. The prediction of a constant surface slope adheres to one of the primary posits of critical Coulomb wedge theory [e.g. *Dahlen*, 1990; *Davis et al.*, 1983]. However, the model slopes are consistently slightly greater than the critical taper theoretical values. The stronger the base the larger the deviation. For example, in our ϕ_b=5° case the mean model surface slope value of 2.0±0.5° is 0.3° greater than the theoretical value of 1.7°. In our ϕ_b=20° case the mean model value of 8.8±1.2° is 1.5° greater than the theoretical value of 7.3°.

3.4.3 Active Surface Faulting

The aforementioned cyclic behavior of wedge widening and thickening is also expressed as time-dependent activity of shear-bands at the model surface. We characterize

this activity to draw analogies to the distribution of wedge faulting and seismic activity in the real world. The location of actively slipping faults is tracked by identifying focused zones of elevated strain at the surface and plotting this location as the normalized distance from the backstop during a time interval when one v-shaped thrust block is at the wedge front (Figure 3.4). Thus, surface faulting associated with the forward-verging wedge-front fault is assigned a value of 1. Two time steps separated by ~0.5 Myr illustrate the variability of observed surface faulting during this interval (Figures 3.4 a and b). The conjugate faults readily apparent in Figure 3.4(b) first form at time, $t \sim 6$ Myr and occupy the wedge-front position until $t \sim 8.25$ Myr when a new set of faults form at a greater distance from the backstop. This time interval represents a period of wedge thickening during which the location of the wedge front remains approximately constant and surface faulting is distributed across the wedge. The broad distribution of faulting is apparent in Figure 3.4(c). From $t \sim 6$-6.25 Myr surface faulting occurs primarily at the wedge front in association with the wedge-front conjugate faults. From $t \sim 6.25$-7.25 Myr almost no surface faulting occurs at the wedge front. Rather, internal thrusts are active. Figure 3.4(a) shows an example of this behavior at $t = 7.01$ Myr when the frontal structure is inactive and three thrusts located in the central portion of the wedge are slipping at the surface and additional buried thrusts are slipping at distances of 10 and 25 km from the backstop. From $t \sim 7.25$-8.25 Myr this pattern reverses and surface faulting once again becomes localized at the wedge front. Figure 3.4(b) shows an example of this behavior at $t = 7.48$ when active thrusting occurs on the wedge-front conjugate faults only and no internal deformation is recorded.

A histogram of the lateral distribution of surface faulting reveals that for the ~2 Myr encompassed by Figure 3.4, surface deformation is nearly evenly distributed across 5-6 conjugate thrust pairs that bound the roughly evenly spaced topographic highs across the wedge (Figure 3.4d). A second histogram showing the lateral distribution of surface faulting for the entire ~10 Myr model run reveals a slightly different yet complimentary pattern. Approximately 25% of the surface faulting occurs at the wedge front and the remaining ~75% is in the wedge interior. The two histograms for this particular model run characterizes the general distribution of surface faulting for all of our model calculations. Neither histogram, however, reflects the deformation associated with active buried thrusts (Figure 3.4). Later we discuss these results in the context of interpreting documented patterns of internal wedge faulting and wedge earthquakes.

3.4.4 Propagation of the Wedge Front

The evolution of the width of the wedges for each of the five basal friction values is illustrated by a plot of the position of the wedge-front surface fault as a function of time [e.g. *Hoth et al.*, 2007b; *Mary et al.*, 2013a; *Ruh et al.*, 2012] (Figure 3.5). The positive slopes of the plots indicate an overall increase in the distance between the backstop and the wedge-front fault with time. In detail the data are characterized by a stair-stepped pattern representative of incremental wedge widening due to jumps in the position of the wedge-front fault as new thrusts form outboard of the previous thrusts, followed by a time period during which the wedge front remains approximately stationary and deformation is

broadly distributed. The height of the steps in Figure 3.5 corresponds to the wedge-front-thrust jump distance, d_f. The flat portions of the curve represent the duration for which each new wedge-front thrust occupies the frontal position (prior to the formation of the next frontal thrust), t_f. Each flat portion has a gentle negative slope indicating that the frontal thrusts move a small distance towards the backstop due to wedge shortening and thickening associated with internal thrust faulting. Subtle variations in the slope of the flats indicate more or less internal shortening. For example, for ϕ_b=15° (Figure 3.5), a steeper slope for the time interval t = 8.3-9.8 Myr indicates more internal shortening/thickening than for other frontal thrusts.

We compute d_f and t_f for the five décollement friction values and find that wedges with weak décollements have longer average jump distances than those with stronger décollements. In contrast, we find no systematic variation in t_f with respect to ϕ_d; the average life span of a frontal thrust in all of our models is 0.86±0.30 Myr. However, the mean values are somewhat misleading and the standard deviations must be considered. For example, the ϕ_b=20° case has the longest average t_f of 1.01 Myr but the standard deviation of 0.96 Myr indicates t_f varies substantially.

In addition to the increase in α, our models also exhibit a general decrease in wedge width (W) with increasing ϕ_b where W is measured between the backstop and the location of the wedge-front thrust fault (Figure 3.2). For example, after ~10 Myr W for the ϕ_b=5° and ϕ_b=20° cases is ~135 km and ~65 km, respectively. Wedge theory provides a simple

explanation for the variation in total width versus time based on the premise that the flux of incoming sediments (HV_xt) balances the growth of the volume of the wedge above the height of the initially flat sediment layer. Preservation of a constant taper angle (α) leads to the flux balance equation [*Dahlen*, 1990]

$$W = \left[\frac{2HV_x t}{\tan(\alpha + \beta)} \right]^{1/2}. \tag{3.6}$$

The relationship shows that W decreases with an increase in taper angle. Further, since eq. (4.5) relates taper angle to wedge friction, the relationship above indicates that wedges with lower ϕ_b will be wider than those with higher ϕ_b.

The model data shown in Figure 3.5 reflect the general decrease in wedge width with increasing ϕ_b. The distance from the backstop to the wedge front at 10 Myr decreases with increasing ϕ_b and a best-fit line through the data would reveal a decrease in wedge-front propagation rate with increasing ϕ_b. However, the wedge front does not propagate outwards linearly with time but rather generally widens more rapidly during the initial stages of wedge development and W is best described by a square root of time $\sqrt{t}$ dependence, which is also predicted by the mass balance flux relationship (Equation 4.6). This behavior is readily apparent in the ϕ_b=5° case where the first 5 Myr of the model is characterized by numerous jumps in the wedge-front position but both the frequency of jumps decreases and t_f increases from 5-10 Myr. The red curves in Figure 3.5 show the best-fit to the wedge models and associated 95% confidence intervals. Despite the general $\sqrt{t}$ form of the wedge-front propagation curves, our numerical models are consistently

narrower than the theoretical values. This discrepancy is illustrated by the blue curves in Figure 3.5, which are based on eq. (4.6) and the mean model wedge α's for the post-1 Myr portion of the slope evolution curves in Figure 3.3. The difference between model and theory is most pronounced for the ϕ_b=5° case although the agreement improves with increasing ϕ_b.

3.4.5 Top-down Thrust Formation

In general, new frontal thrusts are predicted to nucleate near the surface and lengthen down-dip until they intersect the décollement (Figure 3.6). This top-down thrust propagation has also been observed in other numerical wedge models [e.g. *Del Castello and Cooke*, 2007; *Hardy et al.*, 2009; *Morgan*, 2015; *Simpson*, 2011].

Before a new frontal thrust forms all of the shortening of the wedge is occurring between the active frontal thrust and the backstop (Figure 3.6b). To track plastic failure we compute a failure ratio where the differential stress (σ_3-σ_1) is a large fraction of the differential yield stress. Specifically, any material within 5 MPa of the yield stress envelope is assigned a failure ratio of 1 [e.g. *Simpson*, 2011] (Figure 3.6). Just prior to the formation of a new frontal thrust (e.g. at 2.026 and 2.1667 Myr in Figure 3.6 b and c) a zone of failure develops near the surface, beyond the frontal fault, where the wedge material approaches Mohr-Coulomb failure. The zone broadens, and a short shear band forms and begins to propagate down dip. Maximum compressive stress (σ_3) orientations remain approximately horizontal in the vicinity of the new shear band.

As the new shear band develops, slip on the decollement is seen to extend well beyond the currently active frontal thrust (t = 2.167 Myr; Figure 3.6c). Slip on the newly extended decollement indicates that the block of sediment material above it is moving toward the backstop slower than the convergence rate. Hence the wedge material is shortening horizontally, and this is accommodated on the incipient thrust fault. The new shear band forms at or near the surface and progressively lengthens in the down-dip direction toward the décollement.

The angle of the shear-band relative to the maximum principal compressive stress orientation (σ_3) is confirmed to be near the Arthur angle of 45° – $\phi/4$ [*Buiter*, 2012; *Kaus*, 2010; *Ruh et al.*, 2012] or ~40° (Figure 3.6). The dip of σ_3 is nearly horizontal near the surface and becomes increasingly tilted toward the right hand side of the model domain with depth. Consequently the orientation of the new shear band changes to lower angles as it lengthens and propagates downward typically resulting in a listric thrust fault geometry.

When the new thrust fault meets the décollement, slip on the décollement ultimately ceases beyond the intersection location (t = 2.2136 Myr; Figure 3.6e) and the situation returns to the state illustrated by Figure 3.6b with shortening of the wedge occurring between the active frontal thrust and the backstop until the next frontal thrust begins to form at ~2.5 Myr. For the high-resolution model run (dx=dy=125 m) shown in Figure 3.6 the complete cycle from prior to the nucleation of a new frontal thrust to linkage of the new

thrust to the décollement takes ~0.2 Myr. This time scale is typical of the models and is several times shorter than t_f (e.g. Section 4.4).

3.4.6 Stress Analysis and Cause of Top-down Propagation

To better determine the cause of the top-down propagation we analyze the state of stress in the sediment layer in front of the wedge (Figure 3.7). Far from the deformation front, near the right hand side of the model domain, normal (σ_{xx}) stress is near lithostatic and shear (σ_{xz}) stress is negligible with slightly negative σ_{xz} values near the base associated with the imposed tangential velocity boundary condition. Approaching the deformation front, however, the stress state is seen to change. For the high-resolution ϕ_b=15° model case shown in Figure 3.7 both σ_{xx} and σ_{xz} decrease (i.e. become more compressive) ~60 km from the backstop. Contours of σ_{xx} are inclined and dip towards the décollement indicating σ_{xx} decreases both towards the backstop and with depth. Contours of σ_{xz} are roughly horizontal with σ_{xz} reaching a maximum value roughly equivalent to $\rho g H \mu_b$ along the décollement.

The stress state described above occurs over a portion of the model extending approximately from the topographic step associated with the frontal thrust fault out towards the right-hand-side of the model domain over a characteristic length scale L that roughly corresponds to the region where σ_{xz} is low and nearly uniform along the base of the wedge. For example, L in Figure 3.7 is the region located between 30 and 60 km from

the backstop. We find that L decreases with increase ϕ_b for the five décollement friction cases (Figure 3.8).

The cause for this stress state is examined with a simple model of a homogeneous elastic volume with rectangular cross-section having height H and width L (Figure 3.7a). Our elastic model boundary conditions include stress free upper and right surfaces, uniform shear stress τ_b acting to the left along the base, and a counteracting normal stress σ_{xx} pushing to the right on the left side of the model, which comes from the simple force balance equation

$$\int_0^L \tau_b \, dx = \int_0^H -\sigma_{xx} \, dz. \tag{3.7}$$

In other words, to maintain equilibrium, basal shear stress τ_b integrated over a width L is equal and opposite to the integrated normal traction σ_{xx} along the left hand side of the wedge with height H. The right hand side of the equation is the horizontal force at the wedge front pushing to the right that balances the shear force along the bottom of the wedge shearing to the left. Note that for this simple elastic model the x axis is reversed (pointing towards the backstop) for algebraic convenience.

Using the standard "stress formulation", the equations of continuity and conservation of momentum are expressed as a 2-D biharmonic equation of the Airy stress function ψ [*Timoshenko and Goodier*, 1970],

$$\nabla^4 \psi = 0. \tag{3.8}$$

The Airy stress function relates to stress according to

$$\sigma_{xx} = \frac{\partial^2 \psi}{\partial z^2} - \rho g z, \quad \sigma_{zz} = \frac{\partial^2 \psi}{\partial x^2} - \rho g z, \quad \text{and} \quad \sigma_{xz} = -\frac{\partial^2 \psi}{\partial x \partial z}. \tag{3.9}$$

A simple set of solutions to eq. (4.8) is represented by the third order polynomial

$$\psi = \frac{A_o}{3} x^3 + \frac{A_1}{2} x^2 z + \frac{A_2}{2} x z^2 + \frac{A_3}{3} z^3. \tag{3.10}$$

The boundary conditions are met with $A_0 = A_1 = A_2 = 0$ and $A_3 = -\tau_b/2H$; and the corresponding stress solutions are

$$\sigma_{xx} = -\frac{\tau_b}{H} x - \rho g z \quad \sigma_{zz} = -\rho g z \quad \sigma_{xz} = \frac{\tau_b}{H} z \tag{3.11}$$

where

$$\tau_b = \rho g H \mu_b \quad and \quad \mu_b = \tan \phi_b.$$

Figure 3.7 d and f illustrates the solutions given by eq. (3.11) for comparison with the corresponding solutions produced by the numerical model. The color contour plots exhibit first-order similarities including the decrease in σ_{xx} and σ_{xz} towards the deformation front and décollement, respectively. The SiStER solution shows short-wavelength structure that differs from the Airy stress solution and is associated with the shear bands at the wedge front and the finite thickness décollement, which are not addressed by the simple elastic model. Stress profiles confirm that σ_{xx}, σ_{zz}, and σ_{xz} are quite similar for the SiStER and Airy

models with departures present near the surface, base, and where the SiStER model is experiencing plastic failure along the shear bands (e.g. Figure 3.7g).

The controls on the size of L can be explained by the following force balance arguments. In the more realistic SiStER model, the compressive horizontal stresses below the frontal thrust are well approximated by the yield criterion [*Dahlen*, 1990]

$$\sigma_{xx} \approx -\left(\frac{1+\sin\phi}{1-\sin\phi}\right)\rho g H. \tag{3.12}$$

Substituting eq. (3.12) into the right-hand side of eq. (3.7) and solving for L yields

$$L = \left(\frac{1+\sin\phi}{1-\sin\phi}\right)\left(\frac{\rho g H^2}{2\tau_b}\right). \tag{3.13}$$

This equation shows that an increase in the basal shear stress τ_b, which is a function ϕ_b, requires a corresponding decrease in L. This relationship is confirmed in our modeling results where the size of the region over which the basal shear stress is approximately constant decreases with increasing ϕ_b (Figure 3.8). A quantitative comparison of L computed using eq. (3.13) and the SiStER model results for different basal friction cases shows excellent agreement (Figure 3.9).

From the above analysis, the cause for the top-down propagation becomes evident. Predicted profiles of differential stress σ_3-σ_1 for both the simple elastic "Airy" model as well as the SiStER model cross the failure stresses near the surface first (Figure 3.7h). More specifically, for the profile furthest from the wedge front, the differential yield stress

envelope is much closer to the observed differential stresses near the surface than deeper in the wedge. Closer to the wedge front, the middle profile shows that both the theoretical and model differential stress profiles cross the yield stress envelopes at shallow depths (<500 m). Thus, the zone above this crossover is experiencing plastic failure resulting in the shallow initiation of new wedge-front thrusts. Closest to the backstop, the differential stresses cross the yield envelopes at a depth of 2-3 km, which reflects the deeper portion of the frontal thrust and promotes the downward fault propagation.

3.5 Discussion

Critical taper theory relates the dips of a wedge surface and base to the internal and basal material properties. SiStER wedges have surface slopes that vary with basal friction, are broadly consistent with critical taper theoretical predications, but are consistently higher than the theory predicts (Figure 3.3). Previous authors have noted similar slope discrepancies between models and theory, attributing the differences to factors such as the influence of surface processes, variations in the wedge mechanical strength, and the way in which the surface slope is measured [*Simpson*, 2011; *Stockmal et al.*, 2007]. One potential explanation for the difference between theory and model slopes relates to cohesion, which is not included in the wedge theory taper equation, and has been shown to increase wedge tapers in some finite element models [e.g. *Ellis et al.*, 2004]. However, introduction of cohesion in the theory lowers both the wedge-front taper resulting in a concave wedge surface [*Dahlen et al.*, 1984] and the overall taper angle [*Dahlen and Suppe*, 1988]. While we do not propose a new explanation for the observed differences, we emphasize that they are

slight and that model slopes remain well within the stability field for critical wedges [*Dahlen*, 1984].

Wedge theory also predicts that wedges will strive to maintain a constant surface slope throughout their evolution. SiStER model wedges adhere to this premise in that after an initial equilibration phase, they achieve and maintain roughly constant surface slopes with minor fluctuations due to alternating phases of wedge-front and internal wedge deformation.

The theory also provides a solution for wedge width and propagation rate based on the balance between the volume flux of incoming sediments and the outward growth of the wedge surface with a critical taper angle (e.g. Equation 3.4). Our model wedges adhere to the prediction that wedge width increases with decreasing ϕ_b; the strong base cases yield significantly narrower wedges than the weak bases cases (Figure 3.2). SiStER model wedges also widen according to the $\sqrt{t}$ mass flux but are consistently narrower than the theoretical predictions.

In general, the SiStER wedges behave similarly to previous numerical modeling results [e.g. *Buiter*, 2012; *Buiter et al.*, 2006; *Ruh et al.*, 2012; *Selzer et al.*, 2007; *Simpson*, 2011; *Simpson*, 2009; *Stockmal et al.*, 2007], which provide detailed analyses of model wedge evolution, stress state, the affects of varying model parameters on the wedge geometry,

comparisons with real-world wedges, etc. We focus on model observations that have not been adequately addressed in the literature.

The first relates to the distribution of surface faulting during model wedge evolution. Once a few structures have formed in our SiStER wedges, surface faulting alternates between phases of thrusting at the wedge-front and primarily internally (Figure 3.4). This behavior is reminiscent of faulting observed in most active subaerial wedges. For example, across the southern Subandes of Bolivia, *Uba et al.* [2009] present evidence for widening of the wedge front fault system via the formation of a new frontal thrust at ~5 Ma followed by retreat of active deformation to internal wedge locations. At ~2 Ma the wedge widened again and the modern wedge-front fault system was established [*Uba et al.*, 2009; *Weiss et al.*, 2015]. However, based on a new GPS-derived velocity field combined with estimates of wedge thrust fault slip rates spanning a variety of timescales, *Weiss et al.* [in prep.] suggest the southern Subandes are experiencing a rejuvenated phase of internal deformation.

Examples of recent internal deformation also exist across the Himalayan wedge despite the general consensus that the majority of surface faulting including large historical earthquakes is currently associated with the Main Frontal Thrust (MFT) [*Kumar et al.*, 2010; *Lavé and Avouac*, 2000; *Sapkota et al.*, 2013]. For example, based on differences in erosion patterns, *Wobus et al.* [2005] find a previously unrecognized zone of active deformation located in the wedge interior ~100 km north of the MFT. More recently, the 2015 M_w 7.8 Ghorka earthquake ruptured a previously locked portion of the main basal

décollement but slip did not propagate to the Himalayan thrust front [*Avouac et al.*, 2015; *Elliott et al.*, 2016; *Lindsey et al.*, 2015]. Further, *Elliott et al.* [2016] show that although the vast majority of the slip was confined to the décollement, the event also surface-ruptured ~26 km of a minor splay located ~10 km north of the MFT. This is despite the notion that in general, the megathrust décollement rupture will preferentially propagate to the wedge toe rather than break upward along pre-existing, internal structures [*Hubbard et al.*, 2015]. The slip on active buried thrusts in the SiStER models (Figure 3.7) is reminiscent of a Ghorka-type style of deformation. Final examples include both the 1999 Chi-Chi, Taiwan (M_w 7.6) and 2008 Wenchuan, China (M_w 7.9) earthquakes, which ruptured internal wedge thrusts located ~15 km and ~200 km, respectively, from the wedge front [*Hubbard et al.*, 2010; *Kao and Chen*, 2000].

Our final point of discussion relates to down-dip fault propagation of the incipient frontal thrusts. On one hand, this prediction is counter to the commonly accepted notion that new frontal thrusts should nucleate from the décollement tip and propagate upwards [*Suppe and Medwedeff*, 1990]. Such reasoning is often used in kinematic models to explain field-based surface observations [e.g. *Allmendinger*, 1998; *Brandes and Tanner*, 2014; *Cardozo and Brandenburg*, 2014; *Erslev*, 1991; *Suppe and Medwedeff*, 1990].

On the other hand, top-down fault propagation is commonly observed in numerical wedges. Finite element models of *Panian and Wiltschko* [2004], for example, predict new shear bands to form at the surface near the "topographic inflection" formed by the previous

thrust, and then lengthen down-dip, towards the base. Using a boundary element method *Del Castello and Cooke* [2007] show that from a minimum work perspective it is mechanically more efficient to nucleate a new thrust at shallow depths rather than at the basal décollement. The thrust then may propagate downwards towards the weak base. Discrete element approaches also predict new thrusts that initiate at or near the surface and propagate down-dip rather than up from the basal décollement in [*Dean et al.*, 2013; *Hardy et al.*, 2009; *Morgan*, 2015]. Our SiStER and simple elastic model calculations predict the top-down behavior to occur because of two main factors: (1) near the surface the confining stress and hence brittle strength is lowest, and (2) the non-lithostatic differential stresses that build in front of the wedge do so equivalently at all depths. Thus the differential stresses exceed the yield stress near the surface first.

Observational evidence for top-down fault propagation in natural systems also exists [e.g. *McConnell et al.*, 1997; *Morley*, 1994]. For example, *McConnell et al.* [1997] show field evidence from the Appalachian Valley and Ridge province of faults with peak displacements near the surface (Figure 3.10) and propose a geometric model where fault growth can occur in both up- and down-dip directions. Evidence for cross-cutting thrust faults nucleating near the surface and/or midway through the sedimentary section - and definitely not near the décollement - is also present in seismic reflection data across the protothrust zones (PTZ) of the Oregon, Nankai, and Hikurangi margin submarine accretionary prisms [*Barnes et al.*, 2010; *MacKay*, 1995; *Orme et al.*, 2015] (Figure 3.10).

We hypothesize that the PTZ's are a manifestation of top-down thrusting and that they occur below the surface because the uppermost marine sediments are porous, weakly consolidated, and do not support brittle failure. A simple test of this hypothesis is provided by a SiStER model calculation that simulates a sediment section with a 1-km-thick, low-viscosity layer ($\nu=1\times10^{21}$) overlying a 3.5-km-thick brittle layer ($\nu=1\times10^{25}$). This model results in the intermittent formation of a zone of material near the Mohr-Coulomb failure envelope beyond the frontal thrust exclusively within the brittle layer (e.g. t = 2.24 Myr; Figure 3.11). The zone broadens as the model evolves and cross-cutting faults nucleate within the zone, which terminates at the interface between the shallow ductile-brittle transition (e.g. t = 2.34 Myr; Figure 3.11), and ultimately propagate down-dip to intersect the basal décollement (e.g. t = 2.39 Myr; Figure 3.11). The depth and nature of this incipient faulting resembles the PTZ's in front of submarine accretionary prisms (Figure 3.10). Also, in all of the models, the base of the sediment layer begins slipping prior to and in front of this incipient faulting (Figure 3.11), thus explaining the presence of a seismically reflective décollement below the proto-thrusts [e.g. *Barnes et al.*, 2010; *Moore et al.*, 1990; *Wang et al.*, 1994]. We agree with *Del Castello and Cooke* [2007] that top-down thrust formation and protothrust zones are difficult to detect in natural systems because most may initiate in the subsurface and are transient features.

3.6 Conclusions

We use SiStER, a two-dimensional, continuum mechanics-based, finite difference method with a visco-elasto-plastic rheology to investigate the spatiotemporal distribution

of deformation during orogenic wedge growth. The surface slopes of the model wedges are generally consistent with critical taper theory; after an initial equilibration phase they maintain a roughly constant angle that increases with increasing friction on the décollement. Model wedges widen via the episodic formation of new frontal thrusts according to the $\sqrt{t}$ relationship derived from the mass flux balance equation where wedge width increases with decreasing strength of the basal décollement. Model surface faulting patterns resemble episodes of internal deformation documented in active subaerial wedges and show that the majority (~75%) of surface faulting occurs in the wedge interior. Models predict wedge-front thrusts to nucleate at the surface and propagate down-dip to intersect the basal décollement. This behavior occurs because (1) near the surface the confining stress and hence brittle strength is lowest and (2) the non-lithostatic differential stress builds in front of the wedge uniformly at all depths. Consequently, the differential stress first exceeds the yield stress near the surface. The protothrust zones observed in high-resolution seismic reflection data from active submarine accretionary prisms may be real-world examples of this behavior. We infer that the termination of protothrust zones beneath the surface is a manifestation of the ductile-to-brittle transition between weakly consolidated material near the seafloor and brittle sediments below since the former cannot support faulting.

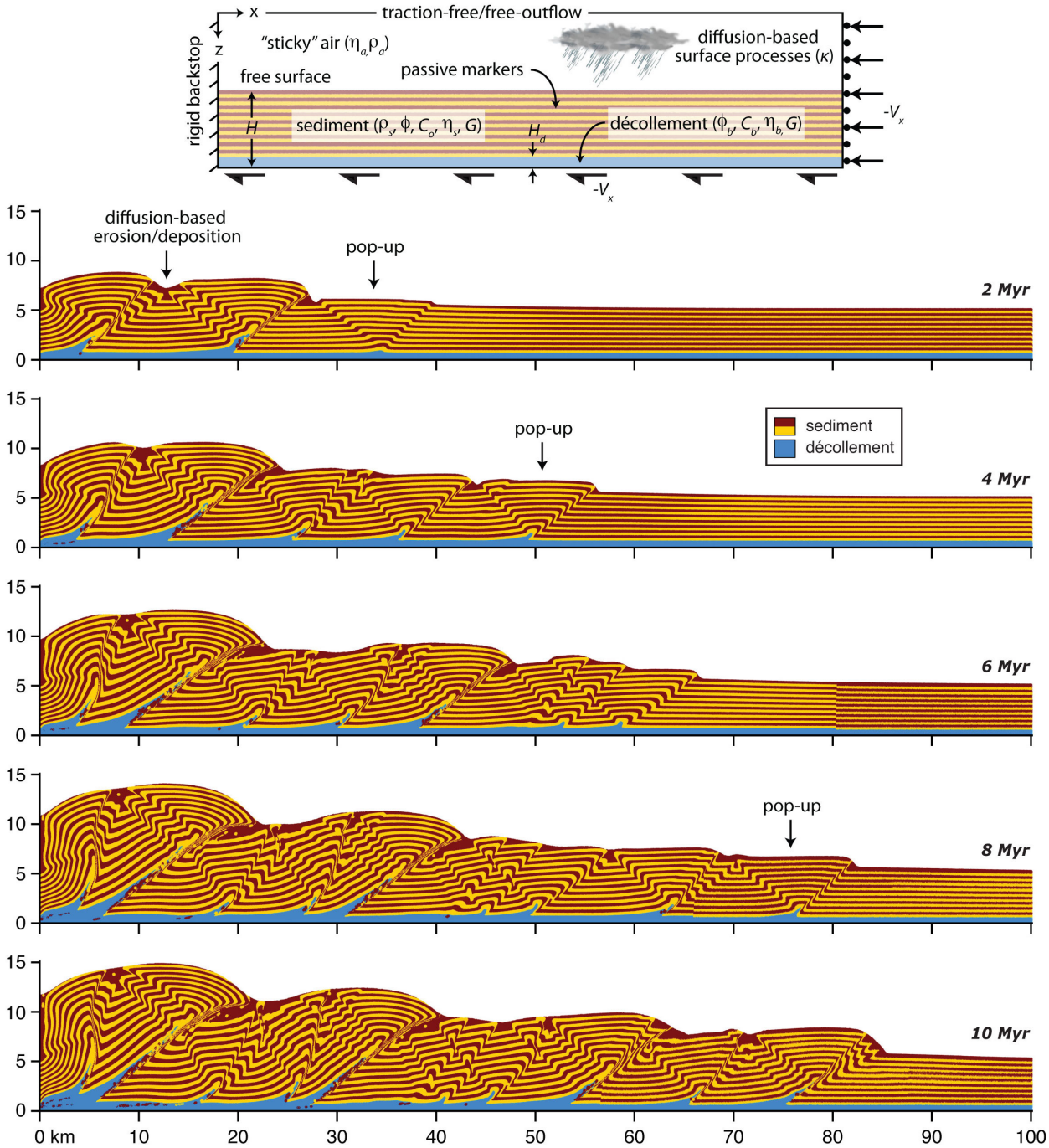

Figure 3.1 The top panel illustrates the boundary conditions for our numerical model. Beneath are panels showing the evolution of a representative SiStER orogenic wedge with 250x250 m grid cells shown at 2 Myr time steps. The strong, brittle sedimentary layer (ϕ=30°) contains passive yellow and brown markers to aid in visualizing accumulated deformation. The weak basal décollement (ϕ_b=10°) is blue. Diffusion-based surface processes ($\kappa=5\times10^{-9}$) simulate erosion/deposition.

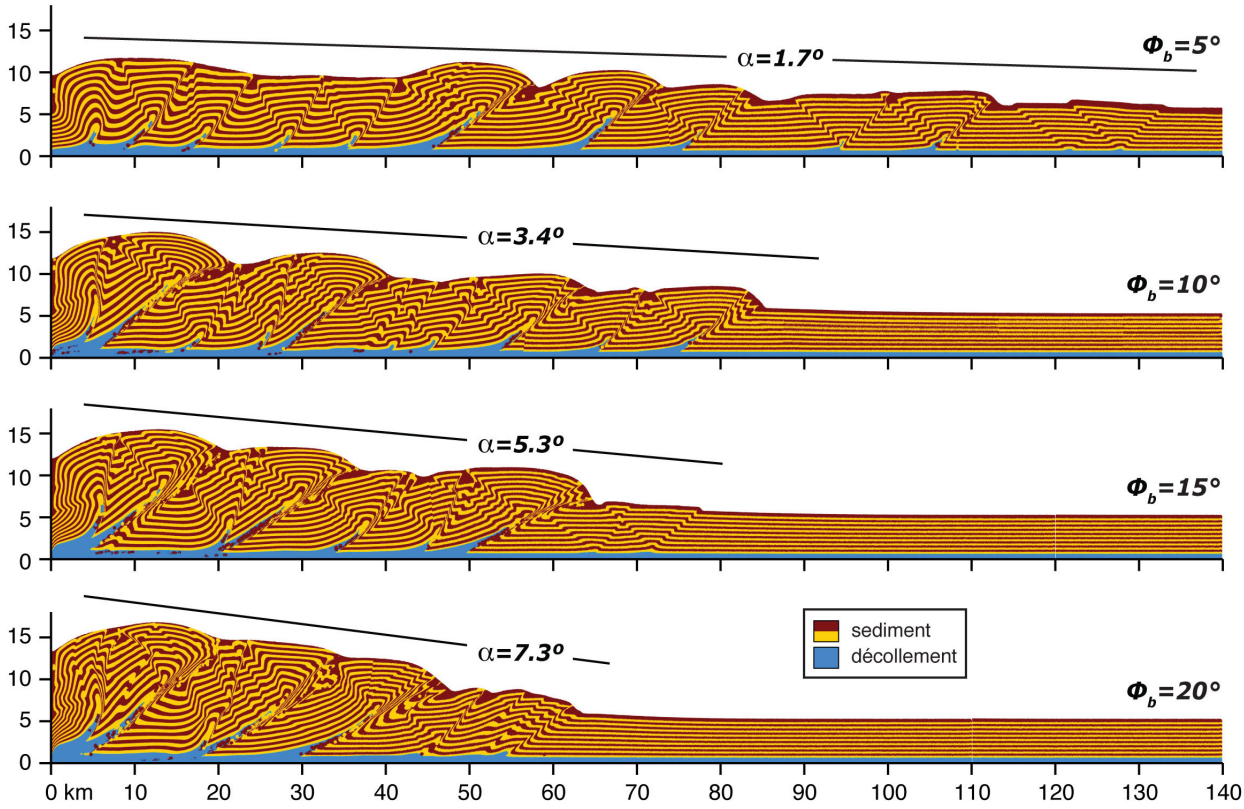

Figure 3.2 SiStER orogenic wedges with progressively increasing (top-to-bottom) basal décollement friction angles. The sedimentary layers in all models have the same friction angle (ϕ=30°). The theoretical surface slopes for cohesionless wedges [*Davis et al.,* 1983] are labeled and indicated with black lines above each of the model wedges.

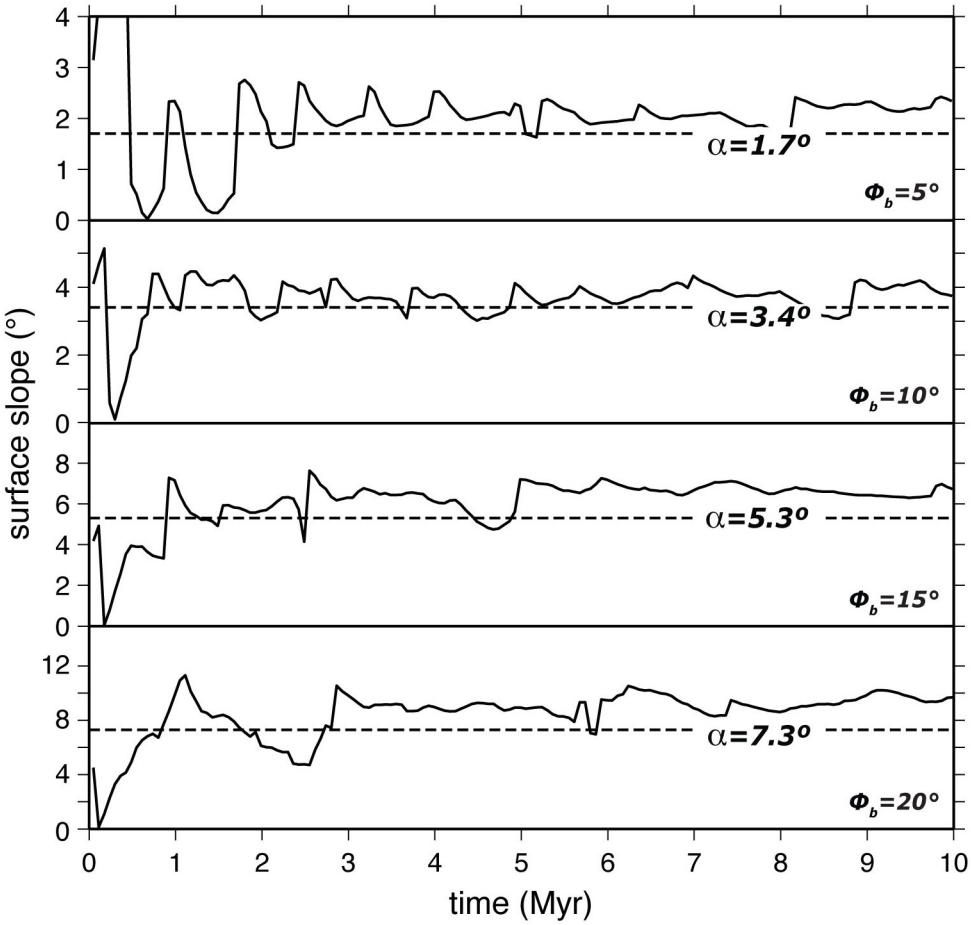

Figure 3.3 Evolution of the surface slopes for the model wedges shown in Figure 3.2. The slopes are those of the least-square linear regression to the topography for the active portion of the wedge every 5 time steps (~62.5 kyr). The dashed lines indicate the theoretical slopes for cohesionless critical wedges [*Davis et al.*, 1983]. After an initial equilibration phase of ~1 Myr the SiStER wedge surfaces achieve tapers that are slightly greater than the theoretical values but remain approximately constant with short-period fluctuations due to alternating phases of wedge widening/thickening.

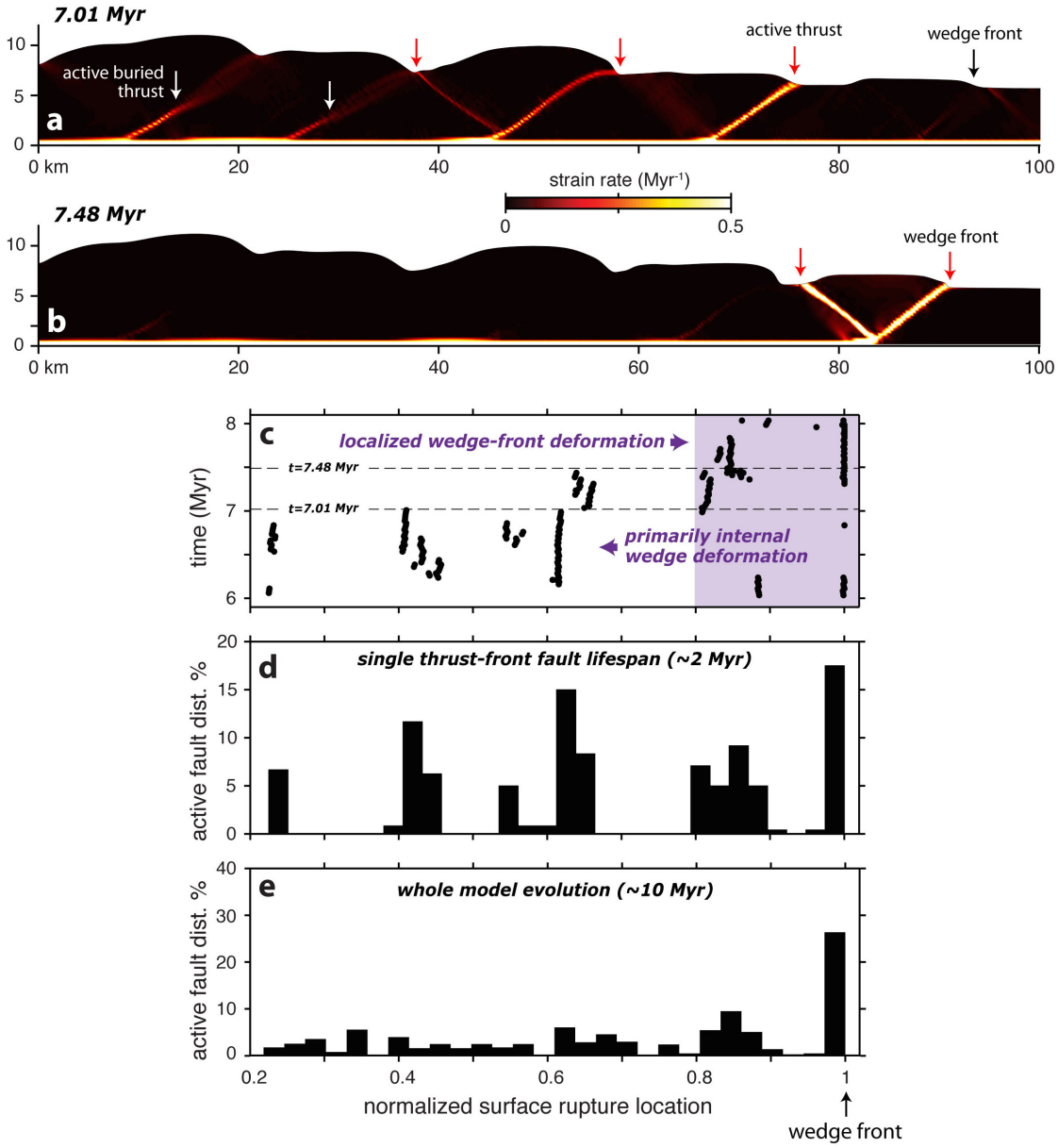

Figure 3.4 The location of surface faulting during SiStER wedge evolution (ϕ=30°; ϕ_b=05°; dx=dy=250 m; κ=5×10^{-9}). (a) and (b) Strain rates for two time steps separated by 0.47 Myr. (a) At 7.01 Myr active surface faulting occurs at internal wedge locations only (red arrows) and not at the wedge front. Additional thrusts near the back of the wedge are active but terminate midway through the sedimentary section (white arrows). (b) At 7.48 Myr active surface faulting is present only on the conjugate thrusts that bound a pop-up structure at the front of the wedge; no internal deformation is observed. (c) Dots show normalized location of surface faulting with respect to the wedge front for the time period that the frontal thrust shown in (a) and (b) remains at the front of the wedge. The dashed lines mark the times of the two top panels. The diagram reveals alternating cycles of surface thrusting at the wedge front and within the wedge. (d) Histogram of the normalized location of surface faulting during for the time period shown in (c) reveals that fault activity is evenly distributed across ~5 major structures located throughout the wedge. (e) Histogram of normalized fault location for the entire SiStER model (~10 Myr). For this particular run ~25% of the surface faulting occurs at the wedge front. The remaining ~75% of surface faulting is associated with internal wedge thrusts.

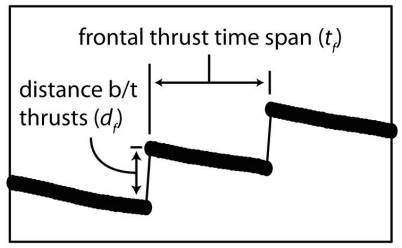

φ_b (°)	t_f (Myr)	d_f (Myr)
5	0.95±0.41	18.58±7.40
10	0.67±0.36	10.59±2.57
15	0.82±0.49	10.18±2.99
20	1.01±0.96	9.23±4.50

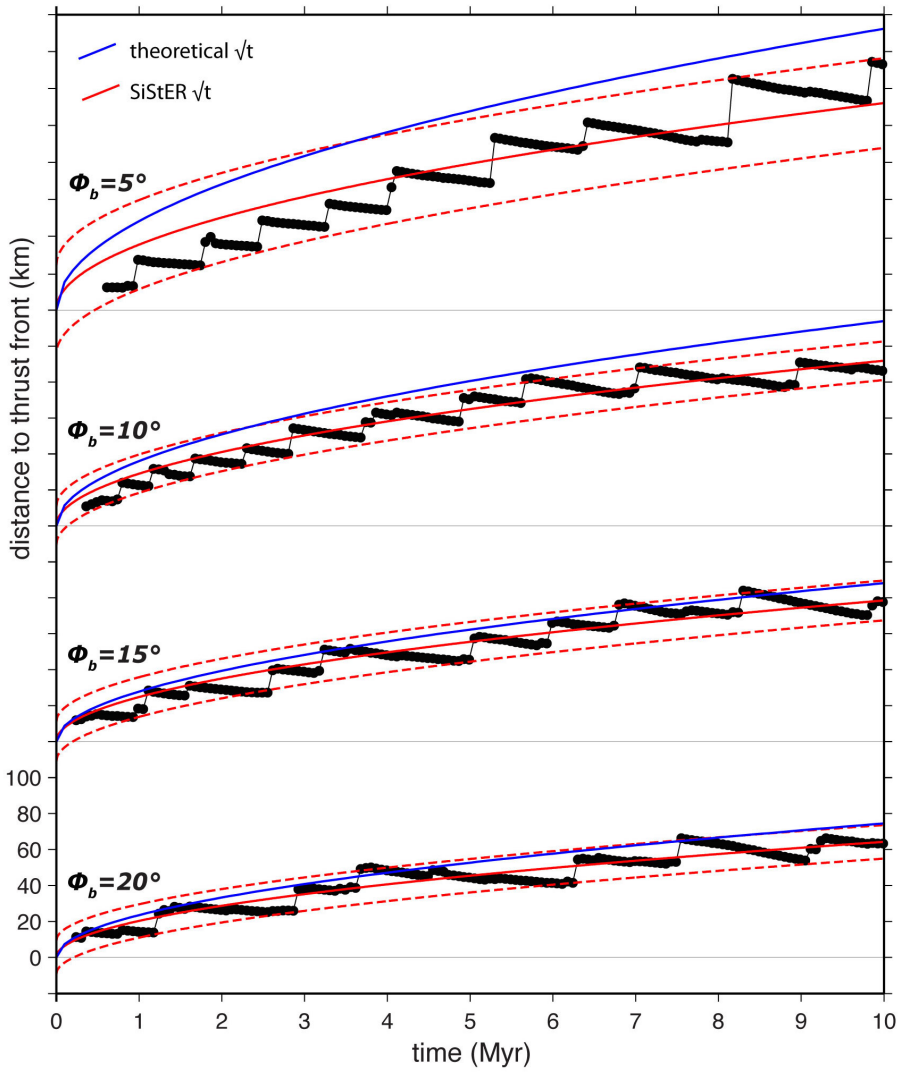

Figure 3.5 Wedge front propagation curves for the four model cases shown in Figure 3.2. Each point represents the position of the wedge front measured every 5th time step (~62.5 kyr). The best-fitting function of $\sqrt{t}$ and 95% confidence bounds are shown in red. The blue line is the theoretical curve from the conservation of mass eq. (3.6) with α from the post-1 Myr mean model slopes in Figure 3.3 and β=0°. The top panel illustrates our interpretation of the propagation rate curves [e.g. *Hoth et al.*, 2007b] where the steps correspond to the formation of a new wedge front thrust fault separated from the previous thrust by a distance d_f and the flat portion corresponding to the time span t_f that the thrust is at the wedge front. The gentle negative slopes reveal a steady migration of the wedge front thrusts towards the backstop as the system continually shortens.

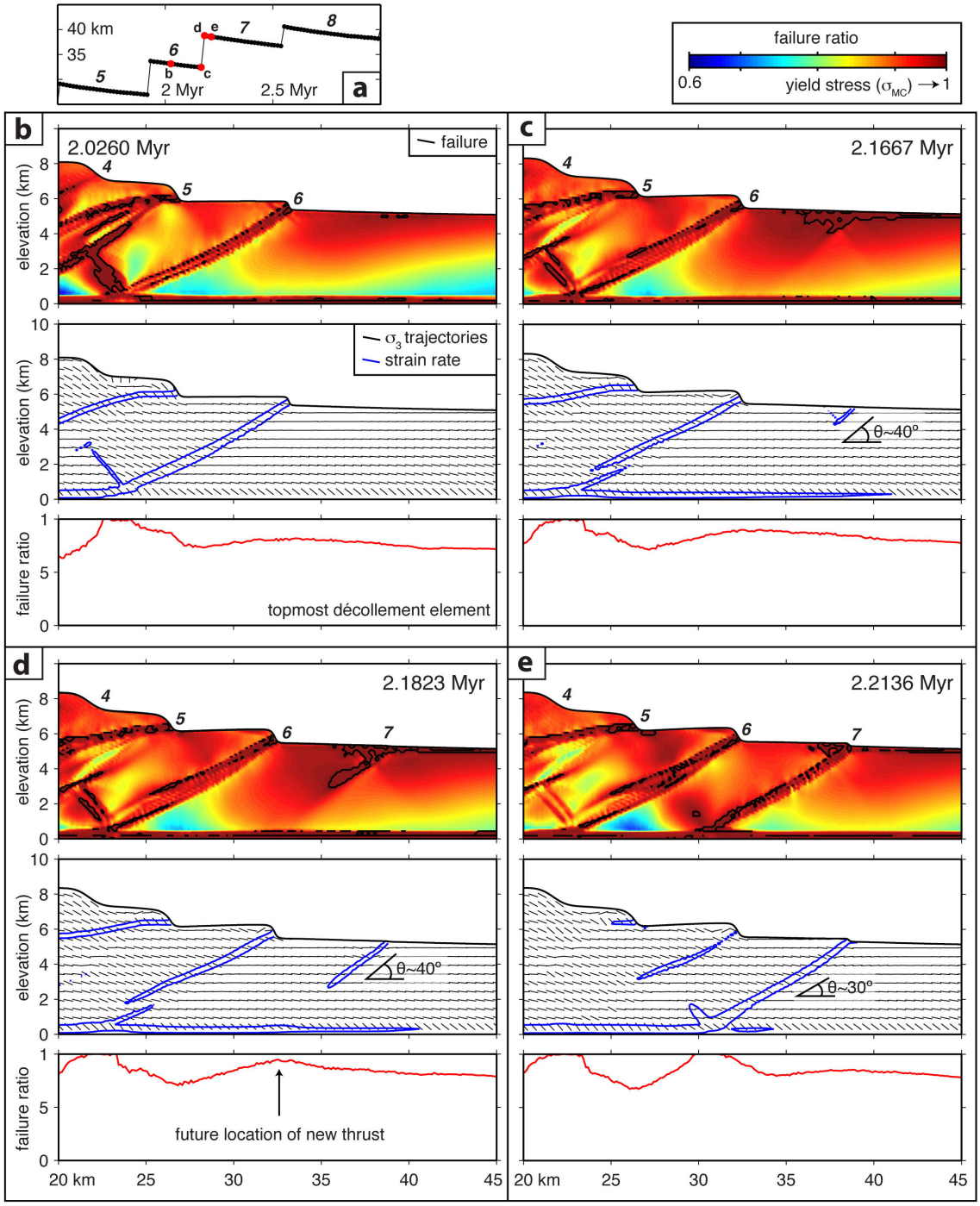

Figure 3.6 SiStER model snapshots showing the formation of a new frontal thrust for a high-resolution SiStER model run (ϕ=30°; ϕ_b=15°; dx=dy=125 m; κ=5×10^{-9}). (a) Wedge front propagation curve for the high-resolution model with each of the thrusts numbered and the time steps associated with the formation of a new frontal thrust labeled with red dots. (b - e) Time steps where the top panel shows the wedge failure ratio with black contours outlining regions with a ratio of 1. The middle panels show the orientations of the most compressive stress (σ_3) as black tick marks with contours of elevated strain rate. The bottom panels show the failure ratio along the top of the basal décollement.

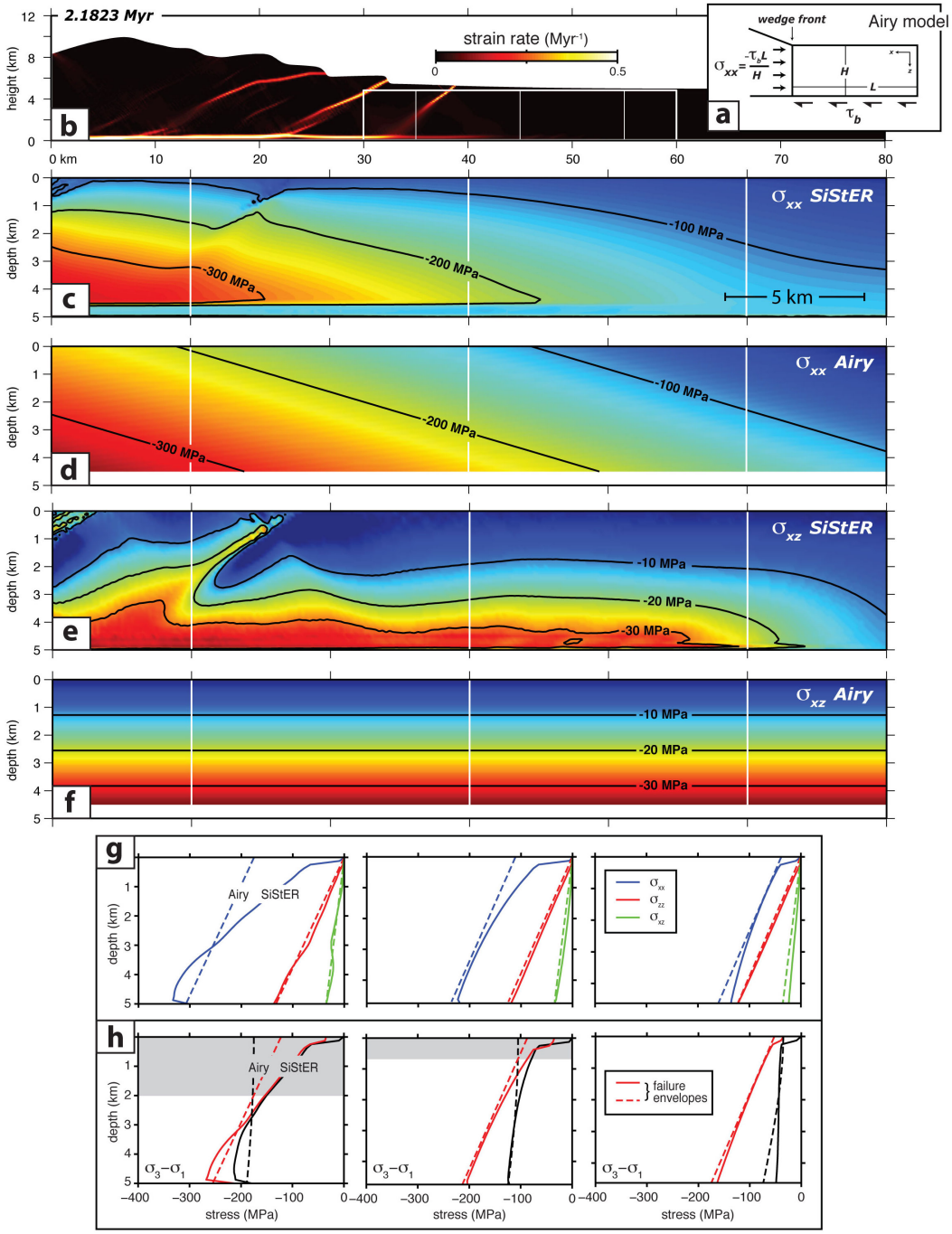

Figure 3.7 Analysis of the stress state in front of the wedge (here the SiStER model parameters are ϕ=30°; ϕ_b=15°; dx=dy=125 m; κ=5×10^{-9}). (a) Cartoon depicting the boundary conditions for the Airy stress analysis. (b) Strain rate just after the formation of a new frontal thrust (same time step as Figure 3.6d). The white box corresponds to the location of the color contour plots shown in panels c and e and the light vertical white lines within the box are the locations of the three stress profiles shown in panels g and h. Color contour plots show σ_{xx} and σ_{xz} for the SiStER (c and e) and Airy (d and f) models. (g and h) Profiles of the (g) stress components and (h) differential stresses and differential failure envelopes through our SiStER and Airy models. The gray shaded area in (h) mark the region where the Airy model predicts brittle failure.

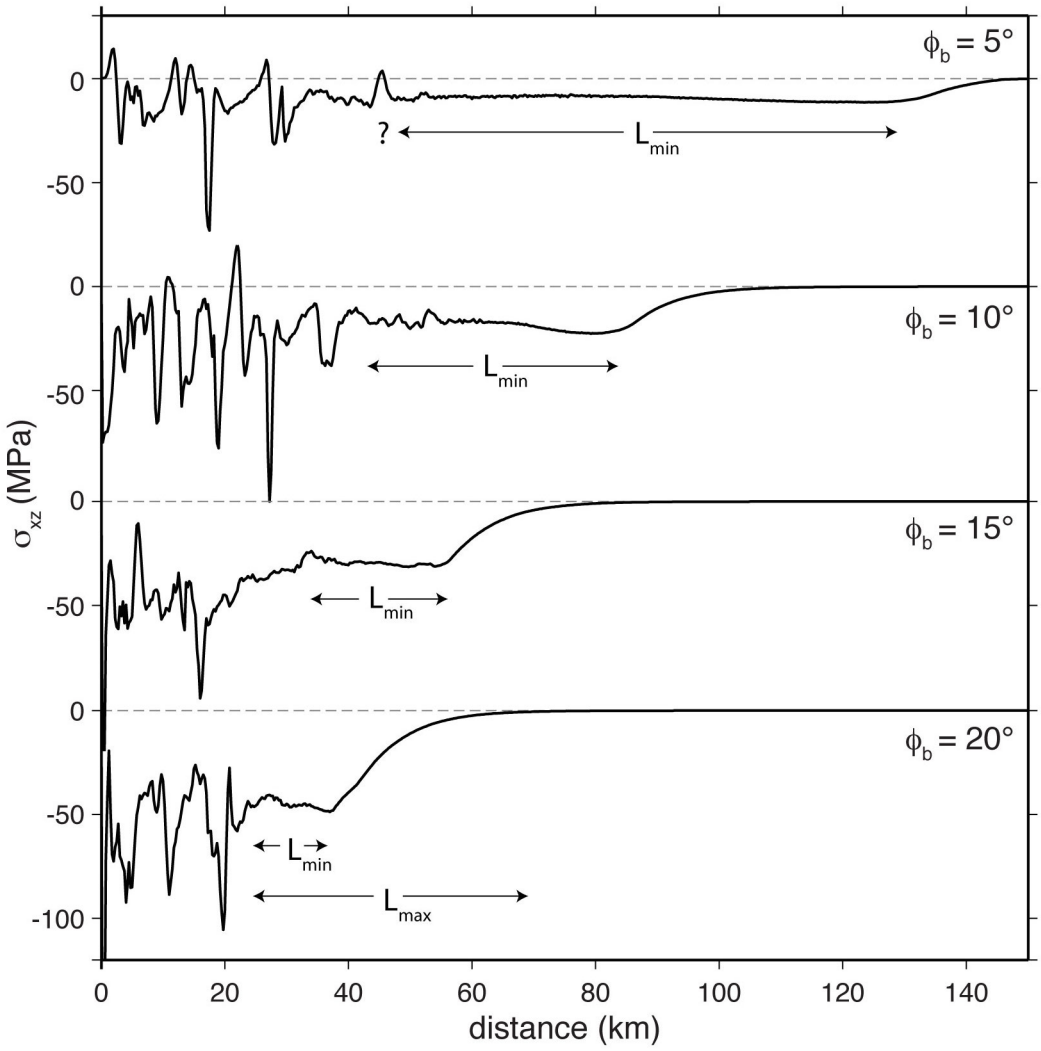

Figure 3.8 Shear stress (τ_b) along the base of model wedges with progressively increasing (top-to-bottom) basal décollement friction angle. L_{min} is the region where τ_b is approximately constant whereas L_{max} extends out to where τ_b is approximately zero.

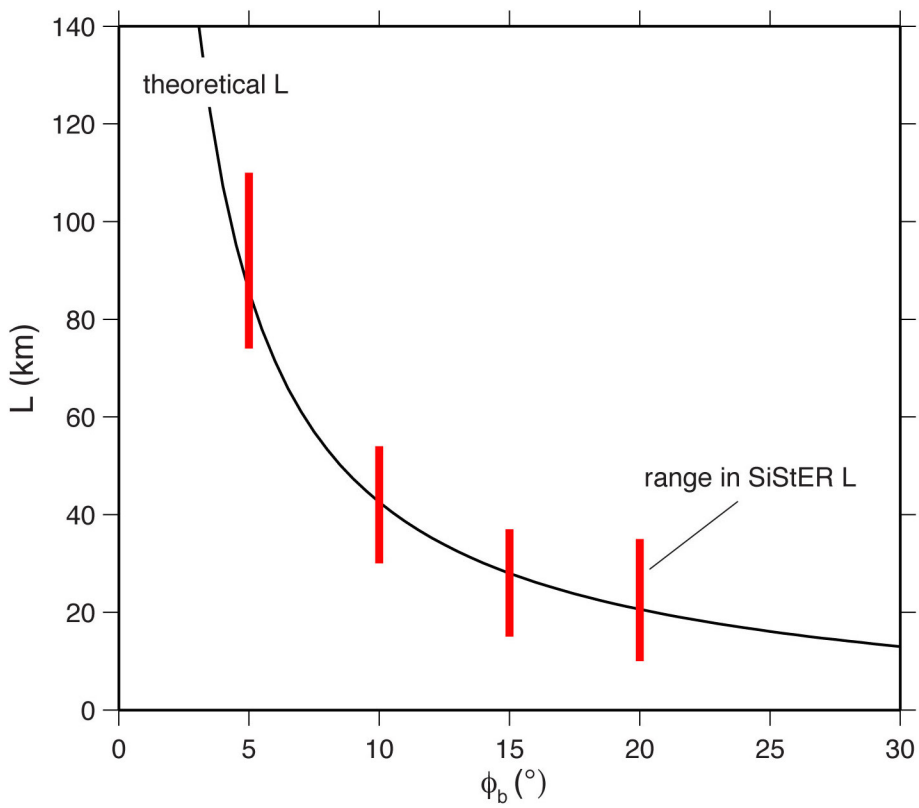

Figure 3.9 A comparison of L versus basal friction angle (ϕ_b) from the simple force balance argument in eq. (3.13) (black curve) compared to L measured from the SiStER models (red bars).

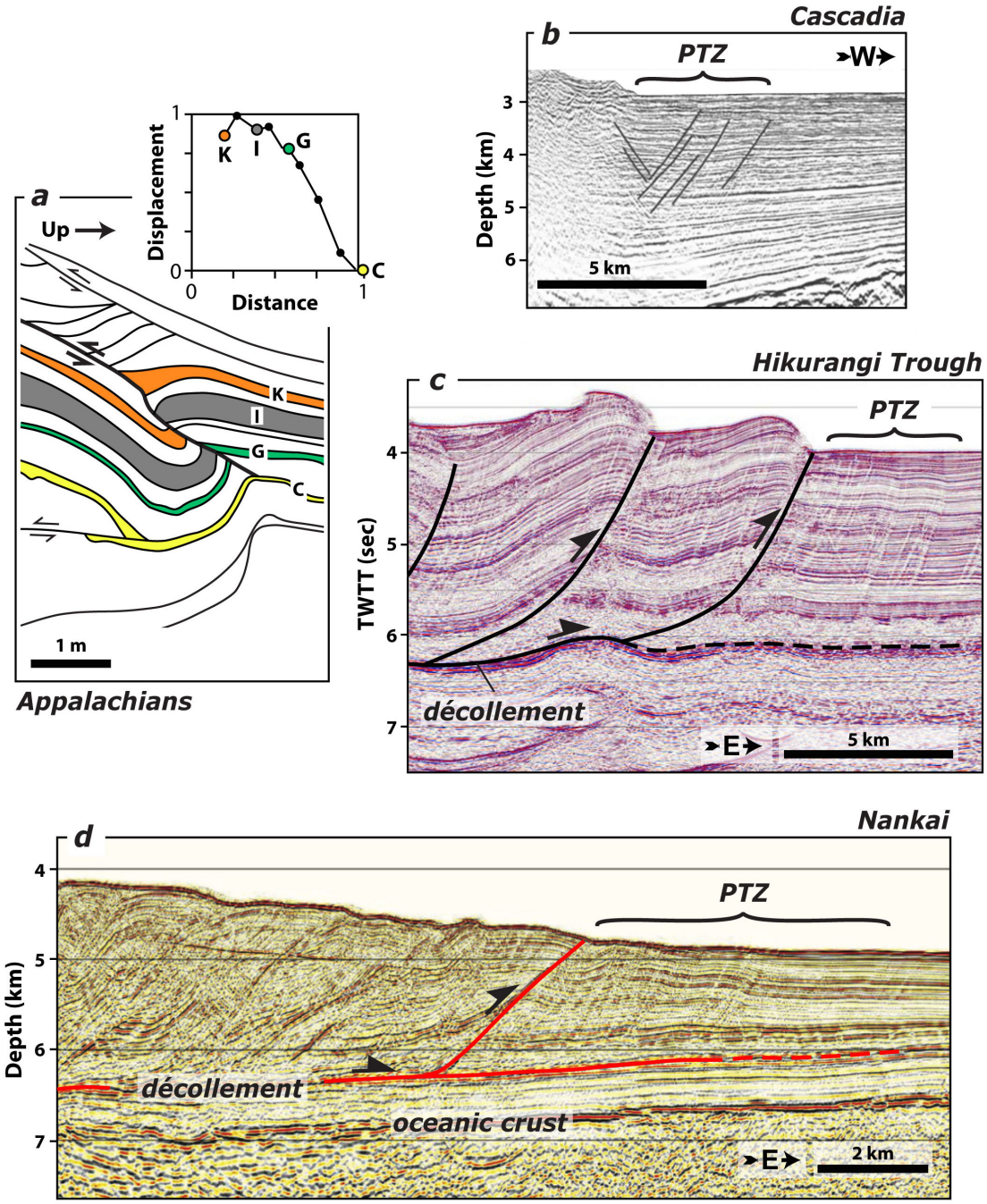

Figure 3.10 Examples from the literature of thrust faults forming at/near the surface. (a) Line drawing from the Appalachian Valley and Ridge province, an ancient fold-and-thrust belt, showing an outcropping thrust fault where measured displacement decreases down-section into the footwall syncline [redrawn from *McConnell et al.*, 1997]. (b) Depth-converted seismic sections from *MacKay* [1995] showing the protothrust zone (PTZ) in front of the Cascadia accretionary prism. (c) Seismic section across the Hikurangi subduction zone from *Barnes et al.* [2010] showing the PTZ developed beyond the main deformation front. (c) Seismic section from the Nankai Trough (Ashizuri Transect) showing the protothrust zone, which is defined by *Moore et al.* [1990] as a region of diffuse thickening, shortening, and porosity reduction that occurs prior to thrusting.

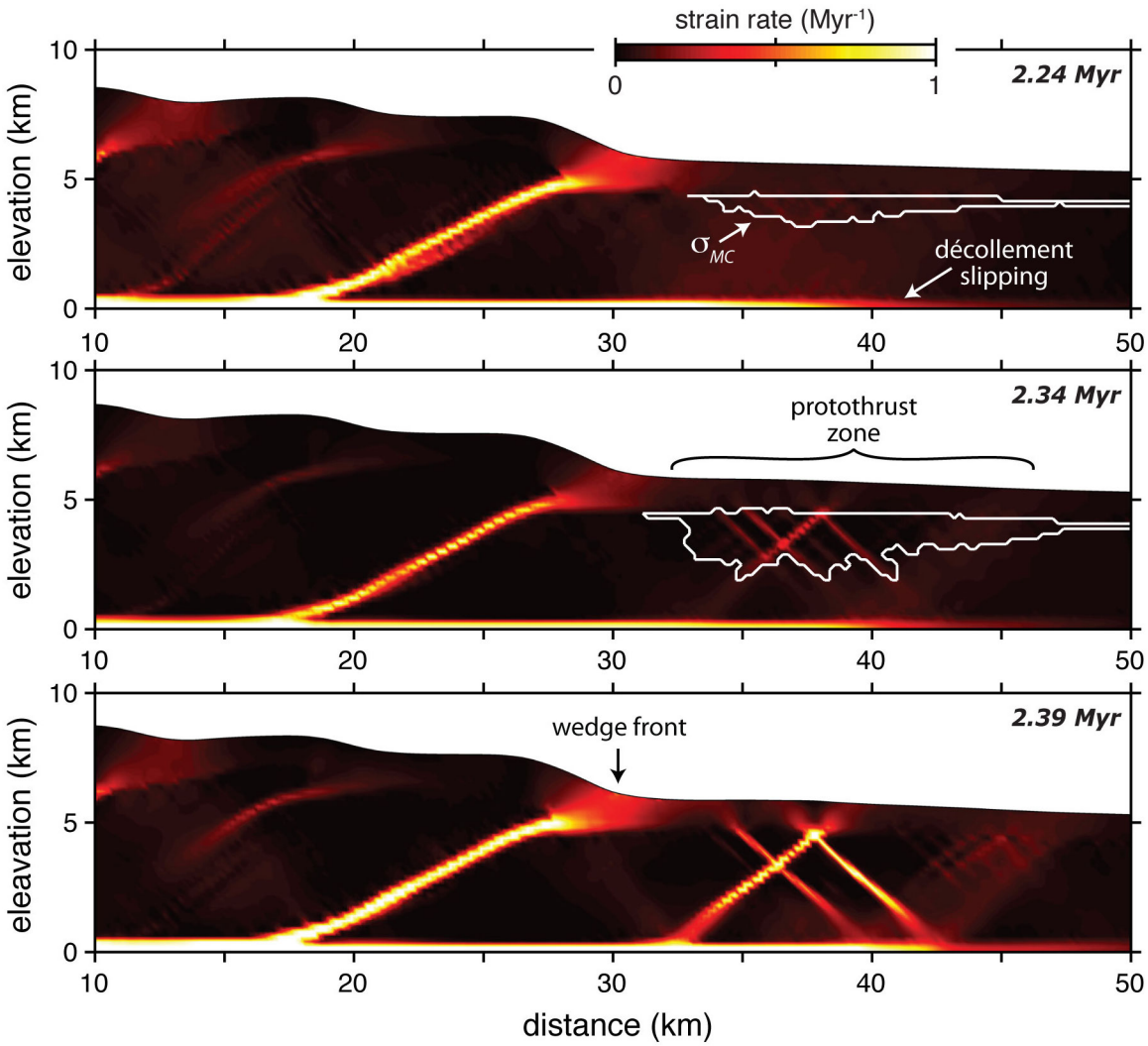

Figure 3.11 Strain rate for 3 time steps from a SiStER model (ϕ=30°; ϕ_b=10°; dx=dy=200 m; κ=5×10^{-9}) with a sedimentary layer composed of a 1-km-thick low-viscosity (η=1×10^{21}), and hence ductile surface layer overlying a 3.5-km-thick brittle layer (η_s=1×10^{25}) that simulates the formation of a protothrust zone below the surface of the sediments. The top two panels show the wedge failure ratio with white contours outlining regions that are failing (σ_{MC}). Shear bands nucleate within this zone at the interface between the shallow ductile-brittle transition and thrusts propagate down-dip to intersect the basal décollement, which has and is continuing to slip (high strain rate) well beyond the wedge front. The pattern is similar to observations from submarine accretionary prisms including Nankai and Cascadia (see Figure 3.10).

References

Adam, J., J. L. Urai, B. Wieneke, O. Oncken, K. Pfeiffer, N. Kukowski, J. Lohrmann, S. Hoth, W. van der Zee, and J. Schmatz (2005), Shear localisation and strain distribution during tectonic faulting - new insights from granular-flow experiments and high-resolution optical image correlation techniques, *Journal of Structural Geology*, *27*(2), 283-301, doi:10.1016/j.jsg.2004.08.008.

Agnew, D. C. (1992), The time-domain behavior of power-law noises, *Geophysical Research Letters*, *19*(4), 333-336, doi:10.1029/91GL02832.

Allmendinger, R. W. (1998), Inverse and forward numerical modeling of trishear fault-propagation folds, *Tectonics*, *17*(4), 640-656, doi:10.1029/98tc01907.

Allmendinger, R. W., V. A. Ramos, T. E. Jordan, M. Palma, and B. L. Isacks (1983), Paleogeography and Andean structural geometry, northwest Argentina, *Tectonics*, *2*(1), 1-16, doi:10.1029/TC002i001p00001.

Allmendinger, R. W., R. Smalley, Jr., M. Bevis, H. Caprio, and B. A. Brooks (2005), Bending the Bolivian orocline in real time, *Geology*, *33*(11), 905-908.

Allmendinger, R. W., and T. R. Zapata (2000), The footwall ramp of the Subandean decollement, northernmost Argentina, from extended correlation of seismic reflection data, *Tectonophysics*, *321*, 37-55.

Angermann, D., J. Klotz, and C. Reigber (1999), Space-geodetic estimation of the Nazca-South America Euler vector, *Earth and Planetary Science Letters*, *171*(3), 329-334.

Aster, R. C., B. Borchers, and C. H. Thurber (2005), *Parameter Estimation and Inverse Problems*, 303 pp., Elsevier Academic Press, Amsterdam.

Avouac, J.-P., L. Meng, S. Wei, T. Wang, and J.-P. Ampuero (2015), Lower edge of locked Main Himalayan Thrust unzipped by the 2015 Gorkha earthquake, *Nature Geosci*, *8*(9), 708-711, doi:10.1038/ngeo2518.

Avouac, J. P. (2008), Dynamic Processes in Extensional and Compressional Settings-Mountain Building: From Earthquakes to Geological Deformation, *Treatise on Geophysics*, *6*, 377-439.

Baby, P., P. Rochat, G. Mascle, and G. Herail (1997), Neogene shortening contribution to crustal thickening in the back arc of the Central Andes, *Geology*, *25*(10), 883-886.

Barbot, S., and Y. Fialko (2010), A unified continuum representation of post-seismic relaxation mechanisms: semi-analytic models of afterslip, poroelastic rebound and viscoelastic flow, *Geophysical Journal International*, *182*(3), 1124-1140, doi:10.1111/j.1365-246X.2010.04678.x.

Barnes, J. B., T. A. Ehlers, N. Insel, N. McQuarrie, and C. J. Poulsen (2012), Linking orography, climate, and exhumation across the central Andes, *Geology*, *40*(12), 1135-1138.

Barnes, J. B., T. A. Ehlers, N. McQuarrie, P. B. O'Sullivan, and J. D. Pelletier (2006), Eocene to recent variations in erosion across the central Andean fold-thrust belt, northern Bolivia: Implications for plateau evolution, *Earth and Planetary Science Letters*, *248*(1-2), 118-133, doi:10.1016/j.epsl.2006.05.018.

Barnes, J. B., and W. A. Heins (2009), Plio-Quaternary sediment budget between thrust belt erosion and foreland deposition in the central Andes, southern Bolivia, *Basin Research*, *21*, 91-109.

Barnes, P. M., G. Lamarche, J. Bialas, S. Henrys, I. Pecher, G. L. Netzeband, J. Greinert, J. J. Mountjoy, K. Pedley, and G. Crutchley (2010), Tectonic and geological framework for gas hydrates and cold seeps on the Hikurangi subduction margin, New Zealand, *Marine Geology*, *272*(1–4), 26-48, doi:10.1016/j.margeo.2009.03.012.

Beaumont, C., P. Fullsack, and J. Hamilton (1992), Erosional control of active compressional orogens, in *Thrust Tectonics*, edited by K. R. McClay, pp. 1-18, Chapman and Hall, New York.

Beck, S. L., and G. Zandt (2002), The nature of orogenic crust in the Central Andes, *Journal of Geophysical Research*, *107*, no.B10, 16.

Bejar-Pizarro, M., et al. (2010), Asperities and barriers on the seismogenic zone in North Chile: state-of-the-art after the 2007 Mw 7.7 Tocopilla earthquake inferred by GPS and InSAR data, *Geophysical Journal International*, *183*(1), 390-406, doi:10.1111/j.1365-246X.2010.04748.x.

Benedetti, L., P. Tapponnier, G. C. P. King, B. Meyer, and I. Manighetti (2000), Growth folding and active thrusting in the Montello region, Veneto, northern Italy, *J Geophys Res-Sol Ea*, *105*(B1), 739-766, doi:10.1029/1999jb900222.

Bevis, M., D. Alsdorf, E. Kendrick, L. P. Fortes, B. Forsberg, R. S. J. Smalley, and J. Becker (2005), Seasonal fluctuations in the mass of the Amazon River system and Earth's elastic response, *Geophysical Research Letters*, *32*, doi:doi:10.1029/2005GL023491.

Bevis, M., Y. Bock, P. Fang, R. Reilinger, T. Herring, J. Stowell, and R. J. Smalley (1997), Blending Old and New Approaches to Regional Geodesy, *Eos, Transactions, American Geophysical Union*, *78*(6), 61,64-66.

Bevis, M., and A. Brown (2014), Trajectory models and reference frames for crustal motion geodesy, *Journal of Geodesy*, *88*(3), 283-311, doi:10.1007/s00190-013-0685-5.

Bevis, M., E. Kendrick, R. J. Smalley, B. A. Brooks, R. Allmendinger, and B. Isacks (2001), On the strength of interplate coupling and the rate of back arc convergence in the

central Andes: An analysis of the interseismic velocity field, *Geochemistry, Geophysics, Geosystems*, *2*(paper number 2001GC000198).

Bevis, M., E. C. Kendrick, R. Smalley Jr., T. Herring, J. Godoy, and F. Galban (1999), Crustal motion north and south of the Arica deflection: Comparing recent geodetic results from the Central Andes, *Geochemisty, Geophysics, Geosystems*, *1*(paper 1999GC000011).

Bevis, M., and S. Martel (2001), Oblique plate convergence and interseismic strain accumulation, *Geochemistry, Geophysics, Geosystems*, *2*(paper number 2000GC000125).

Bilham, R., F. Blume, R. Bendick, and V. K. Gaur (1998), Geodetic constraints on the translation and deformation of India: Implications for future great Himalayan earthquakes, *Current Science*, *74*(3), 213-229.

Bilham, R., V. K. Gaur, and P. Molnar (2001), Himalayan seismic hazard, *Science*, *293*(5534), 1442-1444, doi:10.1126/science.1062584.

Bilham, R., et al. (1997), GPS measurements of present-day convergence across the Nepal Himalaya, *Nature*, *386*(6620), 61-64.

Bird, P. (2007), Uncertainties in long-term geologic offset rates of faults: General principles illustrated with data from California and other western states, *Geosphere*, *3*(6), 577-595, doi:Doi 10.1130/Ges00127.1.

Bischke, R. E. (1994), Interpreting Sedimentary Growth Structures from Well Log and Seismic Data (with Examples), *Aapg Bull*, *78*(6), 873-892.

Blewitt, G., and D. Lavallée (2002), Effect of annual signals on geodetic velocity, *Journal of Geophysical Research: Solid Earth*, *107*(B7), ETG 9-1-ETG 9-11, doi:10.1029/2001JB000570.

Bollinger, L., S. N. Sapkota, P. Tapponnier, Y. Klinger, M. Rizza, J. Van der Woerd, D. R. Tiwari, R. Pandey, A. Bitri, and S. Bes de Berc (2014), Estimating the return times of great Himalayan earthquakes in eastern Nepal: Evidence from the Patu and Bardibas strands of the Main Frontal Thrust, *Journal of Geophysical Research: Solid Earth*, *119*(9), 7123-7163, doi:10.1002/2014JB010970.

Brandes, C., and D. C. Tanner (2014), Fault-related folding: A review of kinematic models and their application, *Earth-Science Reviews*, *138*, 352-370, doi:10.1016/j.earscirev.2014.06.008.

Brooks, B. A., R. Arrowsmith, A. Echalar, D. Yagupsky, T. L. Ericksen, J. R. Weiss, K. Ahlgren, M. G. Bevis, and K. X. Whipple (2011a), Great Earthquakes and Orogenic Wedge

Front Processes in the Bolivian Backarc, paper presented at the 2011 AGU Fall Meeting, San Francisco.

Brooks, B. A., M. Bevis, R. J. Smalley, E. Kendrick, R. Manceda, E. Lauria, R. Maturana, and M. Araujo (2003), Crustal Motion in the Southern Andes (26°-36°S): Do the Andes Behave Like a Microplate?, *Geochemistry, Geophysics, Geosystems*.

Brooks, B. A., et al. (2011b), Orogenic-wedge deformation and potential for great earthquakes in the central Andean backarc, *Nature Geoscience*, *4*(6), 380-383, doi:Doi 10.1038/Ngeo1143.

Brooks, B. A., and L. N. Frazer (2005), Importance reweighting reduces dependence on temperature in Gibbs samplers: an application to the coseismic geodetic inverse problem, *Geophys. J Int.*, *161*, 12-20.

Buiter, S. J. H. (2012), A review of brittle compressional wedge models, *Tectonophysics*, *530-531*, 1-17.

Buiter, S. J. H., A. Y. Babeyko, S. Ellis, T. V. Gerya, B. J. P. Kaus, A. Kellner, G. Schreurs, and Y. Yamada (2006), The numerical sandbox: comparison of model results for a shortening and an extension experiment, in *Analogue and Numerical Modelling of Crustal-Scale Processes*, edited by S. J. H. Buiter and G. Schreurs, p. 445, Geological Society of London, doi:10.1144/gsl.sp.2006.253.

Burbank, D., A. Meigs, and N. Brozovic (1996), Interactions of growing folds and coeval depositional systems, *Basin Research*, *8*, 199-223.

Burbank, D. W., and R. S. Anderson (2012), *Tectonic Geomorphology*, 2 ed., 454 pp., Wiley-Blackwell, Oxford, UK.

Bürgmann, R., P. A. Rosen, and E. J. Fielding (2000), Synthetic Aperture Radar Interferometry to Measure Earth's Surface Topography and Its Deformation, *Annual Review of Earth and Planetary Sciences*, *28*(1), 169-209, doi:doi:10.1146/annurev.earth.28.1.169.

Cardozo, N., and J. P. Brandenburg (2014), Kinematic modeling of folding above listric propagating thrusts, *Journal of Structural Geology*, *60*, 1-12, doi:Doi 10.1016/J.Jsg.2013.12.004.

Cardozo, N., C. A. L. Jackson, and P. S. Whipp (2011), Determining the uniqueness of best-fit trishear models, *Journal of Structural Geology*, *33*(6), 1063-1078, doi:10.1016/j.jsg.2011.04.001.

Chapple, W. M. (1978), Mechanics of thin-skinned fold-and-thrust belts, *Geol. Soc. Am. Bull.*, *89*, 1189-1198.

Chen, W.-P., and P. Molnar (1977), Seismic moment of major earthquakes and the average rate of slip in central Asia, *Journal of Geophysical Research*, *82*(20), 2945-2969.

Chlieh, M., H. Perfettini, H. Tavera, J. P. Avouac, D. Remy, J. M. Nocquet, F. Rolandone, F. Bondoux, G. Gabalda, and S. Bonvalot (2011), Interseismic coupling and seismic potential along the Central Andes subduction zone, *J Geophys Res-Sol Ea*, *116*, doi:10.1029/2010jb008166.

Cooke, M. L., and E. H. Madden (2014), Is the Earth Lazy? A review of work minimization in fault evolution, *Journal of Structural Geology*, *66*, 334-346, doi:10.1016/j.jsg.2014.05.004.

Cruz, L., J. Malinski, A. Wilson, W. A. Take, and G. Hilley (2010), Erosional control of the kinematics and geometry of fold-and-thrust belts imaged in a physical and numerical sandbox, *J Geophys Res-Sol Ea*, *115*, doi:10.1029/2010jb007472.

Cubas, N., Y. M. Leroy, and B. Maillot (2008), Prediction of thrusting sequences in accretionary wedges, *J Geophys Res-Sol Ea*, *113*(B12), doi:10.1029/2008jb005717.

Currie, C. A., and R. D. Hyndman (2006), The thermal structure of subduction zone back arcs, *Journal of Geophysical Research*, *111*(B08404), doi:10.1029/2005JB004024.

Dahlen, F. A. (1984), Noncohesive critical Coulomb wedges: an exact solution, *Journal of Geophysical Research*, *89*, 10,125-110,133.

Dahlen, F. A. (1990), Critical taper model of fold-and-thrust belts and accretionary wedges, *Annual Review of Earth and Planetary Sciences*, *18*, 55-99.

Dahlen, F. A., and J. Suppe (1988), Mechanics, growth, and erosion of mountain belts, in *Processes in Continental Lithospheric Deformation: Geological Society of America Special Paper 218*, edited, pp. 161-178, Boulder, CO.

Dahlen, F. A., J. Suppe, and D. Davis (1984), Mechanics of fold-and-thrust belts and accretionary wedges-cohesive Coulomb theory, *Journal of Geophysical Research*, *89*(NB12), 87-101, doi:10.1029/JB089iB12p10087.

Davis, D., J. Suppe, and F. A. Dahlen (1983), Mechanics of fold-and-thrust belts and accretionary wedges, *Journal of Geophysical Research*, *88*(NB2), 1153-1172, doi:10.1029/JB088iB02p01153.

Dean, S. L., J. K. Morgan, and T. Fournier (2013), Geometries of frontal fold and thrust belts: Insights from discrete element simulations, *Journal of Structural Geology*, *53*, 43-53, doi:10.1016/j.jsg.2013.05.008.

DeDontney, N., and J. Hubbard (2012), Applying Wedge Theory to Dynamic Rupture Modeling of Fault Junctions, *Bulletin of the Seismological Society of America*, *102*(4), 1693-1711, doi:10.1785/0120110190.

DeDontney, N., J. R. Rice, and R. Dmowska (2012), Finite Element Modeling of Branched Ruptures Including Off-Fault Plasticity, *Bulletin of the Seismological Society of America*, *102*(2), 541-562, doi:10.1785/0120110134.

Del Castello, M., and M. L. Cooke (2007), Underthrusting-accretion cycle: Work budget as revealed by the boundary element method, *J Geophys Res-Sol Ea*, *112*(B12), doi:B12404/10.1029/2007jb004997.

Delouis, B., M. Pardo, D. Legrand, and T. Monfret (2009), The M-w 7.7 Tocopilla Earthquake of 14 November 2007 at the Southern Edge of the Northern Chile Seismic Gap: Rupture in the Deep Part of the Coupled Plate Interface, *Bulletin of the Seismological Society of America*, *99*(1), 87-94, doi:10.1785/0120080192.

Dominguez, S., J. P. Avouac, and R. Michel (2003), Horizontal coseismic deformation of the 1999 Chi-Chi earthquake measured from SPOT satellite images: Implications for the seismic cycle along the western foothills of central Taiwan, *J Geophys Res-Sol Ea*, *108*(B2), doi:doi 10.1029/2001jb000951.

Dunn, J. F., K. G. Hartshorn, and P. W. Hartshorn (1995), Structural Styles and Hydrocarbon Potential of the Sub-Andean Thrust Belt of Southern Bolivia, in *Petroleum Basins of South America*, edited by A. J. Tankard, R. Suarez Soruco and H. J. Welsink, pp. 523-543.

Echavarria, L., R. Hernandez, R. Allmendinger, and J. Reynolds (2003), Subandean thrust and fold belt of northwestern Argentina; geometry and timing of the Andean evolution, *AAPG Bulletin*, *87*(6), 965-985.

Elliott, J. R., R. Jolivet, P. J. Gonzalez, J. P. Avouac, J. Hollingsworth, M. P. Searle, and V. L. Stevens (2016), Himalayan megathrust geometry and relation to topography revealed by the Gorkha earthquake, *Nature Geosci*, *advance online publication*.

Ellis, M. A., and A. L. Densmore (2006), First-order topography over blind thrusts, in *Tectonics, Climate, and Landscape Evolution*, edited by S. D. Willett, N. Hovius, M. T. Brandon and D. M. FIsher, pp. 251-266.

Ellis, S., G. Schreurs, and M. Panien (2004), Comparisons between analogue and numerical models of thrust wedge development, *Journal of Structural Geology*, *26*(9), 1659-1675, doi:10.1016/j.jsg.2004.02.012.

England, P., and J. Jackson (1989), Active Deformation of the Continents, *Annual Review of Earth and Planetary Sciences*, *17*(1), 197-226, doi:10.1146/annurev.ea.17.050189.001213.

England, P., and J. Jackson (2011), Uncharted seismic risk, *Nature Geoscience*, *4*(6), 348-349, doi:10.1038/ngeo1168.

England, P., and D. McKenzie (1982), A thin viscous sheet model for continental deformation, *Geophysical Journal of the Royal Astronomical Society*, *70*(2), 295-321, doi:10.1111/j.1365-246X.1982.tb04969.x.

England, P., and P. Molnar (1997), Active Deformation of Asia: From Kinematics to Dynamics, *Science*, *278*(5338), 647-650, doi:10.1126/science.278.5338.647.

Epard, J. L., and R. H. Groshong (1993), Excess Area and Depth to Detachment, *Aapg Bull*, *77*(8), 1291-1302.

Ergintav, S., S. McClusky, E. Hearn, R. Reilinger, R. Cakmak, T. Herring, H. Ozener, O. Lenk, and E. Tari (2009), Seven years of postseismic deformation following the 1999, M=7.4 and M=7.2, Izmit-Duzce, Turkey earthquake sequence, *J Geophys Res-Sol Ea*, *114*, doi:10.1029/2008jb006021.

Erslev, E. A. (1991), Trishear Fault-Propagation Folding, *Geology*, *19*(6), 617-620, doi:Doi 10.1130/0091-7613(1991)019<0617:Tfpf>2.3.Co;2.

Feldl, N., and R. Bilham (2006), Great Himalayan earthquakes and the Tibetan plateau, *Nature*, *444*(7116), 165-170, doi:Doi 10.1038/Nature05199.

Fujiwara, T., S. Kodaira, T. No, Y. Kaiho, N. Takahashi, and Y. Kaneda (2011), The 2011 Tohoku-Oki Earthquake: Displacement Reaching the Trench Axis, *Science*, *334*(6060), 1240-1240, doi:10.1126/science.1211554.

Gephart, J. W. (1994), Topography and subduction geometry in the central Andes: Clues to the mechanics of a noncollisional orogen, *Journal of Geophysical Research*, *99*(B6), 12279-12288.

Gerya, T. (2010), *Introduction to Numerical Geodynamic Modelling*, 345 pp., Cambridge University Press, Cambridge, U.K.

Giraudo, R., and R. Limachi (2001), Pre-Silurian control in the genesis of the central and southern Bolivian fold belt, *Journal of South American Earth Sciences*, *14*, 665-680, doi:10.1016/S0895-9811(01)00068-2.

Gonzalez-Mieres, R., and J. Suppe (2006), Relief and shortening in detachment folds, *Journal of Structural Geology*, *28*(10), 1785-1807, doi:10.1016/j.jsg.2006.07.001.

Gonzalez-Mieres, R., and J. Suppe (2011), Shortening Histories in Active Detachment Folds Based on Area-of-relief Methods, in *Thrust fault-related folding: AAPG Memoir 94*, edited by K. McClay, J. H. Shaw and J. Suppe, pp. 39-68.

Gubbels, T. L., B. L. Isacks, and E. Farrar (1993), High-level surfaces, plateau uplift, and foreland development, Bolivian Central Andes, *Geology*, *21*(8), 695-698.

Hackl, M., R. Malservisi, U. Hugentobler, and R. Wonnacott (2011), Estimation of velocity uncertainties from GPS time series: Examples from the analysis of the South African TrigNet network, *J Geophys Res-Sol Ea*, *116*, doi:10.1029/2010jb008142.

Hardy, S., C. Duncan, J. Masek, and D. Brown (1998), Minimum work, fault activity and the growth of critical wedges in fold and thrust belts, *Basin Research*, *10*, 365-373.

Hardy, S., and M. Ford (1997), Numerical modeling of trishear fault propagation folding, *Tectonics*, *16*(5), 841-854, doi:10.1029/97TC01171.

Hardy, S., K. McClay, and J. A. Munoz (2009), Deformation and fault activity in space and time in high-resolution numerical models of doubly vergent thrust wedges, *Marine and Petroleum Geology*, *26*(2), 232-248, doi:10.1016/j.marpetgeo.2007.12.003.

Hayes, G. P., M. W. Herman, W. D. Barnhart, K. P. Furlong, S. Riquelme, H. M. Benz, E. Bergman, S. Barrientos, P. S. Earle, and S. Samsonov (2014), Continuing megathrust earthquake potential in Chile after the 2014 Iquique earthquake, *Nature*, *512*(7514), 295-298, doi:10.1038/nature13677.

Healy, D., N. Kusznir, and G. Yielding (2004a), Fracture prediction for the 1980 El Asnam, Algeria earthquake via elastic dislocation modeling, *Tectonics*, *23*(6), TC6005.

Healy, D., N. Kusznir, and G. Yielding (2004b), An inverse method to derive fault slip and geomtry from seismically observed vertical stratigraphic displacements using elastic dislocation theory, *Marine and Petroleum Geology*, *21*, 923-932.

Hearn, E. H. (2003), What can GPS data tell us about the dynamics of post-seismic deformation?, *Geophysical Journal International*, *155*(3), 753-777, doi:10.1111/j.1365-246X.2003.02030.x.

Herring, T. (2000), Documentation for GLOBK: Global Kalman Filter VLBI and GPS analysis program, edited, MIT.

Hilley, G. E., I. Mynatt, and D. D. Pollard (2010), Structural geometry of Raplee Ridge monocline and thrust fault imaged using inverse Boundary Element Modeling and ALSM data, *Journal of Structural Geology*, *32*(1), 45-58, doi:Doi 10.1016/J.Jsg.2009.06.015.

Hilley, G. E., and M. R. Strecker (2004), Steady state erosion of critical Coulomb wedges with applications to Taiwan and the Himalaya, *J Geophys Res-Sol Ea*, *109*(B1), doi:10.1029/2002jb002284.

Horton, B. K. (1999), Erosional control on the geometry and kinematics of thrust belt development in the central Andes, *Tectonics*, *18*(6), 1292-1304.

Hoth, S., J. Adam, N. Kukowsi, and O. Oncken (2007a), Influence of erosion on the kinematics of bivergent orogens: Results from scaled sandbox simulations, in *Tectonics, Climate, and Landscape Evolution: Geological Society of America Special Paper 398*, edited by S. D. Willett, N. Hovius, M. T. Brandon and D. M. Fisher, pp. 201-225.

Hoth, S., A. Hoffmann-Rothe, and N. Kukowski (2007b), Frontal accretion: An internal clock for bivergent wedge deformation and surface uplift, *Journal of Geophysical Research: Solid Earth*, *112*(B6), n/a-n/a, doi:10.1029/2006JB004357.

Houseman, G., and P. England (1986), Finite strain calculations of continental deformation: 1. Method and general results for convergent zones, *Journal of Geophysical Research: Solid Earth*, *91*(B3), 3651-3663, doi:10.1029/JB091iB03p03651.

Hsu, Y. J., J. P. Avouac, S. B. Yu, C. H. Chang, Y. M. Wu, and J. Woessner (2009), Spatio-temporal slip, and stress level on the faults within the Western Foothills of Taiwan: Implications for Fault Frictional Properties, *Pure and Applied Geophysics*, *166*(10-11), 1853-1884.

Hsu, Y. J., M. Simons, J. P. Avouac, J. Galetzka, K. Sieh, M. Chlieh, D. Natawidjaja, L. Prawirodirdjo, and Y. Bock (2006), Frictional afterslip following the 2005 Nias-Simeulue earthquake, Sumatra, *Science*, *312*(5782), 1921-1926, doi:10.1126/science.1126960.

Hsu, Y. J., M. Simons, S. B. Yu, L. C. Kuo, and H. Y. Chen (2003), A two-dimensional dislocation model for interseismic deformation of the Taiwan mountain belt, *Earth and Planetary Science Letters*, *211*(3-4), 287-294, doi:10.1016/s0012-821x(03)00203-6.

Hu, Y., and K. L. Wang (2008), Coseismic strengthening of the shallow portion of the subduction fault and its effects on wedge taper, *J Geophys Res-Sol Ea*, *113*(B12), doi:10.1029/2008jb005724.

Hubbard, J., S. Barbot, E. M. Hill, and P. Tapponnier (2015), Coseismic slip on shallow décollement megathrusts: implications for seismic and tsunami hazard, *Earth-Science Reviews*, *141*(0), 45-55.

Hubbard, J., and J. H. Shaw (2009), Uplift of the Longmen Shan and Tibetan plateau, and the 2008 Wenchuan (M=7.9) earthquake, *Nature*, *458*, doi:10.1038/nature07837.

Hubbard, J., J. H. Shaw, and Y. Klinger (2010), Structural Setting of the 2008 M-w 7.9 Wenchuan, China, Earthquake, *Bulletin of the Seismological Society of America*, *100*(5B), 2713-2735, doi:10.1785/0120090341.

Isacks, B. L. (1988), Uplift of the Central Andean Plateau and Bending of the Bolivian Orocline, *Journal of Geophysical Research*, *93*(B4), 3211-3231.

Ito, Y., T. Tsuji, Y. Osada, M. Kido, D. Inazu, Y. Hayashi, H. Tsushima, R. Hino, and H. Fujimoto (2011), Frontal wedge deformation near the source region of the 2011 Tohoku-Oki earthquake, *Geophysical Research Letters*, *38*, doi:10.1029/2011gl048355.

Johnson, K. M., Y.-J. Hsu, P. Segall, and S.-B. Yu (2001), Fault geometry and slip distribution of the 1999 Chi-chi, Taiwan earthquake imaged from inversion of GPS data, *Geophysical Research Letters*, *28*(11), 2285-2288.

Kanamori, H. (1977), The energy release in great earthquakes, *Journal of Geophysical Research*, 2981-2987.

Kanamori, H. (1983), Magnitude scale and quantification of earthquakes, *Tectonophysics*, *93*(3-4), 185-199, doi:10.1016/0040-1951(83)90273-1.

Kao, H., and W. P. Chen (2000), The Chi-Chi earthquake sequence: Active, out-of-sequence thrust faulting in Taiwan, *Science*, *288*(5475), 2346-2349, doi:10.1126/science.288.5475.2346.

Kaus, B. J. P. (2010), Factors that control the angle of shear bands in geodynamic numerical models of brittle deformation, *Tectonophysics*, *484*(1–4), 36-47, doi:10.1016/j.tecto.2009.08.042.

Kendrick, E., M. Bevis, R. J. Smalley, and B. A. Brooks (2001), An integrated crustal velocity field for the central Andes, *Geochemistry, Geophysics, Geosystems*, *2*(Paper number 2001GC000191).

Kendrick, E., M. Bevis, R. J. Smalley, B. A. Brooks, R. B. Vargas, E. Lauría, and L. P. S. Fortes (2003), The Nazca-South America Euler Vector and its Rate of Change, *Journal of South American Earth Sciences*, *16*(2), 125-131.

Kendrick, E., B. A. Brooks, M. Bevis, R. Smalley Jr., E. Lauria, M. Araujo, and H. Parra (2006), Active Orogeny of the South-Central Andes Studied with GPS Geodesy, *Rev. Asoc. Geol. Argent.*, *61*(4), 555-566.

Kendrick, E. C., M. Bevis, R. F. Smalley, Jr., O. Cifuentes, and F. Galban (1999), Current rates of convergence across the Central Andes; estimates from continuous GPS observations, *Geophysical Research Letters*, *26*(5), 541-544.

Kido, M., Y. Osada, H. Fujimoto, R. Hino, and Y. Ito (2011), Trench-normal variation in observed seafloor displacements associated with the 2011 Tohoku-Oki earthquake, *Geophysical Research Letters*, *38*, doi:10.1029/2011gl050057.

King, G. C. P., R. S. Stein, and J. B. Rundle (1988), The Growth of Geological Structures by Repeated Earthquakes .1. Conceptual Framework, *Journal of Geophysical Research-Solid Earth and Planets*, *93*(B11), 13307-13318, doi:Doi 10.1029/Jb093ib11p13319.

King, R., and Y. Bock (2000), Documentation for the GAMIT GPS Analysis Software, edited, MIT and Scripps Inst. of Oceanogr., Cambridge, Mass.

Kley, J. (1996), Transition from basement-involved to thin-skinned thrusting in the Cordillera Oriental of southern Bolivia, *Tectonics*, *15*(4), 763-775.

Kumar, S., S. G. Wesnousky, R. Jayangondaperumal, T. Nakata, Y. Kumahara, and V. Singh (2010), Paleoseismological evidence of surface faulting along the northeastern Himalayan front, India: Timing, size, and spatial extent of great earthquakes, *Journal of Geophysical Research*, *115*(B12), doi:10.1029/2009jb006789.

Kumar, S., S. G. Wesnousky, T. R. Rockwell, R. W. Briggs, V. C. Thakur, and R. Jayangondaperumal (2006), Paleoseismic evidence of great surface rupture earthquakes along the Indian Himalaya, *Journal of Geophysical Research*, *111*(B03304), doi:10.1029/2004JB003309.

Lamb, S. (2000), Active deformation in the Bolivian Andes, South America, *Journal of Geophysical Research*, *105*(B11), 25,627-625,653.

Lamb, S., and E. Smith (2013), The nature of the plate interface and driving force of interseismic deformation in the New Zealand plate-boundary zone, revealed by the continuous GPS velocity field, *Journal of Geophysical Research: Solid Earth*, *118*(6), 3160-3189, doi:10.1002/jgrb.50221.

Langbein, J. (2004), Noise in two-color electronic distance meter measurements revisited, *J Geophys Res-Sol Ea*, *109*(B4), doi:10.1029/2003jb002819.

Langbein, J. (2012), Estimating rate uncertainty with maximum likelihood: differences between power-law and flicker–random-walk models, *Journal of Geodesy*, *86*(9), 775-783, doi:10.1007/s00190-012-0556-5.

Langbein, J., and H. Johnson (1997), Correlated errors in geodetic time series: Implications for time-dependent deformation, *J Geophys Res-Sol Ea*, *102*(B1), 591-603, doi:10.1029/96jb02945.

Lapusta, N. (2009), The roller coaster of fault friction, *Nature Geoscience*, *2*(10), 676-677, doi:Doi 10.1038/Ngeo645.

Lavé, J., and J. P. Avouac (2000), Active folding of fluvial terraces across the Siwalik Hills (Himalaya of central Nepal), *J. Geophys. Res.*, *105*, 5735-5770.

Lavé, J., D. Yule, S. Sapkota, K. Basant, C. Madden, M. Attal, and R. Pandey (2005), Evidence for a great medieval earthquake (approximate to 1100 AD) in the Central Himalayas, Nepal, *Science*, *307*(5713), 1302-1305, doi:10.1126/science.1104804.

Lavenu, A., R. Thiele, M. N. Machette, R. L. Dart, L. Bradley, and K. M. Haller (2000), *Maps and Database of Quaternary Faults in Bolivia and Chile*.

Lay, T., and S. Bilek (2007), Anomalous earthquake ruptures at shallow depths on subduction zone megathrusts, in *The Seismogenic Zone of Subduction Thrust Faults*, edited by T. H. Dixon and J. C. Moore, pp. 476-511, Columbia Univ. Press, New York.

Lay, T., et al. (2005), The great Sumatra-Andaman earthquake of 26 December 2004, *Science*, *308*(5725), 1127-1133, doi:10.1126/science.1112250.

Leturmy, P., J. L. Mugnier, P. Vinour, P. Baby, B. Colletta, and E. Chabron (2000), Piggyback basin development above a thin-skinned thrust belt with two detachment levels as a function of interactions between tectonic and superficial mass transfer: the case of the Subandean Zone (Bolivia), *Tectonophysics*, *320*(1), 45-67, doi:Doi 10.1016/S0040-1951(00)00023-8.

Lin, Y. N. N., et al. (2013), Coseismic and postseismic slip associated with the 2010 Maule Earthquake, Chile: Characterizing the Arauco Peninsula barrier effect, *J Geophys Res-Sol Ea*, *118*(6), 3142-3159, doi:10.1002/jgrb.50207.

Lindsey, E. O., R. Natsuaki, X. Xu, M. Shimada, M. Hashimoto, D. Melgar, and D. T. Sandwell (2015), Line-of-sight displacement from ALOS-2 interferometry: Mw 7.8 Gorkha Earthquake and Mw 7.3 aftershock, *Geophysical Research Letters*, *42*(16), 6655-6661, doi:10.1002/2015GL065385.

MacKay, M. E. (1995), Structural variation and landward vergence at the toe of the Oregon accretionary prism, *Tectonics*, *14*(6), 1309-1320, doi:10.1029/95TC02320.

Malavieille, J. (2010), Impact of erosion, sedimentation, and structural heritage on the structure and kinematics of orogenic wedges: Analog models and case studies, *GSA Today*, *20*(1), 4-10.

Mao, A. L., C. G. A. Harrison, and T. H. Dixon (1999), Noise in GPS coordinate time series, *J Geophys Res-Sol Ea*, *104*(B2), 2797-2816, doi:10.1029/1998jb900033.

Mary, B. C. L., B. Maillot, and Y. M. Leroy (2013a), Deterministic chaos in frictional wedges revealed by convergence analysis, *International Journal for Numerical and Analytical Methods in Geomechanics*, *37*(17), 3036-3051, doi:10.1002/nag.2177.

Mary, B. C. L., B. Maillot, and Y. M. Leroy (2013b), Predicting orogenic wedge styles as a function of analogue erosion law and material softening, *Geochemistry Geophysics Geosystems*, *14*(10), 4523-4543, doi:10.1002/ggge.20262.

Masek, J. G., and C. C. Duncan (1998), Minimum-work mountain building, *Journal of Geophysical Research*, *103*, 907-917.

Masek, J. G., B. L. Isacks, T. L. Gubbels, and E. J. Fielding (1994), Erosion and tectonics at the margins of continental plateaus, *Journal of Geophysical Research*, *99*(B7), 13,941-913,956.

McConnell, D. A., S. A. Kattenhorn, and L. M. Benner (1997), Distribution of fault slip in outcrop-scale fault-related folds, Appalachian Mountains, *Journal of Structural Geology*, *19*(3-4), 257-267, doi:10.1016/s0191-8141(96)00094-6.

McQuarrie, N. (2002a), Initial plate geometry, shortening variations, and evolution of the Bolivian Orocline, *Geology*, *30*(10), 867-870.

McQuarrie, N. (2002b), The kinematic history of the Central Andean fold-thrust belt, Bolivia; implications for building a high plateau, *Geological Society of America Bulletin*, *114*(8), 950-963.

McQuarrie, N., J. B. Barnes, and T. A. Ehlers (2008a), Geometric, kinematic, and erosional history of the central Andean Plateau, Bolivia (15-17 degrees S), *Tectonics*, *27*, no. 3, Paper no. TC3007, 3024.

McQuarrie, N., T. A. Ehlers, J. B. Barnes, and B. Meade (2008b), Temporal variation in climate and tectonic coupling in the Central Andes, *Geology*, *36*(12), 999-1002.

McQuarrie, N., B. K. Horton, G. Zandt, S. Beck, and P. G. DeCelles (2005), Lithospheric evolution of the Andean fold-thrust belt, Bolivia, and the origin of the central Andean Plateau, *Tectonophysics*, *399*(1-4), 15-37.

Meade, B. J. (2007), Algorithms for the calculation of exact displacements, strains, and stresses for triangular dislocation elements in a uniform elastic half space, *Computers & Geosciences*, *33*, 1064-1075.

Meade, B. J., Y. Klinger, and E. A. Hetland (2013), Inference of Multiple Earthquake-Cycle Relaxation Timescales from Irregular Geodetic Sampling of Interseismic Deformation, *Bulletin of the Seismological Society of America*, *103*(5), 2824-2835, doi:10.1785/0120130006.

Melnick, D., M. Moreno, M. Motagh, M. Cisternas, and R. L. Wesson (2012), Splay fault slip during the M-w 8.8 2010 Maule Chile earthquake, *Geology*, *40*(3), 251-254, doi:10.1130/g32712.1.

Menke, W. (1989), *Geophysical Data Analysis: Discrete Inverse Theory*, 289 pp., Academic Press, Inc., San Diego.

Montgomery, D. R., G. Balco, and S. D. Willett (2001), Climate, tectonics, and the morphology of the Andes, *Geology*, *29*(7), 579-582.

Moore, G. F., N. L. Bangs, A. Taira, S. Kuramoto, E. Pangborn, and H. J. Tobin (2007), Three-dimensional splay fault geometry and implications for tsunami generation, *Science*, *318*(5853), 1128-1131, doi:10.1126/science.1147195.

Moore, G. F., T. H. Shipley, P. L. Stoffa, D. E. Karig, A. Taira, S. Kuramoto, H. Tokuyama, and K. Suyehiro (1990), Structure of the Nankai Trough Accretionary Zone from multichannel seismic reflection data, *Journal of Geophysical Research: Solid Earth*, *95*(B6), 8753-8765, doi:10.1029/JB095iB06p08753.

Moreno, M., M. Rosenau, and O. Oncken (2010), 2010 Maule earthquake slip correlates with pre-seismic locking of Andean subduction zone, *Nature*, *467*(7312), 198-U184, doi:Doi 10.1038/Nature09349.

Moretti, I., P. Baby, E. Mendez, and D. Zubieta (1996), Hydrocarbon generation in relation to thrusting in the Sub Andean Zone from 18 to 22 S, Bolivia, *Petroleum Geoscience*, *2*, 17-28.

Morgan, J. K. (2015), Effects of cohesion on the structural and mechanical evolution of fold and thrust belts and contractional wedges: Discrete element simulations, *Journal of Geophysical Research: Solid Earth*, *120*(5), 3870-3896, doi:10.1002/2014JB011455.

Morley, C. K. (1994), Fold-generated imbricates - examples from the Caledonides of southern Norway, *Journal of Structural Geology*, *16*(5), 619-631, doi:10.1016/0191-8141(94)90114-7.

Mugnier, J.-L., D. Becel, and D. Granjeon (2006), Active tectonics in the Subandean belt inferred from the morphology of the Rio Pilcomayo (Bolivia), *GSA Special Paper*, *398*, 353-369, doi:10.1130/2006.2398(15).

Myers, D. J., J. L. Nabelek, and R. S. Yeats (2003), Dislocation modeling of blind thrusts in the eastern Los Angeles basin, California, *J Geophys Res-Sol Ea*, *108*(B9), doi:10.1029/2002jb002150.

Mynatt, I., G. E. Hilley, and D. D. Pollard (2007), Inferring fault characteristics using fold geometry constrained by airborne laser swath mapping at Raplee Ridge, Utah, *Geophysical Research Letters*, *34*(16), doi:10.1029/2007gl030548.

Norabuena, E., L. Leffler-Griffin, A. Mao, T. Dixon, S. Stein, I. S. Sacks, L. Ocola, and M. Ellis (1998), Space geodetic observations of Nazca-South America convergence across the Central Andes, *Science*, *279*(5349), 358-362.

Okada, Y. (1985), Surface deformation due to shear and tensile faults in a half-space, *Bulletin of the Seismological Society of America*, *75*, 1135-1154.

Okada, Y. (1992), Internal Deformation Due to Shear and Tensile Faults in a Half-Space, *Bulletin of the Seismological Society of America*, *82*(2), 1018-1040.

Olive, J.-A., M. D. Behn, E. Mittelstaedt, G. Ito, and B. Klein (in press), The role of elasticity in simulating long-term tectonic extension, *Geophysical Journal International*.

Oncken, O., D. Hindle, J. Kley, K. Elger, P. Victor, and K. Schemmann (2007), Deformation of the Central Andean upper plate system; facts, fiction, and constraints for plateau models, edited by O. Oncken, et al., Springer, Berlin.

Orme, H., R. E. Bell, and C. A.-L. Jackson (2015), Thrust fault growth within accretionary wedges; new insights from 3D seismic reflection data, paper presented at the 2015 AGU Fall Meeting, San Francisco.

Panian, J., and D. Wiltschko (2004), Ramp initiation in a thrust wedge, *Nature*, *427*(6975), 624-627.

Paul, J., A. R. Lowry, R. Bilham, S. Sen, and R. Smalley (2007), Postseismic deformation of the Andaman Islands following the 26 December, 2004 Great Sumatra-Andaman earthquake, *Geophysical Research Letters*, *34*(19), doi:10.1029/2007gl031024.

Pflaker, G. (1972), Alaskan earthquake of 1964 and Chilean earthquake of 1960: Implications for arc tectonics, *Journal of Geophysical Research*, *77*, 901-925.

Poblet, J., and R. J. Lisle (2011), *Kinematic evolution and structural styles of fold-and-thrust belts*, 255 p. pp., Geological Society, Bath, UK ; Williston, VT.

Ramos, V. A., T. Zapata, E. Cristallini, and A. Introcaso (2004), The Andean thrust system-Latitudinal variations in structural styles and orogenic shortening, in *Thrust tectonics and hydrocarbon systems: AAPG Memoir 82*, edited by K. R. McClay, pp. 30-50.

Reilinger, R., et al. (2006), GPS constraints on continental deformation in the Africa-Arabia-Eurasia continental collision zone and implications for the dynamics of plate interactions, *Journal of Geophysical Research: Solid Earth*, *111*(B5), B05411, doi:10.1029/2005JB004051.

Ruh, J. B., T. Gerya, and J. P. Burg (2013), High-resolution 3D numerical modeling of thrust wedges: Influence of decollement strength on transfer zones, *Geochemistry Geophysics Geosystems*, *14*(4), 1131-1155, doi:10.1002/ggge.20085.

Ruh, J. B., T. Gerya, and J. P. Burg (2014), 3D effects of strain vs. velocity weakening on deformation patterns in accretionary wedges, *Tectonophysics*, *615*, 122-141, doi:10.1016/j.tecto.2014.01.003.

Ruh, J. B., B. J. P. Kaus, and J. P. Burg (2012), Numerical investigation of deformation mechanics in fold-and-thrust belts: Influence of rheology of single and multiple decollements, *Tectonics*, *31*, doi:10.1029/2011tc003047.

Sapkota, S. N., L. Bollinger, Y. Klinger, P. Tapponnier, Y. Gaudemer, and D. Tiwari (2013), Primary surface ruptures of the great Himalayan earthquakes in 1934 and 1255, *Nature Geosci*, *6*(1), 71-76.

Savage, J. C. (1983), A Dislocation Model of Strain Accumulation and Release at a Subduction Zone, *Journal of Geophysical Research*, *88*(B6), 4984-4996.

Scharer, K. M., D. W. Burbank, J. Chen, R. J. Weldon, C. Rubin, R. Zhao, and J. Shen (2004), Detachment folding in the Southwestern Tian Shan-Tarim foreland, China: shortening estimates and rates, *Journal of Structural Geology*, *26*(11), 2119-2137, doi:10.1016/j.jsg.2004.02.016.

Scholz, C. H. (1988), The brittle-plastic transition and the depth of seismic faulting, *Geologische Rundschau*, *77*(1), 319-328, doi:10.1007/bf01848693.

Scholz, C. J. (1998), Earthquakes and friction laws, *Nature*, *391*, 37-42.

Schurr, B., et al. (2014), Gradual unlocking of plate boundary controlled initiation of the 2014 Iquique earthquake, *Nature*, *512*(7514), 299-302, doi:10.1038/nature13681.

Schurr, B., G. Asch, M. Rosenau, R. Wang, O. Oncken, S. Barrientos, P. Salazar, and J. P. Vilotte (2012), The 2007 M7.7 Tocopilla northern Chile earthquake sequence: Implications for along-strike and downdip rupture segmentation and megathrust frictional behavior, *J Geophys Res-Sol Ea*, *117*, doi:10.1029/2011jb009030.

Segall, P., and J. L. Davis (1997), GPS applications for geodynamics and earthquake studies, *Annual Review of Earth and Planetary Sciences*, *25*, 301-336, doi:Doi 10.1146/Annurev.Earth.25.1.301.

Selzer, C., S. J. H. Buiter, and O. A. Pfiffner (2007), Sensitivity of shear zones in orogenic wedges to surface processes and strain softening, *Tectonophysics*, *437*(1–4), 51-70, doi:10.1016/j.tecto.2007.02.020.

Shamir, G., and Y. Eyal (1995), Elastic modeling of fault-driven monoclinal fold patterns, *Tectonophysics*, *245*(1–2), 13-24, doi:10.1016/0040-1951(94)00250-D.

Simoes, M., J. P. Avouac, and Y. G. Chen (2007a), Slip rates on the Chelungpu and Chushiang thrust faults inferred from a deformed strath terrace along the Dungpuna river, west central Taiwan, *J Geophys Res-Sol Ea*, *112*(B3), doi:10.1029/2005jb004200.

Simoes, M., J. P. Avouac, Y. G. Chen, A. K. Singhvi, C. Y. Wang, M. Jaiswal, Y. C. Chan, and S. Bernard (2007b), Kinematic analysis of the Pakuashan fault tip fold, west central

Taiwan: Shortening rate and age of folding inception, *J Geophys Res-Sol Ea*, *112*(B3), doi:10.1029/2005jb004198.

Simons, M. (2007), Interferometric Synthetic Aperture Radar Geodesy, in *Treatise on Geophysics*, edited by G. Schubert, pp. 351-390.

Simpson, G. (2011), Mechanics of non-critical fold-thrust belts based on finite element models, *Tectonophysics*, *499*(1-4), 142-155, doi:10.1016/j.tecto.2011.01.004.

Simpson, G. D. H. (2006), Modelling interactions between fold-thrust belt deformation, foreland flexure and surface mass transport, *Basin Research*, *18*(2), 125-143, doi:10.1111/j.1365-2117.2006.00287.x.

Simpson, G. D. H. (2009), Mechanical modelling of folding versus faulting in brittle-ductile wedges, *Journal of Structural Geology*, *31*(4), 369-381, doi:10.1016/j.jsg.2009.01.011.

Stein, R. S., and S. E. Barrientos (1985), Planar High-Angle Faulting in the Basin and Range: Geodetic Analysis of the 1983 Borah Peak, Idaho, Earthquake, *Journal of Geophysical Research-Solid Earth and Planets*, *90*(NB13), 1355-1366, doi:10.1029/JB090iB13p11355.

Stein, R. S., and G. Ekstrom (1992), Seismicity and Geometry of a 110-km-Long Blind Thrust Fault 2. Sythesis of the 1982-1985 California Earthquake Sequence, *J Geophys Res-Sol Ea*, *97*(B4), 4865-4883, doi:10.1029/91jb02847.

Stein, R. S., and G. C. P. King (1984), Seismic Potential Revealed by Surface Folding: 1983 Coalinga, California, Earthquake, *Science*, *224*(4651), 869-872, doi:10.2307/1692290.

Stein, R. S., G. C. P. King, and J. B. Rundle (1988), The Growth of Geological Structures by Repeated Earthquakes .2. Field Examples of Continental Dip-Slip Faults, *Journal of Geophysical Research-Solid Earth and Planets*, *93*(B11), 13319-13331, doi:Doi 10.1029/Jb093ib11p13319.

Stein, R. S., and S. Toda (2013), Megacity Megaquakes-Two Near Misses, *Science*, *341*(6148), 850-852, doi:10.1126/science.1238944.

Stockmal, G. S. (1983), Modeling of large-scale accretionary wedge deformation, *Journal of Geophysical Research*, *88*(NB10), 8271-8287, doi:10.1029/JB088iB10p08271.

Stockmal, G. S., C. Beaumont, M. Nguyen, and B. Lee (2007), Mechanics of thin-skinned fold-and-thrust belts: Insights from numerical models, in *Whence the Mountains? Inquiries into the Evolution of Orogenic Systems: A Volume in Honor of Raymond A. Price*, edited by J. W. Sears, T. A. Hairns and C. A. Evenchick, pp. 63-98, The Geological Society of America.

Stolar, D., G. Roe, and S. Willett (2007), Controls on the patterns of topography and erosion rate in a critical orogen, *J Geophys Res-Earth*, *112*(F4), doi:10.1029/2006jf000713.

Storti, F., and K. McClay (1995), INFLUENCE OF SYNTECTONIC SEDIMENTATION ON THRUST WEDGES IN ANALOG MODELS, *Geology*, *23*(11), 999-1002, doi:10.1130/0091-7613(1995)023<0999:iossot>2.3.co;2.

Strecker, M. R., R. N. Alonso, B. Bookhagen, B. Carrapa, G. E. Hilley, E. R. Sobel, and M. H. Trauth (2007a), Tectonics and climate of the southern Central Andes, *Annual Review of Earth and Planetary Sciences*, *35*, 747-787.

Strecker, M. R., A. Mulch, C. Uba, A. Schmitt, and P. Chamberlain (2007b), Climate change in the southern central Andes at 8 Ma, *Geochimica Et Cosmochimica Acta*, *71*(15), A980-A980.

Suppe, J., G. T. Chou, and S. C. Hook (1992), Rates of folding and faulting determined from growth strata, in *Thrust Tectonics*, edited by K. R. McClay, pp. 105-122, Chapman and Hall, London.

Suppe, J., and D. Medwedeff (1990), Geometry and kinematics of fault-propagation folding, *Eclogae Geologicae Helvetiae*, *83*(3), 409-454.

Timoshenko, S. P., and J. N. Goodier (1970), *Theory of Elasticity*, 587 pp., McGraw-Hill Inc.

Toké, N. A., J. R. Arrówsmith, M. J. Rymer, A. Landgraf, D. E. Haddad, and M. Busch (2012), Lat Holocene slip rate of the San Andreas fault and its accommodation by creep and moderate-magnitude earthquakes at Parkfield, California, *Geology*, *39*(3), 243-246, doi:10.1130/G31498.1.

Tregoning, P., R. Burgette, S. C. McClusky, S. Lejeune, C. S. Watson, and H. McQueen (2013), A decade of horizontal deformation from great earthquakes, *Journal of Geophysical Research: Solid Earth*, *118*(5), 2371-2381, doi:10.1002/jgrb.50154.

Uba, C. E., C. Heubeck, and C. Hulka (2006), Evolution of the late Cenozoic Chaco foreland basin, southern Bolivia, *Basin Research*, *18*(2), 145-170.

Uba, C. E., J. Kley, M. Strecker, and A. K. Schmitt (2009), Unsteady evolution of the Bolivian Subandean thrust belt: The role of enhanced erosion and clastic wedge progradation, *Earth and Planetary Science Letters*, *281*, 134-146.

Uba, C. E., M. R. Strecker, and A. K. Schmitt (2007), Increased sediment accumulation rates and climatic forcing in the Central Andes during the late Miocene, *Geology*, *35*(11), 979-982.

van Dinther, Y., P. M. Mai, L. A. Dalguer, and T. V. Gerya (2014), Modeling the seismic cycle in subduction zones: The role and spatiotemporal occurrence of off-megathrust

earthquakes, *Geophysical Research Letters*, *41*(4), 1194-1201, doi:10.1002/2013GL058886.

Vergés, J., D. W. Burbank, and A. Meigs (1996), Unfolding: an inverse approach to fold kinematics, *Geology*, *24*, 175-178.

Vergne, J., R. Cattin, and J. P. Avouac (2001), On the use of dislocations to model interseismic strain and stress build-up at intracontinental thrust faults, *Geophys. J Int.*, *147*, 155-162.

Vigny, C., et al. (2005), Insight into the 2004 Sumatra-Andaman earthquake from GPS measurements in southeast Asia, *Nature*, *436*(7048), 201-206, doi:10.1038/nature03937.

Vigny, C., et al. (2011), The 2010 Mw 8.8 Maule Megathrust Earthquake of Central Chile, Monitored by GPS, *Science*, *332*(6036), 1417-1421, doi:10.1126/science.1204132.

Wang, C.-y., W.-t. Hwang, and G. R. Cochrane (1994), Tectonic dewatering and mechanics of protothrust zones: Example from the Cascadia accretionary margin, *Journal of Geophysical Research: Solid Earth*, *99*(B10), 20043-20050, doi:10.1029/94JB01545.

Wang, K. L., and Y. Hu (2006), Accretionary prisms in subduction earthquake cycles: The theory of dynamic Coulomb wedge, *J Geophys Res-Sol Ea*, *111*(B6), doi:10.1029/2005jb004094.

Wang, K. L., Y. Hu, and J. H. He (2012), Deformation cycles of subduction earthquakes in a viscoelastic Earth, *Nature*, *484*(7394), 327-332, doi:10.1038/nature11032.

Ward, S. N., and G. Valensise (1994), The Palos-Verdes Terraces, California - Bathtub Rings from a Buried Reverse-Fault, *J Geophys Res-Sol Ea*, *99*(B3), 4485-4494, doi:Doi 10.1029/93jb03362.

Weiss, J. R., B. A. Brooks, J. R. Arrowsmith, and G. Vergani (2015), Spatial and temporal distribution of deformation at the front of the Andean orogenic wedge in southern Bolivia, *Journal of Geophysical Research: Solid Earth*, *120*(3), 1909-1931, doi:10.1002/2014JB011763.

Weiss, J. R., B. A. Brooks, J. Foster, M. Bevis, A. Echalar, D. Caccamise, and J. Heck (in prep.), Isolating active orogenic wedge deformation in the southern Bolivian Subandes.

Wessel, P., W. H. F. Smith, R. Scharroo, J. Luis, and F. Wobbe (2013), Generic Mapping Tools: Improved Version Released, *Eos, Transactions American Geophysical Union*, *94*(45), 409-410, doi:10.1002/2013EO450001.

Whipple, K. X. (2009), The influence of climate on the tectonic evolution of mountain belts, *Nature Geoscience*, *2*, doi:doi: 10.1038/ngeo413.

Whipple, K. X., and B. J. Meade (2004), Controls on the strength of coupling among climate, erosion, and deformation in two-sided, frictional orogenic wedges at steady state, *Journal of Geophysical Research*, *109*, no.F1, 24.

Willett, S., C. Beaumont, and P. Fullsack (1993), Mechanical model for the tectonics of doubly vergent compressional orogens, *Geology*, *21*(4), 371-374, doi:10.1130/0091-7613(1993)021<0371:mmftto>2.3.co;2.

Willett, S. D. (1992), Dynamic and kinematic growth and change of a Coulomb wedge, in *Thrust Tectonics*, edited by K. R. McClay, pp. 19-31, Chapman and Hall, London.

Willett, S. D. (1999), Orogeny and orography: The effects of erosion on the structure of mountain belts, *J Geophys Res-Sol Ea*, *104*(B12), 28957-28981, doi:Doi 10.1029/1999jb900248.

Williams, S. D. P. (2003), The effect of coloured noise on the uncertainties of rates estimated from geodetic time series, *Journal of Geodesy*, *76*(9-10), 483-494, doi:Doi 10.1007/S00190-002-0283-4.

Williams, S. D. P., Y. Bock, P. Fang, P. Jamason, R. M. Nikolaidis, L. Prawirodirdjo, M. Miller, and D. J. Johnson (2004), Error analysis of continuous GPS position time series, *J Geophys Res-Sol Ea*, *109*(B3), doi:10.1029/2003jb002741.

Wobus, C., A. Heimsath, K. Whipple, and K. Hodges (2005), Active out-of-sequence thrust faulting in the central Nepalese Himalaya, *Nature*, *434*, 1008-1010.

Wright, T. J. (2002), Remote Monitoring of the Earthquake Cycle Using Satellite Radar Interferometry, *Philosophical Transactions: Mathematical, Physical and Engineering Sciences*, *360*(1801), 2873-2888, doi:10.2307/3558932.

Yagupsky, D., B. A. Brooks, K. X. Whipple, C. C. Duncan, and M. Bevis (2014), Distribution of active faulting along orogenic wedges: Minimum-work models and natural analogue, *Journal of Structural Geology*, *66*, 237-247.

Ye, L., T. Lay, H. Kanamori, and K. Koper (2015), Rapidly Estimated Seismic Source Parameters for the 16 September 2015 Illapel, Chile M w 8.3 Earthquake, *Pure and Applied Geophysics*, 1-12, doi:10.1007/s00024-015-1202-y.

Yue, L.-F., J. Suppe, and J.-H. Hung (2005), Structural geology of a classic thrust belt earthquake: the 1999 Chi-Chi earthquake Taiwan (Mw=7.6), *Journal of Structural Geology*, *27*(11), 2058-2083.

Yue, L. F., J. Suppe, and J.-H. Hung (2011), Two contrasting kinematic styles of active folding above thrust ramps, western Taiwan, in *Thrust fault-related folding: AAPG Memoir 94*, edited by K. McClay, J. H. Shaw and J. Suppe, pp. 153-186.

Zechar, J. D., and K. L. Frankel (2009), Incorporating and reporting uncertainties in fault slip rates, *J Geophys Res-Sol Ea*, *114*, doi:10.1029/2009jb006325.

Zhang, J., Y. Bock, H. Johnson, P. Fang, S. Williams, J. Genrich, S. Wdowinski, and J. Behr (1997), Southern California Permanent GPS Geodetic Array: Error analysis of daily position estimates and site velocities, *J Geophys Res-Sol Ea*, *102*(B8), 18035-18055, doi:Doi 10.1029/97jb01380.

Zilio, L. D., Y. v. Dinther, and T. Gerya (2015), The long-term seismic cycle in collisional margins: insights from Seismo-Thermo-Mechanical models, paper presented at the 2015 AGU Fall Meeting, San Francisco.